POLITECNICO DI TORINO

SCUOLA DI DOTTORATO
Dottorato in Ingegneria Aerospaziale – XXIV ciclo

Tesi di Dottorato

Modelling-based design of anisotropic piezocomposite transducers and multi-domain analysis of smart structures

Fabio Biscani

Tutore
Prof. Erasmo Carrera
Dr. Houssein Nasser

Coordinatore del corso di dottorato

Prof.ssa Fulvia Quagliotti

Acknowledgements

This PhD research project is supported by the National Research Fund (FNR) of Luxembourg in the context of the FNR CORE project "Advanced Non-Linear Modelling of the Electromechanical Effective Properties of Macro Fibre Composites and Design of a Directional Dynamic Actuation Device - MAFICOMECH". The financial support of Universitá Italo Francese under Bando UIF 2009 is also gratefully acknowledged.

I would like to thank Erasmo Carrera and Houssein Nasser for their support, their guidance and their substantial contribution to this thesis. The time I spent in Luxembourg in CRP Henri Tudor would not have been so fruitful and enjoyable without the advises, the ideas and the company of Salim Belouettar. The help of the staff of the AMS department, in particular of the MODSI unit, is greatly appreciated. I am most grateful to Yao Koutsawa, for his generous support and precious contribution, to Gaetano Giunta, for teaching me a job and for a friendship that will last, and to Heng Hu, for introducing me to multi-domain techniques. I want to extend my warm gratitude to my colleagues at DIASP Alberto Torasso, Davide Lasagna and Guido Ridolfi, to my supervisor-mates, in particular Maria Cinefra, Marco Petrolo and Enrico Zappino, to Vanessa Georges, for her contribution, and to Pietro Nali, whose support is highly appreciated.

Summary

Piezocomposites are attracting widespread interest since they can offer greater flexibility and better performances in specific applications with respect to traditional piezoelectric wafers. Design of piezocomposites requires accurate homogenisation models for the prediction of the equivalent electro-mechanical properties. In macro-scale models of structures with piezocomposite transducers, these properties are adopted in order to avoid the complexity of the piezocomposite microstructure. In the case of smart structures the accurate modelling of the actuation and the response of the structure is of primary importance. If classical structural finite elements are not sufficiently accurate, higher order or solid elements should be adopted. Thanks to adaptation or mixed-dimensional methods, it is possible to adopt computationally expensive higher order or solid elements only in some sub-domains of the structure.

In this work, the modelling of smart structures equipped with thin piezoelectric transducers is considered in a multi-scale framework. Micromechanical homogenisation models are developed and employed for the prediction of the equivalent properties of piezocomposites. A micromechanical model based on the concept of inclusion is proposed to investigate the influence of the shape of the inclusions, of the constituent materials and of the polarisation on the equivalent properties. It has been found that fibre-shaped inclusions should be considered in order to obtain piezocomposites with strong piezoelectric effect and to have at the same time high direction-dependence. The equivalent properties of Macro Fiber Composites are determined via the Asymptotic Homogenisation Method (AHM) with an analytical solution and with a numerical solution via FEM which takes into account the effect of the electrodes.

AHM analytical solution is adopted to investigate the effect of the material properties of the matrix on the overall piezocomposite. Results indicate that low values of the Young's modulus and of the Poisson's ratio yield high directional dependence in the piezoelectric properties. A laminated design with anisotropic layers and a piezocomposite layer is investigated via UFM. A configuration with maximum directional dependence in terms of equivalent piezoelectric strain constants is proposed, whereas maximum directional dependence in terms of piezoelectric stress constants is proved to be not achievable with such a design.

Hierarchical finite elements for structural analyses based on a Unified Formulation (UF) by Carrera are developed and coupled via the Arlequin method proposed by Ben Dhia. Solid, plate and beam finite elements for mechanical and for piezoelectric problems are presented. Via UF, higher order and piezoelectric elements can be formulated

straightforwardly. These elements are combined in variable kinematic solutions in the Arlequin framework. Higher-order elements are adopted locally where the stress field is three-dimensional, whereas the remaining parts of the structure are modelled with computationally cheap lower-order elements. Two electro-mechanical coupling operator for the Arlequin method in the context of piezoelectric analyses are proposed. Results are validated towards monomodel solutions and three-dimensional analytical and numerical reference solutions. Accurate solutions are obtained reducing the computational costs.

Sommario

I compositi piezoelettrici attraggono grande interesse poiché offrono maggiore flessibilità e prestazioni migliori rispetto ai wafer piezoelettrici tradizionali in alcune applicazioni. Il design di un composito piezoelettrico richiede modelli di omogenizzazione accurati per predire le proprietà elettro-meccaniche equivalenti. In modelli macro-scala di strutture con trasduttori compositi piezoelettrici, queste proprietà sono adottate in modo da evitare la complessità della microstruttura del composito piezoelettrico. Nel caso di strutture intelligenti, la modellizzazione accurata dell'attuazione e della risposta della struttura è di primaria importanza. Se gli elementi finiti strutturali classici non sono sufficientemente accurati, elementi di alto ordine o solidi possono essere adottati. Grazie a metodi di adattamento o mixed-dimensional è possibile adottare elementi di alto ordine o solidi, che sono costosi dal punto di vista computazionale, solo in alcuni sotto-domini della struttura.

In questo lavoro, la modellazione di strutture intelligenti munite di trasduttori piezoelettrici sottili è considerata in un ambito multi-scala. Modelli micromeccanici di omogenizzazione sono sviluppati e impiegati per la predizione delle proprietà equivalenti di compositi piezoelettrici. Un modello micromeccanico basato sul concetto d'inclusione è proposto per investigare l'influenza della forma dell'inclusione, dei materiali impiegati e della polarizzazione sulle proprietà equivalenti. I risultati indicano che inclusioni a forma di fibra dovrebbero essere considerate per ottenere compositi piezoelettrici con forte effetto piezoelettrico e per avere allo stesso tempo alta dipendenza direzionale. Le proprietà equivalenti di Macro Fiber Composites sono determinate con l'Asymptotic Homogenisation Method (AHM) attraverso una soluzione analitica e una numerica via FEM che prende in considerazione l'effetto degli elettrodi.

La soluzione AHM analitica è adottata per investigare l'effetto delle proprietà del materiale della matrice sull'intero composito piezoelettrico. I risultati indicano che bassi valori del modulo di Young e del coefficiente di Poisson portano ad un alta dipendenza direzionale delle proprietà piezoelettriche. Un design di un laminato con strati anisotropi e uno strato composito piezoelettrico è investigato attraverso lo Uniform Field Method. Una configurazione con massima dipendenza direzionale in termini di costanti piezoelettriche di deformazione è proposta, mentre si dimostra che massima dipendenza direzionale in termini di costanti piezoelettriche di tensione non è realizzabile con questo design.

Elementi finiti gerarchici per analisi strutturali basati su un Unified Formulation (UF) ideata da Carrera sono sviluppati ed accoppiati con il metodo Arlequin proposto da Ben Dhia. Elementi solidi, piastra e trave per problemi meccanici e piezoelettrici sono presentati. Attraverso l'UF, elementi finiti di alto ordine possono essere formulati facilmente.

Questi elementi sono accoppiati in soluzioni a cinematica variabile nell'ambito del metodo Arlequin. Elementi di alto ordine sono adottati localmente dove il campo di tensioni è tridimensionale, mentre le alte parti della struttura sono modellate con elementi di basso ordine che sono economici dal punto di vista computazionale. Due operatori di accoppiamento per il metodo Arlquin nel contesto di analisi piezoelettriche sono proposti. I risultati sono validati rispetto a soluzioni mono-modello e soluzioni tridimensionali di riferimento analitiche o numeriche. Risultati accurati sono ottenuti riducendo il costo computazionale.

Résumé

Les capteurs/actionneurs composite à fibres piézoélectriques avec des polymères ont des avantages en termes de flexibilité et de performance par rapport au capteur piézoélectrique monolithique. La conception de piezocomposites nécessite des modèles d'homogénéisation précise pour la prédiction de ses propriétés équivalentes électromécaniques. Ces propriétés sont adoptées en modèles macro-échelle des structures avec des capteurs/actionneurs piezocomposites afin d'éviter la complexité de la microstructure. Dans le cas des structures intelligentes la modélisation précise de l'actionnement et de la réponse de la structure active est d'une importance primordiale. Dans le cas où les éléments finis classiques structurelles ne sont pas suffisamment précis, des éléments d'ordre supérieur ou solides doivent être adoptés. Grace à des méthodes d'adaptation ou à dimensions mixte il est possible désigner des éléments d'ordre supérieur ou des éléments solides qu'ils ont coût numérique élevé, que dans certains sous-domaines de la structure.

Dans le cadre de ce travail, la modélisation de structures intelligentes équipées de capteurs/actionneurs piézoélectriques minces est considérée dans un cadre multi-échelle. Différents modèles d'homogénéisation micromécanique sont développés et utilisés pour la prédiction des propriétés équivalentes du piezocomposites. Le premier modèle micromécanique basé sur le concept d'inclusion est proposé pour étudier l'influence de la forme des inclusions, des matériaux constitutifs et de la polarisation sur les propriétés équivalentes. On a constaté que les inclusions en forme de fibre doivent être considérées afin d'obtenir piezocomposites avec effet piézoélectrique important et d'avoir en même temps maximum dépendance à la direction de la déformation. Les propriétés équivalentes de Macro Fiber Composites sont déterminées par la Méthode d'Homogénéisation Asymptotique (MHA) avec une solution analytique et une solution numérique Eléments Finis EF qui prend en compte l'effet des électrodes.

La solution analytique AHM est adoptée pour étudier l'effet des propriétés du matériau de la matrice sur le piezocomposite globale. Les résultats indiquent que de faibles valeurs de module d'Young et du coefficient de Poisson donnent haut dépendance directionnelle pour les propriétés piézoélectriques. Un design stratifié avec des couches anisotropes et une couche piezocomposite est étudié en utilisant la méthode des champs uniformes. Une configuration avec dépendance directionnelle maximale de la réponse du capteur en termes des constantes piézoélectriques des déformations équivalent est faisable, tandis que la dépendance directionnelle maximale en termes de constantes piézoélectrique des contraints est démontré de ne pas être réalisable avec une telle conception.

Éléments finis hiérarchiques pour l'analyse structurale basée sur une Formulation Unifiée (FU) de Carrera sont développés et couplés via la méthode Arlequin proposée par Ben Dhia. Éléments finis solide, plaque et poutre pour des problèmes mécanique et piézo-électriques sont présentés. Avec le FU, éléments d'ordre supérieur et piézo-électriques peuvent être formulé d'une façon directe. Ces éléments sont combinés dans solutions à cinématiques variable dans le cadre d'Arlequin. Éléments d'ordre supérieur sont adoptées localement là où le champ de contrainte est trois dimensionnelle, tandis que les autres parties de la structure sont modélisés par éléments d'ordre inférieur avec un cout de calcul réduit. Deux opérateurs de couplage électromécaniques pour la méthode Arlequin dans le

contexte des analyses piézoélectriques sont proposés. Les résultats sont validés en utilisant des solutions mono-model et des solutions analytiques et numériques de référence en trois dimensions.

Contents

Chapter 1

Introduction

Much research in the last decades has focused on smart structures with piezoelectric layers or patches. Piezocomposite transducers have found application as commercial products in different engineering fields, such as automotive, aerospace, biomedical and civil engineering. In smart structures, piezocomposite have been adopted as sensors and actuators for structural health monitoring and vibration control applications. Their appealing factor is represented by the possibility to obtain tailored electro-mechanical properties for specific applications and to overcome classical limitations of monolithic transducers in terms of flexibility, durability and reliability. The adoption of light and flexible non-piezoelectric polymers in combination with piezoelectric ceramics in a multiphase construction leads to a more robust device, capable of conforming to complex surface shapes.

In general, piezoelectric effect is transverse isotropic with respect to the poling direction of the material: a classical monolithic piezoelectric transducer has isotropic in-plane behaviour, i.e. its response as a strain sensor is independent of its orientation. In piezocomposites this is no longer valid, since the electro-mechanical interaction among the phases changes the global piezoelectric response of the transducer. Piezocomposite transducers such as Macro Fiber Composite (MFC) and Active Fiber Composite (AFC), have anisotropic electromechanical behaviours since the active fibres are aligned in one direction and embedded into a soft epoxy matrix. As a consequence, piezoelectric response can be highly directional dependent and varies with the angle between the in-plane strain component and the fibres direction. The directionality of the piezoelectric effect can be employed to realise transducers that can detect the direction of propagation of elastic waves, such as ultrasounds or Lamb-waves, or can measure the components of the stress and strain tensors with different sensibility.

The investigation of piezocomposite transducers requires accurate models for the prediction of the behaviour of the transducer on the basis of its microstructure. Non-conventional electrode patterns and complex microstructures require more detailed homogenisation models, for which analytical solutions are not generally available. Most of the time these techniques are developed as extensions of the ones already established for pure elastic materials. Design of piezoelectric transducers requires a clear understanding of the electromechanical

behaviour of smart structures, comprehensive analytical models and multi-domain methods. The research work of this thesis associates modelling based design of piezoelectric transducers and hierarchical finite element modelling of smart structures. The first objective is dedicated to the modelling and the design of unidirectional piezoelectric transducers. Such transducers have the advantage of measuring in one direction in contrast of the existing piezoelectric transducers. This result allows developing a multi-axial sensor/actuator for vibration and noise control systems.

Piezocomposites are usually employed as surface-bonded patches on smart structures. Once accurate equivalent properties are retrieved for piezoelectric transducers, numerically or experimentally, the response of the structure can be predicted via finite element analyses. Finite elements of different type, for instance beam, plate and solid elements, can be adopted to model the structure. Solid elements, being not based on a particular cinematic model, are the most general elements and can be always used. The drawback is that they are computationally expensive when adopted to model thin or slender structures. Beam and plate elements should be preferred in these cases. In the most accurate and computationally efficient approach, the structure should be decomposed in sub-domains and modelled with different kind of finite elements depending on the characteristics of the sub-domains. Computational techniques known as adaptation or mixed-dimensional methods have been developed to address this possibility. In this way, memory requirements and time consumptions of the analysis can be reduced drastically.

Nevertheless, classical beam and plate finite elements may be inaccurate under some conditions: when material properties are highly anisotropic and vary in space, as in multilayered plates; when thickness ratio are small, as in thick plates; when the beam cross section is thin-walled or is subject to warping or torsion; when a three-dimensional strain/stress state is locally present due to localised loading conditions, as with actuated piezoelectric patches. Classical structural elements are usually not suited in the case of smart plates or beams with piezoelectric layers or patches. In order to increase the accuracy, higher order elements can be developed in a hierarchical framework. In this framework, developed by Carrera and known as Unified Formulation (UF), it is also possible to develop multifield elements, such as piezoelectric elements that model the electric potential as a primary unknown together with displacement components. Solid elements and higher order elements can be adopted locally where the stress field is three-dimensional, whereas the remaining parts of the structure can be modelled with computationally cheap lower-order beam and plate finite elements. The second objective is dedicated to develop a consistent framework for the multi-domain analysis of smart structures.

The organisation of the thesis is detailed in the following. The constitutive equations and governing equations of linear piezo-elasticity are introduced in chapter 2. A global overview on piezoelectric transducers is also presented. Many piezocomposite transducers are described and commented on the basis of characteristics and performances. The problem of the homogenisation of the electro-mechanical properties of a piezocomposite is tackled in chapter 3. A micromechanical model to predict the equivalent properties based on the concept of inclusion is developed. The influence of the constituent material, of the shape of the inclusions and of the direction of polarisation on the equivalent piezoelectric properties is investigated in terms of magnitude and directionality. The equivalent

properties of Macro Fiber Composites (MFC) are computed on the basis of the Asymptotic Homogenisation Method (AHM) and results are validated towards the Uniform Field Method (UFM), the Periodic Homogenisation Method and manufacturer's datasheet. The influence of the electrodes is discussed. The effect of the properties of the matrix on the equivalent properties of MFC is investigated in chapter 4 via the AHM. Directionality of the piezoelectric effect is considered varying the volume fraction, the Young's modulus and the Poisson's ratio of the matrix. A similar study is presented in chapter 5, where additional anisotropic mechanical layers are considered via UFM. On the basis of the orientation and of the thickness of these layers, tailored equivalent piezoelectric properties can be achieved. Directionality of the piezoelectric effect is examined both for the single transducer and for a transducer mounted as a patch on a structure.

A particular set of hierarchical finite elements for the analysis of structures is the subject of chapter 6. Solid, plate and beam finite elements for mechanical problem as well as for piezoelectric ones are developed thanks to UF. Higher order and multifield elements are obtained straightforwardly from fundamental nucleus that depends only on the chosen variational principle. These finite elements are coupled in linear static analyses in chapter 7 via the Arlequin method. Coupling among finite elements of different order and based on different variational principles is addressed. Two electro-mechanical coupling operators for the Arlequin method are proposed in chapter 8. Variable-kinematic results in the UF framework for piezoelectric plates are presented. A user defined element to implement the Arlequin method for piezoelectric problems in the commercial software ABAQUS is also addressed.

Chapter 2

Piezoceramics and piezocomposite materials

Piezoelectricity is the ability of some materials to convert an electric stimulus into mechanical energy, and vice versa. Piezoelectric materials are currently being used in a number of applications such as submarine hydrophones, accelerometers, microphones, ultrasonic devices, electronic resonators, *etc.* In this thesis, particular attention is devoted to devices that can be adopted as sensors and actuators in structures. Different types of piezoelectric devices are used as components of passive or active system in smart structures, including Active Fiber Composite (AFC), Macro Fiber Composite (MFC), THUNDER transducers, etc. Typical applications are control of vibrations, noise reduction, morphing and structural health monitoring.

Piezoceramic materials such as lead zirconate titanium (PZT) and barium titanate ($PbTiO_3$) are used extensively. They possess strong piezoelectric effect but they are exposed to crack damage due to their brittle nature and are non-conformable to curved surfaces. Piezoelectric polymers such as polyvinylidene fluoride (PVDF) are characterised by low density and good flexibility, but the electromechanical coupling is weaker with respect to piezoceramic materials.

This chapter introduces the general constitutive equations of piezoelectric materials. Piezoelectric and dielectric properties are detailed both in matrix and tensor form. The governing equations of piezoelasticity are also presented. A global overview on piezoelectric transducers follows. Several monolithic as well as piezocomposite transducers are discussed.

2.1 Constitutive and governing equations

During the machining process, after sintering, polycrystalline piezoceramics have isotropic properties at the macro-scale. After the poling process, the behaviour of the piezoelectric material becomes transverse isotropic with respect to the poling direction, usually referred to as direction 3. The linear constitutive equations of piezoelectric materials involve linear coupling between stress, strain, electric field and electric displacement (or between force, displacement, electric charge and electric potential). Linear piezoelectricity discards effects

like time-dependent responses, hysteresis and electrostriction. In this paragraph Voigt's notation is adopted: in a Cartesian coordinate system, the subscripts 1, 2, 3, 4, 5 and 6 represent the subscripts x, y, z, yz, xz and xy, respectively. The constitutive equations for orthotropic piezoelectric materials using the notations of the *IEEE standard on piezoelectricity* [1] are as follows:

Sensing: the direct piezoelectric effect refers to the conversion of mechanical energy into electric energy:

$$\{\mathbf{D}\} = [\mathbf{e}]\{\mathbf{S}\} + \left[\boldsymbol{\varepsilon}^S\right]\{\mathbf{E}\} \tag{2.1}$$

Actuation: the converse piezoelectric effect refers to the conversion of electric energy into mechanical energy:

$$\{\mathbf{T}\} = \left[\mathbf{C}^E\right]\{\mathbf{S}\} - \left[\mathbf{e}^T\right]\{\mathbf{E}\} \tag{2.2}$$

where $\{\mathbf{E}\}$, $\{\mathbf{D}\}$ are the electric field vector and the electric displacement vector, and $\{\mathbf{T}\}$, $\{\mathbf{S}\}$ are the stress and strain vectors. $\left[\mathbf{C}^E\right]$, $[\mathbf{e}]$ and $\left[\boldsymbol{\varepsilon}^S\right]$ are respectively the stiffness matrix at constant electric field, the stress piezoelectric coefficients and the permittivity at constant strain. The piezoelectric material is assumed to be polarised along direction 3.

The constitutive Eqs. 2.1 and 2.2 can be expressed as:

$$\underbrace{\begin{Bmatrix} T_1 \\ T_2 \\ T_3 \\ T_4 \\ T_5 \\ T_6 \\ D_1 \\ D_2 \\ D_3 \end{Bmatrix}}_{\mathbf{T_g}} = \underbrace{\begin{bmatrix} C_{11}^E & C_{12}^E & C_{13}^E & 0 & 0 & 0 & 0 & 0 & -e_{31} \\ C_{12}^E & C_{22}^E & C_{23}^E & 0 & 0 & 0 & 0 & 0 & -e_{32} \\ C_{13}^E & C_{23}^E & C_{33}^E & 0 & 0 & 0 & 0 & 0 & -e_{31} \\ 0 & 0 & 0 & C_{44}^E & 0 & 0 & 0 & -e_{24} & 0 \\ 0 & 0 & 0 & 0 & C_{55}^E & 0 & -e_{15} & 0 & 0 \\ 0 & 0 & 0 & 0 & 0 & C_{66}^E & 0 & 0 & 0 \\ 0 & 0 & 0 & 0 & e_{15} & 0 & \epsilon_{11}^s & 0 & 0 \\ 0 & 0 & 0 & e_{24} & 0 & 0 & 0 & \epsilon_{22}^s & 0 \\ e_{31} & e_{32} & e_{33} & 0 & 0 & 0 & 0 & 0 & \epsilon_{33}^s \end{bmatrix}}_{\text{generalised constitutive matrix } \mathbf{C_g}} \underbrace{\begin{Bmatrix} S_1 \\ S_2 \\ S_3 \\ S_4 \\ S_5 \\ S_6 \\ E_1 \\ E_2 \\ E_3 \end{Bmatrix}}_{\mathbf{S_g}} \tag{2.3}$$

The left hand vector $\{\mathbf{T_g}\}$, called vector of generalised stresses, contains the stress and the electric displacement components. The right hand vector $\{\mathbf{S_g}\}$ is the vector of generalised strains and it contains the strain and the electric field components. The matrix $[\mathbf{C_g}]$ is called generalised constitutive matrix. It is built on the basis of the elastic, the piezoelectric and the dielectric properties.

Eqs. 2.1 and 2.2 are written as stresses and electric displacements in terms of strains and electric field. Alternatively, the constitutive equations can be written in another form as strains and electric displacements in terms of stresses and electric field:

$$\begin{cases} \{\mathbf{D}\} = [\mathbf{d}]\{\mathbf{T}\} + \left[\boldsymbol{\varepsilon}^T\right]\{\mathbf{E}\} \\ \{\mathbf{S}\} = \left[\mathbf{S}^E\right]\{\mathbf{T}\} + \left[\mathbf{d}^T\right]\{\mathbf{E}\} \end{cases} \tag{2.4}$$

where $\left[\mathbf{S}^E\right]$, $\{\mathbf{T}\}$ and $\left[\boldsymbol{\varepsilon}^T\right]$ are respectively the compliance matrix at constant electric field, the strain piezoelectric properties and the permittivity at constant stress. The relationships

between the two considered forms of constitutive equations are:

$$\begin{aligned} \left[\mathbf{S}^{\mathbf{E}}\right] &= \left[\mathbf{C}^{\mathbf{E}}\right]^{-1} \\ [\mathbf{d}] &= [\mathbf{e}]\left[\mathbf{S}^{\mathbf{E}}\right] \\ \left[\varepsilon^{T}\right] &= \left[\varepsilon^{S}\right] + [\mathbf{e}]\left[\mathbf{S}^{\mathbf{E}}\right][\mathbf{e}]^{T} \end{aligned} \tag{2.5}$$

[**e**] and [**d**] are related to the free stress and free strain conditions, respectively. [**e**] represents the stresses induced by a unitary electric field at constant strain, whereas [**d**] represents the strains induced by a unitary electric field at constant stress. In real application, for thin layer piezoelectric transducers mounted on a surface, the electric field is in the poling direction ($E_1 = E_2 = 0$). The same applies to the electric displacement ($D_1 = D_2 = 0$). This is known as unidirectional electric field (UDEF) assumption. Once the piezoelectric transducer is manufactured with the electrode layers, the polarisation process can be carried out applying an electric potential jump at the electrodes. The polarisation direction coincide with that of the applied electric field.

Alternatively, the tensor notation can be adopted. In this case the constitutive Eqs. 2.1 and 2.2 can be written in tensorial form:

$$\left\{ \begin{array}{rcl} \sigma_{ij} & = & C^{E}_{ijkl}\varepsilon_{kl} - e_{kij}E_k \\ D_i & = & e_{ikl}\varepsilon_{kl} + \epsilon^{\varepsilon}_{ik}E_k \end{array} \right. \tag{2.6}$$

Here σ_{ij} and ε_{kl} are the components of the stress and the strain tensors, E_i and D_i are the components of the electric field and the electric displacement vectors, C^{E}_{ijmn} are the components of the elastic modulus tensor measured at a constant electric field, $\epsilon^{\varepsilon}_{ik}$ are the components of the dielectric tensor at fixed strain and e_{kmn} are the components of the piezoelectric constants tensor. In the preceding equations and in what follows the summation convention applies to repeated Latin subscripts. The lowercase Latin subscripts range from 1 to 3.

Extending the shorthand notation introduced in many works such as [2, 3], the electroelastic constants can be expressed on equal footing in the following as

$$L_{iJMn} = \left\{ \begin{array}{ll} C^{E}_{ijmn}, & J,M = 1,2,3 \\ e_{nij}, & J = 1,2,3; M = 4 \\ e_{imn}, & M = 1,2,3; J = 4 \\ -\epsilon^{\varepsilon}_{in}, & J = M = 4 \end{array} \right. \tag{2.7}$$

Uppercase subscripts range from 1 to 4. With this shorthand notation, the linear constitutive Eqs. 2.6 can be unified as:

$$\Sigma_{iJ} = L_{iJKl}Z_{Kl} \tag{2.8}$$

where:

$$\Sigma_{iJ} = \left\{ \begin{array}{ll} \sigma_{ij}, & J = 1,2,3 \\ D_i, & J = 4 \end{array} \right. \quad \text{and} \quad Z_{Kl} = \left\{ \begin{array}{ll} \varepsilon_{kl}, & K = 1,2,3 \\ -E_l, & K = 4 \end{array} \right. \tag{2.9}$$

In Eq. 2.9 the elastic strain and the electric field are derivable from:

$$U_M = \left\{ \begin{array}{ll} u_m, & M = 1,2,3, \\ \phi, & M = 4 \end{array} \right. \tag{2.10}$$

where u_m is the elastic displacement and ϕ the electric potential, through the equations:

$$\left\{ \begin{array}{lcl} \varepsilon_{ij} & = & \frac{1}{2}\left(u_{i,j} + u_{j,i}\right) \\ E_i & = & -\phi_{,i} \end{array} \right. \tag{2.11}$$

Comma denotes partial differentiation with respect to a coordinate. Recall that the quantities in the above shorthand notations are not tensors. Each individual tensor must be transformed by the well known laws of tensor transformations. Then, the resulting tensors can be reunified.

The following governing equations are considered in piezoelasticity:

$$\left\{ \begin{array}{lcl} \sigma_{ij,j} & = & \rho\ddot{u}_i \\ D_{i,i} & = & 0 \end{array} \right. \tag{2.12}$$

in the volume V. ρ is the mass density. The boundary conditions are defined on the boundary $\partial V = \Gamma$, where $\Gamma = \Gamma_t \cup \Gamma_u = \Gamma_q \cup \Gamma_\phi$, and $\Gamma_t \cap \Gamma_u = \Gamma_q \cap \Gamma_\phi = \emptyset$. Traction and displacement boundary conditions are defined as:

$$\left\{ \begin{array}{lcl} \sigma_{ij} n_j & = & \bar{t}_i \text{ on } \Gamma_t \\ u_i & = & \bar{u}_i \text{ on } \Gamma_u \end{array} \right. \tag{2.13}$$

where n_j are the components of a vector normal to the surface. $\bar{t}$ and $\bar{u}$ are prescribed stresses and displacements. Charge and electric potential boundary conditions are defined as:

$$\left\{ \begin{array}{lcl} D_i n_i & = & -\bar{q} \text{ on } \Gamma_q \\ \phi & = & \bar{\phi} \text{ on } \Gamma_\phi \end{array} \right. \tag{2.14}$$

where $\bar{q}$ and $\bar{\phi}$ are prescribed charges and electric potentials.

2.2 Piezoelectric transducers

2.2.1 Monolithic piezoelectric wafers

Historically, improvements in piezoelectric materials have been focused on the development of single phase materials. Monolithic piezoceramic wafer are widely adopted. In several studies they are employed as thin layer mounted patches on smart structures. In health monitoring applications they generate and receives acoustic, ultrasound or Lamb waves. In vibration control they are used in passive and active vibration control systems. They are relatively cheap and their fabrication is relatively simple: after sintering of piezoceramic materials, wafers can be cut with machining tools. They possess strong piezoelectric properties and exhibit an isotropic behaviour in the plane of the wafer. Drawbacks of piezoelectric wafers are brittleness and non-conformability to curved surfaces. An interesting example of advanced monolithic piezoceramic wafer is presented in [4]. A typical ceramic wafer is transverse isotopic: if material is removed along multiple parallel lines, as shown in Fig. 2.1, the ceramic remains continuous and exhibits an anisotropic behaviour. The effective stiffness in the direction transverse to the cuts is reduced. This device could be considered as a composite of ceramic strips with air in-between.

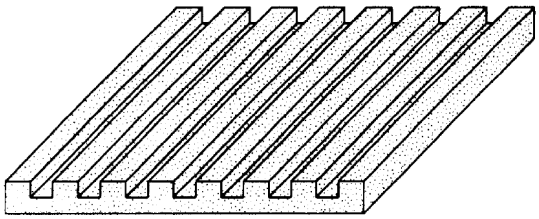

Figure 2.1. Ceramic wafer with cuts [4].

2.2.2 Unimorph transducers

An interesting design of ceramic wafer on a substrate is THUNDER® [5](thin-layer composite unimorph ferroelectric driver and sensor), developed at NASA Langley Research Center and investigated by Mossi et al. [6]. It consist of piezoelectric ceramic wafer prestressed against a foundation material, which is usually in stainless steel, see Fig. 2.2. The

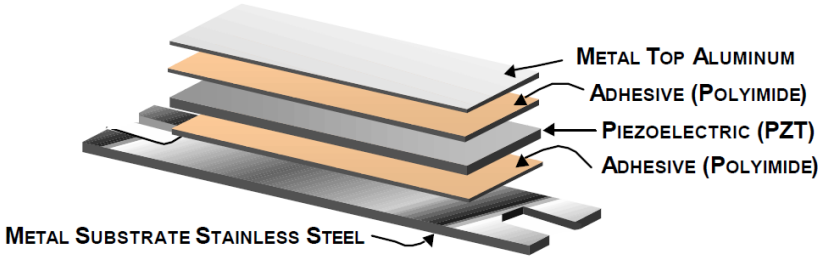

Figure 2.2. THUNDER®schematics [5].

ceramic is pre-compressed whereas the substrate is pre-tensed. The bond is assured by a high temperature thermoplastic polyimide. Tanks to the pre-stress, THUNDER®can be deflected more than standard piezoceramics, leading to larger displacements along a axis. The piezoceramic wafer is protected by the metallic top and bottom layers, that are suited to be used as electrodes.

Haertling [7] proposed the RAINBOW transducer, which is similar to THUNDER®in concept and operation, but differ in manufacturing: oxygen is removed at high temperature on a side of a monolithic ceramic. At room temperature, the difference in thermal-expansion coefficients between the ceramic and reduced layers produce high residual stresses. Wise [8] found that RAINBOW devices have output axial displacements greater by about 10 to 25% with respect to those of THUNDER®because of higher internal stresses.

2.2.3 1-3 composites

Single phase piezoelectric materials can only partially meet the desired requirements such as high strength and low dielectric constants for many new transducers and sensors. It has been shown that some composite materials can provide superior properties compared to their mother monolithic constituent materials in terms of flexibility, durability and reliability. It has been proved in [9, 10] that piezocomposites can provide a higher piezoelectric strain modulus d_{31} than the constituents in hydrophone applications and medical ultrasonic transducers. The replacement of a portion of a piezoceramic with a non-piezoelectric polymer, which is light and flexible, yields to a multiphase construction of a more robust actuator that is capable of conforming to complex surface shapes. Such composites inherit the characteristics of functional materials, such as the piezoelectric properties, which can be tailored to meet specific applications.

Designs of piezoelectric ceramic-polymer composites are classified according to the concept of connectivity, which is related to the continuity of each phase in spatial dimensions. Different arrangements of the material phases are considered by Safari [11], see Fig. 2.3. For example, in a 1-3 composite the reinforcement phase is continuous in one dimension,

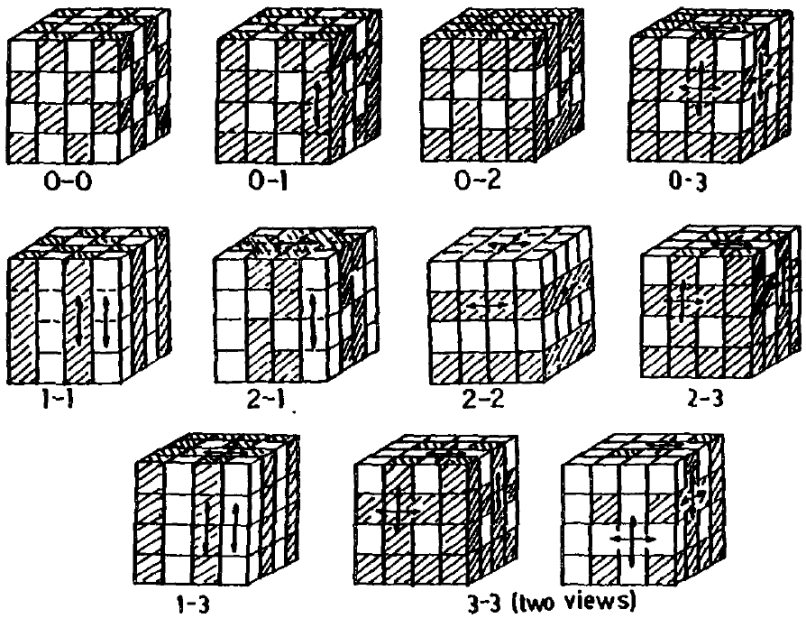

Figure 2.3. Spatial connectivity for a diphase composite [11].

whereas the matrix phase is three-dimensional continuous. An overview of composite transducers with piezoceramic fibres is presented by Williams et al. [12]. This class of composites is of great interest since the flexible nature of the polymer matrix protects the fibres and allows the device to conform to curved surfaces.

The standard method of 1-3 composite fabrication is the dice and fill method. A more

refined method, known as arrange and fill, was developed at the Fraunhofer Institute for Ceramic Technologies and Systems IKTS [13]. This method consists in epoxy infiltration of arranged piezoelectric fibre bundles. Commercially available products, manufactured by Smart Material Corp., are presented in Figs. 2.4. Fibres are aligned in the through-

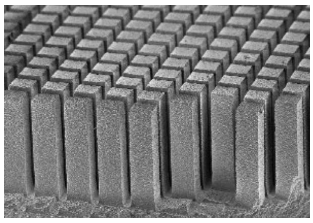

(a) rectangular fibres

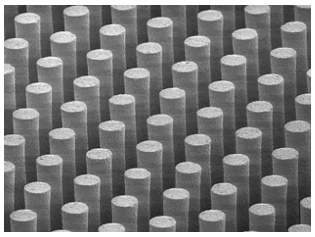

(b) circular fibres

Figure 2.4. 1-3 composites manufactured by Smart Material Corp. [12].

the-thickness direction of the device. They are currently employed as high performance ultrasound transducer since they guarantee higher bandwith with respect to monolithic piezoceramics.

2.2.4 Piezoelectric fibre composites

Piezoelectric fibre composites called Active Fibre Composite (AFC) were introduced by Hagood and Bent [14] as an alternative to monolithic piezoceramic wafers for structural actuation applications. They have uniaxially aligned piezoceramic fibres surrounded by a polymer matrix. Due to the arrangement of fibres along a specific in-plane direction, the piezoelectric response in the plane of the device is direction-dependent. AFCs were first developed using surface electrodes. When equipped with interdigitated electrodes (IDEs) [15, 16, 17, 18], AFCs are more responsive than with conventional surface electrodes since piezoelectric properties in the direction of the fibres are higher. In fact, fibres are polarised approximately along their length instead of transversely. AFC with IDEs is depicted in Fig. 2.5. Developed by the NASA Langley Research Center, the Macro Fiber Composite (MFC) actuator and sensor presents superior qualities among AFCs in performance, behaviour and repeatability as well as in manufacturability [20], and thus attracted great interest for new industrial applications and in the academic community as well. MFC has uniaxially aligned fibres with rectangular cross-section surrounded by a polymeric matrix. The cross section and the schematic of MFC are presented in Figs. 2.6. They are 2-2 composites in terms of connectivity. Rectangular fibres allow a better contact between fibres and electrodes with respect to AFC. In AFC, the circular fibres are in close contact with electrode only in a small portion. Therefore electric field acting on the fibre is somewhat diminished. Rectangular fibres are also easier and cheaper to produce: they are diced form a piezoelectric wafer, whereas the circular fibres of AFC are extruded in a complex and expensive process. Optimisation of IDEs for piezoelectric fibre composites has been investigated by Bowen et al. [21] in terms of geometry. Electrode width and

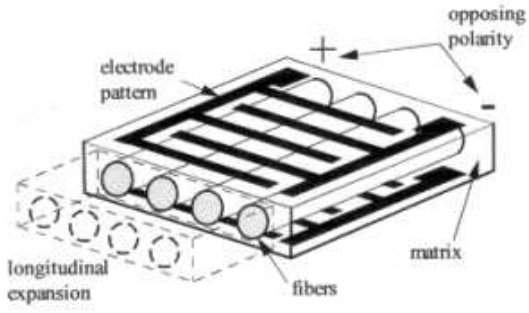

Figure 2.5. Active Fiber Composite with interdigitated electrodes [19].

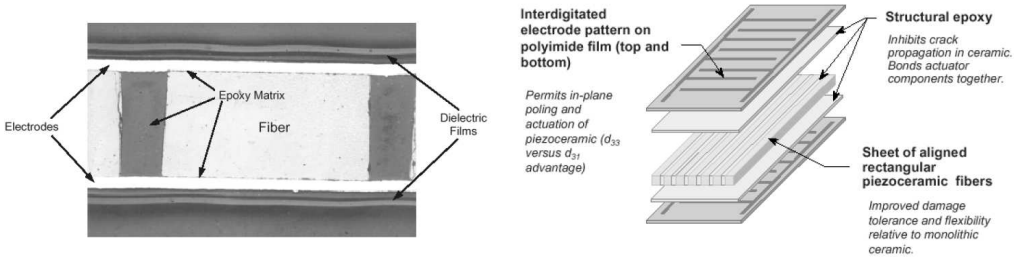

(a) cross-section (b) schematic

Figure 2.6. Macro Fiber Composites, manufactured by Smart Material Corp. [12].

spacing as well as device thickness have been taken into account in the optimisation. Both d_{31}- and d_{33}-type MFCs have been commercialised. The former adopts conventional electrodes, whereas the latter uses interdigitated electrodes, see Fig. 2.7. MFCs are the most

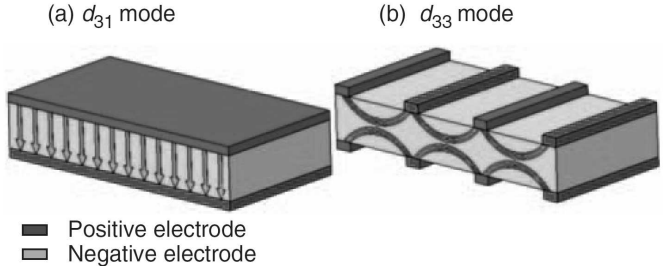

Figure 2.7. Electric field distribution for (a) conventional and (b) interdigitated electrodes [22].

promising piezoelectric devices with anisotropic behaviour that are commercially available. Their properties are thoroughly investigated in Ch. 3.

There are other interesting concept designs of piezoelectric composites. The hollow

fibre topology has been explored by Cannon and Brei [23]. Electrodes are on both the inner and outer surfaces of the fibre, giving a radial poling direction as shown in Fig. 2.8. Lower operating voltage is required with respect to AFC and MFC and an electrically

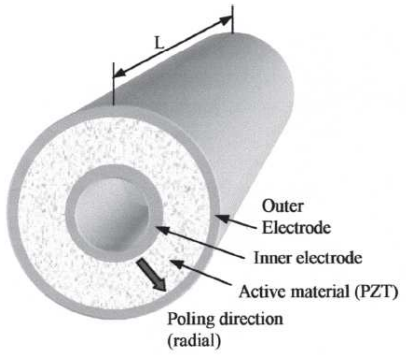

Figure 2.8. Hollow fibres design [23].

conductive matrix can be employed. Fibres have been manufactured through an extrusion process and a lamina prototype built of epoxy matrix with embedded fibres has been tested. The fabrication process is quite complex: after the extrusion, the fugitive material has to be burn out. Electrodes are realised individually for each fibre using silver paint.

Lin and Sodano [24] presented the concept of a piezoelectric structural fibre built of a carbon fibre core coated with a piezoelectric layer. The carbon fibre enhance the mechanical properties, assuming a load-carrying structural function, and act as inner electrode. Schematic of fibre cross-section is shown in Fig. 2.9. Theoretical and finite element models

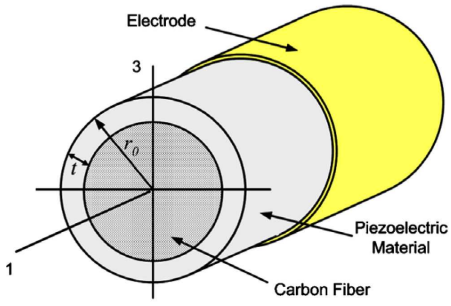

Figure 2.9. Cross-section of the active structural fibre [24].

have been developed to predict the electromechanical properties of composite with the proposed fibre in an epoxy matrix. Results show that such a composite material could achieve piezoelectric coupling coefficients as high as 70% of the active constituent.

Chapter 3

Micromechanics and homogenisation of piezoelectric composites

In an effort to obtain piezoelectric materials with the competing properties, many conventional piezoelectric materials are engineered to incorporate inclusions, such as particles, short fibres, long fibres and in some cases even voids, to achieve the desired electro-elastic properties. Combining two or more distinct constituents, piezoelectric composite materials can take the advantages of each constituent since an important application of composite structures is the use of the product property, which is found in the composite structures but is absent in the individual phases [25]. However, the introduction of inclusions or voids into base media will generally lead to the material being anisotropic, complicated and, in some situations, even detrimental to the performance of the composite. Therefore, in order for the composite to offer a favourable behaviour, it is necessary to clearly examine the electro-elastic responses from a micromechanics point of view so that the influence of each material parameter can be understood thoroughly [26]. Inspired by the above interesting and exciting modelling tools as well as by the excellent designability of composites including piezoelectric composites, scientists and engineers pursue the optimal design for the desired applications. With the rapid advancement in technological research, it is expected that composites and completely novel materials could be conveniently designed and manufactured by direct engineering of their constituents [27, 28].

In the last decade, an increasing number of investigations focused on the homogenisation of composite materials have been accomplished to predict mechanical and electromechanical properties of piezoceramic composites. Most of the time these techniques are obtained as extension of the ones developed for pure elastic materials. Significant works in this area are those in Refs. [29, 30, 31, 32, 3]. Different techniques have been developed based on analytical mixing rules [18, 33, 34] and on the finite element modelling techniques [35, 36, 37, 38]. Hagood and Bent [15] used a mixing rule technique to predict the effective properties of AFCs. The results of this investigation were in reasonable agreement with experimental data. Moreover, Bent and Hagood [18] adopted the Uniform Field Method (UFM) to derive a constitutive model for a new AFC design. The model was implemented into a finite element code and numerical simulations have been performed.

In [33, 34], Tan and Tong proposed three-dimensional micro-electromechanical models for piezoelectric fibre reinforced composite materials. Analytical formulas of overall electromechanical properties have been derived using the UFM under single and multiple loads conditions. The developed model showed good agreement with experimental data. Using similar approach, Deraemaeker et al. [22, 39] proposed a simplified form of the analytical mixing rules based on the work of Tan and Tong [33]. The results of the investigated simplified analytical solution have shown a good agreement with the numerical solution computed using the periodic homogenisation method [35, 40] under plane stress assumption and with the experimental results available in literature. Aboudi extended the generalised method of cells to piezoelectric materials in [41] by imposing mechanical equilibrium and Maxwell's charge equation in the constituent regions in conjunction with the continuity of mechanical displacements, tensions, electric potential and electric displacements. Tang and Yu [36], starting from the total electric enthalpy of the heterogeneous continuum, formulated a micromechanics model as a constrained minimisation problem using the variational asymptotic method and implemented it using the finite element method. In [29, 30], homogenisation techniques based on Eshelby tensor [42] have been developed to predict the mechanical and coupled piezoelectric properties of composites. In the same context, Li [43] considered the Mori-Tanaka [44] and the self consistent [45] approaches to predict the effective thermoelastic moduli of composites. Two different models that belong to the same family can be found in [28, 46]. Both are based on the self-consistent model: Tong et al. [28] consider a three-phase cylindrical model for analysing fibre composite, whereas Levin et al. [46] are concerned with composite materials that consist of a homogeneous matrix phase with a set of inclusions uniformly distributed in the matrix. The method of Asymptotic Expansion Homogenization (AEH) is a powerful method that allows computing the effective properties of composite materials and heterogeneous media using a periodic Representative Volume Element (RVE). It is often used in many global/local and periodical problems. For instance, AEH method is able also to characterise the micro field of stress, strain, electric displacement and electric fields [47, 48]. The AEH method for periodic media has been formulated, in a weak form derivation, by Guedes and Kikuchi [49]. Recently, a strong form derivation of the AEH for linear elasticity problems has been presented in [37, 48] and applied to several composite geometries, where detailed mathematical formulation and numerical implementation for elastic properties can be found. The influence of the reinforcement volume fraction on the overall material properties for different composite geometries has also been analysed in these works. In [50], Bravo-Castillero et al. applied AEH method to obtain the overall effective properties of periodic multi-laminated magneto-electro-elastic composites.

In this chapter, the problem of piezoelectric inclusions in a host material is considered and conclusions are drawn on the basis of the characteristics of the inclusion such as shape and polarisation. The equivalent properties of a well known piezoelectric composite (MFC) are also addressed.

3.1 Piezoelectric inhomogeneities

The multi-coating micromechanical model introduced in [51, 52] for elastic and viscoelastic composite materials is adopted and extended to the effective electro-elastic properties of piezoelectric composite materials containing multi-coated inhomogeneities. It is based on the generalised self consistent incremental scheme in which the composite inclusion has an ellipsoidal shape and the number of coatings is a free parameter. The incremental approach assures a better prediction of the effective properties in case of great difference among the properties of the constituent material, in particular for high volume fractions. The multi-coating formulation has the potential to study the effect of non-trivial inclusions, such as the ones made of functionally graded materials. A finite element analysis is also performed for two-phase piezoelectric composite materials using ABAQUS finite element software. The inhomogeneities's shape effect as well as the poling direction and the coating effects is investigated.

3.1.1 Micromechanical model

Constitutive equations, notations and topology

Tensorial notation is adopted. Constitutive equations are reported in Sec. 2.1. The topology of the present multi-coated inhomogeneity problem (see Fig. 3.1) consists of an inhomo-

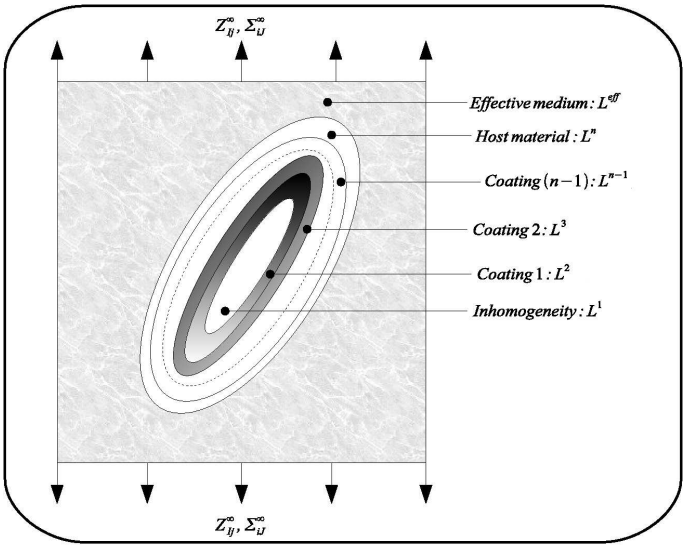

Figure 3.1. Topology of the multi-coated inhomogeneity problem. Σ^{∞}_{iJ} and Z^{∞}_{Ij} represent the macroscopically applied fields.

geneity phase occupying a volume, V_1, whose behaviour is described by the electro-elastic moduli pseudo-tensor $\mathbf{L}^1$. Surrounding this inhomogeneity phase are $(n-1)$ layers of coatings of other materials whose behaviours are described by their respective electro-elastic

moduli pseudo-tensor $\mathbf{L}^i$ and that occupies a volume, V_i, $i \in \{2,3,...,n\}$. Note that the coating n is a shell of the matrix material. This multi-coated inhomogeneity is then embedded in the effective material described by the unknown effective electro-elastic moduli pseudo-tensor $\mathbf{L}^{\text{eff}}$. The following derivation is limited to the case of small perturbation theory and the interfaces matrix-coating, coating-coating and coating-inhomogeneity are assumed to be perfect, thus ensuring continuity of tension and displacements across these boundaries. Note that this kind of topology has been used for elastic composites [51] and viscoelastic composites [52].

Integral equation and localisations

Micromechanical schemes are based on two distinct steps: (i) localisation, which determines the relationship between the microscopic (local) fields and the macroscopic (global) loading, and (ii) homogenisation, which employs averaging techniques to approximate the macroscopic behaviour. The beginning point of the present homogenisation scheme is based on the integral equation of Zeller and Dederichs [53] who have proposed to model the composite material shown in Fig. 3.1 as a homogeneous material whose electro-elastic behaviour varies spatially, that is:

$$\mathbf{L}(\mathbf{r}) = \mathbf{L}^{\text{eff}} + \delta\mathbf{L}(\mathbf{r}) \tag{3.1}$$

where $\mathbf{r} \in V$, V is the volume of the homogeneous medium, $\delta\mathbf{L}(\mathbf{r})$ and $\delta\boldsymbol{\beta}(\mathbf{r})$ are the spatially dependent electro-elastic moduli variations, $\mathbf{L}^{\text{eff}}$ and $\boldsymbol{\beta}^{\text{eff}}$ represent the unknown electro-elastic moduli of the effective material which are constant for all $\mathbf{r}$. To complete the formulation of the stationary linear response of a electro-elastic material, Eqs. 2.9 and 2.11 must be supplemented with the equations of the elastic equilibrium and the Gauss's law of electrostatics, see Eqs. 2.12, which in the absence of body forces and free charge sources are:

$$\begin{cases} \sigma_{ij,i} &= 0 \\ D_{i,i} &= 0 \end{cases} \tag{3.2}$$

Based on the shorthand notations, Eq. 3.2 gives:

$$\Sigma_{iJ,i} = 0. \tag{3.3}$$

Using the symmetries of $\mathbf{C}$, $\mathbf{e}$, $\boldsymbol{\epsilon}$, $\boldsymbol{\sigma}$ and $\boldsymbol{\varepsilon}$, Eq. 3.3 yields:

$$L^{\text{eff}}_{iJKl} U_{K,li} = \left[-\delta L_{iJKl} Z_{Kl}\right]_{,i}. \tag{3.4}$$

Employing Green's formalism, it is possible to get the simplified equation for the strain and the electrical fields, $Z_{Ij}(\mathbf{r})$, at any point in the medium as [54, 53]:

$$Z_{Ij}(\mathbf{r}) = Z^{\infty}_{Ij} - \int_V \Gamma^{\text{eff}}_{IjkL}(\mathbf{r}-\mathbf{r}') \left[\delta L_{kLMm}(\mathbf{r}') Z_{Mn}(r')\right] \mathrm{d}\mathbf{r}', \tag{3.5}$$

where $\boldsymbol{\Gamma}^{\text{eff}}(\mathbf{r}-\mathbf{r}')$ is the modified Green's electro-elastic pseudo-tensor, $\mathbf{Z}^{\infty}$ is the macroscopic elastic strain and electric fields that have no spatial dependence. Here the superscript

"eff" denotes that the Green's pseudo-tensor is computed using the electro-elastic properties, $\mathbf{L}^{\text{eff}}$, of the effective medium. The fluctuation parts of the electro-elastic constants with respect to the effective medium are given by the following relations:

$$\delta\mathbf{L}(\mathbf{r}) = \sum_{k=1}^{n} \Delta\mathbf{L}^{(k/\text{eff})}\theta_k(\mathbf{r}), \quad \text{with} \quad \Delta\mathbf{L}^{(k/\text{eff})} = \left(\mathbf{L}^k - \mathbf{L}^{\text{eff}}\right) \tag{3.6}$$

where the characteristic function $\theta_k(\mathbf{r})$ of the phase k, occupying the volume V_k, is defined as:

$$\theta_k(\mathbf{r}) = \left\{ \begin{array}{ll} 1 & \forall \mathbf{r} \in V_k \\ 0 & \forall \mathbf{r} \notin V_k \end{array} \right. , \quad \text{with } k \in \{0,1,2,...,n\}\,. \tag{3.7}$$

For the following, certain notation conventions need to be mentioned. The volume V_{I} of the composite inhomogeneity, I, consists of the inhomogeneity and $(n-1)$ coatings and the volume fraction, φ_k, of the phase k are defined as:

$$V_{\text{I}} = \sum_{k=1}^{n} V_k \quad \text{and} \quad \varphi_k = \frac{V_k}{V_{\text{I}}}, \quad k \in \{1,2,...,n\}\,. \tag{3.8}$$

The average strain and electrical fields, $\overline{\mathbf{Z}}^{\text{I}}$, in the composite inhomogeneity, I, is defined by:

$$\overline{\mathbf{Z}}^{\text{I}} = \frac{1}{V_{\text{I}}}\int_{V_{\text{I}}} \mathbf{Z}(\mathbf{r})\text{d}\mathbf{r} = \mathbf{Z}^{\infty} - \mathbf{T}^{\text{I}}(\mathbf{L}^{\text{eff}}) : \boldsymbol{\tau}^{\text{I}}, \tag{3.9}$$

where:

$$\left\{ \begin{array}{rcl} \mathbf{T}^{\text{I}}(\mathbf{L}^{\text{eff}}) & = & \frac{1}{V_{\text{I}}}\int_{V_{\text{I}}}\int_{V_{\text{I}}} \boldsymbol{\Gamma}^{\text{eff}}(\mathbf{r}-\mathbf{r}')\text{d}\mathbf{r}\text{d}\mathbf{r}', \\ \boldsymbol{\tau}^{\text{I}} & = & \sum_{k=1}^{n}\varphi_k\left(\Delta\mathbf{L}^{(k/\text{eff})} : \overline{\mathbf{Z}}^{k}\right), \\ \overline{\mathbf{Z}}^{k} & = & \frac{1}{V_k}\int_{V_k}\mathbf{Z}(\mathbf{r})\text{d}\mathbf{r}. \end{array} \right. \tag{3.10}$$

It is apparent from Eq. 3.9 that if one can find the local concentration pseudo-tensors $\mathbf{a}^k$ such that

$$\overline{\mathbf{Z}}^{k} = \mathbf{a}^k : \overline{\mathbf{Z}}^{\text{I}} \tag{3.11}$$

then, the localisation pseudo-tensors $\mathbf{A}^{\text{I}}$ in the composite inhomogeneity I which are defined by the relation

$$\overline{\mathbf{Z}}^{\text{I}} = \mathbf{A}^{\text{I}} : \overline{\mathbf{Z}}^{\infty} \tag{3.12}$$

can be determined as

$$\mathbf{A}^{\text{I}} = \left[\mathbf{I}^4 + \mathbf{T}^{\text{I}}(\mathbf{L}^{\text{eff}}) : \left(\sum_{k=1}^{n}\varphi_k\Delta\mathbf{L}^{(k/\text{eff})} : \mathbf{a}^k\right)\right]^{-1} \tag{3.13}$$

In Eq. 3.13, $\mathbf{I}^4$ is the shorthand notation for the fourth order and the second order identity tensors:

$$I^4_{IjMn} = \left\{ \begin{array}{ll} \left(\delta_{im}\delta_{jn} + \delta_{in}\delta_{jm}\right), & I,M = 1,2,3 \\ 0, & I = 1,2,3; M = 4 \\ 0, & M = 1,2,3; I = 4 \\ \delta_{jn}, & I = M = 4 \end{array} \right. \tag{3.14}$$

where δ_{ij} is the Kronecker delta. To complete the localisation step, the local localisation pseudo-tensors $\mathbf{a}^k$ must be found. If one introduces the localisation pseudo-tensors $\mathbf{A}^k$ in each phase, k, such as:

$$\overline{\mathbf{Z}}^k = \mathbf{A}^k : \mathbf{Z}^\infty + \mathbf{B}^k \Delta T, \tag{3.15}$$

then, Eqs. 3.11 and 3.12 give:

$$\mathbf{A}^k = \mathbf{a}^k : \mathbf{A}^{\mathrm{I}} \tag{3.16}$$

Using the fact that

$$\overline{\mathbf{Z}}^{\mathrm{I}} = \left\langle \overline{\mathbf{Z}}^k \right\rangle = \sum_{k=1}^{n} \varphi_k \overline{\mathbf{Z}}^k, \tag{3.17}$$

one gets the following equations to solve for $\mathbf{a}^k$:

$$\left\langle \mathbf{a}^k \right\rangle = \sum_{k=1}^{n} \varphi_k \mathbf{a}^k = \mathbf{I}^4 \tag{3.18}$$

Here, the notation, $\langle \boldsymbol{\zeta} \rangle$, denotes the average value of the quantity, $\boldsymbol{\zeta}$, over the whole volume of the composite inhomogeneity, I. Eqs. 3.18 constitute the solution of the posed problem given as function of the unknown n local localisation pseudo-tensors $\mathbf{a}^k$ which can be determined if one takes into account the boundary conditions through the different interfaces in the composite inhomogeneity. Interfacial operators [55] are a very convenient mathematical tool that efficiently calculates the stress or strain jump across a material interface (an interface separating two dissimilar materials). These operators are derived by writing the equations for the continuity of displacement and tension across the material interface (hypothesis of perfect interface). The derivation begins with the general case of two solid phases k and $(k+1)$, with the electro-elastic constants $\mathbf{L}^k$ and $\mathbf{L}^{k+1}$ separated by a surface with unit normal, $\mathbf{N}$, directed from phase k to phase $(k+1)$. Using the electro-elastic constants of these two phases, the jump of $\mathbf{Z}(\mathbf{r})$ across the material interface is given as [55]:

$$Z_{Ij}^{k+1}(\mathbf{r}) - Z_{Ij}^{k}(\mathbf{r}) = P_{IjmN}^{k+1} \left[\left(L_{mNPq}^{k} - L_{mNPq}^{k+1} \right) Z_{Pq}^{k}(\mathbf{r}) \right]. \tag{3.19}$$

The interfacial operator, P_{IjmN}^{k+1}, depends only on the constituent materials's properties and the unit normal vector of the interface. In the following, some notation conventions need to be defined

$$\Omega_j = \bigcup_{k=1}^{j} V_k \quad \text{and} \quad \Delta\mathbf{L}^{(p/q)} = \mathbf{L}^p - \mathbf{L}^q. \tag{3.20}$$

Substituting $\mathbf{Z}^k(\mathbf{r})$ by the average value, $\overline{\mathbf{Z}}^{\Omega_k}$, of $\mathbf{Z}(\mathbf{r})$ over the volume Ω_k and taking the average, $\overline{\mathbf{Z}}^{k+1}$, of $\mathbf{Z}(\mathbf{r})$ over the volume V_{k+1}, Eq. 3.19 yields:

$$\overline{\mathbf{Z}}^{k+1} = \overline{\mathbf{Z}}^{\Omega_k} + \mathbf{T}^{k+1} \left(\mathbf{L}^{k+1} \right) : \left[\Delta\mathbf{L}^{(\Omega_k/k+1)} : \overline{\mathbf{Z}}^{\Omega_k} \right], \tag{3.21}$$

where $\mathbf{L}^{\Omega_k}$ are the electro-elastic moduli of the composite formed by the volume Ω_k:

$$\mathbf{T}^{k+1}\left(\mathbf{L}^{k+1}\right) = \frac{1}{V_{k+1}}\int_{V_{k+1}} \mathbf{P}^{k+1}\mathrm{d}\mathbf{r}, \tag{3.22}$$

and:

$$\overline{\mathbf{Z}}^{\Omega_k} = \sum_{i=1}^{k} \frac{V_i}{\Omega_k}\overline{\mathbf{Z}}^i = \frac{\sum_{i=1}^{k}\varphi_i\overline{\mathbf{Z}}^i}{\sum_{i=1}^{k}\varphi_i}. \tag{3.23}$$

Following [56], it can be shown that:

$$\mathbf{T}^{k+1}\left(\mathbf{L}^{k+1}\right) = \mathbf{T}^{\Omega_k}\left(\mathbf{L}^{k+1}\right) - \frac{\sum_{i=1}^{k}\varphi_i}{\varphi_{k+1}}\left[\mathbf{T}^{\Omega_{k+1}}\left(\mathbf{L}^{k+1}\right) - \mathbf{T}^{\Omega_k}\left(\mathbf{L}^{k+1}\right)\right], \tag{3.24}$$

with:

$$\mathbf{T}^{\Omega_p}\left(\mathbf{L}^q\right) = \frac{1}{\Omega_p}\int_{\Omega_p}\int_{\Omega_p} \mathbf{\Gamma}\left(\mathbf{L}^q\right)(\mathbf{r}-\mathbf{r}')\mathrm{d}\mathbf{r}\mathrm{d}\mathbf{r}'. \tag{3.25}$$

Since $\mathbf{T}^{\Omega_p}\left(\mathbf{L}^q\right)$ are not size-dependent but shape dependent, it is apparent that in the specific case of homothetic inhomogeneities, one has:

$$\mathbf{T}^{k+1}\left(\mathbf{L}^{k+1}\right) = \mathbf{T}^{\Omega_k}\left(\mathbf{L}^{k+1}\right) = \mathbf{T}^{\Omega_{k+1}}\left(\mathbf{L}^{k+1}\right). \tag{3.26}$$

Using some algebraic manipulations, one gets:

$$\Delta\mathbf{L}^{(\Omega_k/k+1)} : \overline{\mathbf{Z}}^{\Omega_k} = \frac{\sum_{j=1}^{k}\varphi_j\left(\Delta\mathbf{L}^{(j/k+1)} : \overline{\mathbf{Z}}^j\right)}{\sum_{j=1}^{k}\varphi_j}. \tag{3.27}$$

If one introduces the pseudo-tensors $\mathbf{\Pi}^k$ defined by:

$$\mathbf{a}^k = \mathbf{\Pi}^k : \mathbf{a}^1 \tag{3.28}$$

then, by using Eqs. 3.21, 3.23 and 3.27, the pseudo-tensors $\mathbf{\Pi}^k$ are obtained as follows:

$$\mathbf{\Pi}^k = \frac{\sum_{j=1}^{k-1}\left(\varphi_j\boldsymbol{\vartheta}^{(j/k)} : \mathbf{\Pi}^j\right)}{\sum_{j=1}^{k-1}\varphi_j} \tag{3.29}$$

In Eq. 3.29, the expressions of the pseudo-tensors $\boldsymbol{\vartheta}^{(j/k)}$ are given as:

$$\boldsymbol{\vartheta}^{(j/k)} = \mathbf{I}^4 + \mathbf{T}^k\left(\mathbf{L}^k\right) : \Delta\mathbf{L}^{(j/k)} \tag{3.30}$$

One can verify that:

$$\mathbf{\Pi}^1 = \mathbf{I}^4 \tag{3.31}$$

Furthermore, Eqs. 3.18 and 3.28 give finally:

$$\mathbf{a}^1 = \left(\sum_{k=1}^{n}\varphi_k\mathbf{\Pi}^k\right)^{-1} \tag{3.32}$$

The localisation step of the present micromechanical model is definitively complete once the pseudo-tensor $\mathbf{a}^1$ is known.

Summary of the localisation step

To sum up, the main objective of the section 3.1.1 is to compute the localisation pseudo-tensors $\mathbf{A}^k$ and $\mathbf{B}^k$ defined by the Eq. 3.15. The steps to get $\mathbf{A}^k$ and $\mathbf{B}^k$ are as follows:

- from the properties $\mathbf{L}^k$ of each phase, compute $\mathbf{T}^k(\mathbf{L}^k)$ using Eq. 3.24;
- compute $\boldsymbol{\vartheta}^{(j/k)}$ and $\boldsymbol{\chi}^{(j/k)}$ from Eq. 3.30 using the properties $\boldsymbol{\beta}^k$;
- compute $\boldsymbol{\Pi}^k$ and $\boldsymbol{\Delta}^k$ from Eqs. 3.29 and 3.31;
- compute $\mathbf{a}^1$ and $\mathbf{b}^1$ from Eq. 3.32 and get $\mathbf{a}^k$ and $\mathbf{b}^k$ from Eq. 3.28;
- compute $\mathbf{A}^{\mathrm{I}}$ and $\mathbf{B}^{\mathrm{I}}$ from Eq. 3.13 and finally get $\mathbf{A}^k$ and $\mathbf{B}^k$ from Eq. 3.16.

Homogenisation schemes and effective properties

In what follows, two approaches are presented to compute the effective properties of a piezoelectric material containing ellipsoidal shaped multi-coated inhomogeneities. Both approaches are based on the classical self-consistent scheme. The first scheme is the basis of the second one that uses it in an incremental way. The second approach has been shown very useful in the case of high volume fractions of inhomogeneities with high contrast between the properties of the host material and the inhomogeneities.

Non-incremental homogenisation scheme The effective electro-elastic properties $\mathbf{L}^{\mathrm{eff}}$ are related to the macroscopic fields $\boldsymbol{\Sigma}^\infty$ and $\mathbf{Z}^\infty$ as:

$$\boldsymbol{\Sigma}^\infty = \mathbf{L}^{\mathrm{eff}} : \mathbf{Z}^\infty \tag{3.33}$$

Using the following relations:

$$\left\{ \begin{array}{rcl} \boldsymbol{\Sigma}^\infty & = & \sum_{k=0}^{n} \varphi_k \overline{\boldsymbol{\Sigma}}^k \\ \mathbf{Z}^\infty & = & \sum_{k=0}^{n} \varphi_k \overline{\mathbf{Z}}^k \\ \overline{\boldsymbol{\Sigma}}^k & = & \mathbf{L}^k : \overline{\mathbf{Z}}^k \end{array} \right. \tag{3.34}$$

in Eq. 3.33, one gets:

$$\mathbf{L}^{\mathrm{eff}} = \sum_{k=0}^{n} \varphi_k \mathbf{L}^k : \mathbf{A}^k \tag{3.35}$$

Eq. 3.35 is a set of nonlinear equations (since the localisation pseudo-tensors $\mathbf{A}^k$ are functions of $\mathbf{L}^{\mathrm{eff}}$) to solve for the effective properties $\mathbf{L}^{\mathrm{eff}}$. The localisation pseudo-tensors $\mathbf{A}^k$ are all determined in the localisation step (Section 3.1.1). This non-incremental homogenisation scheme is called herein the generalised self-consistent method (GSCM). The implementation of this micromechanical modelling technique requires the numerical approximation of the integral of the modified Green's electro-elastic pseudo-tensor $\boldsymbol{\Gamma}\left(\mathbf{L}^X\right)$ needed to compute $\mathbf{T}^{\mathrm{I}}\left(\mathbf{L}^{\mathrm{eff}}\right)$ (see Eq. 3.13) and $\mathbf{T}^{\Omega_p}\left(\mathbf{L}^q\right)$ (see Eq. 3.24). The implementation details of theses pseudo-tensors can be found in the appendix B of [3]. Note that,

$\mathbf{T}^{\Omega_p}(\mathbf{L}^q)$ can be also obtained from the Eshelby's electro-elastic pseudo-tensor, $\mathbf{S}^{\Omega_p}(\mathbf{L}^q)$, as

$$\mathbf{T}^{\Omega_p}(\mathbf{L}^q) = \mathbf{S}^{\Omega_p}(\mathbf{L}^q) : (\mathbf{L}^q)^{-1}. \tag{3.36}$$

Expressions for the components of $\mathbf{S}^{\Omega_p}(\mathbf{L}^q)$ can be found in [57, 58].

Incremental homogenisation scheme It has been noticed that the classical self-consistent method (CSCM) poorly estimates the effective properties of composites at high concentrations of reinforcements and is limited to very low concentrations for composite materials containing voids [31] or composites with high contrast between the properties of the matrix and the inhomogeneities. In order to avoid this drawback, an improvement of the CSCM has been proposed in [59] for the elastic case, which gives a progressive construction of the composite material in an incremental way in the same manner as the differential scheme (DS). In this paper, this incremental method is extended to the electro-elastic behaviour of piezoelectric composite materials. In the incremental scheme, the construction of the material is made by placing a finite increments of the volume fractions of the inhomogeneities in a certain effective medium, and for each increment the GSCM is applied to calculate the effective electro-elastic properties of the piezoelectric composite material. If S is the number of steps to use, the expression of the volume fraction increment, $\Delta\varphi_k^i$, of the k^{th} inhomogeneity phase at the i^{th} step is given as [59]

$$\Delta\varphi_k^i = \frac{\Delta\varphi_k}{1-(i-1)\sum_{j=1}^{n-1}\Delta\varphi_j}, \quad k \in \{1,2,...,n-1\}, \tag{3.37}$$

where

$$\Delta\varphi_k = \frac{\varphi_k}{S}. \tag{3.38}$$

At the i^{th} step, the matrix phase becomes the effective material obtained at the $(i-1)^{\text{th}}$ step using the GSCM with the volume fractions $\Delta\varphi_k^{i-1}$. This incremental scheme is referred as IGSCM hereafter. Recall that this incremental scheme does not affect the expression of the concentration pseudo-tensors $\mathbf{A}^k$ on which the method is based. So, the formulation used in this case is the same as in the GSCM. The two methods differ only in the manner the reinforcements volume fractions are introduced.

3.1.2 Numerical periodic homogenisation

A finite element analysis (FEA) of the representative volume element (RVE) is performed to verify the results obtained from the micromechanical models presented in Section 3.1.1. It consists of a cube containing an ellipsoidal inhomogeneity (see Fig. 3.2). The number of elements in the RVE varies from 1000 to 1500, depending on the volume fraction of the inhomogeneities. A convergence study is always carried out to determine the appropriate number of elements to be used for each case. For geometrical reasons the volume fraction of the inhomogeneity can't rise up to the unity. In the case of spherical inclusion, the theoretical limit is 0.523, whereas in this analysis it is limited to 0.45 to avoid meshing problems. The computation of the effective properties is based on the numerical Periodic

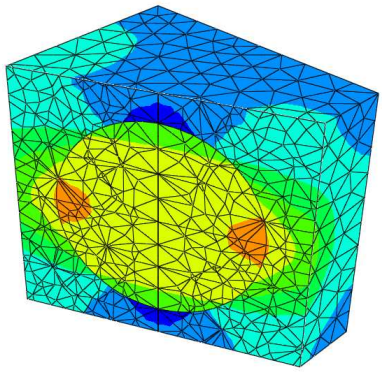

Figure 3.2. Finite element modelling of the RVE, cut with a skew plane. In colours, stress distribution σ_{11} corresponding to a particular load case for the evaluation of the components of the elastic moduli tensor.

Homogenisation Method (PHM) [35]. Rigorously, the boundary conditions should be applied on the surface of the RVE point wise in order to guarantee the periodicity condition. However, for this kind of problem, it is sufficient to apply uniform boundary condition on the faces of the cubic RVE. In order to compute the values in the constitutive matrix of the homogeneous model a proper approach is to apply the periodic boundary condition in such a way that only one generalised average strain is different from zero. The corresponding column in the generalised stiffness matrix in Eq. 2.3 can be computed with the averaged values of the generalised stress components. If (x_1,x_2,x_3) denotes an orthogonal reference system whose axes are perpendicular to the faces of the cubic RVE, the appropriate boundary conditions can be expressed more easily naming A^- and A^+ the faces perpendicular to direction x_1, B^- and B^+ the faces perpendicular to direction x_2, C^- and C^+ the faces perpendicular to direction x_3. Six different load cases with the corresponding computed properties, in the case of transversal isotropic materials, are shown in Table 3.1, where q is an arbitrary quantity, u are the displacements and ϕ is the electric potential. The finite elements used to evaluate the electro-mechanical properties are standard ABAQUS's 8-node linear piezoelectric brick elements (C3D8E). Differently from the work in [35], all the mechanical boundary conditions are expressed in terms of the displacements, not in terms of both displacements and loads.

3.1.3 Numerical results and discussions

The effective properties of a polymeric matrix containing piezoelectric material inhomogeneities are evaluated with the proposed micromechanical models and with the finite element analysis. The electro-elastic properties of the constituent materials are shown in Table 3.2. In what follows, the inhomogeneity semi-axis along the x_1, x_2 and x_3 directions will be denoted a, b and c respectively. The special case of $a = b$ will be considered. The matrix is made of Epoxy material while the inhomogeneity is made of one of the piezoelectric materials ($BaTiO_3$, PZT-4, PZT-4 or PZT-7A) in Table 3.2. The polarisation

Case	Mechanical and electrical BC			Properties
	A faces	B faces	C faces	
1	$u_{1A^+} = q$; $u_{1A^-} = 0$	$u_{2B^+} = 0$; $u_{2B^-} = 0$	$u_{3C^+} = 0$; $u_{3C^-} = 0$	C^E_{11},C^E_{21}
	$\phi_{A^+} = 0$; $\phi_{A^-} = 0$	$\phi_{B^+} = 0$; $\phi_{B^-} = 0$	$\phi_{C^+} = 0$; $\phi_{C^-} = 0$	
2	$u_{1A^+} = 0$; $u_{1A^-} = 0$	$u_{2B^+} = 0$; $u_{2B^-} = 0$	$u_{3C^+} = q$; $u_{3C^-} = 0$	C^E_{13},C^E_{33}
	$\phi_{A^+} = 0$; $\phi_{A^-} = 0$	$\phi_{B^+} = 0$; $\phi_{B^-} = 0$	$\phi_{C^+} = 0$; $\phi_{C^-} = 0$	
3	$u_{1A^+} = 0$; $u_{1A^-} = 0$	$u_{3B^+} = q$; $u_{3B^-} = 0$	$u_{2C^+} = q$; $u_{2C^-} = 0$	C^E_{44},e_{24}
	$\phi_{A^+} = 0$; $\phi_{A^-} = 0$	$\phi_{B^+} = 0$; $\phi_{B^-} = 0$	$\phi_{C^+} = 0$; $\phi_{C^-} = 0$	
4	$u_{2A^+} = q$; $u_{2A^-} = 0$	$u_{1B^+} = q$; $u_{1B^-} = 0$	$u_{3C^+} = 0$; $u_{3C^-} = 0$	C^E_{66}
	$\phi_{A^+} = 0$; $\phi_{A^-} = 0$	$\phi_{B^+} = 0$; $\phi_{B^-} = 0$	$\phi_{C^+} = 0$; $\phi_{C^-} = 0$	
5	$u_{1A^+} = 0$; $u_{1A^-} = 0$	$u_{2B^+} = 0$; $u_{2B^-} = 0$	$u_{3C^+} = 0$; $u_{3C^-} = 0$	$\epsilon^\varepsilon_{33}$,$e_{31}$,$e_{33}$
	$\phi_{A^+} = 0$; $\phi_{A^-} = 0$	$\phi_{B^+} = 0$; $\phi_{B^-} = 0$	$\phi_{C^+} = q$; $\phi_{C^-} = 0$	
6	$u_{1A^+} = 0$; $u_{1A^-} = 0$	$u_{2B^+} = 0$; $u_{2B^-} = 0$	$u_{3C^+} = 0$; $u_{3C^-} = 0$	$\epsilon^\varepsilon_{11}$
	$\phi_{A^+} = q$; $\phi_{A^-} = 0$	$\phi_{B^+} = 0$; $\phi_{B^-} = 0$	$\phi_{C^+} = 0$; $\phi_{C^-} = 0$	

Table 3.1. Periodic boundary conditions for different load cases.

	C_{11}	C_{12}	C_{13}	C_{33}	C_{44}	e_{31}	e_{33}	e_{15}	ϵ_{11}/ϵ_0	ϵ_{33}/ϵ_0
Epoxy	8	4.4	4.4	8	1.8	0	0	0	4.2	4.2
$BaTiO_3$	150	66	66	146	4.4	-4.3	17.5	11.4	1115	1260
PZT-4	139	77.8	74.3	115	25.6	-5.2	15.1	12.7	730	645
PZT-5	121	75.4	75.2	111	21.1	-5.4	15.8	12.3	916	830
PZT-7A	148	76.2	74.2	131	25.4	-2.1	12.3	9.2	460	235

Table 3.2. Electro-elastic material properties. C_{ij} in GPa, e_{ij} in C m^{-2}, $\epsilon_0 = 8.854 \times 10^{-12}$ C N^{-1} m^{-2}.

direction is assumed to be x_3 direction if not otherwise specified. The feasibility of such a polarisation on a large number of inclusions inside a matrix is not addressed.

Results obtained with the micromechanical models in the case of fibre shape inhomogeneity (aspect ratio $c/a = \Psi = 1000$) are shown in Fig. 3.3. The results for PZT-7A are in good agreement with the experimental data found in [60]. For this particular geometry there is no significant difference between the results obtained with the incremental (solid lines) and the non-incremental (dashed lined) schemes. This is not the case if the inhomogeneity has a spherical shape ($\Psi = 1$), see Fig. 3.4. The results obtained with the micromechanical models are plotted together with the results from the finite element homogenisation up to the volume fraction of 0.5. The effective properties obtained from the incremental scheme are higher than the ones given by the non-incremental scheme for all the considered properties. This difference increases with the volume fraction of the inhomogeneities and it is more pronounced above the volume fraction of 0.2. Table 3.3 reports a comparison between the results shown in Fig. 3.4 for different volume

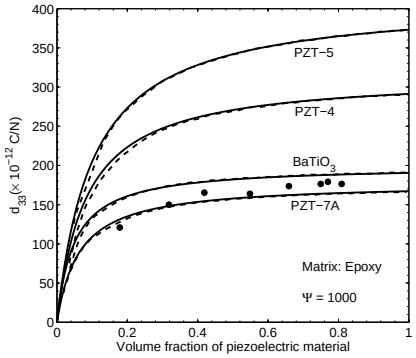

Figure 3.3. Effective d_{33} calculated with inclusion of different materials. Incremental scheme in solid lines (-), non-incremental scheme in dashed lines (- -), experimental results from [60] in dots (•).

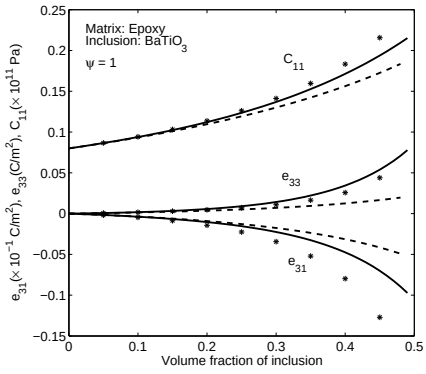

Figure 3.4. Comparison between incremental scheme (solid lines -), non-incremental scheme (dashed lines - -) and FEA results (asterisks $*$).

fractions. The results obtained from the FEM homogenisation are in better agreement with the incremental scheme rather than with the non-incremental scheme. Moreover the non-piezoelectric properties predicted by the micromechanical model are closer than the piezoelectric properties to the FEM homogenisation results. It is important to notice that, the effective piezoelectric coefficients are very small with respect to the ones of the piezoelectric constituent material. The reason of this behaviour is the great mismatch between the dielectric coefficients, $\epsilon_{ij}^{\varepsilon}$, of the matrix and the inclusion materials. For a matrix material having dielectric coefficients similar to that of the inhomogeneity, the predicted piezoelectric coefficients are much larger.

The influence of the aspect ratio on the effective properties computed with the micromechanical models is shown in Fig. 3.5. The volume fraction is fixed at 0.4. With $\Psi < 10^{-1}$ and with $\Psi > 10^{2}$ the effective properties do not have significant variations

Volume fraction	Property	FEM	NI	I	err(NI)	err(I)
0.1	C11	0.942	0.933	0.939	-0.94	-0.33
	e31	-0.465	-0.363	-0.381	-22.0	-18.1
	e33	0.166	0.145	0.177	-12.7	6.21
0.2	C11	1.14	1.10	1.12	-3.54	-1.27
	e31	-1.44	-0.909	-1.03	-36.7	-28.0
	e33	0.475	0.364	0.562	-23.5	18.3
0.3	C11	1.41	1.30	1.37	-7.87	-2.98
	e31	-3.44	-1.75	-2.24	-48.9	-34.6
	e33	1.09	0.703	1.42	-35.5	30.6
0.4	C11	1.83	1.56	1.71	-14.7	-6.51
	e31	-7.97	-3.13	-4.74	-60.7	-40.4
	e33	2.57	1.25	3.44	-51.3	33.7

Table 3.3. Comparison between results obtained with the FEM homogenisation, the non-incremental scheme (NI) and the incremental scheme (I). The differences between the results of the micromechanical models and that of the FEM homogenisation are reported in percentage. C11 in $(\times 10^{10})$Pa, e_{31} in $(\times 10^{-3})$C m^{-2}, e_{33} in $(\times 10^{-2})$Cm^{-2}. Matrix: Epoxy. Inclusion: $BaTiO_3$. $\Psi = 1$.

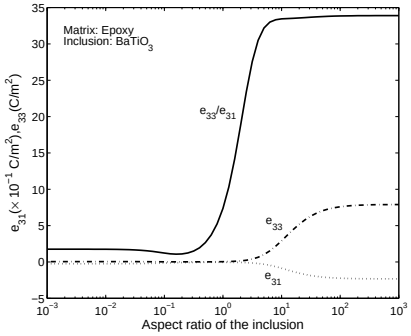

Figure 3.5. Effect of the aspect ratio of the inclusion on the effective properties. The volume fraction of inclusion is 0.4.

and have an asymptotic behaviour. This means that, for this model, $\Psi = 10^{-1}$ is a good approximation of a penny-shaped inclusion while $\Psi = 10^2$ is a good approximation of a fibre-like inclusion. Fibre-shaped inclusions give the largeset equivalent piezoelectric properties. They also give the largest ratio e_{33}/e_{31}, which is an index of directionality of the piezoelectric effect.

The effect of the rotation of the polarisation direction with respect to the x_3 axis for an inclusion with $\Psi = 10$ and a volume fraction of 0.4 is shown in Fig. 3.6. When the polarisation direction is perpendicular to the x_3 direction, the piezoelectric properties e_{31}

and e_{33} are correctly null. Polarisation along the largest axis of the inclusion gives the

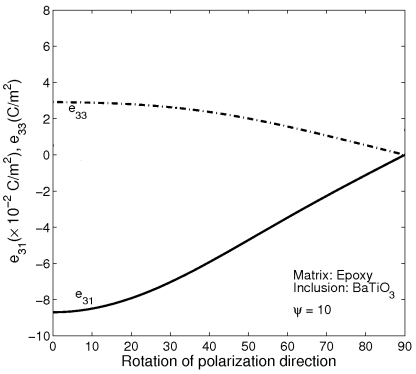

Figure 3.6. Effect of the rotation of the polarisation of the inclusion with respect to the x_3 axis on the effective properties. The volume fraction of inclusion is 0.4.

largest values for the piezoelectric coefficients. The effect of a spherical coating in PZT-4 on a spherical inclusion in $BaTiO_3$ is shown in Fig. 3.7, where $\gamma = a_1/a_2 = b_1/b_2 = c_1/c_2$, as it is defined in [43] (the subscript 1 stands for the inclusion and 2 stands for the coating). The volume fraction of the matrix is fixed at 0.6.

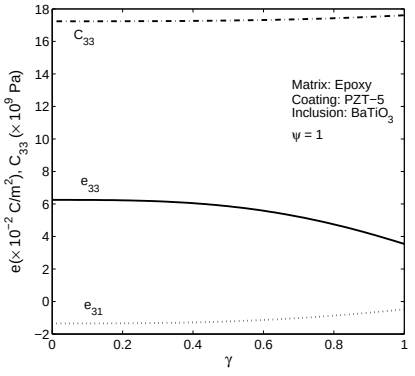

Figure 3.7. Effect of the variation of the coating thickness with volume fraction of matrix fixed at 0.6.

The presented results, see in particular Fig. 3.5, suggest that higher directionality of the piezoelectric effect can be achieved adopting piezoelectric fibres. Different shapes of the inclusions give less direction-dependent properties. MFCs are the most promising commercially available fibre-based devices with anisotropic response and are therefore investigated in the next section.

3.2 Macro Fiber Composite

While the MFC's attributes render it an exceptionally useful device, limited modelling and experimental characterisation research on the MFC has took place. Among these studies, Williams et al. [61] have analysed experimentally the nonlinear tensile and shear stress-strain behaviour and Poisson effects of the MFC. Williams et al. [62] have later developed a nonlinear model for a piezoelectric continuum taking into account nonlinear mechanical behaviour and actuation characteristic of MFC. This section aims to model and compute the effective electromechanical properties of MFC transducers with conventional electrodes (d_{31}-type). MFC schematic and its representative volume element (RVE) are shown in Fig. 3.8. Since the semi-analytical method developed in Sec. 3.1 cannot

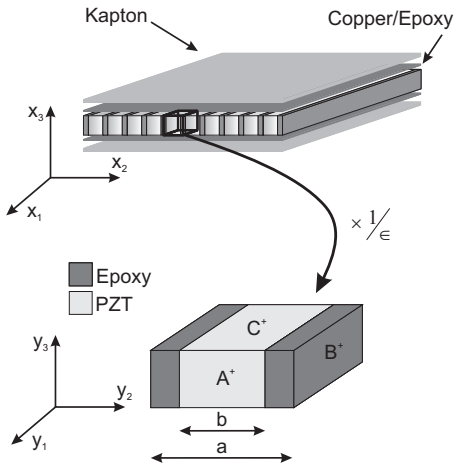

Figure 3.8. MFC schematic. According to Smart Materials datasheets, Kapton®layers thickness is 0.04 mm, copper/epoxy layers thickness is 0.0018 mm and active layer thickness is 0.18 mm. The RVE of the active layer is depicted.

be adopted (MFC fibres are not ellipsoidal), the Asymptotic Expansion Homogenization method is considered. Results are validated toward the Uniform Field Method, the Periodic Homogenisation Method and manufacturer's datasheet.

3.2.1 Asymptotic expansion homogenisation method

The method of Asymptotic Expansion Homogenization (AEH) [37, 47, 48, 49] is a powerful method that allows computing the homogeneous model of composite materials and heterogeneous media through an analysis of a periodic Representative Volume Element (RVE). It is often used in many global/local and periodical problems. Loading of such materials gives periodic oscillations in the fields at microstructural level as a consequence of periodicity. Two different scales can be identified. There is a "fast" variable y over the RVE and a "slow" variable x over the structure, related through

$$y = x/\epsilon \tag{3.39}$$

where $\epsilon << 1$ is a scale parameter.

The periodicity of the RVE in the structure is assumed. The components of the generalised elasticity tensor (tensor form of the generalised constitutive matrix $\mathbf{C_g}$) is described as:

$$D_{ijkl} = D_{ijkl}(y) \tag{3.40}$$

The expression of the Y-periodic generalised elasticity tensor in the macroscale x is:

$$D_{ijkl}(x/\epsilon) = D^{\epsilon}_{ijkl}(x) \tag{3.41}$$

A generic quantity $Q(x)$, function of x and Y-periodic over the scale ϵ, is given as $Q^{\epsilon}(x)$. In the following, the generalised elasticity tensor is assumed as

$$D_{ijkl} = C^{E}_{ijkl}, D_{4jkl} = e_{jkl}, D_{ij4l} = e_{lij}, D_{4j4l} = -\epsilon_{jl} \tag{3.42}$$

with indexes varying from 1 to 3. C^{E}_{ij} are the components of the elastic modulus tensor at constant electric field; ϵ_{ij} are the components of the dielectric tensor at fixed strain (it should not be confounded with the scale parameter ϵ, which is without indexes); e_{ij} are the components of the piezoelectric constants tensor at fixed strain or electric field. In order to derive the relation of the AEH, the dimension of the RVE is assumed to be infinitesimal with respect to the structure ($\epsilon \to 0$). This allows to consider x and y as separate variables. The generalised displacement field (physical displacement and potential) is approximated using an asymptotic expansion in ϵ as:

$$u^{\varepsilon}_{i}(x) = u^{(0)}_{i}(x,y) + \epsilon u^{(1)}_{i}(x,y) + \epsilon^2 u^{(2)}_{i}(x,y) + ... \tag{3.43}$$

where $u^{(j)}_{i}(x,y)$, with $i = 1,...,4$ and $j \in N_0$, are the correctors of the generalised displacement field. Since x and y are independent variables, one can write:

$$\frac{\partial}{\partial x^{\epsilon}_{i}} = \frac{\partial}{\partial x_i} + \frac{1}{\epsilon}\frac{\partial}{\partial y_i} \tag{3.44}$$

Applying Eq. 3.44 to the asymptotically expanded generalised displacement field of equation 3.43, the expressions of the generalised strains and stresses is obtained as function of ϵ. Substituting these expressions into the generic Boundary Value Differential (BVD) problem and grouping the terms according to the power of ϵ, the original BVD problem can be split in a series of simpler BVD problems. The solution of this set of simpler BVD problems corresponds to the solution of the original one asymptotically (with $j \to \infty$ in Eq. 3.43) if the hypothesis of this approach are verified, i.e. if the material is periodic and the dimension of the RVE tends to zero. It comes out from the third lowest order BVD that

$$D^{h}_{ijmn} = \frac{1}{|Y|}\int_{Y} D_{ijkl}(y)\left[I^{mn}_{kl} - \frac{\partial \chi^{mn}_{k}(y)}{\partial y_l}\right] \mathrm{d}y \tag{3.45}$$

where D^{h}_{ijmn} is the equivalent generalised elasticity tensors, Y is the domain of the RVE, $|Y|$ is the RVE volume, I^{mn}_{kl} is the identity tensor and χ^{mn}_{k} is called the characteristics

displacement tensor that can be computed thanks to a relation derived from the two lowest order BVDs:

$$\frac{\partial}{\partial y_j}\left[D_{ijkl}(y)\left(I_{kl}^{mn}-\frac{\partial \chi_k^{mn}(y)}{\partial y_l}\right)\right]=0 \tag{3.46}$$

In order to solve this equation it is necessary to consider the boundary conditions, which involves also the quantity

$$\sigma_{ij}^{(1)}=\left[D_{ijkl}(y)\left(I_{kl}^{mn}-\frac{\partial \chi_k^{mn}(y)}{\partial y_l}\right)\right]\frac{\partial u_m^{(0)}}{\partial x_n}(x) \tag{3.47}$$

derived from the two lowest order BVD. $\sigma_{ij}^{(1)}$ is the term multiplying ϵ^0 in the asymptotic expansion of the generalised stresses.

AEH analytical solution

Due to the simple geometry of the MFC, the material properties are given as:

$$D_{ijkl}(y_2)=\begin{cases} D_{ijkl}^{\text{fibre}} & \text{for } 0<y_2<=\rho\,|Y| \\ D_{ijkl}^{\text{matrix}} & \text{for } \rho\,|Y|<y_2<|Y| \end{cases} \tag{3.48}$$

Electrodes are neglected. The Eqs. 3.45, 3.46 and 3.47 could be written respectively as

$$D_{ijmn}^{h}=\frac{1}{|Y|}\int_Y D_{ijk2}(y_2)\left[I_{k2}^{mn}-\frac{\partial \chi_k^{mn}(y_2)}{\partial y_2}\right]\mathrm{d}y_2 \tag{3.49}$$

$$\frac{\partial}{\partial y_2}\left[D_{i2k2}(y_2)\left(I_{k2}^{mn}-\frac{\partial \chi_k^{mn}(y_2)}{\partial y_2}\right)\right]=0 \tag{3.50}$$

$$\sigma_{i2}^{(1)}=\left[D_{i2k2}(y_2)\left(I_{k2}^{mn}-\frac{\partial \chi_k^{mn}(y_2)}{\partial y_2}\right)\right]\frac{\partial u_m^{(0)}}{\partial x_n}(x) \tag{3.51}$$

where y_2 is the direction along which the material properties varies in the RVE (see Fig. 3.8) and $|Y|$ is the length of the RVE along y_2. The Eq. 3.50 is a system of differential equations that can be solved as:

$$\begin{cases} \frac{\partial \chi_{k_1}^{mn}}{\partial y_2}=(D_{k2o2})^{-1}D_{o2mn}-(D_{k2o2})^{-1}K_{omn_1} & \text{for } 0<y<=\rho\,|Y| \\ \frac{\partial \chi_{k_2}^{mn}}{\partial y_2}=(D_{k2o2})^{-1}D_{o2mn}-(D_{k2o2})^{-1}K_{omn_2} & \text{for } \rho\,|Y|<y<|Y| \end{cases} \tag{3.52}$$

K_{omn_1} and K_{omn_2} are constant terms. The subscript 1 stands for the fibre phase and the subscript 2 stands for the matrix phase. Hereafter, expressions such as $(D_{k2o2})^{-1}$ stand for the inverse of a bidimensional matrix. The values of K_{omn} can be obtained from the boundary conditions. Since the BCs are applied on χ_k^{mn} and on $\frac{\partial \chi_k^{mn}}{\partial y_2}$, the Eq. 3.52 can be solved:

$$\begin{cases} \chi_{k_1}^{mn}(y_2)=(D_{k2o2})^{-1}D_{o2mn}y_2-(D_{k2o2})^{-1}K_{omn_1}y_2+G_{kmn_1} \\ \chi_{k_2}^{mn}(y_2)=(D_{k2o2})^{-1}D_{o2mn}y_2-(D_{k2o2})^{-1}K_{omn_2}y_2+G_{kmn_2} \end{cases} \tag{3.53}$$

with G_{omn_1} and G_{omn_2} as constant terms. The BCs are considered to find the values of the constant terms K_{omn_1}, K_{omn_2}, G_{kmn_1} and G_{kmn_2} in Eq. 3.53:

- perfect bonding between the phases

$$\chi_{k1}^{mn}(\rho Y) = \chi_{k2}^{mn}(\rho Y) \tag{3.54}$$

- continuity of the stress between the phases

$$\sigma_{i2_1}^{(1)}(\rho Y) = \sigma_{i2_2}^{(1)}(\rho Y) \tag{3.55}$$

- Y-periodicity

$$\chi_{k_1}^{mn}(0) = \chi_{k_2}^{mn}(Y) \tag{3.56}$$

$$\sigma_{i2_1}^{(1)}(0) = \sigma_{i2_2}^{(1)}(Y) \tag{3.57}$$

- unicity condition, i.e. zero average on Y

$$\overline{\chi_k^{mn}} = \frac{1}{|Y|}\int_Y \chi_k^{mn}(y_2)\mathrm{d}y_2 = 0 \tag{3.58}$$

As a matter of fact, only $K_{omn_1} = K_{omn_2} = K_{omn}$ is needed to compute the equivalent properties

$$K_{omn} = \left(\overline{(D_{o2p2})^{-1}}\right)^{-1}\overline{(D_{p2q2})^{-1}D_{q2mn}} \tag{3.59}$$

where the operator $\overline{\bullet}$ performs an average over the RVE:

$$\overline{X} = \frac{1}{|Y|}\int_Y X(y_2)\mathrm{d}y_2 \tag{3.60}$$

Substituting Eq. 3.59 in Eq. 3.52:

$$\frac{\partial\chi_k^{mn}}{\partial y_2} = (D_{k2o2})^{-1}D_{o2mn} - (D_{k2o2})^{-1}\left(\overline{(D_{o2p2})^{-1}}\right)^{-1}\overline{(D_{p2q2})^{-1}D_{q2mn}} \tag{3.61}$$

The equivalent properties for the AEH can be computed with the substitution of Eq. 3.61 in Eq. 3.49:

$$\begin{aligned} D_{ijmn}^h = \overline{D_{ijmn}} \quad &- \quad \overline{D_{ijk2}(D_{k2o2})^{-1}D_{o2mn}} \\ &+ \quad \left(\overline{D_{ijk2}(D_{k2o2})^{-1}(D_{o2p2})^{-1}}\right)^{-1}\overline{(D_{p2q2})^{-1}D_{q2mn}} \end{aligned} \tag{3.62}$$

AEH numerical solution

The analytical solution for the AEH could be obtained since the material properties vary only in one direction, leading to a 1D homogenisation problem. However, this is not sufficient to take into account the electrodes. To overcome this limitation a 3D homogenisation

model has been developed. The equations to be considered are Eqs. 3.45 and 3.46, here rewritten for convenience:

$$D^h_{ijmn} = \frac{1}{|Y|}\int_Y D_{ijkl}(y)\left[I^{mn}_{kl} - \frac{\partial \chi^{mn}_k(y)}{\partial y_l}\right]\mathrm{d}y \tag{3.63}$$

$$\frac{\partial}{\partial y_j}\left[D_{ijkl}(y)\left(I^{mn}_{kl} - \frac{\partial \chi^{mn}_k(y)}{\partial y_l}\right)\right] = 0 \tag{3.64}$$

In order to calculate the effective properties with Eq. 3.63, Eq. 3.64 have to be solved. This is equivalent to solving the following auxiliary variational problem

$$\int_Y D_{ijkl}\frac{\partial \chi^{mn}_k}{\partial y_l}\frac{\partial v_i}{\partial y_j}\mathrm{d}Y = \int_Y D_{ijmn}\frac{\partial v_i}{\partial y_j}\mathrm{d}Y, \quad v_i \in V_Y \tag{3.65}$$

$\chi^{mn}_k \in V_Y$, where V_Y is the set of Y-periodic continuous and sufficiently regular functions with zero average value in Y [48]. This problem is similar to a electro-mechanical one in which χ^{mn}_k is the generalised displacement field. It is solved using FEM. Details about how to enforce the periodicity of χ^{mn}_k can be found in [37]. It can be derived that the right-hand side of Eq. 3.65 corresponds to generalised surface loads acting at interfaces between different materials, with direction and module dependent on the material properties jump across the interface. It can be stated that these loads ensures the fulfilment of the boundary conditions in Eq. 3.55. In fact the continuity of χ^{mn}_k across the material interfaces is guaranteed by the finite element model but the continuity of the physical stress of the Eq. 3.47 is enforced through a discontinuity in the "mathematical" stress of the mechanical-like problem of Eq. 3.65.

In the piezoelectric case, given a 9x9 generalised constitutive matrix $\mathbf{C_g}$ (matrix form of the tensor D_{ijmn}), each column corresponds to a particular load case. If the interface among the different materials has a normal vector

$$\overrightarrow{\mathbf{n}} = (n_1,n_2,n_3) \tag{3.66}$$

and the orthonormal system of vectors is $\overrightarrow{\mathbf{i_1}},\overrightarrow{\mathbf{i_2}},\overrightarrow{\mathbf{i_3}}$ then:

$$\begin{aligned}
\overrightarrow{\mathbf{F}} &= \Delta C_{g1\lambda}n_1\overrightarrow{\mathbf{i_1}} + \Delta C_{g2\lambda}n_2\overrightarrow{\mathbf{i_2}} + \Delta C_{g3\lambda}n_3\overrightarrow{\mathbf{i_3}} + \\
&\quad \Delta C_{g4\lambda}n_2\overrightarrow{\mathbf{i_3}} + \Delta C_{g4\lambda}n_3\overrightarrow{\mathbf{i_2}} + \Delta C_{g5\lambda}n_1\overrightarrow{\mathbf{i_3}} + \\
&\quad \Delta C_{g5\lambda}n_3\overrightarrow{\mathbf{i_1}} + \Delta C_{g6\lambda}n_1\overrightarrow{\mathbf{i_2}} + \Delta C_{g6\lambda}n_2\overrightarrow{\mathbf{i_1}} \\
Q &= \Delta C_{g7\lambda}n_1 + \Delta C_{g8\lambda}n_2 + \Delta C_{g9\lambda}n_3
\end{aligned} \tag{3.67}$$

$\overrightarrow{\mathbf{F}}$ is a surface mechanical load and Q is a surface electrical charge. λ is an index that corresponds to a couple m,n, i.e to a column of matrix $\mathbf{C_g}$. In the case of MFC the interface between the two phases is perpendicular to y_2. Therefore $n_1 = n_3 = 0$ and $n_2 = 1$ and Eqs. 3.67 become:

$$\overrightarrow{\mathbf{F}} = \Delta C_{g2\lambda}n_2\overrightarrow{\mathbf{i_2}} + \Delta C_{g4\lambda}n_2\overrightarrow{\mathbf{i_3}} + \Delta C_{g6\lambda}n_2\overrightarrow{\mathbf{i_1}} \tag{3.68}$$

$$Q = \Delta C_{g8\lambda}n_2 \tag{3.69}$$

In the RVE model there are two interfaces that have opposite signs for a given applied surface mechanical load or surface charge. Because of the orthotropy of the materials of the MFC, only seven load cases could be considered instead of nine. Load cases are presented in Table 3.4. Four of these, namely λ = 1,2,3,9, differ only in the magnitude

Case	Surface force			Surface charge
	y_1 component	y_2 component	y_3 component	
$\lambda = 1$	$F_1 = 0$	$F_2 = \Delta C_{g21}$	$F_3 = 0$	$Q = 0$
$\lambda = 2$	$F_1 = 0$	$F_2 = \Delta C_{g22}$	$F_3 = 0$	$Q = 0$
$\lambda = 3$	$F_1 = 0$	$F_2 = \Delta C_{g23}$	$F_3 = 0$	$Q = 0$
$\lambda = 4$	$F_1 = 0$	$F_2 = 0$	$F_3 = \Delta C_{g44}$	$Q = \Delta C_{g84}$
$\lambda = 6$	$F_1 = \Delta C_{g66}$	$F_2 = 0$	$F_3 = 0$	$Q = 0$
$\lambda = 8$	$F_1 = 0$	$F_2 = 0$	$F_3 = \Delta C_{g48}$	$Q = \Delta C_{g88}$
$\lambda = 9$	$F_1 = 0$	$F_2 = \Delta C_{g29}$	$F_3 = 0$	$Q = 0$

Table 3.4. Applied surface loads and surface charges to the RVE in numerical AEH.

of the applied loads. Thanks to the linearity of the problem only four load cases out of seven need to be solved and the other three load cases are computed with a simple ratio. A graphical representation of the load cases is given in Fig. 3.9. The RVE is meshed with 1300 8-node brick piezoelectric elements using commercial FEM software ABAQUS. A mesh convergence analysis has been performed. The adopted mesh guarantees the convergence of at least three significant digits of the computed equivalent material properties. In ABAQUS Theory Manual [63] it is shown that the part of the generalised load vector corresponding to applied charges has a negative sign. Although this is correct for the physical piezoelectric problem, it is not valid for the variational problem of AEH. Therefore, surface charges in Eqs. 3.67 and 3.69 must be changed of sign. Moreover, during the postprocessing phase, in which the effective properties are computed via Eq. 3.63, the signs of the electric field components given by the FEM solver must be changed due to the definition of the electric field as the gradient of the electric potential changed of sign. The problem can be numerically ill conditioned for the load cases that correspond to $\lambda = 8$ and $\lambda = 9$ because of the small entity of the applied generalised loads. A simple solution is to magnify the loads by a factor that will be used in the postprocessing phase to scale the FEM results. Without electrodes the results correspond to the analytical solution found in Sec. 3.2.1. This does not apply when electrodes are considered. This is performed imposing a constant zero electrical potential on the electrodes surface via boundary conditions. Fig. 3.10 shows the deformed RVE for the four load cases together with the colourmap of the electric potential distribution.

3.2.2 Uniform field method

The Uniform Field Method (UFM) [18, 33, 22] is adopted to obtain analytical formulae for the equivalent properties of the MFC. UFM is based on the hypothesis that fields such as stress fields and strain fields are uniform in each phase of the RVE. At this stage the

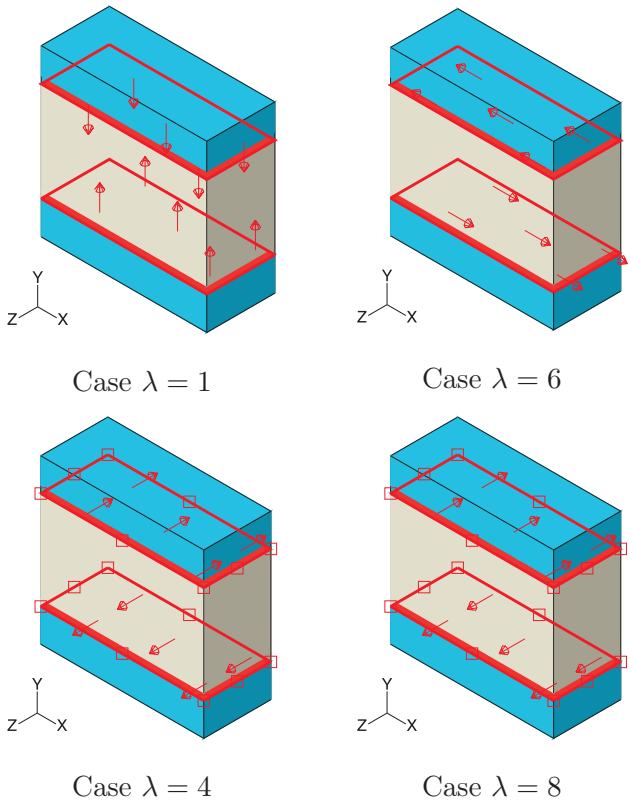

Figure 3.9. Representation of the four load cases. Arrows stand for applied surface forces and squares stand for applied surface charges. Cases $\lambda = 4$ and $\lambda = 8$ differ in the magnitude of applied loads and charges (see table 3.4).

relations among fields, which are necessary to derive the effective properties, are presented.

Relationships among fields

The effective properties derived with the UFM depend on the relationships among fields in the RVE as a whole and in the phases. These relationships depend on the geometry of the RVE and derive directly from the uniform field hypothesis. In the case of a two phase piezoelectric composite, relationships among the fields can be of either of the following form:

- in the case of independent variable, the fields are equal in each constituent:

$$\overline{X_i} = X_i^p = X_i^m \tag{3.70}$$

- in the case of dependent variable, the fields are related through a linear mixture relation:

$$\overline{X_i} = \rho X_i^p + (1-\rho) X_i^m \tag{3.71}$$

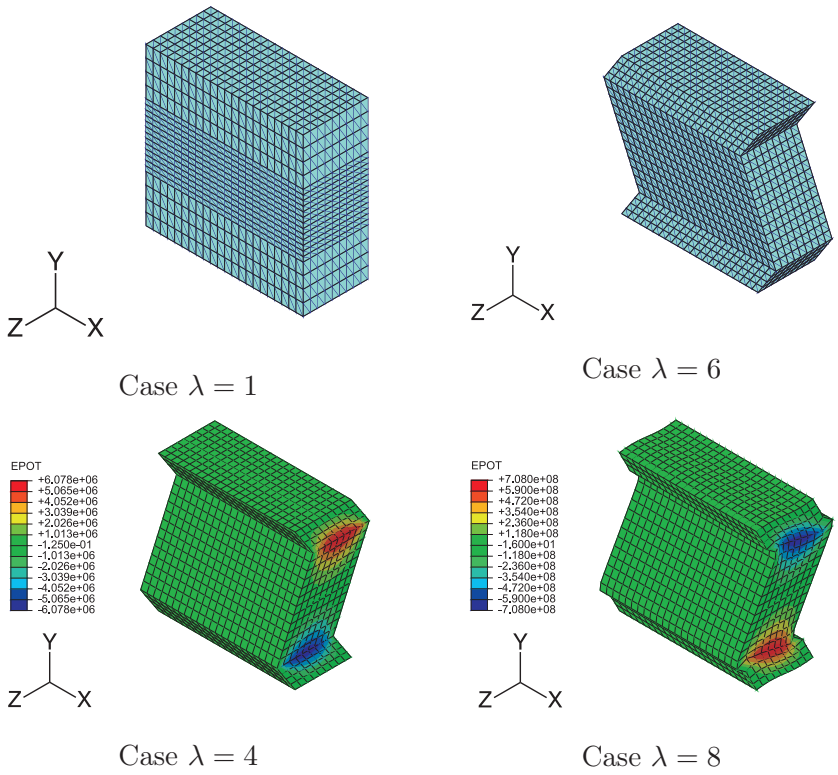

Figure 3.10. Deformed RVE. Colourmap represents the electric potential distribution. In the cases $\lambda = 1$ and $\lambda = 6$ the electric potential is uniform.

where ρ is the volume fraction of the piezoelectric phase. $\overline{X_i}$ is a generic generalised stress or strain for the whole RVE (mean value); X_i^p is its value in the piezoelectric phase and X_i^m is its value in the matrix phase. Corresponding generalised stress and strain have different kinds of relationships, i.e. if $\overline{T_1} = T_1^p = T_1^m$ then $\overline{S_1} = \rho S_1^p + (1-\rho) S_1^m$.

Each generalised stress or strain has its own relationship among fields. In the case of MFC, provided that y_2 is the direction along which the materials properties change (see Fig. 3.8), S_1, S_3, S_5, E_1 and E_3 are independent, whereas S_2, S_4, S_6 and E_2 are dependent. Stress and electric displacement components are dependent or independent accordingly.

Matrix-based procedure

A matrix-based procedure has been implemented in a symbolic manipulation software to obtain the formulae for the equivalent properties and in a numerical software to obtain the values of the equivalent properties. Due to this approach lengthy and error prone manual computations are avoided. The procedure is based on the partition of the vector of generalised stresses $\mathbf{T_g}$, the generalised constitutive matrix $\mathbf{C_g}$ and the vector of generalised strains $\mathbf{S_g}$ according to the dependency or independency property of each generalised stress and strain. The procedure is divided into a series of steps:

1. Rearrangement of Eq. 2.3 separating dependent and independent generalised stresses and strains

$$\begin{Bmatrix} \{\mathbf{T_I}\} \\ \{\mathbf{T_D}\} \end{Bmatrix} = \begin{bmatrix} [\mathbf{C_{II}}] & [\mathbf{C_{ID}}] \\ [\mathbf{C_{DI}}] & [\mathbf{C_{DD}}] \end{bmatrix} \times \begin{Bmatrix} \{\mathbf{S_I}\} \\ \{\mathbf{S_D}\} \end{Bmatrix} \tag{3.72}$$

where $[\mathbf{C_{II}}]$, $[\mathbf{C_{DI}}]$, $[\mathbf{C_{ID}}]$, $[\mathbf{C_{DD}}]$ can be derived from $\mathbf{C}$ with row and column permutations, according to the rearrangement of $\mathbf{T}$ and $\mathbf{S}$.

2. Extraction of the dependent variables in terms of the independent ones:

$$\begin{Bmatrix} \{\mathbf{T_D}\} \\ \{\mathbf{S_D}\} \end{Bmatrix} = \begin{bmatrix} [\mathbf{A_1}] & [\mathbf{A_2}] \\ [\mathbf{A_3}] & [\mathbf{A_4}] \end{bmatrix} \times \begin{Bmatrix} \{\mathbf{T_I}\} \\ \{\mathbf{S_I}\} \end{Bmatrix} \tag{3.73}$$

The vector on the left hand side is called $\{\mathbf{X}\}_D$ and the vector on the right hand side is called $\{\mathbf{X}\}_I$. It can be shown that

$$[\mathbf{A_1}] = [\mathbf{C_{DD}}]\,[\mathbf{C_{ID}}]^{-1} \tag{3.74}$$

$$[\mathbf{A_2}] = [\mathbf{C_{DI}}] - [\mathbf{C_{DD}}]\,[\mathbf{C_{ID}}]^{-1}\,[\mathbf{C_{II}}] \tag{3.75}$$

$$[\mathbf{A_3}] = [\mathbf{C_{ID}}]^{-1} \tag{3.76}$$

$$[\mathbf{A_4}] = -\,[\mathbf{C_{ID}}]^{-1}\,[\mathbf{C_{II}}] \tag{3.77}$$

and the matrix containing $\mathbf{A_1}$, $\mathbf{A_2}$, $\mathbf{A_3}$ and $\mathbf{A_4}$ is called $\mathbf{A}$.

3. According to the boundary conditions in Eq. 3.71

$$\left\{\overline{\mathbf{X}}\right\}_D = \rho\,\{\mathbf{X}\}_D^f + (1-\rho)\,\{\mathbf{X}\}_D^m \tag{3.78}$$

where the superscript f stands for the piezoelectric phase and the superscript m for the matrix phase. According to Eq. 3.73, Eq. 3.78 can be written as

$$\left[\mathbf{A^h}\right]\left\{\overline{\mathbf{X}}\right\}_I = \rho\left[\mathbf{A^f}\right]\{\mathbf{X}\}_I^f + (1-\rho)\,[\mathbf{A^m}]\,\{\mathbf{X}\}_I^m \tag{3.79}$$

where the superscript h stands for homogeneous. Because of the boundary conditions in Eq. 3.70, Eq. 3.79 can be simplified as:

$$\left[\mathbf{A^h}\right] = \rho\left[\mathbf{A^f}\right] + (1-\rho)\,[\mathbf{A^m}] \tag{3.80}$$

4. Equivalent properties can be obtained from A^e. Inverting equations 3.74, 3.75, 3.76 and 3.77 one can get:

$$\left[\mathbf{C_{ID}^h}\right] = \left[\mathbf{A_3^h}\right]^{-1} \tag{3.81}$$

$$\left[\mathbf{C_{DD}^h}\right] = \left[\mathbf{A_1^h}\right]\left[\mathbf{C_{ID}^h}\right] \tag{3.82}$$

$$\left[\mathbf{C_{II}^h}\right] = -\left[\mathbf{C_{ID}^h}\right]\left[\mathbf{A_4^h}\right] \tag{3.83}$$

$$\left[\mathbf{C_{DI}^h}\right] = \left[\mathbf{A_2^h}\right] + \left[\mathbf{C_{DD}^h}\right]\left[\mathbf{A_3^h}\right]\left[\mathbf{C_{II}^h}\right] \tag{3.84}$$

The output of this calculation is the matrix $\mathbf{C_g}^{\mathbf{h}}$, which contains in each element the formula to evaluate the corresponding equivalent property or its value. For example in the first row, first column, if a symbolic manipulation software is used there is the formula to evaluate the equivalent C_{11}. If a numerical software is used there is the value of the equivalent C_{11}. Formulae to evaluate equivalent properties of anisotropic materials can become very lengthy. Error prone manual computations are avoided with the presented procedure.

In order to implement this procedure $\mathbf{C_{ID}}$ and $\mathbf{A_3^h}$ must be invertible. In the case of MFC, provided that materials properties change along direction 2 (see Fig. 3.8), S_1, T_2, S_3, T_4, S_5, T_6, E_1, D_2 and E_3 are independent, whereas T_1, S_2, T_3, S_4, T_5, S_6, D_1, E_2 and D_3 are dependent. Following the procedure presented:

$$\mathbf{C_{ID}} = \begin{bmatrix} C_{22}^E & 0 & 0 & 0 \\ 0 & C_{44}^E & 0 & e_{24} \\ 0 & 0 & C_{66}^E & 0 \\ 0 & e_{24} & 0 & \epsilon_{22}^T \end{bmatrix} \tag{3.85}$$

This matrix is invertible if its determinant:

$$C_{22}^E C_{66}^E (C_{44}^E \epsilon_{22}^T - e_{24}^2) \neq 0 \tag{3.86}$$

The determinant is null only if $C_{44}^E \epsilon_{22}^T = e_{24}^2$, being C_{22}^E and C_{66}^E not null.

Equivalence between UFM and AEH for MFCs

Expressions for the Equivalent properties in Eq. 3.62 obtained using AEH method correspond exactly to the formulae derived according to the UFM in the case of the MFC. Eq. 3.61 is considered in order to understand this equivalence. It should be stated that:

- $\frac{\partial \chi_k^{mn}}{\partial y_2}$ is piecewise constant, depending only on the material properties that are piecewise constant.
- Integrating $\frac{\partial \chi_k^{mn}}{\partial y_2}$ in y_2, χ_k^{mn} can be computed. It is piecewise linear in y_2 and is independent of y_1,y_3.

The displacement, strain and stress fields obtained with the AEH method are considered. In the AEH method, the first order approximation of the generalised displacement field (see Eq. 3.43) is expressed as:

$$u_i^\epsilon(x) = u_i^{(0)}(x) + \epsilon u_i^{(1)}(x,y) \tag{3.87}$$

$u_i^{(0)}$ is dependent only on x considering the lowest order BVD problem among the BVD problems in which the original BVD problem is split due to the AEH. This means that $u_i^{(0)}$ corresponds to the macroscopic displacement field of the homogenised material. From the second lowest order BVD problem it is possible to derive

$$u_i^{(1)}(x,y) = -\chi_i^{kl}(y) \frac{\partial u_k^{(0)}}{\partial x_l}(x) + \bar{u}_i^1 \tag{3.88}$$

where $\bar{u}_i^1$ can be considered null [48]. Eq. 3.87 becomes:

$$u_i^\epsilon(x) = u_i^{(0)}(x) - \epsilon\chi_i^{kl}(y)\frac{\partial u_k^{(0)}}{\partial x_l}(x) \tag{3.89}$$

Eq. 3.89 must be differentiated according to Eq. 3.44 in order to find the expression of the strain fields:

$$\frac{\partial u_i^\epsilon(x)}{\partial x_j^\epsilon} = \frac{\partial u_i^{(0)}(x)}{\partial x_j} - \frac{\partial \chi_i^{kl}(y)}{\partial y_j}\frac{\partial u_k^{(0)}}{\partial x_l}(x) - \epsilon\chi_i^{kl}(y)\frac{\partial^2 u_k^{(0)}}{\partial x_l \partial x_j}(x) \tag{3.90}$$

The last term can be neglected because it is a second order derivative of the macroscopic displacement and the current analysis is restricted to linear strain. Therefore Eq. 3.90 can be rewritten as:

$$\frac{\partial u_i^\epsilon(x)}{\partial x_j^\epsilon} = \frac{\partial u_k^{(0)}(x)}{\partial x_l}\left(I_{kl}^{ij} - \frac{\partial \chi_i^{kl}(y)}{\partial y_j}\right) \tag{3.91}$$

Considering the properties of χ_k^{mn} stated above it is now clear that the strain field is different in the two phases only when $j = 2$. Therefore:

- S_1, S_3, S_5, E_1 and E_3 have the same values in both the phases.
- S_2, S_4, S_6 and E_2 are different between the two phases, but uniform inside each phase.

Stress fields and electric displacement fields, similarly, are uniform inside each phase. This means that for AEH in the case of the MFC has the same hypothesis of uniformity of the strain and stress fields inside each phase that is typical of the UFM. Moreover, the so called dependent and independent generalised strains in the UFM (see section 3.2.2) are such also for the AEH. These are the reasons why the formulae for the equivalent properties are the same for AEH and UFM in the case of MFCs. Eq. 3.91 provides an effective way to calculate the strain fields in the phases given the macroscopic strain fields.

3.2.3 Numerical periodic homogenisation for MFC

The numerical Periodic Homogenisation Method (PHM) [35, 22, 40], first introduced in Sec. 3.1.2, is here adopted in the case of MFC. Using finite element analysis, it is possible to take into account the effect of electrodes and therefore results can be compared to the ones of the AEH numerical solution. At the macroscale, MFCs can be defined as periodic repetition of RVEs (see Fig. 3.8). In order to take into account this repetition, periodic boundary conditions must be applied between opposite faces of the RVE. These boundary conditions are required to ensure the continuity of the generalised displacement (mechanical displacement and electric potential) through consecutive RVE models. The RVE has a parallelepiped geometry, see Fig. 3.8. Boundary conditions can be expressed more conveniently with reference to opposite faces of the RVE (A^- and A^+ are the opposite faces perpendicular to direction 1, B^- and B^+ to direction 2, C^- and C^+ to direction 3).

ABAQUS Implementation

The RVE is analysed using ABAQUS commercial finite element software. The RVE is discretised using 1300 8-node brick piezoelectric elements. The adopted mesh guarantees the convergence of at least three significant digits of the computed equivalent material properties. Mesh is uniform in order to have corresponding nodes on opposite faces. Boundary condition are applied node to node thanks to the *Equation Constraint* feature available in ABAQUS. Table 3.5 presents a detailed description of the boundary conditions for each load case and the corresponding computed material coefficients. The magnitude of the

Case	Mechanical and electrical BC			Computed coefficients
	A^+ and A^-	B^+ and B^-	C^+ and C^-	
1	$u^i_{1A+} - u^i_{1A-} = q$ $\varphi^i_{A+} - \varphi^i_{A-} = 0$	$u^i_{2B+} - u^i_{2B-} = 0$ $\varphi^i_{B+} - \varphi^i_{B-} = 0$	$u^i_{3C+} - u^i_{3C-} = 0$ $\varphi^i_{C+} - \varphi^i_{C-} = 0$	C^E_{11},C^E_{21},C^E_{31},e_{31}
2	$u^i_{1A+} - u^i_{1A-} = 0$ $\varphi^i_{A+} - \varphi^i_{A-} = 0$	$u^i_{2B+} - u^i_{2B-} = q$ $\varphi^i_{B+} - \varphi^i_{B-} = 0$	$u^i_{3C+} - u^i_{3C-} = 0$ $\varphi^i_{C+} - \varphi^i_{C-} = 0$	C^E_{12},C^E_{22},C^E_{32},e_{32}
3	$u^i_{1A+} - u^i_{1A-} = 0$ $\varphi^i_{A+} - \varphi^i_{A-} = 0$	$u^i_{2B+} - u^i_{2B-} = 0$ $\varphi^i_{B+} - \varphi^i_{B-} = 0$	$u^i_{3C+} - u^i_{3C-} = q$ $\varphi^i_{C+} - \varphi^i_{C-} = 0$	C^E_{13},C^E_{23},C^E_{33},e_{33}
4	$u^i_{1A+} - u^i_{1A-} = 0$ $\varphi^i_{A+} - \varphi^i_{A-} = 0$	$u^i_{3B+} - u^i_{3B-} = q$ $\varphi^i_{B+} - \varphi^i_{B-} = 0$	$u^i_{2C+} - u^i_{2C-} = q$ $\varphi^i_{C+} - \varphi^i_{C-} = 0$	C^E_{44},e_{24}
5	$u^i_{3A+} - u^i_{3A-} = q$ $\varphi^i_{A+} - \varphi^i_{A-} = 0$	$u^i_{2B+} - u^i_{2B-} = 0$ $\varphi^i_{B+} - \varphi^i_{B-} = 0$	$u^i_{1C+} - u^i_{1C-} = q$ $\varphi^i_{C+} - \varphi^i_{C-} = 0$	C^E_{55},e_{15}
6	$u^i_{2A+} - u^i_{2A-} = q$ $\varphi^i_{A+} - \varphi^i_{A-} = 0$	$u^i_{1B+} - u^i_{1B-} = q$ $\varphi^i_{B+} - \varphi^i_{B-} = 0$	$u^i_{3C+} - u^i_{3C-} = 0$ $\varphi^i_{C+} - \varphi^i_{C-} = 0$	C^E_{66}
7	$u^i_{1A+} - u^i_{1A-} = 0$ $\varphi^i_{A+} - \varphi^i_{A-} = 0$	$u^i_{2B+} - u^i_{2B-} = 0$ $\varphi^i_{B+} - \varphi^i_{B-} = 0$	$u^i_{3C+} - u^i_{3C-} = 0$ $\varphi^i_{C+} - \varphi^i_{C-} = q$	ϵ^S_{33},e_{31},e_{32},e_{33}
8	$u^i_{1A+} - u^i_{1A-} = 0$ $\varphi^i_{A+} - \varphi^i_{A-} = 0$	$u^i_{2B+} - u^i_{2B-} = 0$ $\varphi^i_{B+} - \varphi^i_{B-} = q$	$u^i_{3C+} - u^i_{3C-} = 0$ $\varphi^i_{C+} - \varphi^i_{C-} = 0$	ϵ^S_{22},e_{24}
9	$u^i_{1A+} - u^i_{1A-} = 0$ $\varphi^i_{A+} - \varphi^i_{A-} = q$	$u^i_{2B+} - u^i_{2B-} = 0$ $\varphi^i_{B+} - \varphi^i_{B-} = 0$	$u^i_{3C+} - u^i_{3C-} = 0$ $\varphi^i_{C+} - \varphi^i_{C-} = 0$	ϵ^S_{11},e_{15}

Table 3.5. Periodic boundary conditions for PHM: u^i_{jK} is the displacement in direction j in the i-th node of the face K, φ^i_K is the electric potential in the i-th node of the face K, q is an arbitrary non-null value.

jump between degrees of freedom of opposite nodes is null or have an arbitrary non-null value q depending on the load case. The equipotential conditions on the faces C^- and C^+ is enforced in order to consider the presence of the electrode. The equivalent coefficients are computed via simple ratios between average values, according to the load cases.

3.2.4 Results

The materials composing the MFC are epoxy matrix and piezoceramic SANOX P502 rectangular fibres. Epoxy is an isotropic material. Its properties are defined by the Young's modulus $E = 2.9$ GPa, the Poisson's ratio $\nu = 0.31$, and the relative permittivity $\epsilon = 4.25$. The piezoceramic SONOX P502 is orthotropic with symmetry around the poling direction, which is direction 3. Its properties are defined in Table 3.6. d_{31}-type MFC has fibre volume fraction equal to 0.865.

Properties	Symbol	Value
Young's modulus in GPa	$E_1 = E_2$	54.05
	E_3	48.30
Shear modulus in GPa	$G_{23} = G_{13}$	19.48
	G_{12}	19.14
Poisson's ratios	$\nu_{23} = \nu_{13}$	0.44
	ν_{12}	0.41
Piezoelectric charge constants in pC/N	$d_{31} = d_{32}$	-185
	d_{33}	440
	$d_{42} = d_{51}$	560
Dielectric relative constants	$\epsilon_{11}^T/\epsilon_0$,$\epsilon_{22}^T/\epsilon_0$	1950
	$\epsilon_{33}^T/\epsilon_0$	1850

Table 3.6. Piezoceramic SONOX P502 properties from CeramTec. ϵ_0 is the vacuum permittivity.

Numerical validation using the PHM

The numerical results obtained using the AEH are compared with the analytical results obtained with formulae derived with the AEH and with the numerical PHM results. The effective values for the mechanical properties, the piezoelectric constants and the dielectric coefficients of the homogeneous MFC model are illustrated in Figs. 3.11, 3.12, 3.13 and 3.14. Analytical mixing rules, numerical AEH and PHM results match for almost every property. The only relevant difference is observed for G_{Tz} in the case of high volume fraction of the piezoelectric phase. The analytical solution is higher than the numerical solutions. This difference is due to the presence of the electrode. Indeed, the imposition of a uniform potential on the electrode surfaces causes the non-uniformity of some fields in the phases, invalidating the hypothesis of the UFM. In particular the electrodes cause a gradient of the electric potential along direction 3, E_3, and, because of the piezoelectric effect, local fields of S_1, S_2, S_3, T_1, T_2, T_3 arise at the interfaces between the two phases. Numerical AEH results take into account the effect of the electrodes and match results obtained with PHM. Predicted effective values obtained for MFC (fibre volume fraction equal to 0.865) with analytical solution, numerical AEH and PHM for mechanical properties, piezoelectric constants and dielectric coefficient are shown in Tables 3.7 and 3.8.

Experimental validations via manufacturer datasheets

The homogenised properties given by the AEH for the active layer, built of epoxy and PZT fibres, cannot be directly compared to the experimental values given by Smart Materials datasheets. In fact MFC is a laminate [61] where the active layer is intercalated between the electrodes (made of copper and epoxy) and Kapton®layers, as shown in Fig. 3.8. For the Kapton®layers, the following properties are used: $E = 2.8$ GPa, $\nu = 0.3$. For the electrode layers, the following properties are used: $E = 30.3$ GPa, $\nu = 0.31$. In-plane

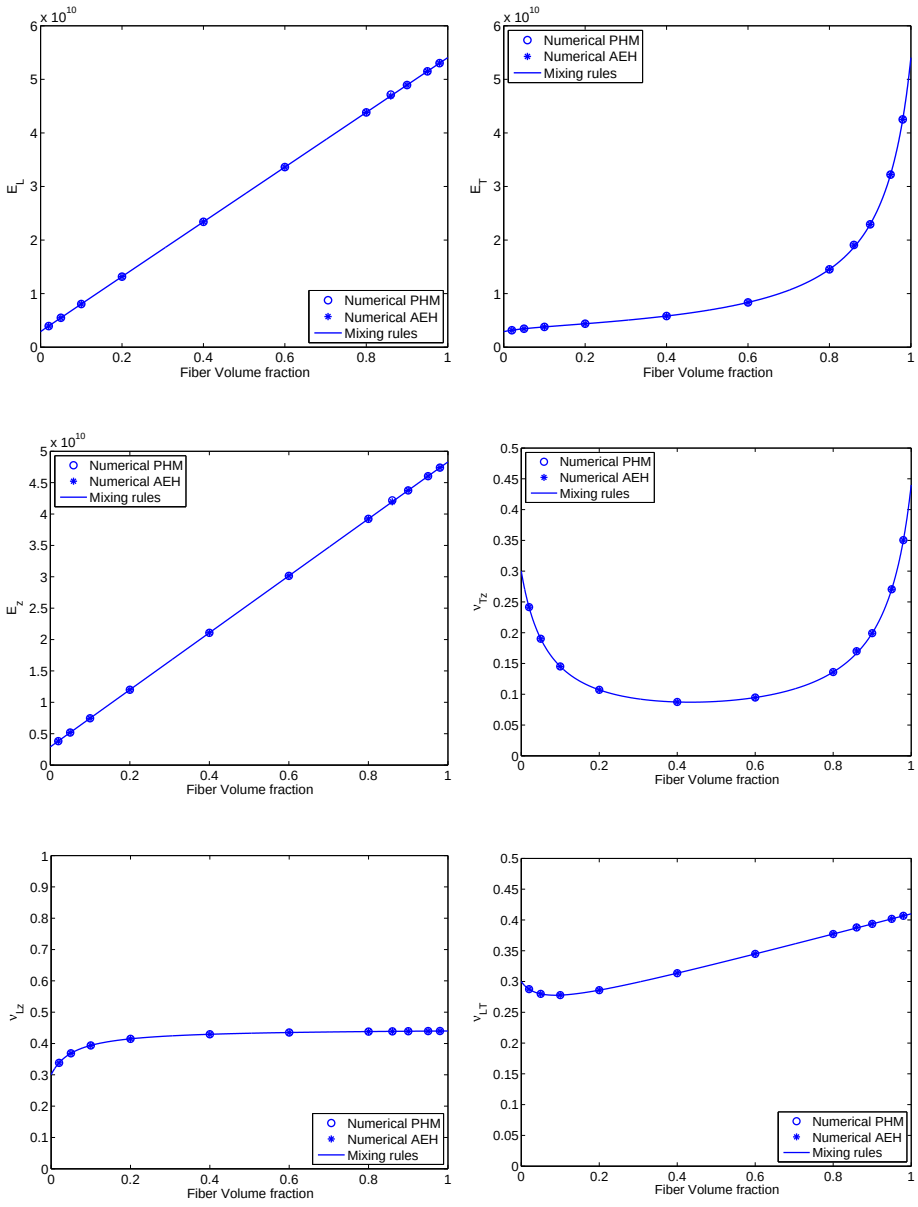

Figure 3.11. Computed mechanical properties of d_{31} MFC as a function of fibre volume fraction ρ. Elastic moduli are in Pa.

equivalent properties of the laminated sequence are computed on the basis of AEH results for the active layer with the Voigt mixing rule. The volume fractions are computed on the basis of layers thickness reported in the caption of Fig. 3.8. The free strain in longitudinal direction is computed as:

$$S_L = d_{31}\frac{V}{h} \tag{3.92}$$

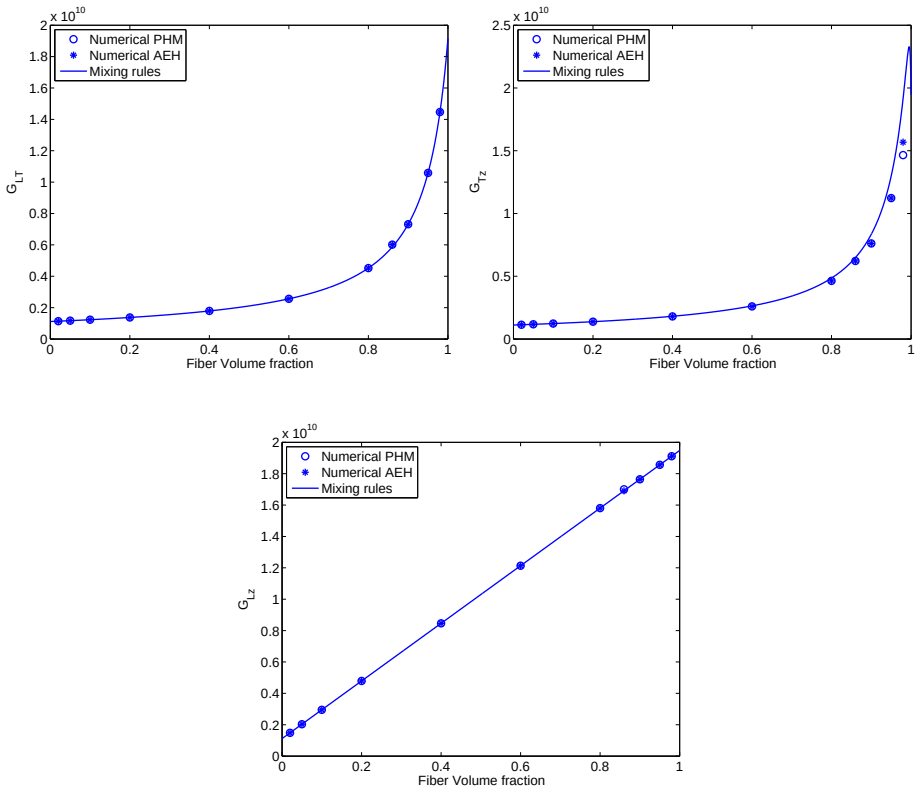

Figure 3.12. Computed mechanical properties of d_{31} MFC as a function of fibre volume fraction ρ. Results are in Pa.

Mechanical properties	Mixing rules UFM/AEH	Numerical AEH	PHM
E_1(GPa)	47.14	46.89	47.15
E_2(GPa)	19.06	19.06	19.08
E_3(GPa)	42.16	41.95	42.17
ν_{12}	0.3878	0.3880	0.3878
ν_{13}	0.4388	0.4387	0.4388
ν_{23}	0.1699	0.1704	0.1700
G_{12}(GPa)	6.011	6.015	6.015
G_{13}(GPa)	16.99	16.90	17.00
G_{23}(GPa)	6.664	6.216	6.216

Table 3.7. Computed mechanical properties for MFC with $\rho = 0.865$.

where V is the applied voltage and h is the thickness of the active layer. Table 3.9 presents a comparison between Smart Materials datasheets values and the computed results. Values

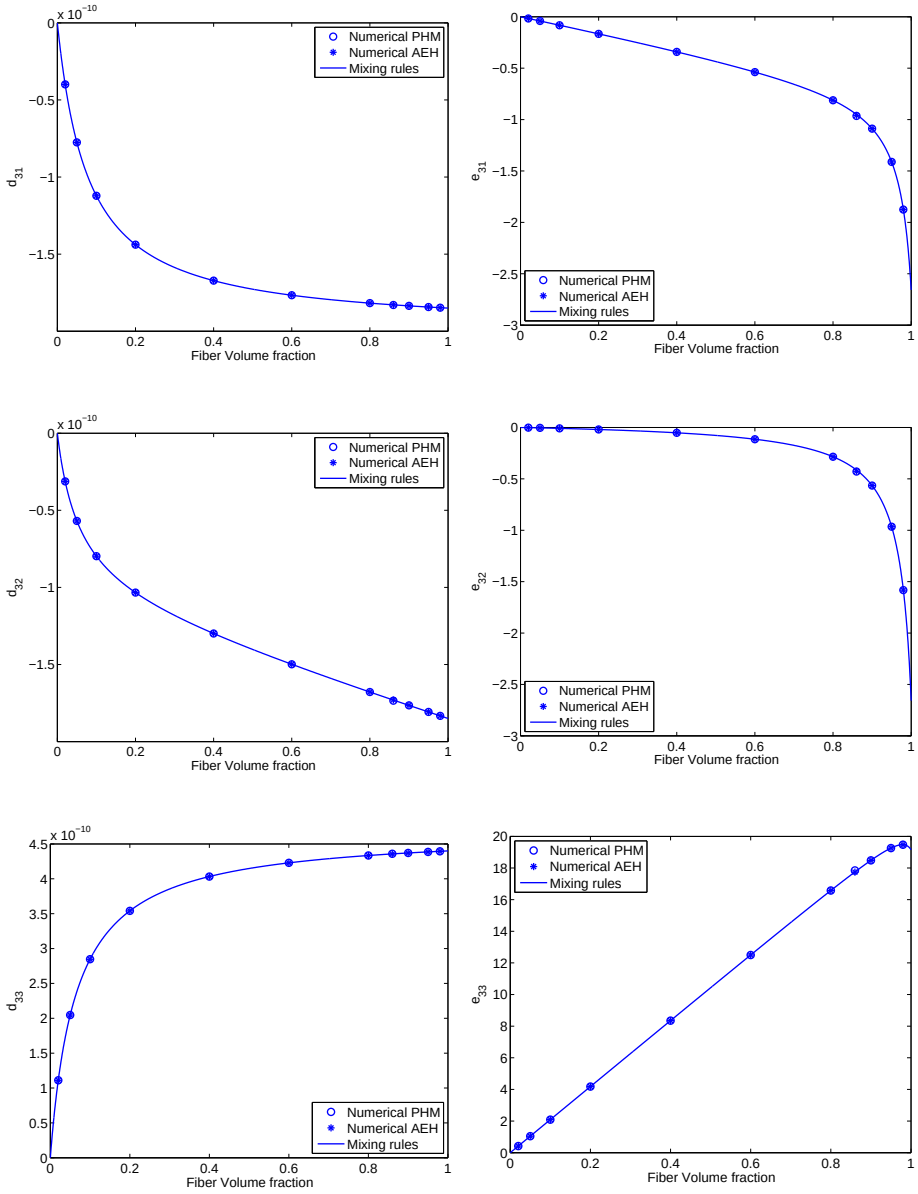

Figure 3.13. Computed strain piezoelectric constants d and stress piezoelectric constants e of d_{31} MFC as a function of fibre volume fraction ρ. d components are given in C/N, e components are given in C/m^2.

are in close agreement.

The presented results show that the proposed analytical mixing rules, obtained via the analytical AEH solution, estimate quite accurately the equivalent properties of MFC and, by extension, of devices with a geometry similar to MFCs.

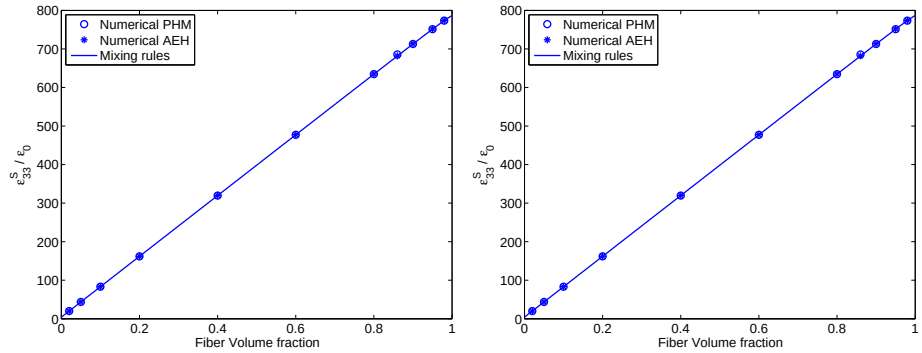

Figure 3.14. Computed dielectric constants of d_{31} MFCs as a function of fibre volume fraction ρ at zero strain (left) and at free strain (right).

Electromechanical properties	Mixing rules UFM/AEH	Numerical AEH	PHM
d_{31}(pC/N)	-182.9	-182.5	-182.9
d_{32}(pC/N)	-173.4	-173.0	-173.4
d_{33}(pC/N)	435.8	435.6	435.8
ϵ_{33}^S(nF/m)	6.068	6.039	6.069

Table 3.8. Computed electric and piezoelectric constants for MFC with $\rho = 0.865$.

Properties	Numerical AEH	Smart Materials datasheets
E_1(GPa)	32.95	30.34
E_2(GPa)	16.03	15.86
ν_{12}	0.35	0.31
$S_L(10^{-6}/\text{V})$	1.01	1.1

Table 3.9. Numerical results and experimental values of MFC properties. MFC is considered globally, not only as its active layer.

Chapter 4

Effect of matrix properties on the overall piezocomposite

Significant ratios between piezoelectric constants in the two in-plane directions have been achieved in piezoelectric composites. The directional dependency of piezocomposite sensors is dependent on the wavelength and the length of the senor itself. Barbezat et al. [64] used AFC as acoustic emission sensors on composites and polymer plates and compared performances with that of commercial acoustic emission sensors. Experimental results showed that AFCs have higher sensitivity along the direction of the piezoelectric fibres. Later, Barbezat et al. [65] investigated sensor properties of AFC in acoustic and acousto-ultrasonic. AFC used as acoustic emission sensors showed an intrinsic anisotropy in sensitivity, depending on the frequency range. Matt and Lanza di Scalea [66] presented a piezoelectric transducer rosettes comprised of MFC for passive damage or impact location in anisotropic structures. The MFC response to flexural ultrasonic guided waves was found to be highly directive. Eaton et al. [67] considered MFC transducers as sensors of acoustic emission. MFCs were observed to be less directionally sensitive than expected in terms of signal feature data. The high level of directional variance observed in the signal cross correlations may be problematic in acoustic emission techniques such as source location.

The optimisation of piezocomposite transducers design has received notable attention in the last two decades. A review on the optimisation of smart structures and actuators was presented by Frecker [68]. Different optimisation strategies are considered, such as the location of the actuators, their controller parameters and the coupling between structure and actuator. Silva et al. [69] presented a procedure of topology optimisation based on an homogenisation method where the primary fields are expanded asymptotically. The distributions of material and void in the periodic microstructure that maximise some performance characteristics of the piezocomposites have been found. Sigmund et al. [70] adopted topology optimisation to design the optimal matrix microstructure of 1-3 piezocomposites. The piezoelectric phase consists of rods and it is not subjected to optimisation. Kang and Tong [71] optimised the spatial distribution of actuation voltage in static structural shape control of plates with piezoelectric layers. The Mindlin plate theory is adopted in the finite element modelling. Kang and Wang [72] optimised the topology of bending actuators with

multilayer piezoelectric material. The distribution of actuation voltage and the structural layout of the actuator are considered in the optimisation. The topology optimisation of piezoelectric flextensional actuators, a flexible mechanical structure connected to a piezoceramic, has been considered by Chen et al. [73]. The output displacement in a specified point of the domain and direction has been maximised. The design of piezoelectric plate and shell actuators using topology optimisation was considered by Kogl and Silva [74]. Two design variables are discretised according to a finite element mesh: the piezoelectric material pseudo-density and its polarisation. The objective function of the optimisation problem is formulated as in [73]. A similar problem was solved by Carbonari et al. [75], optimising simultaneously the distribution of non-piezoelectric and piezoelectric material in the actuator.

The directional-dependence of the piezoelectric response in statics is examined in this chapter. It is presented in the case of planar piezoelasticity in order to highlight the significant parameters and ratios in the practical case of thin transducers. The influence of the matrix properties on the overall piezoelectric constants of piezocomposite transducers similar to MFC is investigated via the mixing rules presented and validated in Sec. 3.2.

4.1 Directional dependence in planar piezoelasticity

Classical plane stress (PS) and unidirectional electric field (UDEF) electromechanical assumptions are adopted. In the hypothesis of PS in the plane 1-2 the following relations holds:

$$\begin{aligned} \hat{Q}^E_{\alpha\beta} &= C^E_{\alpha\beta} - \frac{C^E_{\alpha 3} C^E_{3\beta}}{C^E_{33}} \\ \hat{e}_{k\alpha} &= e_{k\alpha} - \frac{e_{k3} C^E_{\alpha 3}}{C^E_{33}} \\ \hat{\epsilon}_{kk} &= \epsilon^{\varepsilon}_{kk} + \frac{e^2_{k3}}{C^E_{33}} \end{aligned} \tag{4.1}$$

with α,β = 1,2, where $\hat{Q}^E_{\alpha\beta}$ are plane stress stiffness properties at constant electric field, $\hat{e}_{k\alpha}$ are the plane stress piezoelectric constants (induced stresses per unit of electric field) and $\hat{\epsilon}_{kk}$ is the plane stress electric permittivity at constant stress. These relations derive from the three-dimensional constitutive Eqs. 2.3 in matrix form. Hat symbol denotes PS quantities. According to UDEF, only one component of the electric field and electric displacement vector is assumed to be non-constant, i.e. the component k. The reduced constitutive equations in tensor form related to the three-dimensional Eqs. 2.6 are written as:

$$\left\{ \begin{array}{c} \boldsymbol{\sigma} \\ D_k \end{array} \right\} = \left[\begin{array}{cc} \hat{\boldsymbol{Q}}^E & -\hat{\boldsymbol{e}}^T \\ \hat{\boldsymbol{e}} & \hat{\varepsilon}_{kk} \end{array} \right] \left\{ \begin{array}{c} \boldsymbol{\varepsilon} \\ E_k \end{array} \right\} \tag{4.2}$$

$\hat{\boldsymbol{Q}}^E$ is a two-dimensional fourth-order tensor. $\boldsymbol{\sigma}$, $\boldsymbol{\varepsilon}$ are two-dimensional second-order tensors, whereas $\hat{\boldsymbol{e}}$ is a vector. Using Voigt notation $\boldsymbol{\epsilon}$ and $\boldsymbol{\sigma}$ can be expressed as vectors:

$$\boldsymbol{\sigma} = \left\{ \begin{array}{c} \sigma_1 \\ \sigma_2 \\ \sigma_6 \end{array} \right\}, \boldsymbol{\varepsilon} = \left\{ \begin{array}{c} \varepsilon_1 \\ \varepsilon_2 \\ \varepsilon_6 \end{array} \right\} \tag{4.3}$$

The constitutive equations for linear piezoelectricity in the d-form are the following:

$$\left\{ \begin{array}{c} \boldsymbol{\varepsilon} \\ D_k \end{array} \right\} = \left[\begin{array}{cc} \boldsymbol{S}^E & \boldsymbol{d}^T \\ \boldsymbol{d} & \epsilon^{\sigma}_{kk} \end{array} \right] \left\{ \begin{array}{c} \boldsymbol{\sigma} \\ E_k \end{array} \right\} \tag{4.4}$$

$\boldsymbol{S}^E$, $\boldsymbol{d}$ and ϵ^{σ}_{kk} are the compliance matrix at constant electric field, the vector of strain piezoelectric constants (induced strains per unit of electric field) and the dielectric coefficient at constant stress respectively. In the case of d-form, coefficients do not change because of PS assumption.

The constitutive equations for linear piezoelectricity in the h-form are the following:

$$\left\{ \begin{array}{c} \boldsymbol{\sigma} \\ E_k \end{array} \right\} = \left[\begin{array}{cc} \hat{\boldsymbol{Q}}^D & -\hat{\boldsymbol{h}}^T \\ -\hat{\boldsymbol{h}} & \hat{\beta}^{\varepsilon}_{kk} \end{array} \right] \left\{ \begin{array}{c} \boldsymbol{\varepsilon} \\ D_k \end{array} \right\} \tag{4.5}$$

$\hat{\boldsymbol{Q}}^D$, $\hat{\boldsymbol{h}}$ and $\hat{\beta}^{\varepsilon}_{kk}$ are the stiffness matrix at constant electric displacement field, the vector of stress piezoelectric constants (induced stresses per unit of electric displacement) and the dielectric resistivity coefficient at constant strain respectively.

The constitutive equations for linear piezoelectricity in the g-form are the following:

$$\left\{ \begin{array}{c} \boldsymbol{\varepsilon} \\ E_k \end{array} \right\} = \left[\begin{array}{cc} \boldsymbol{S}^D & \boldsymbol{g}^T \\ -\boldsymbol{g} & \beta^{\sigma}_{kk} \end{array} \right] \left\{ \begin{array}{c} \boldsymbol{\sigma} \\ D_k \end{array} \right\} \tag{4.6}$$

$\boldsymbol{S}^D$, $\boldsymbol{g}$ and β^{σ}_{kk} are the compliance matrix at constant electric displacement field, the vector of strain piezoelectric coefficients (induced strains per unit of electric displacement) and the dielectric resistivity coefficient at constant stress respectively.

4.1.1 Directional dependence in terms of $\hat{e}$ or d

Piezoelectric transducers are usually activated via the application of an electric field (open-circuit condition) as actuators, whereas as sensors they measure charge (short-circuit condition). A transducer built of a material having the following piezoelectric stress constants:

$$\hat{\boldsymbol{e}} = \{e_1 \quad 0 \quad 0\} \tag{4.7}$$

with $e_1 \neq 0$, is according to Eq. 4.2 an actuator of stress with maximum directional dependence if strains are null, whereas it is a sensor of strain with maximum directional dependence if the electric field is null. Maximum directional dependence means that specific quantities related to a direction perpendicular to that of maximum actuation or sensing are not actuated or sensed: the contribution of the actuation to the stress component σ_2 is null in the actuator case; the strain component ϵ_2 does not contribute to the measured charge in the sensor case.

A transducer built of a material having the following piezoelectric strain constants:

$$\boldsymbol{d} = \{d_1 \quad 0 \quad 0\} \tag{4.8}$$

with $d_1 \neq 0$, is according to Eq. 4.4 an actuator of strain with maximum directional dependence if stresses are null whereas it is a sensor of stress with maximum directional dependence if the electric field is null.

$\boldsymbol{d}$ and $\hat{\boldsymbol{e}}$ are linked through the following relations:

$$\begin{aligned} \boldsymbol{d} &= \hat{\boldsymbol{e}}\boldsymbol{S}^E \\ \hat{\boldsymbol{e}} &= \boldsymbol{d}\hat{\boldsymbol{Q}}^E \end{aligned} \tag{4.9}$$

If Eq. 4.7 hold then according to Eq. 4.9

$$\hat{\boldsymbol{e}} = \{d_1 \quad 0 \quad 0\} \begin{bmatrix} \hat{Q}_{11} & \hat{Q}_{12} & \hat{Q}_{16} \\ \hat{Q}_{21} & \hat{Q}_{22} & \hat{Q}_{26} \\ \hat{Q}_{61} & \hat{Q}_{62} & \hat{Q}_{66} \end{bmatrix} = \begin{Bmatrix} \hat{Q}_{11}d_1 & \hat{Q}_{12}d_1 & \hat{Q}_{16}d_1 \end{Bmatrix} \tag{4.10}$$

and similarly, if Eq. 4.8 hold then according to Eq. 4.9:

$$\boldsymbol{d} = \{e_1 \quad 0 \quad 0\} \begin{bmatrix} S_{11} & S_{12} & S_{16} \\ S_{21} & S_{22} & S_{26} \\ S_{61} & S_{62} & S_{66} \end{bmatrix} = \{S_{11}e_1 \quad S_{12}e_1 \quad S_{16}e_1\} \tag{4.11}$$

Therefore maximum directionality in terms of piezoelectric strain constants is mutually exclusive with the one in terms of piezoelectric stress constants.

4.1.2 Directional dependence in terms of $\hat{h}$ or g

Actuator that are activated via the application of a charge (short-circuit condition) and sensors that measure voltage (open-circuit condition) are considered. The following relations between piezoelectric coefficients hold:

$$\begin{aligned} \hat{\boldsymbol{h}} &= \hat{\boldsymbol{\beta}}^{\epsilon}_{kk}\hat{\boldsymbol{e}} \\ \boldsymbol{g} &= \boldsymbol{\beta}^{\sigma}_{kk}\boldsymbol{d} \end{aligned} \tag{4.12}$$

Being dielectric matrixes diagonal, maximum directionality in terms of $\boldsymbol{d}$ guarantees the one in terms $\boldsymbol{g}$, whereas the one in terms of $\hat{\boldsymbol{e}}$ guarantees the one in terms $\hat{\boldsymbol{h}}$. A transducer with maximum directionality in terms of $\hat{\boldsymbol{h}}$ according to Eq. 4.5 is an actuator of stress with maximum directional dependence if strains are null, whereas it is a sensor of strain with maximum directional dependence if the electric displacement field is null. A transducer with maximum directionality in terms of $\boldsymbol{g}$ according to Eq. 4.6 is an actuator of strain with maximum directional dependence if stresses are null, whereas it is a sensor of stress with maximum directional dependence if the electric displacement field is null. $\boldsymbol{g}$ and $\hat{\boldsymbol{h}}$ are linked through the following relations:

$$\begin{aligned} \boldsymbol{g} &= \hat{\boldsymbol{h}}\boldsymbol{S}^D \\ \hat{\boldsymbol{h}} &= \boldsymbol{g}\hat{\boldsymbol{Q}}^D \end{aligned} \tag{4.13}$$

4.2 Effect of matrix properties

The aim of this section is to study the effect of matrix properties (E^m,ν^m) and fibre volume fraction ρ on the effective piezoelectric properties. This is done on the basis of

the mixing rules obtained in Sec. 3.2 using the AEH analytical solution. The efficiency of piezocomposite transducers is largely influenced by the d_{3j} coefficients in free deformation mode, by the e_{3j} coefficients in a fully constrained mode and by a mixture of both for intermediate configurations. $j = 1{,}2$ since a configuration similar to that of d_{31}-type MFC is analysed. PZT fibre properties are reported in Tables 4.1 and 4.2.

	E_1 [GPa]	E_2 [GPa]	E_3 [GPa]	ν_{12}	ν_{13}	ν_{23} [GPa]	G_{12} [GPa]	G_{13}	G_{23}
Epoxy	2.9	2.9	2.9	0.3	0.3	0.3	1.11	1.11	1.11
SONOX P502	54.05	54.05	48.30	0.41	0.44	0.44	19.14	19.48	19.48

Table 4.1. Elastic properties.

	d_{31} [pC/N]	d_{32} [pC/N]	d_{33} [pC/N]	$\varepsilon_{33}^{\sigma}$
Epoxy	-	-	-	4.25
SONOX P502	-185	-185	440	1850

Table 4.2. Electro-elastic properties.

d_{31} and d_{32} correspond to the components d_1 and d_2, respectively, in planar piezoelasticity, see Sec. 4.1. Similarly, e_{31} and e_{32} correspond to e_1 and e_2, respectively. The in-plane piezoelectric capability of the sensor/actuator device is a direct consequence of the anisotropy of the effective piezoelectric constants tensor: the degree of "directionality" is related to the ratio between longitudinal (31) and transverse (32) piezoelectric properties.

Firstly the influence of the Young's modulus of the matrix, assumed to be isotropic, is assessed. Figs. 4.1(a), 4.1(b) illustrates respectively the evolution of the effective longitudinal (d_{31}) and transverse (d_{32}) piezoelectric constants with the volume fraction and with the Young's modulus of the matrix. Poisson ratio is equal to 0.3 and the Young's modulus span from 1 GPa to the elastic stiffness of the fibre. Both constants increase with decreasing matrix volume fraction and elastic stiffness. The physical interpretation is straightforward:

1. Increasing the volume fraction of the fibres enhances the piezoelectric properties of the composite, which become closer to those of the fibre,

2. Choosing a matrix with a low Young's modulus ensures that the fibres face low mechanical resistance. This guarantees limited degradation of the overall piezoelectric effect of the composite.

According to the mixing rules established in Sec. 3.2, the evolution of the effective properties with the fibre volume fraction becomes linear when the stiffness of the matrix is

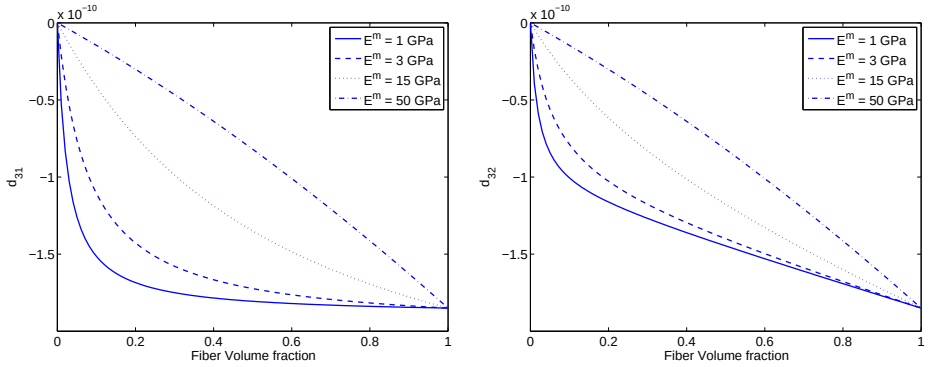

(a) Longitudinal direction. (b) Transverse direction.

Figure 4.1. Variation of the piezoelectric constants (d_{31},d_{32}) as a function of volume fraction ρ and for different values of Young's modulus E^m of the matrix. The Poisson's ratio ν^m is equal to 0.3.

close to that of the fibre. The evolution of the ratio d_{31}/d_{32} with volume fraction of the fibre is shown in Fig. 4.2(a) for different values of the Young's modulus. The ratio has higher magnitudes for lower Young's moduli and higher matrix content. A similar analysis

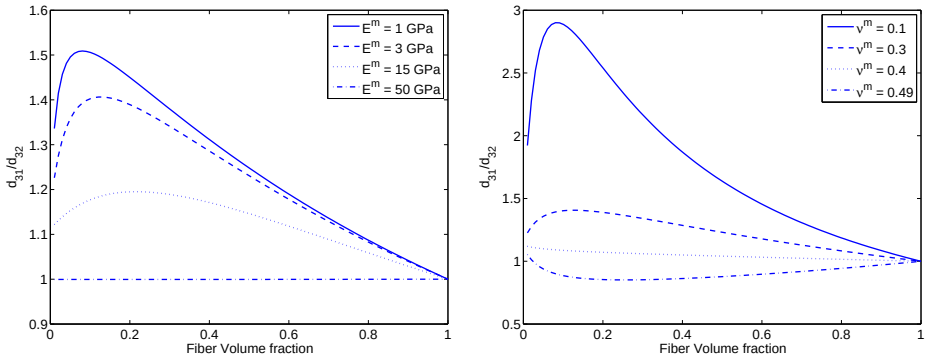

(a) varying Young's modulus. (b) varying Poisson's ratio.

Figure 4.2. Ratio between the piezoelectric constants in the longitudinal and transverse directions (d_{31}/d_{32}).

is carried out considering the evolution of the equivalent properties and their ratio with respect to the Poisson's ratio of the matrix (Fig. 4.3). The Young's modulus is equal to 3 GPa. It is found that the longitudinal constant d_{31} is practically insensitive to the variation of the Poisson's ratio because all the PZT fibres are aligned in the same direction, Fig. 4.3(a). d_{32}, however, is significantly influenced by the variation of the Poisson's ratio of the matrix as can be seen from Fig. 4.3(b). The dependence of the ratio d_{31}/d_{32} on the Poisson's ratio is shown in Fig. 4.2(b). Observing Figs. 4.2(a) and 4.2(b) it can be

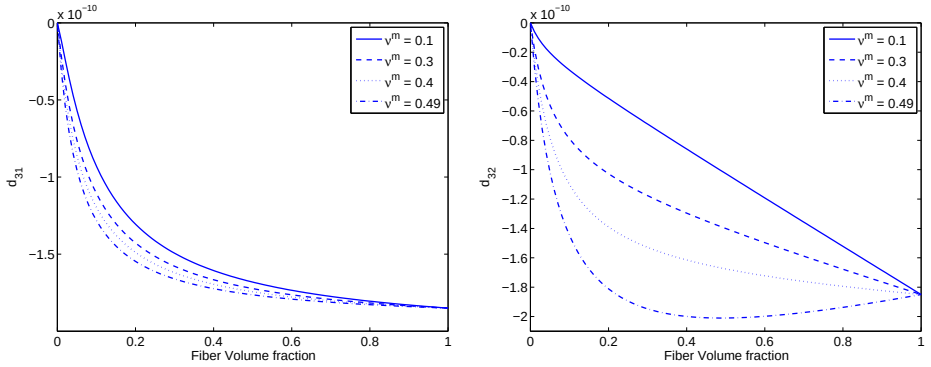

(a) Longitudinal direction. (b) Transverse direction.

Figure 4.3. Variation of the piezoelectric constants (d_{31},d_{32}) as a function of volume fraction ρ and for different values of Poisson's ratio ν^m of the matrix. The Young's modulus E^m is equal to 3 GPa.

seen that the highest magnitude for the ratio d_{31}/d_{32} is obtained when both the Young's modulus and the Poisson's ratio of the matrix are low.

A similar analysis is made considering fully-constrained piezoelectric transducers to determine the e_{3j} constants. The influence of the Young's modulus of the matrix is firstly assessed. Figs. 4.4(a) and 4.4(b) present the evolution of the effective longitudinal (e_{31}) and transverse (e_{32}) piezoelectric constants with the volume fraction and with the Young's modulus of the matrix, respectively. The evolution of the equivalent properties with respect

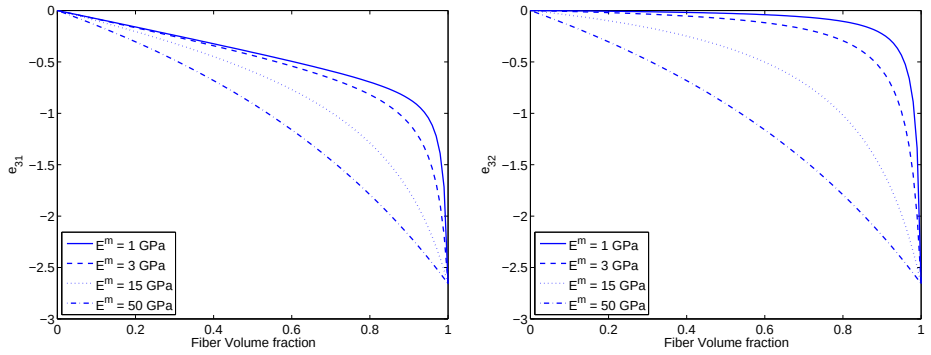

(a) Longitudinal direction. (b) Transverse direction.

Figure 4.4. Variation of the piezoelectric constants (e_{31},e_{32}) as a function of volume fraction ρ and for different values of Young's modulus E^m of the matrix. The Poisson's ratio ν^m is equal to 0.3.

to the Poisson's ratio of the matrix is addressed in Figs. 4.5. Fig. 4.6 illustrates the evolution of the ratio e_{31}/e_{32} in terms of fibre volume fraction and for different Young's moduli of the matrix, Fig. 4.6(a) and for different Poisson's ratios, Fig. 4.6(b). Both e_{31}

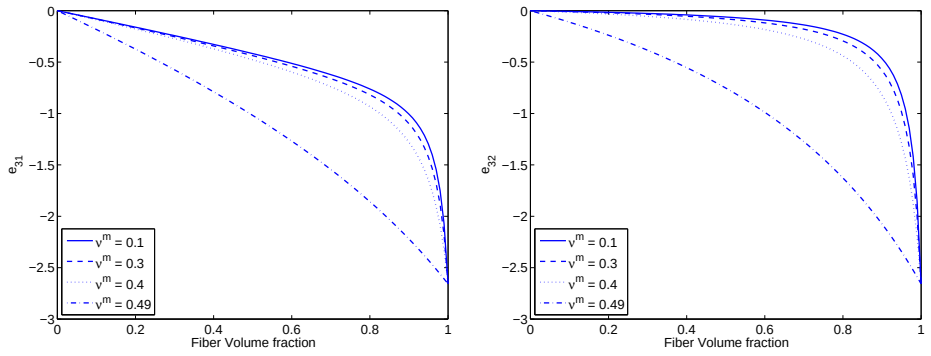

(a) Longitudinal direction. (b) Transverse direction.

Figure 4.5. Variation of the piezoelectric constants (d_{31},d_{32}) as a function of volume fraction ρ and for different values of Poisson's ratio ν^m of the matrix. The Young's modulus E^m is equal to 3 GPa.

and e_{32} increase with decreasing matrix volume fraction and Poisson's ratio. From Figs. 4.2 and 4.6 it can be seen that the ratio of the effective piezoelectric constants (d_{31}/d_{32}) is more sensitive to the variation of the Poisson's ratio. Conversely, the ratio (e_{31}/e_{32}) is more sensitive to the variation of the Young's modulus. In general the presented results show

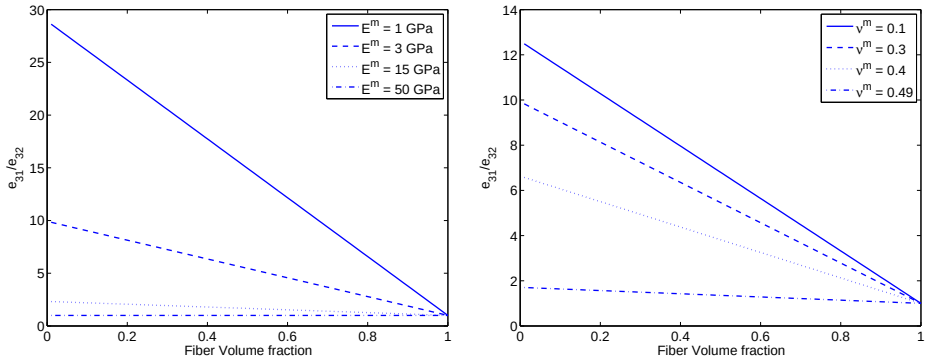

(a) varying Young's modulus of the matrix. (b) varying Poisson's ratio of the matrix.

Figure 4.6. Evolution of the ratio e_{31}/e_{32}.

that low Young's modulus and Poisson's ratio maximise the ratio between piezoelectric properties in longitudinal and transverse direction, i.e. the directional dependency of sensing and actuation.

4.2.1 Piezoelectric properties with existing polymer materials

Ratios d_{31}/d_{32} and e_{31}/e_{32} as a function of the volume fraction of the fibre in epoxy matrix (LOCTITE®Hysol®E-120HP: $E^m = 2.9$ GPa, $\nu^m = 0.31$) for commercially available

MFC $d_{31} - type$ are presented in Fig. 4.7(a). The choice of a different matrix material may

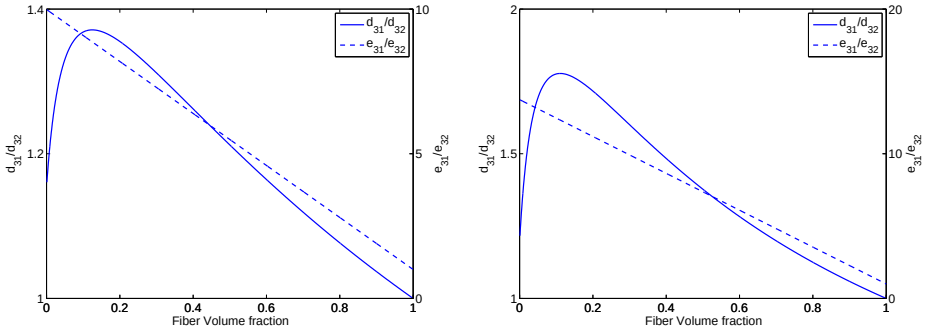

(a) LOCTITE®Hysol®E-120HP matrix. (b) DSM Somos®14120 matrix.

Figure 4.7. Evolution of the ratios d_{31}/d_{32} and e_{31}/e_{32}.

lead to higher directionality of the piezoelectric response. In the following, some existing polymer materials are considered instead of MFC epoxy. They are chosen in order to have lower Young's modulus and Poisson's ratio with respect to MFC epoxy, according to the conclusions drawn from the presented results. DSM Somos®14120 ($E^m = 2.46$ GPa, $\nu^m = 0.23$) is a low viscosity photopolymer used to produce prototypes and concept models. It is adopted in automotive, medical and consumer electronics products. Ratios are presented in Fig. 4.7(b). Dow BETABRACE$^{\text{TM}}$85001 ($E^m = 1.47$ GPa, $\nu^m = 0.11$) is composed of a curing tacky polymer, woven glass fabric and release paper. Fig. 4.8(a) shows the ratios d_{31}/d_{32} and e_{31}/e_{32}. BASF Elastollan$^{\text{TM}}$1100 ($E^m = 0.025$ GPa, $\nu^m = 0.25$) is

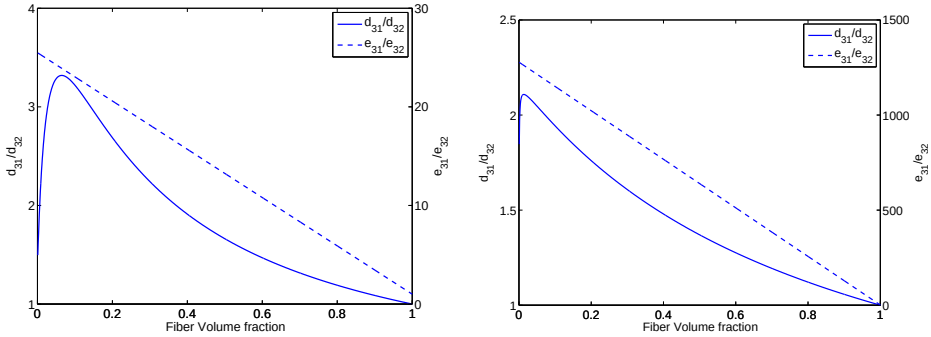

(a) Dow BETABRACE$^{\text{TM}}$85001 matrix. (b) BASF Elastollan$^{\text{TM}}$1100 matrix.

Figure 4.8. Evolution of the ratios d_{31}/d_{32} and e_{31}/e_{32}.

a polyether-based thermoplastic polyurethane. It may be processed by extrusion, injection and blow molding. These results show that it is possible to increase the ratio between piezoelectric properties in longitudinal and transverse direction of MFC with a different choice of the matrix material. Other design issues, like manufacturing, durability and

strength, have not been considered in this analysis.

Chapter 5

Piezoelectric laminates with direction-dependent properties

Laminates are built of several layers that can have different orientation. Thickness of the layers and their material in most of the application are identical, but they can in the most general case vary layer wise. Such variety of design parameters allows obtaining tailored properties for specific applications. In this chapter the possibility to adopt a laminated configuration in a piezoelectric composite device is addressed in terms of directionality of the response. A review on the optimisation techniques adopted to design the stacking sequence of composite materials was presented by Ghiasi et al. [76, 77]. Typical studies deal with the stiffness, the strength, the natural frequencies and the stability of laminates. Such optimisations are not limited to the pure mechanical domain. An example of multi physics design is the work proposed by Spallino and Thierauf [78], where the thermal buckling of laminated composite plates subject to a temperature rise is considered. Classical lamination plate theory (CLPT) has been adopted by Vannucci and Pouget [79] to homogenise the electro-elastic behaviour of a composite laminated plate with piezoelectric layers at the top and at the bottom. Laminates having null expansion coefficients in extension in a particular direction or having the same expansion coefficient in each direction have been found via a polar representation of the mechanical properties (see Vannucci and Verchery [80]). Later, Vannucci [81] presented a similar optimisation problem in which the stacking sequence of laminates having null bending in one direction is computed via a particle swarm algorithm.

A design for a multi-layered piezoelectric patch is proposed and the influence of design parameters on the response is investigated. Direction-dependency of the behaviour of a piezoelectric patch bonded to a structure is also addressed. Planar piezoelasticity as described in Sec. 4.1 is adopted.

5.1 Uniform field method for layered composites

A n-layer piezoelectric laminate is considered, with a piezoelectric layer and $n-1$ mechanical layers. Direction 1 and 2 are two orthogonal in-plane directions, whereas direction 3

is the out of plane direction. Classical plane stress (PS) and unidirectional electric field (UDEF) electromechanical assumptions are adopted. A generic matrix-based procedure to implement the UFM is presented in Sec. 3.2.2. In the UFM variables are splitted in dependent and independent ones:

- in the case of independent variable, fields are equals in each constituent:

$$\overline{X_i} = X_i^j \quad \text{with} \quad j = 1,\, 2,\, \ldots,\, n \tag{5.1}$$

- in the case of dependent variable, fields are related through a linear mixture relation:

$$\overline{X_i} = \sum_{j=1}^{n} \rho_j X_i^j \tag{5.2}$$

where ρ_j is the volume fraction of the j-th constituent, $\overline{X_i}$ is a generic generalised stress or strain for the whole RVE (mean value) and X_i^j is its value in the j-th layer. According to the geometry of the RVE, depicted in Fig. 5.1, the independent variables are ε_1, ε_2, ε_6 and D, whereas the dependent variables are σ_1, σ_2 and σ_6 and E. The electrodes are at the top

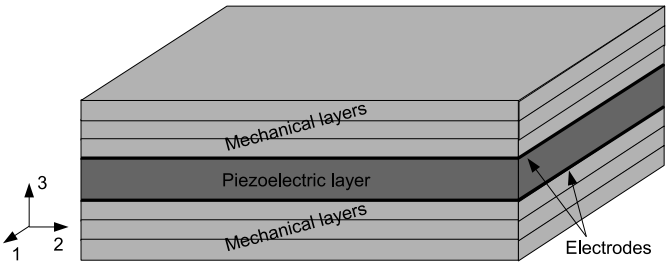

Figure 5.1. RVE of a laminated piezoelectric transducer.

and bottom of the piezoelectric layer, not of the whole laminate. The electrode physical layers, usually made of copper and epoxy, are not considered in the following. The electric field is null in the mechanical layers:

$$\overline{E_k} = \rho_p E_k^p \tag{5.3}$$

where subscript p denotes the piezoelectric layer. For a generic layer j-th layer:

$$\left\{ \begin{array}{c} \boldsymbol{\sigma}^j \\ {D_k}^j \end{array} \right\} = \left[\begin{array}{cc} \boldsymbol{Q}^{jE} & -\hat{\boldsymbol{e}}^{jT} \\ \hat{\boldsymbol{e}}^j & \hat{\epsilon}_{kk}^j \end{array} \right] \left\{ \begin{array}{c} \boldsymbol{\varepsilon}^j \\ {E_k}^j \end{array} \right\} \tag{5.4}$$

According to the linear mixture in Eq. 5.2 the mean stress field is:

$$\overline{\boldsymbol{\sigma}} = \sum_{j=1}^{n} \rho_j \boldsymbol{\sigma}_j \tag{5.5}$$

According Eq. 5.1 the mean strain field is:

$$\overline{\boldsymbol{\varepsilon}} = \boldsymbol{\varepsilon}_j \tag{5.6}$$

Considering the linear mixture in Eq. 5.3, the constitutive equations 5.4 and Eq.5.6, it is possible to rewrite Eq. 5.5 as:

$$\overline{\boldsymbol{\sigma}} = \sum_{j=1}^{n} \rho_j \hat{\boldsymbol{Q}}^{jE} \overline{\boldsymbol{\varepsilon}} - \rho_p \hat{\boldsymbol{e}}^{pT} E_k^p = \sum_{j=1}^{n} \rho_j \hat{\boldsymbol{Q}}^{jD} \overline{\boldsymbol{\varepsilon}} - \hat{\boldsymbol{e}}^{pT} \overline{E}_k \tag{5.7}$$

According to Eq. 5.1 the mean electric displacement field is:

$$\overline{\boldsymbol{D}}_k = \boldsymbol{D}_k^p \tag{5.8}$$

Considering the linear mixture in Eq. 5.3, the constitutive equations 5.4 and Eq. 5.8, the electric displacement field in the piezoelectric layers is:

$$\overline{D}_k = D_k^p = \hat{\boldsymbol{e}}^p \overline{\boldsymbol{\varepsilon}} + \hat{\epsilon}_{kk}^{\varepsilon p} E_k^p = \hat{\boldsymbol{e}}^p \overline{\boldsymbol{\varepsilon}} + \frac{\hat{\epsilon}_{kk}^{\varepsilon p}}{\rho_p} \overline{E}_k \tag{5.9}$$

Grouping Eq. 5.7 and 5.9 and rearranging, the constitutive equations for the whole laminate are retrieved:

$$\begin{gathered} \left\{ \begin{array}{c} \overline{\boldsymbol{\varepsilon}} \\ \overline{D}_k \end{array} \right\} = \left[\begin{array}{cc} \boldsymbol{S}^E & \boldsymbol{d}^T \\ \boldsymbol{d} & \epsilon_{kk}^T \end{array} \right] \left\{ \begin{array}{c} \overline{\boldsymbol{\sigma}} \\ \overline{E}_k \end{array} \right\} = \\ \left[\begin{array}{cc} \left[\sum_{j=1}^{n} \rho_j \hat{\boldsymbol{Q}}_j^{jE} \right]^{-1} & \left[\sum_{j=1}^{n} \rho_j \hat{\boldsymbol{Q}}_j^{jE} \right]^{-1} \hat{\boldsymbol{e}}^{pT} \\ \hat{\boldsymbol{e}}^{\boldsymbol{p}} \left[\sum_{j=1}^{n} \rho_j \hat{\boldsymbol{Q}}_j^{jE} \right]^{-1} & \frac{\hat{\epsilon}_{kk}^{\varepsilon p}}{\rho_p} + \hat{\boldsymbol{e}}^{\boldsymbol{p}} \left[\sum_{j=1}^{n} \rho_j \hat{\boldsymbol{Q}}_j^{jE} \right]^{-1} \hat{\boldsymbol{e}}^{pT} \end{array} \right] \left\{ \begin{array}{c} \overline{\boldsymbol{\sigma}} \\ \overline{E}_k \end{array} \right\} \end{gathered} \tag{5.10}$$

These equations show that maximum directionality in terms of $\hat{\boldsymbol{e}}$ is not achievable with a layered configuration according to the UFM. Values of $\hat{\boldsymbol{e}}$ homogenised via UFM are the same as for the piezoelectric layer. This is a consequence of the multilayered structure, which is conceptually similar to a parallel configuration of the different layers in the electric circuit analogy. Actually, the influence of the lamination on the values of $\hat{\boldsymbol{e}}$ exist but it is low, as reported in Sec. 5.3. On the contrary, a series configuration like that of MFC phases (epoxy and PZT) has a decisive influence on the values of $\hat{\boldsymbol{e}}$, see Sec. 4.2.

When the transducer is modelled as its equivalent material in a FE analysis, the electrodes are on the top and the bottom of the whole laminate. In actuator mode, the applied potential corresponds to an electric field in the homogenised material which is lower than in the case of the actual laminated composite where the electrodes are at the top and at the bottom of the piezoelectric layer (see Eq. 5.3). This is the reason why effective values of the piezoelectric properties may be higher than those of the piezoelectric phase.

In this analysis the piezoelectric layer can be monolithic or composite in the sense of MFC. UFM has already been applied to MFC under PS in [22], where the reader can

find the derivation of the analytical formulae for the effective properties. The complete formulae are the following:

$$\begin{aligned}
S_{11}^E &= \left(\rho_f \tfrac{1}{S_{11f}^E} + (1-\rho_f)\tfrac{1}{S_{11e}^E}\right)^{-1} \\
S_{21}^E &= S_{11}^E + \left(\rho_f \tfrac{S_{21f}^E}{S_{11f}^E} + (1-\rho_f)\tfrac{S_{21e}^E}{S_{11e}^E}\right) \\
S_{22}^E &= \tfrac{S_{21}^{E2}}{S_{11}^E} + \left(\rho_f \left(S_{22f}^E - \tfrac{S_{21f}^{E2}}{S_{11f}^E}\right) + (1-\rho_f)\left(S_{22e}^E - \tfrac{S_{21e}^{E2}}{S_{11e}^E}\right)\right) \\
S_{66}^E &= \left(\rho_f S_{66f}^E + (1-\rho_f) S_{66e}^E\right) \\
d_1 &= S_{11}^E + \left(\rho_f \tfrac{d_{1f}}{S_{11f}^E} + (1-\rho_f)\tfrac{d_{1e}}{S_{11e}^E}\right) \\
d_2 &= \tfrac{d_1 S_{21}^E}{S_{11}^E} + \left(\rho_f \left(d_{2f} - \tfrac{d_{1f} S_{21f}^E}{S_{11f}^E}\right) + (1-\rho_f)\left(d_{2e} - \tfrac{d_{1e} S_{21e}^E}{S_{11e}^E}\right)\right)
\end{aligned} \tag{5.11}$$

Subscripts f and e stands for the two phases. Both the phases may exhibit piezoelectric effect. In the case of MFC d_{31}-type the poling direction k, which corresponds to the direction of the electric field, is the out-of-plane direction 3 and $d_1 = d_{31}$, $d_2 = d_{32}$. With MFC d_{33}-type the poling direction is the in-plane direction 1 and $d_1 = d_{33}$ and $d_2 = d_{32}$.

As highlighted in [33], in the case of a composite in which material properties varies in two direction UFM is applied in two subsequent steps, one for each direction. In this analysis direction 3 is the out-of-plane direction whereas 2 is the direction of variation of material properties if the piezoelectric layer is a composite. There are two possible choices (see Fig. 5.2):

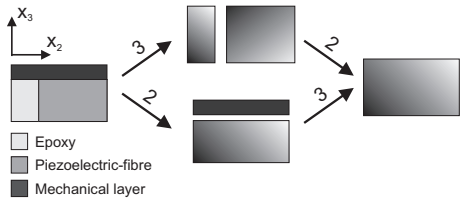

Figure 5.2. UFM is composed of two subsequent steps. Two choices are possible regarding the order of the steps.

- UFM_{23}: apply UFM in the direction 2, between epoxy and piezoelectric-fibre , and then in direction 3, between the piezoelectric layer and the mechanical layers.

- UFM_{32}: apply UFM in the direction 3, between epoxy and mechanical layers one one hand and piezoelectric-fibre and mechanical layers on the other hand, and then in direction 2.

Results in general do not coincide, as reported in [33].

5.2 Transducers with maximum directional dependence

UFM is adopted to compute the equivalent properties of layered transducers. As actuators they are activated via the application of an electric field, whereas as sensors they measure a charge. A balanced lamination is considered. The mechanical layers are of the same materials and are orthotropic. The piezoelectric layer is considered to be orthotropic with principal directions aligned in directions 1 and 2. This, together with the balanced lamination of the mechanical layers, guarantees that mechanical equivalent properties are orthotropic. Moreover the in-plane shear piezoelectric coefficient is null. Three different kind of piezoelectric layer are considered in the following. Fibre volume fraction in the case of composite piezoelectric layers is that of MFC, i.e. 0.865. A detailed sensitivity analysis concerning fibre volume fraction and properties of the matrix in MFC has been carried out in Sec. 4.2. The mechanical layers are made of T300/5208 (unidirectional carbon fibres in epoxy matrix), see Tab. 5.1, because of its high degree of orthotropy. As

	E_1 [GPa]	E_2 [GPa]	E_3 [GPa]	ν_{12}	ν_{13}	ν_{23} [GPa]	G_{12} [GPa]	G_{13}	G_{23}
T300/5208	181.0	10.3	10.3	0.28	0.28	0.49	7.17	7.17	5.00
Epoxy	2.9	2.9	2.9	0.3	0.3	0.3	1.11	1.11	1.11
SONOX P502	54.05	54.05	48.30	0.41	0.44	0.44	19.14	19.48	19.48

Table 5.1. Elastic properties of the considered materials.

	d_{31} [pC/N]	d_{32} [pC/N]	d_{33} [pC/N]	$\varepsilon^{\sigma}_{33}$
Epoxy	-	-	-	4.25
SONOX P502	-185	-185	440	1850

Table 5.2. Electro-elastic properties of the considered materials.

shown in Sec. 5.1, a layered configuration has little influence on directional dependence in terms of equivalent piezoelectric stress constants, therefore only maximum directionality in terms of equivalent piezoelectric strain constants is investigated. A large number of mechanical layers have been considered initially, but results showed that solutions with highest directional dependence are characterised only by an angle. Therefore only the stacking sequence $[\delta/-\delta/0]$, where the the piezoelectric layer is oriented along direction 1 (that is 0°), is considered. The problem is function of two variables: the volume fraction of the piezoelectric layer $\rho_p \in \{0,1\}$ and the orientation of the mechanical layers $\delta \in \{0,\pi/2\}$.

In order to maximise the directional dependence of a sensor the following problem can be stated:

$$\begin{aligned} &\max \left| f_s\left(\rho_p,\delta\right)\right| = \left|d_1\left(\rho_p,\delta\right)\right| \\ &\text{with } g\left(\rho_p,\delta\right) = d_2\left(\rho_p,\delta\right) = 0 \end{aligned} \tag{5.12}$$

In the case of actuator with maximum directional dependence the following function may be maximised instead of f_s:

$$|f_a(\rho_p,\delta)| = |\rho_p d_1(\rho_p,\delta)| \tag{5.13}$$

This function takes into account directly the volume fraction of the piezoelectric layer. A sensitivity analysis is carried out via graphical representation of functions in Eqs. 5.12 and 5.13.

5.2.1 Monolithic piezoelectric layer

A piezoelectric layer with the properties of SONOX P502 is considered, see Tabs. 5.1 and 5.2. The poling direction k, which corresponds to the direction of the electric field, is the out-of-plane direction 3, i.e. electrodes are conventional. Function g is plotted as a colour map in Fig. 5.3. Maximum directional dependence is fulfilled only for low values of

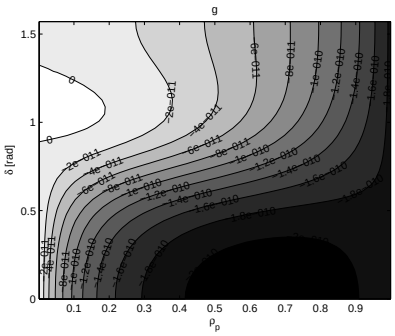

Figure 5.3. Variation of function g with monolithic piezoelectric layer.

the volume fraction of the piezoelectric layer, confirming results reported in [79].

5.2.2 Composite piezoelectric layer

Two electrode configurations are considered: conventional electrodes and interdigitated electrodes. Conventional electrodes are continuous and cover the top and bottom surfaces of the piezocomposite, see Fig. 5.4. They were the first to be developed and the in-plane piezoelectric coefficients are d_{31} and d_{32}. Interdigitated electrodes have been introduced to take advantage of d_{33} constant, which is usually higher than d_{31} and d_{32}, as in-plane property. Positive and negative electrodes are interdigitated as fingers on both top and bottom surfaces of the piezocomposite, see Fig. 5.4.

Composite piezoelectric layer of d_{33}-type A composite piezoelectric layer with interdigitated electrodes and with the same volume fraction of piezoelectric material of MFC is considered. Epoxy properties are listed in Tabs. 5.1 and 5.2. The poling direction k is the in-plane direction 1. Functions g according to UFM_{23} and UFM_{32} are plotted in

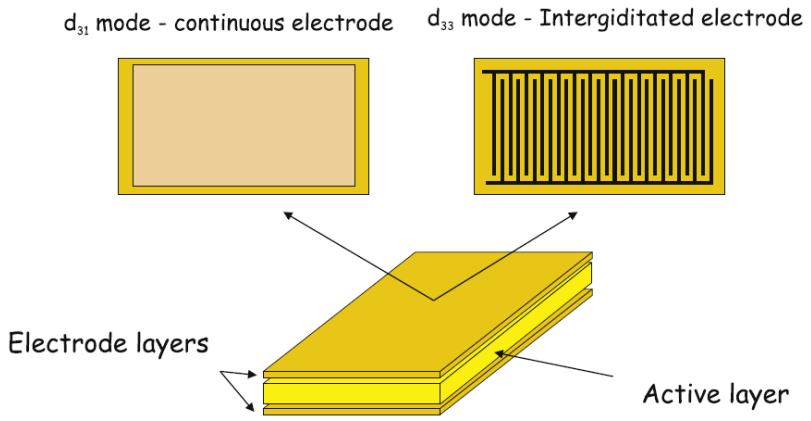

Figure 5.4. Electrodes configurations, [39].

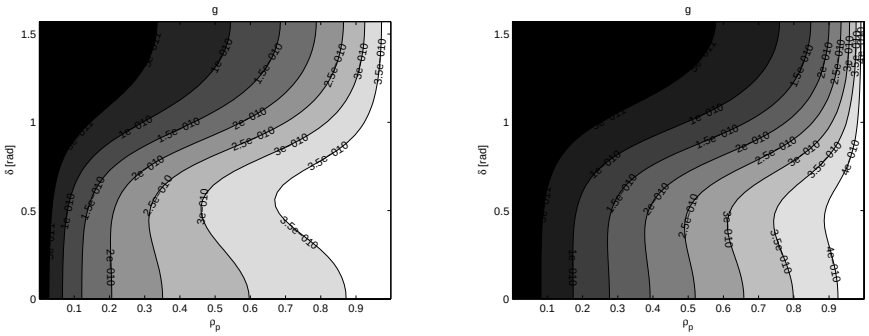

(a) UFM_{32} (b) UFM_{23}

Figure 5.5. Variation of function g with d_{33}-type piezoelectric layer.

Figs. 5.5. In this case g is never null. Therefore it is not possible to obtain properties with maximum directional dependence. Maximum directionality in terms of equivalent piezoelectric strain constants is achieved with the monolithic piezoelectric layer because its piezoelectric constant d_2 is contrasted by the Poisson's effect of the whole laminate due to d_1. In the present case, the piezoelectric constant d_2 is of opposite sign with respect to d_1, i.e. a negative Poisson's coefficient for the whole laminate would be required to have maximum directional dependence.

Composite piezoelectric layer of d_{31}-type A composite piezoelectric layer with conventional electrodes is considered. The poling direction k is the out-of-plane direction 3. Functions g according to UFM_{23} and UFM_{32} are plotted in Figs. 5.6. Like in the case of monolithic piezoelectric layer, d_1 and d_2 have the same sign and therefore it is possible to

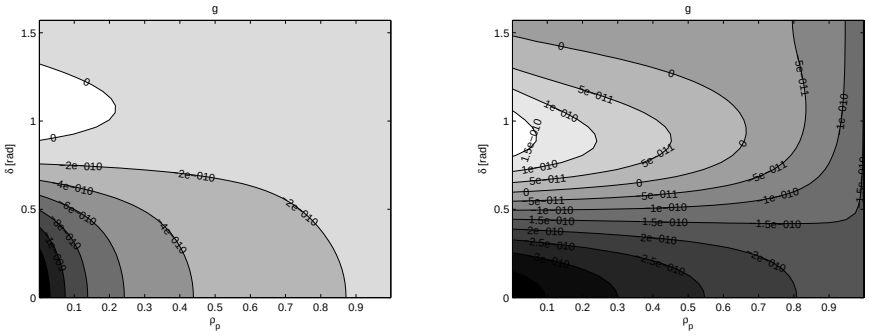

(a) UFM_{32} (b) UFM_{23}

Figure 5.6. Variation of function g with d_{31}-type piezoelectric layer.

obtain maximum directionality in terms of equivalent piezoelectric strain constants. Solutions having maximum directional dependence with UFM_{23} can be found with higher values of ρ_p than for UFM_{32}. Functions f_a in the case of actuator to plotted in Figs. 5.7, whereas in the case of sensor f_s are plotted in Figs. 5.8. With UFM_{23}, f_a and f_s are

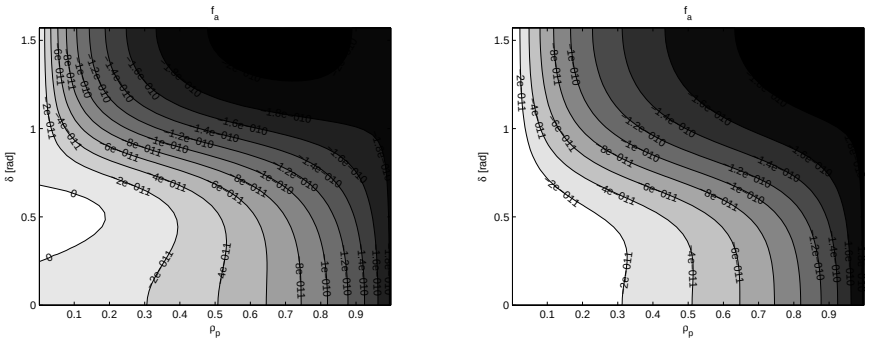

(a) UFM_{32} (b) UFM_{23}

Figure 5.7. Variation of function f_a with d_{31}-type piezoelectric layer.

positive in a region corresponding to low values of ρ_p and δ.

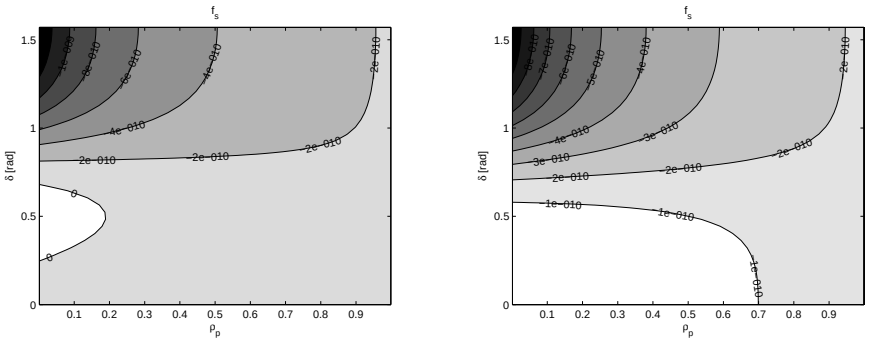

(a) UFM_{32} (b) UFM_{23}

Figure 5.8. Variation of f_s with d_{31}-type piezoelectric layer.

5.3 Numerical investigation via numerical periodic homogenisation

The numerical Periodic Homogenisation Method (PHM) presented in Sec. 3.1.2 is based on FEM analysis of the RVE. It is used as validation of the results presented in Sec. 5.2.2. The electrodes are at the top and at the bottom of the piezoelectric layer. The RVE is a parallelepiped. Figs. 5.9 presents results obtained via PHM for g, where $\rho_p \in \{0.15,0.75\}$ and $\delta \in \{3\pi/18,7\pi/18\}$. UFM results are also reported. The curve denoting the couples of values (ρ_p, δ) for which maximum directional dependence is achieved is in between the ones for UFM_{32} and UFM_{23}. Functions f_a and f_s are plotted in Figs. 5.10. They are negative for the considered values of ρ_p and δ. A comparison between results obtained with UFM and PHM for $\rho_p = 0.35$ and $\delta = 6\pi/18$ is presented in Tab. 5.3. The considered design is

	UFM_{23}	UFM_{32}	PHM
d_1 [C/N]	$-3.51E-010$	$-3.83E-10$	$-3.71E-10$
d_2 [C/N]	$5.46E-011$	$-3.31E-11$	$-1.44E-12$
$\hat{e}_1$ [C/m^2]	-10.2	-14.4	-12.7
$\hat{e}_2$ [C/m^2]	-4.05	-14.0	-10.0
E_1 [Pa]	$25.6E9$	$25.8E9$	$25.8E9$
E_2 [Pa]	$60.4E9$	$66.4E9$	$64.1E9$
G_{12} [Pa]	$25.9E9$	$29.5E9$	$28.6E9$
ν_{12}	0.304	0.320	0.315

Table 5.3. Comparison between UFM and PHM results with d_{31}-type piezoelectric layer, $\rho_p = 0.35$ and $\delta = 6\pi/18$.

depicted in Fig. 5.11. For all the considered properties PHM results lie in-between UFM_{23} and UFM_{32} ones. In a certain sense, the two UFM approaches bound the PHM solution.

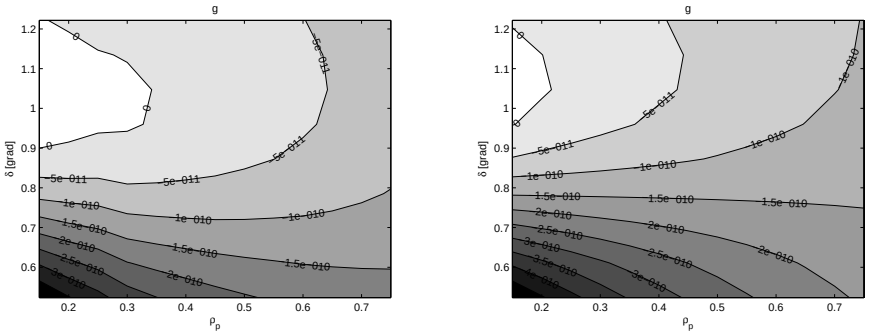

(a) PHM

(b) UFM_{32}

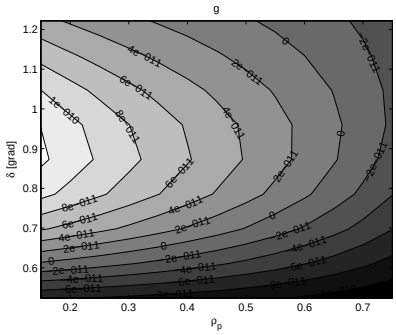

(c) UFM_{23}

Figure 5.9. PHM results for the function g with d_{31}-type piezoelectric layer, compared to UFM results.

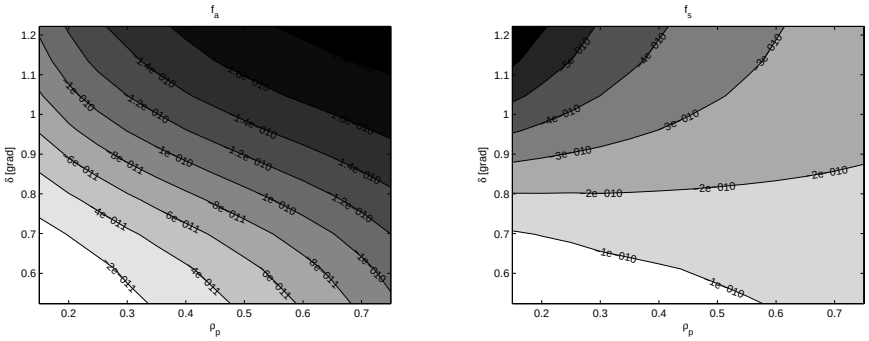

(a) f_a

(b) f_s

Figure 5.10. PHM results for the functions f_a and f_s with d_{31}-type piezoelectric layer.

Such a laminated transducer is a sensor of stress with maximum directional dependence. According to the constitutive equation in absence of electric field:

$$D_3 = \boldsymbol{d}\boldsymbol{\sigma} \tag{5.14}$$

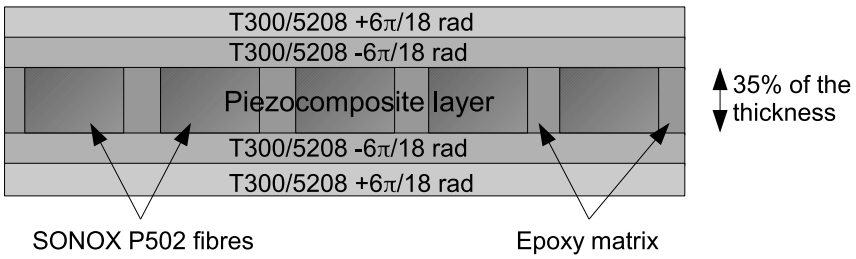

Figure 5.11. Design of a layered piezocomposite transducer with maximum directionality in terms of equivalent piezoelectric strain constants.

with an uniaxial stress state and on the basis of the stress tensor rotation law, the response of the device in terms of transverse electric displacement is shown in Fig. 5.12. The angle

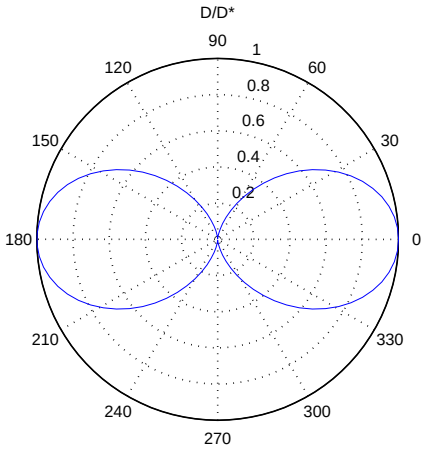

Figure 5.12. Response of the sensor with an uniaxial stress state in the different directions. Transverse electric displacement is put in non-dimensional form with respect to its value at 0°.

accounts for the direction of the uniaxial stress state, being the direction 1 of the patch at 0°. With an uniaxial stress state along direction 2 (90°):

$$\boldsymbol{\sigma} = \{0, \ \sigma_2, \ 0\}^T \tag{5.15}$$

the sensor output is null.

5.4 Piezoelectric patch on a structure

Up to this point, only the mechanics of the stand-alone piezoelectric device has been considered. The behaviour of a patch bonded to a structure, as piezoelectric transducers are commonly employed, is addressed in this section. Piezoelectric layers embedded in a structure are not considered.

In the following, quantities with subscript P refer to the piezoelectric patch and quantities with subscript S refer to the structure. The patch is assumed to have negligible dimensions with respect to the structure. Plane stress (PS) assumption is adopted. It is assumed a perfect bonding between the patch and the structure, i.e. in-plane strains are coincident:

$$\boldsymbol{\varepsilon}_S = \boldsymbol{\varepsilon}_P \tag{5.16}$$

In general $\boldsymbol{\sigma}_S \neq \boldsymbol{\sigma}_P$. If the structure is not in a piezoelectric material then:

$$\boldsymbol{\varepsilon}_S = \boldsymbol{Q}_S^{-1}\boldsymbol{\sigma}_S \tag{5.17}$$

where $\boldsymbol{Q}_S^{-1}$ is the compliance matrix of the structure.

First an actuator activated via the application of an electric field (open-circuit condition) and a sensor that measures charge is considered (short-circuit condition). According to Eq. 4.4, a sensor of stress is such that:

$$D_k = \boldsymbol{d}\boldsymbol{\sigma}_P = \boldsymbol{d}\hat{\boldsymbol{Q}}_P^E\boldsymbol{\varepsilon}_P \tag{5.18}$$

Considering Eqs. 5.16 and 5.17, Eq. 5.18 reads:

$$D_k = \boldsymbol{d}\hat{\boldsymbol{Q}}_P^E\boldsymbol{\varepsilon}_S = \boldsymbol{d}\hat{\boldsymbol{Q}}_P^E\boldsymbol{Q}_S^{-1}\boldsymbol{\sigma}_S \tag{5.19}$$

If $\boldsymbol{Z}^E = \hat{\boldsymbol{Q}}_P^E\boldsymbol{Q}_S^{-1}$ is such that $Z_{12}^E = Z_{13}^E = 0$ and $\boldsymbol{d}$ is as in Eq. 4.8, then the patch is a sensor of the stress in the structure with maximum directional dependence. If the patch and the structure have the same mechanical properties this condition is fulfilled. $\boldsymbol{Z}^E$ can be interpreted as a filter: in a certain sense, the action of the stress tensor of the structure in the patch is filtered by $\boldsymbol{Z}^E$. According to Eqs. 4.2 and 5.16, a sensor of strain is such that:

$$D_k = \hat{\boldsymbol{e}}\boldsymbol{\varepsilon}_P = \hat{\boldsymbol{e}}\boldsymbol{\varepsilon}_S \tag{5.20}$$

If $\hat{\boldsymbol{e}}$ is as in Eq. 4.7, then the patch is a sensor of the strain in the structure with maximum directional dependence. For a sensor, maximum directionality in terms of $\hat{\boldsymbol{e}}$ is independent of the structure, contrary to what happens for maximum directionality in terms of $\boldsymbol{d}$. The properties of actuators are instead always dependent on the strains and stress state of the structure, see Eqs. 4.2 and 4.4, respectively. Maximum directionality in terms of $\boldsymbol{d}$ or $\hat{\boldsymbol{e}}$ does not guarantee actuation with maximum directional dependence. Usually, piezoelectric patch is such that constant strain condition in nearly satisfied, i.e. the structure is much more rigid than the patch. Therefore, according to Eq. 4.2 and Eq. 4.4, if $\hat{\boldsymbol{e}}$ is as in Eq. 4.7 the patch applies stress with maximum directional dependence, whereas maximum directionality in terms of $\boldsymbol{d}$ does not correspond to strain applied in only one direction.

The case of actuator activated via the application of a charge (short-circuit condition) and sensor that measures a voltage (open-circuit condition) is now considered. According to Eq. 4.6, a sensor of stress is such that:

$$E_k = \boldsymbol{g}\boldsymbol{\sigma}_P = \boldsymbol{g}\hat{\boldsymbol{Q}}_P^D\boldsymbol{\varepsilon}_P = \boldsymbol{g}\hat{\boldsymbol{Q}}_P^D\boldsymbol{\varepsilon}_S = \boldsymbol{g}\hat{\boldsymbol{Q}}_P^D\boldsymbol{Q}_S^{-1}\boldsymbol{\sigma}_S \tag{5.21}$$

similarly to Eq. 5.19. This time, if $\boldsymbol{Z}^D = \hat{\boldsymbol{Q}}_P^D\boldsymbol{Q}_S^{-1}$ is such that $Z_{12}^D = Z_{13}^D = 0$ and $\boldsymbol{g}$ has a form similar to Eq. 4.7 then the patch is a sensor of the stress in the structure with maximum directional dependence. According to Eq. 4.5 and 5.16, a sensor of strain is such that:

$$E_k = \hat{\boldsymbol{h}}\boldsymbol{\varepsilon}_P = \hat{\boldsymbol{h}}\boldsymbol{\varepsilon}_S \tag{5.22}$$

similarly to Eq. 5.20. As for actuator and sensor with maximum directionality in terms of $\hat{\boldsymbol{e}}$ or $\boldsymbol{d}$, maximum directionality in terms of $\hat{\boldsymbol{h}}$ is independent of the structure, contrary to what happens for the one in terms of $\boldsymbol{g}$. The properties of the actuator are instead always dependent on the strains and stress state of the structure, see Eqs. 4.5 and 4.6, respectively.

If a material is orthotropic then:

$$\boldsymbol{S} = \begin{bmatrix} \frac{1}{E_1} & \frac{-\nu_{12}}{E_1} & 0 \\ \frac{-\nu_{12}}{E_1} & \frac{1}{E_2} & 0 \\ 0 & 0 & \frac{1}{G_{12}} \end{bmatrix} \tag{5.23}$$

$$\hat{\boldsymbol{Q}} = \begin{bmatrix} \frac{E_1}{1-\nu_{12}\nu_{21}} & \frac{\nu_{12}E_2}{1-\nu_{12}\nu_{21}} & 0 \\ \frac{\nu_{12}E_2}{1-\nu_{12}\nu_{21}} & \frac{E_2}{1-\nu_{12}\nu_{21}} & 0 \\ 0 & 0 & G_{12} \end{bmatrix} \tag{5.24}$$

If both the structure and the piezoelectric patch are orthotropic and aligned, then:

$$\begin{gathered} Z_{12} = \frac{E_{1P}}{1-\nu_{12P}\nu_{21P}}\frac{-\nu_{12S}}{E_{1S}} + \frac{\nu_{12P}E_{2P}}{1-\nu_{12P}\nu_{21P}}\frac{1}{E_{2S}} \\ Z_{13} = 0 \end{gathered} \tag{5.25}$$

The condition $Z_{12} = 0$ equals to:

$$\nu_{12P}\frac{E_{2P}}{E_{1P}} = \nu_{12S}\frac{E_{2S}}{E_{1S}} \tag{5.26}$$

This condition in conjunction with maximum directionality in terms of $\boldsymbol{d}$ guarantees sensing of the stress of the structure in terms of charge with maximum directional dependence. Being $\frac{\nu_{12}}{E_1} = \frac{\nu_{21}}{E_2}$ then Eq. 5.26 reads:

$$\nu_{21P} = \nu_{21S} \tag{5.27}$$

Another possibility to have maximum directional dependence in sensing of stress is to have (see Eq. 5.19):

$$\boldsymbol{d}\hat{\boldsymbol{Q}}_P^E\boldsymbol{Q}_S^{-1} = \boldsymbol{z} = \{z_1 \quad 0 \quad 0\} \tag{5.28}$$

The condition $z_3 = 0$ is automatically satisfied. The condition $z_2 = 0$ can be expressed in terms of d_2:

$$d_2 = d_1 \frac{E_{1P}}{E_{2P}} \frac{\nu_{21S} - \nu_{21P}}{1 - \nu_{12P}\frac{E_{2S}}{E_{1S}}} \tag{5.29}$$

or in terms of e_2 :

$$e_2 = e_1 \nu_{21S} \tag{5.30}$$

This expression does not depend on the mechanical properties of the patch. The directionality can be quantified by the ratio:

$$\frac{z_1}{z_2} = \frac{E_{2S}}{E_{1S}} \frac{e_1 - e_2\nu_{12S}}{e_2 - e_1\nu_{21S}} \tag{5.31}$$

that does not depend on the the mechanical properties of the patch. If the material of the structure is isotropic it reduces to:

$$\frac{z_1}{z_2} = \frac{e_1 - e_2\nu_S}{e_2 - e_1\nu_S} \tag{5.32}$$

5.4.1 Results for a sensor patch

The behaviour of a patch bonded to a structure is investigated in terms of directionality. The case of sensor that measures charge is considered (short-circuit condition). The laminated transducer whose properties are presented in Tab. 5.3 is considered. It has maximum directionality in terms of equivalent piezoelectric strain constants. As pointed out in Sec. 5.4, this does not guarantee maximum directionality in sensing of stress in the structure.

Analytical results obtained via Eq. 5.19, considering an uniaxial stress state and the stress tensor rotation law, are compared to results obtained via FEM analyses with the commercial software ABAQUS. The model is shown in Fig. 5.13: the diameter of the patch is one tenth the major dimension of the structure; its thickness is one hundredth its diameter. These ratios have been chosen in order to respect the hypotheses in Sec. 5.4. The

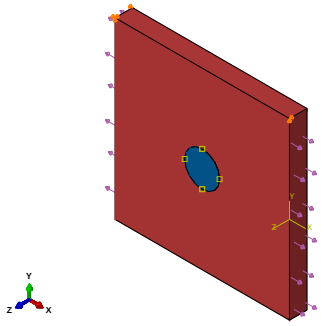

Figure 5.13. Finite element model adopted to investigate the behaviour of a surface bonded patch. Arrows represent the loading conditions.

patch is circular and its material properties are rotated around the z-axis. This circular shape is chosen in order to reduce the influence of the in-plane patch shape on the results. A uniform traction is applied on the structure along the x-axis. 8000 elements (C3D20RE, 20-node quadratic piezoelectric brick with reduced integration [63]) have been employed. The structure is in isotropic material ($E_S = 73$ GPa, $\nu_S = 0.3$). The properties of the patch are the homogeneous material properties obtained with PHM. Fig. 5.14 presents the response of the sensor patch in terms of mean transverse electric displacement. Results

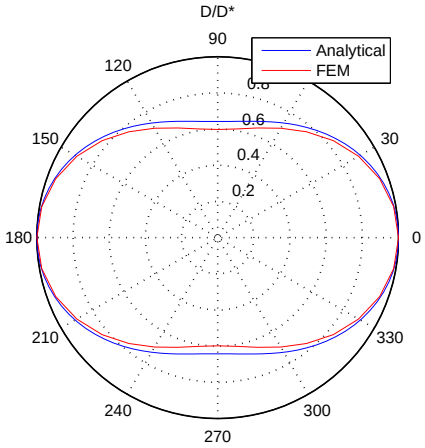

Figure 5.14. Response of the sensor in the different directions. Transverse electric displacement is put in non-dimensional form with respect to its value at 0°

are put in non-dimensional form with respect to the value at 0°. The angle accounts for the rotation of patch properties. Analytical results are in good agreement with numerical results. The direction dependency of sensing is ensured.

Chapter 6

Hierarchical finite elements for structural analysis

Structural components, depending on their characteristics (in particular their shape), may be modelled with finite elements of different type, for instance with beam, plate and solid elements. Solid elements have no underlying cinematic model and are the most general and flexible elements. On the other hand, when adopted to model thin or slender structures, they are computationally expensive since the aspect ratio of the single element should not exceed an upper limit (usually in the range $5 \div 50$). Beam and plate elements are formulated according to a kinematic model and should be preferred for computational reasons when a structural component is slender or thin, respectively. Classical beam and plate finite elements, available in any commercial FEM software, may be inaccurate depending on the geometry and the material of the structural component. In order to increase the accuracy, higher order elements can be developed in a hierarchical framework. This framework, developed by Carrera [82] and known as Unified Formulation (UF), is also well suited to develop multifield elements, such as piezoelectric elements that account for electric degrees of freedom. In this chapter, hierarchical solid elements are initially considered to introduce the UF. Beam and plate elements, whose formulation is less evident, are later presented. Piezoelectric solid and plate elements are also developed.

6.1 Preliminaries

A Cartesian reference system x, y and z is adopted. The displacement field is:

$$\mathbf{u}^T(x,y,z) = \left\{ \; u_x(x,y,z), \quad u_y(x,y,z), \quad u_z(x,y,z) \; \right\} \tag{6.1}$$

in which u_x, u_y and u_z are the displacement components along x-, y- and z-axes. Superscript 'T' represents the transposition operator. Stress, $\boldsymbol{\sigma}$, and strain, $\boldsymbol{\varepsilon}$, vectors are defined as:

$$\begin{aligned} \boldsymbol{\sigma}^T &= \left\{ \; \sigma_{xx}, \quad \sigma_{yy}, \quad \sigma_{zz}, \quad \sigma_{yz}, \quad \sigma_{xz}, \quad \sigma_{xy} \; \right\} \\ \boldsymbol{\varepsilon}^T &= \left\{ \; \varepsilon_{xx}, \quad \varepsilon_{yy}, \quad \varepsilon_{zz}, \quad \gamma_{yz}, \quad \gamma_{xz}, \quad \gamma_{xy} \; \right\} \end{aligned} \tag{6.2}$$

In the case of small displacements with respect to a characteristic dimension, linear relations between strain and displacement components hold. γ_{ij} with $i \neq j$ in Eq. 6.2 is the double of ε_{ij} in Eq. 2.11. A compact vectorial notation can be adopted:

$$\boldsymbol{\varepsilon} = \boldsymbol{D}\boldsymbol{u} \tag{6.3}$$

D is the following differential matrix operator:

$$\mathbf{D} = \begin{bmatrix} \dfrac{\partial}{\partial x} & 0 & 0 \\ 0 & \dfrac{\partial}{\partial y} & 0 \\ 0 & 0 & \dfrac{\partial}{\partial z} \\ 0 & \dfrac{\partial}{\partial z} & \dfrac{\partial}{\partial y} \\ \dfrac{\partial}{\partial z} & 0 & \dfrac{\partial}{\partial x} \\ \dfrac{\partial}{\partial y} & \dfrac{\partial}{\partial x} & 0 \end{bmatrix} \tag{6.4}$$

Under the hypothesis of linear elastic materials, generalised Hooke's law holds. It reads:

$$\boldsymbol{\sigma} = \boldsymbol{C}\boldsymbol{\varepsilon} \tag{6.5}$$

where $\boldsymbol{C}$ is the material stiffness matrix. In the most general case of anisotropic material, it is a full matrix.

6.2 Solid elements

A unified formulation is adopted for deriving solid finite elements. The number of nodes is formally considered as a free parameter of the formulation. The displacement vector $\boldsymbol{u}$ is expressed in terms of shape functions N_i:

$$\boldsymbol{u}\,(x,y,z) = N_i(x,y,z)\boldsymbol{q}_i \quad i = 1,2,\ldots,N_n \tag{6.6}$$

where $\mathbf{q}_i$ contains the nodal displacements:

$$\mathbf{q}_i^T = \left\{ q_{u_{xi}} \quad q_{u_{y_i}} \quad q_{u_{zi}} \right\} \tag{6.7}$$

N_n denotes the number of nodes of the considered element. The summation convention of Einstein's notation is adopted. The geometrical relations in Eqs. 6.3 due to the FE discretisation read:

$$\boldsymbol{\varepsilon} = \boldsymbol{D}(N_i\boldsymbol{I})\boldsymbol{q}_i \tag{6.8}$$

where $\boldsymbol{I}$ is the identity matrix. The Principle of Virtual Displacements (PVD) is adopted:

$$\int_V \delta\boldsymbol{\varepsilon}^T \boldsymbol{\sigma} dV = \delta L_{ext} \tag{6.9}$$

The integration domain V indicates the volume. δ represents a virtual variation. L_{ext} is the expression of the external work that accounts for external loads. After the substitution of Eqs. 6.8 and 6.6 in Eq. 6.9, the internal energy reads:

$$\delta L_{int} = \int_V \delta\boldsymbol{\varepsilon}^T \boldsymbol{\sigma} dV = \int_V \delta \boldsymbol{q}_i^T (N_i \boldsymbol{I})^T \boldsymbol{D}^T \boldsymbol{C} \boldsymbol{D} (N_j \boldsymbol{I}) \boldsymbol{q}_j dV \tag{6.10}$$

Eq. 6.10 can be rewritten in a compact form as:

$$\delta L_{int} = \delta \boldsymbol{q}_i^T \boldsymbol{K}^{ij} \boldsymbol{q}_j \tag{6.11}$$

$\boldsymbol{K}^{ij} \in \mathbb{R}^{3\times 3}$ is the nucleo of the element stiffness matrix. Its components are:

$$K_{ro}^{ij} = \triangleleft D_{rl}^T N_i C_{lm} D_{mo} N_j \triangleright_V = \triangleleft D_{lr} N_i C_{lm} D_{mo} N_j \triangleright_V \quad r,o = 1,2,3 \tag{6.12}$$

Symbol $\triangleleft \ldots \triangleright_V$ denotes integration over V. The components of the nucleo are here written in extended form:

$$\begin{aligned} K_{11}^{ij} \;=\; & \triangleleft C_{11}\frac{\partial N_i}{\partial x}\frac{\partial N_j}{\partial x} + C_{15}\left(\frac{\partial N_i}{\partial x}\frac{\partial N_j}{\partial z} + \frac{\partial N_i}{\partial z}\frac{\partial N_j}{\partial x}\right) \\ & + C_{16}\left(\frac{\partial N_i}{\partial x}\frac{\partial N_j}{\partial y} + \frac{\partial N_i}{\partial y}\frac{\partial N_j}{\partial x}\right) + C_{55}\frac{\partial N_i}{\partial z}\frac{\partial N_j}{\partial z} \\ & + C_{56}\left(\frac{\partial N_i}{\partial z}\frac{\partial N_j}{\partial y} + \frac{\partial N_i}{\partial y}\frac{\partial N_j}{\partial z}\right) + C_{66}\frac{\partial N_i}{\partial y}\frac{\partial N_j}{\partial y} \triangleright_V \end{aligned} \tag{6.13}$$

$$\begin{aligned} K_{12}^{ij} \;=\; & \triangleleft C_{12}\frac{\partial N_i}{\partial x}\frac{\partial N_j}{\partial y} + C_{14}\frac{\partial N_i}{\partial x}\frac{\partial N_j}{\partial z} + C_{16}\frac{\partial N_i}{\partial x}\frac{\partial N_j}{\partial x} \\ & + C_{25}\frac{\partial N_i}{\partial z}\frac{\partial N_j}{\partial y} + C_{45}\frac{\partial N_i}{\partial z}\frac{\partial N_j}{\partial z} + C_{56}\frac{\partial N_i}{\partial z}\frac{\partial N_j}{\partial x} \\ & + C_{26}\frac{\partial N_i}{\partial y}\frac{\partial N_j}{\partial y} + C_{46}\frac{\partial N_i}{\partial y}\frac{\partial N_j}{\partial z} + C_{66}\frac{\partial N_i}{\partial y}\frac{\partial N_j}{\partial x} \triangleright_V \end{aligned} \tag{6.14}$$

$$\begin{aligned} K_{13}^{ij} \;=\; & \triangleleft C_{13}\frac{\partial N_i}{\partial x}\frac{\partial N_j}{\partial z} + C_{14}\frac{\partial N_i}{\partial x}\frac{\partial N_j}{\partial y} + C_{15}\frac{\partial N_i}{\partial x}\frac{\partial N_j}{\partial x} \\ & + C_{35}\frac{\partial N_i}{\partial z}\frac{\partial N_j}{\partial z} + C_{45}\frac{\partial N_i}{\partial z}\frac{\partial N_j}{\partial y} + C_{55}\frac{\partial N_i}{\partial z}\frac{\partial N_j}{\partial x} \\ & + C_{36}\frac{\partial N_i}{\partial y}\frac{\partial N_j}{\partial z} + C_{46}\frac{\partial N_i}{\partial y}\frac{\partial N_j}{\partial y} + C_{56}\frac{\partial N_i}{\partial y}\frac{\partial N_j}{\partial x} \triangleright_V \end{aligned} \tag{6.15}$$

$$\begin{aligned} K_{21}^{ij} \;=\; & \triangleleft C_{12}\frac{\partial N_i}{\partial y}\frac{\partial N_j}{\partial x} + C_{25}\frac{\partial N_i}{\partial y}\frac{\partial N_j}{\partial z} + C_{26}\frac{\partial N_i}{\partial y}\frac{\partial N_j}{\partial y} \\ & + C_{14}\frac{\partial N_i}{\partial z}\frac{\partial N_j}{\partial x} + C_{45}\frac{\partial N_i}{\partial z}\frac{\partial N_j}{\partial z} + C_{46}\frac{\partial N_i}{\partial z}\frac{\partial N_j}{\partial y} \\ & + C_{16}\frac{\partial N_i}{\partial x}\frac{\partial N_j}{\partial x} + C_{56}\frac{\partial N_i}{\partial x}\frac{\partial N_j}{\partial z} + C_{66}\frac{\partial N_i}{\partial x}\frac{\partial N_j}{\partial y} \triangleright_V \end{aligned} \tag{6.16}$$

$$
\begin{aligned}
K_{22}^{ij} \;=\; & \lhd C_{22}\frac{\partial N_i}{\partial y}\frac{\partial N_j}{\partial y} + C_{24}\left(\frac{\partial N_i}{\partial y}\frac{\partial N_j}{\partial z} + \frac{\partial N_i}{\partial z}\frac{\partial N_j}{\partial y}\right) \\
& + C_{26}\left(\frac{\partial N_i}{\partial y}\frac{\partial N_j}{\partial x} + \frac{\partial N_i}{\partial x}\frac{\partial N_j}{\partial y}\right) + \frac{\partial N_i}{\partial z}C_{44}\frac{\partial N_j}{\partial z} \\
& + C_{46}\left(\frac{\partial N_i}{\partial z}\frac{\partial N_j}{\partial x} + \frac{\partial N_i}{\partial x}\frac{\partial N_j}{\partial z}\right) + \frac{\partial N_i}{\partial x}C_{66}\frac{\partial N_j}{\partial x}\rhd_V
\end{aligned} \tag{6.17}
$$

$$
\begin{aligned}
K_{23}^{ij} \;=\; & \lhd C_{23}\frac{\partial N_i}{\partial y}\frac{\partial N_j}{\partial z} + C_{24}\frac{\partial N_i}{\partial y}\frac{\partial N_j}{\partial y} + C_{25}\frac{\partial N_i}{\partial y}\frac{\partial N_j}{\partial x} \\
& + C_{34}\frac{\partial N_i}{\partial z}\frac{\partial N_j}{\partial z} + C_{44}\frac{\partial N_i}{\partial z}\frac{\partial N_j}{\partial y} + C_{45}\frac{\partial N_i}{\partial z}\frac{\partial N_j}{\partial x} \\
& + C_{36}\frac{\partial N_i}{\partial x}\frac{\partial N_j}{\partial z} + C_{46}\frac{\partial N_i}{\partial x}\frac{\partial N_j}{\partial y} + C_{56}\frac{\partial N_i}{\partial x}\frac{\partial N_j}{\partial x}\rhd_V
\end{aligned} \tag{6.18}
$$

$$
\begin{aligned}
K_{31}^{ij} \;=\; & \lhd C_{13}\frac{\partial N_i}{\partial z}\frac{\partial N_j}{\partial x} + C_{35}\frac{\partial N_i}{\partial z}\frac{\partial N_j}{\partial z} + C_{36}\frac{\partial N_i}{\partial z}\frac{\partial N_j}{\partial y} \\
& + C_{14}\frac{\partial N_i}{\partial y}\frac{\partial N_j}{\partial x} + C_{45}\frac{\partial N_i}{\partial y}\frac{\partial N_j}{\partial z} + C_{46}\frac{\partial N_i}{\partial y}\frac{\partial N_j}{\partial y} \\
& + C_{15}\frac{\partial N_i}{\partial x}\frac{\partial N_j}{\partial x} + C_{55}\frac{\partial N_i}{\partial x}\frac{\partial N_j}{\partial z} + C_{56}\frac{\partial N_i}{\partial x}\frac{\partial N_j}{\partial y}\rhd_V
\end{aligned} \tag{6.19}
$$

$$
\begin{aligned}
K_{32}^{ij} \;=\; & \lhd C_{23}\frac{\partial N_i}{\partial z}\frac{\partial N_j}{\partial y} + C_{34}\frac{\partial N_i}{\partial z}\frac{\partial N_j}{\partial z} + C_{36}\frac{\partial N_i}{\partial z}\frac{\partial N_j}{\partial x} \\
& + C_{24}\frac{\partial N_i}{\partial y}\frac{\partial N_j}{\partial y} + C_{44}\frac{\partial N_i}{\partial y}\frac{\partial N_j}{\partial z} + C_{46}\frac{\partial N_i}{\partial y}\frac{\partial N_j}{\partial x} \\
& + C_{25}\frac{\partial N_i}{\partial x}\frac{\partial N_j}{\partial y} + C_{45}\frac{\partial N_i}{\partial x}\frac{\partial N_j}{\partial z} + C_{56}\frac{\partial N_i}{\partial x}\frac{\partial N_j}{\partial x}\rhd_V
\end{aligned} \tag{6.20}
$$

$$
\begin{aligned}
K_{33}^{ij} \;=\; & \lhd C_{33}\frac{\partial N_i}{\partial z}\frac{\partial N_j}{\partial z} + C_{34}\left(\frac{\partial N_i}{\partial z}\frac{\partial N_j}{\partial y} + \frac{\partial N_i}{\partial y}\frac{\partial N_j}{\partial z}\right) \\
& + C_{44}\frac{\partial N_i}{\partial y}\frac{\partial N_j}{\partial y} + C_{45}\left(\frac{\partial N_i}{\partial y}\frac{\partial N_j}{\partial x} + \frac{\partial N_i}{\partial x}\frac{\partial N_j}{\partial y}\right) \\
& + C_{35}\left(\frac{\partial N_i}{\partial z}\frac{\partial N_j}{\partial x} + \frac{\partial N_i}{\partial x}\frac{\partial N_j}{\partial z}\right) + C_{55}\frac{\partial N_i}{\partial x}\frac{\partial N_j}{\partial x}\rhd_V
\end{aligned} \tag{6.21}
$$

As far as the whole structure is concerned, the FEM problem in the framework of the proposed UF is governed by the following equation:

$$
\delta\overline{\boldsymbol{q}}_i : \quad \overline{\boldsymbol{K}}^{ij}\overline{\boldsymbol{q}}_j = \overline{\boldsymbol{P}}_i \tag{6.22}
$$

where $\overline{\boldsymbol{K}}^{ij}$ and $\overline{\boldsymbol{q}}_j$ are the global FE stiffness matrix and nodal unknowns vector. $\overline{\boldsymbol{P}}_i$ is a loading vector that is variationally coherent to the mechanical model through the external work.

Lagrange polynomials are considered as shape functions:

$$
l_k^n(\xi) = \prod_{i=0, i\neq k}^{n} \frac{\xi - \xi_i}{\xi_k - \xi_i} \tag{6.23}
$$

where n is the order of the polynomial and ξ is a normalised coordinate. Prisms of the Lagrange family are adopted. Shape functions are defined as:

$$N_i = l_p^n(\xi) l_q^n(\eta) l_r^n(\zeta) \tag{6.24}$$

where η and ζ are also normalised coordinates. Only quadratic ($N_n = 27$) elements are considered. They are addressed as S27. Shear locking can arise in linear prism elements in bending applications. Reduced integration should be adopted to contrast this phenomenon. It should be noted that the expression of the nucleo of the stiffness matrix does not depend formally on the number of nodes of the element.

6.2.1 Extension to piezoelasticity

The vector of primary variables is:

$$\mathbf{a}^T(x,y,z) = \left\{ \begin{array}{cc} \mathbf{u}^T(x,y,z) & \phi(x,y,z) \end{array} \right\} \tag{6.25}$$

in which ϕ denotes the electric potential field. Superscript 'T' represents the transposition operator. Generalised stress, $\boldsymbol{\sigma}_G$, and generalised strain, $\boldsymbol{\varepsilon}_G$, vectors are defined as:

$$\begin{array}{l} \boldsymbol{\sigma}_G^T = \left\{ \begin{array}{cc} \boldsymbol{\sigma}^T & \boldsymbol{D}^T \end{array} \right\} \\ \boldsymbol{\varepsilon}_G^T = \left\{ \begin{array}{cc} \boldsymbol{\varepsilon}^T & \boldsymbol{E}^T \end{array} \right\} \end{array} \tag{6.26}$$

where $\boldsymbol{D}$ and $\boldsymbol{E}$ are the electric displacement vector and the electric field vector, respectively:

$$\begin{array}{l} \boldsymbol{D}^T = \left\{ \begin{array}{ccc} D_x & D_y & D_z \end{array} \right\} \\ \boldsymbol{E}^T = \left\{ \begin{array}{ccc} E_x & E_y & E_z \end{array} \right\} \end{array} \tag{6.27}$$

$\boldsymbol{\sigma}_G$ and $\boldsymbol{\varepsilon}_G$ correspond to $\boldsymbol{T}_G$ and $\boldsymbol{S}_G$ in Eq. 2.3, respectively. Linear relations between generalised strain and primary variables hold. On the basis of Eq. 2.11, a compact vectorial notation can be adopted:

$$\boldsymbol{\varepsilon}_G = \boldsymbol{D_G a} \tag{6.28}$$

$$\tag{6.29}$$

$\mathbf{D}_G$ is the following differential matrix operator:

$$\mathbf{D}_G = \begin{bmatrix} \frac{\partial}{\partial x} & 0 & 0 & 0 \\ 0 & \frac{\partial}{\partial y} & 0 & 0 \\ 0 & 0 & \frac{\partial}{\partial z} & 0 \\ 0 & \frac{\partial}{\partial z} & \frac{\partial}{\partial y} & 0 \\ \frac{\partial}{\partial z} & 0 & \frac{\partial}{\partial x} & 0 \\ \frac{\partial}{\partial y} & \frac{\partial}{\partial x} & 0 & 0 \\ 0 & 0 & 0 & \frac{\partial}{\partial x} \\ 0 & 0 & 0 & \frac{\partial}{\partial y} \\ 0 & 0 & 0 & \frac{\partial}{\partial z} \end{bmatrix} \tag{6.30}$$

Under the hypothesis of linear piezoelasticity, the constitutive equations read:

$$\boldsymbol{\sigma}_G = \boldsymbol{C}_G \boldsymbol{\varepsilon}_G \tag{6.31}$$

where $\boldsymbol{C}_G$ can have the same form as in Eq. 2.3 or, more in general, the following form:

$$\boldsymbol{C}_G = \begin{bmatrix} \boldsymbol{C} & -\boldsymbol{e}^T \\ \boldsymbol{e} & \boldsymbol{\epsilon} \end{bmatrix} \tag{6.32}$$

$\boldsymbol{e}$ is the matrix of the piezoelectric coefficients and $\boldsymbol{\epsilon}$ is the matrix of the dielectric coefficients. They are, in the most general case, full matrixes. The Principle of Virtual Displacements (PVD) reads:

$$\int_V \left\{ \delta \boldsymbol{\varepsilon}^T \boldsymbol{\sigma} - \delta \boldsymbol{E}^T \boldsymbol{D} \right\} dV = \delta L_{ext} \tag{6.33}$$

The primary variable vector $\boldsymbol{a}$ is expressed in terms of nodal unknowns and shape functions N_i:

$$\boldsymbol{a}\,(x,y,z) = N_i(x,y,z)\boldsymbol{q}_i \quad i = 1,2,\ldots,N_n \tag{6.34}$$

where

$$\boldsymbol{q}_i = \left\{ q_{u_x i}, q_{u_y i}, q_{u_z i}, q_{\phi i} \right\} \tag{6.35}$$

The internal energy can be rewritten in the same form as Eq. 6.11 where $\boldsymbol{K}^{ij}$ is a 4 x 4 array. Its components are:

$$K^{ij}_{ro} = \triangleleft D_{Glr} N_i C_{Glm} D_{Gmo} N_j \triangleright_V \quad r,o = 1,2,3,4 \tag{6.36}$$

For example, the component (4,4) of the nucleo is here written in its extended form:

$$\begin{aligned} K_{44}^{ij} \;=\; & \triangleleft \frac{\partial N_i}{\partial x}\epsilon_{11}\frac{\partial N_j}{\partial x} + \frac{\partial N_i}{\partial x}\epsilon_{12}\frac{\partial N_j}{\partial y} + \frac{\partial N_i}{\partial x}\epsilon_{13}\frac{\partial N_j}{\partial z} \\ & + \frac{\partial N_i}{\partial y}\epsilon_{21}\frac{\partial N_j}{\partial x} + \frac{\partial N_i}{\partial y}\epsilon_{22}\frac{\partial N_j}{\partial y} + \frac{\partial N_i}{\partial y}\epsilon_{23}\frac{\partial N_j}{\partial z} \\ & + \frac{\partial N_i}{\partial z}\epsilon_{31}\frac{\partial N_j}{\partial x} + \frac{\partial N_i}{\partial z}\epsilon_{32}\frac{\partial N_j}{\partial y} + \frac{\partial N_i}{\partial z}\epsilon_{33}\frac{\partial N_j}{\partial z} \triangleright_V \end{aligned} \tag{6.37}$$

6.3 Beam elements

Beam structures are widely used in many industrial fields. Helicopter rotor blades in aerospace engineering and concrete made beams in civil engineering represent just two examples. In order to achieve an effective design, the mechanics of beam structures should be modelled as accurate as possible, especially in the case of non-trivial cross sections or composite materials. A brief discussion on refined beam formulation follows. In the case of bending mechanics, classical one-dimensional models are represented by Euler-Bernoulli's (EB) and Timoshenko's (TB) theories (see Timoshenko [83, 84]). The cross-section is considered to be rigid on its plane. EB discards the shear deformation while TB accounts for a constant value. In the case of torsion, Saint-Venant's [85] and Prandtl's [86] models are the classical solutions. Classical theories do not yield accurate results in the case of unconventional cross-section geometries, short beams, anisotropic materials and non-homogeneous sections. In these contexts, refined theories are necessary. Improvements in classical models have been proposed to account for non-classical effects and non-conventional materials. A general review on beam modelling was proposed by Kapania and Raciti [87, 88] accounting for static, buckling, free-vibration and wave propagation analysis. Other reviews are the ones by Hodges [89] and Jung et al. [90]. A UF of axiomatically refined beam models was proposed by Carrera et Giunta [91]. Displacement-based theories accounting for non-classical effects (such as transverse shear and cross-section in- and out-of-plane warping) were derived. EB and TB models were retrieved as particular cases. Through a concise notation for the displacement field, problem governing equations were reduced to a 'fundamental nucleo' that does not depend upon the approximation order, which is a free parameter of the formulation. The corresponding hierarchical finite elements were addressed by Carrera et al. [92].

6.3.1 Geometry and constitutive equations

A beam is a structure whose axial extension (l) is predominant with respect to any other dimension orthogonal to it. The cross-section (Ω) is defined by intersecting the beam with planes orthogonal to its axis. The x coordinate is coincident to the axis of the beam and it is bounded such that $0 \leq x \leq l$, y- and z-axis are two orthogonal directions laying on Ω. The cross-section is considered to be constant along x. Stress ($\boldsymbol{\sigma}$) and strain ($\boldsymbol{\varepsilon}$) vectors are grouped into vectors $\boldsymbol{\sigma}_n$, $\boldsymbol{\varepsilon}_n$ acting on the cross-section:

$$\boldsymbol{\sigma}_n^T = \left\{ \begin{array}{ccc} \sigma_{xx} & \sigma_{xy} & \sigma_{xz} \end{array} \right\} \quad \boldsymbol{\varepsilon}_n^T = \left\{ \begin{array}{ccc} \varepsilon_{xx} & \gamma_{xy} & \gamma_{xz} \end{array} \right\} \tag{6.38}$$

and $\boldsymbol{\sigma}_p$, $\boldsymbol{\varepsilon}_p$ acting on planes orthogonal to Ω:

$$\boldsymbol{\sigma}_p^T = \left\{ \begin{array}{ccc} \sigma_{yy} & \sigma_{zz} & \sigma_{yz} \end{array} \right\} \quad \boldsymbol{\varepsilon}_p^T = \left\{ \begin{array}{ccc} \varepsilon_{yy} & \varepsilon_{zz} & \gamma_{yz} \end{array} \right\} \tag{6.39}$$

Strain vectors can be expresses in a compact vectorial notation as:

$$\boldsymbol{\varepsilon}_n = \mathbf{D}_{np}\mathbf{u} + \mathbf{D}_{nx}\mathbf{u} \quad \boldsymbol{\varepsilon}_p = \mathbf{D}_{pp}\mathbf{u} \tag{6.40}$$

$\mathbf{D}_{np}$, $\mathbf{D}_{nx}$, and $\mathbf{D}_{pp}$ are the following differential matrix operators:

$$\mathbf{D}_{np} = \begin{bmatrix} 0 & 0 & 0 \\ \dfrac{\partial}{\partial y} & 0 & 0 \\ \dfrac{\partial}{\partial z} & 0 & 0 \end{bmatrix} \quad \mathbf{D}_{nx} = \mathbf{I}\frac{\partial}{\partial x} \quad \mathbf{D}_{pp} = \begin{bmatrix} 0 & \dfrac{\partial}{\partial y} & 0 \\ 0 & 0 & \dfrac{\partial}{\partial z} \\ 0 & \dfrac{\partial}{\partial z} & \dfrac{\partial}{\partial y} \end{bmatrix} \tag{6.41}$$

$\mathbf{I}$ is the unit matrix. According to Eqs. 6.38 and 6.39, the generalised Hooke law reads:

$$\begin{array}{l} \boldsymbol{\sigma}_p = \tilde{\mathbf{C}}_{pp}\boldsymbol{\varepsilon}_p + \tilde{\mathbf{C}}_{pn}\boldsymbol{\varepsilon}_n \\ \boldsymbol{\sigma}_n = \tilde{\mathbf{C}}_{np}\boldsymbol{\varepsilon}_p + \tilde{\mathbf{C}}_{nn}\boldsymbol{\varepsilon}_n \end{array} \tag{6.42}$$

In the case of fibres laying on planes parallel to the x-y one, matrices $\tilde{\mathbf{C}}_{pp}$, $\tilde{\mathbf{C}}_{pn}$, $\tilde{\mathbf{C}}_{np}$ and $\tilde{\mathbf{C}}_{nn}$ are:

$$\begin{array}{c} \tilde{\mathbf{C}}_{pp} = \begin{bmatrix} \tilde{C}_{22} & \tilde{C}_{23} & 0 \\ \tilde{C}_{23} & \tilde{C}_{33} & 0 \\ 0 & 0 & \tilde{C}_{44} \end{bmatrix} \quad \tilde{\mathbf{C}}_{pn} = \tilde{\mathbf{C}}_{np}^T = \begin{bmatrix} \tilde{C}_{12} & \tilde{C}_{26} & 0 \\ \tilde{C}_{13} & \tilde{C}_{36} & 0 \\ 0 & 0 & \tilde{C}_{45} \end{bmatrix} \\ \tilde{\mathbf{C}}_{nn} = \begin{bmatrix} \tilde{C}_{11} & \tilde{C}_{16} & 0 \\ \tilde{C}_{16} & \tilde{C}_{66} & 0 \\ 0 & 0 & \tilde{C}_{55} \end{bmatrix} \end{array} \tag{6.43}$$

For sake of brevity, coefficients $\tilde{C}_{ij}$ in Eqs. 6.43 are not reported here. They can be found as function of the engineering material constants and fibre rotation angle measured versus x-axis in Reddy [93]. In the case of classical models, the material stiffness coefficients should be corrected in order to contrast a phenomenon known in literature as Poisson's locking (see Carrera and Brischetto [94, 95]). Poisson's ratio couples the normal deformations along the spatial directions. Because of this, a constant approximation of the displacement components u_y and u_z does not yield accurate results, even in the case of slender beams. A modified version of material's constitutive equations, in which the stiffness coefficients are opportunely modified, is obtained imposing σ_{yy} and σ_{zz} equal to zero in Hooke's law. An algebraic linear system in ε_{yy} and ε_{zz} is obtained. By substituting its solution into Hooke's equations regarding σ_{xx} and σ_{xy} the reduced stiffness coefficients $\tilde{Q}_{11}$, $\tilde{Q}_{16}$ and

$\tilde{Q}_{66}$ are obtained:

$$\begin{aligned}
\tilde{Q}_{11} &= \tilde{C}_{11} + \tilde{C}_{12}\frac{\tilde{C}_{12}\tilde{C}_{33} - \tilde{C}_{13}\tilde{C}_{23}}{\tilde{C}_{23}^2 - \tilde{C}_{22}\tilde{C}_{33}} + \tilde{C}_{13}\frac{\tilde{C}_{22}\tilde{C}_{13} - \tilde{C}_{12}\tilde{C}_{23}}{\tilde{C}_{23}^2 - \tilde{C}_{22}\tilde{C}_{33}} \\
\tilde{Q}_{16} &= \tilde{C}_{16} + \tilde{C}_{26}\frac{\tilde{C}_{12}\tilde{C}_{33} - \tilde{C}_{13}\tilde{C}_{23}}{\tilde{C}_{23}^2 - \tilde{C}_{22}\tilde{C}_{33}} + \tilde{C}_{36}\frac{\tilde{C}_{22}\tilde{C}_{13} - \tilde{C}_{12}\tilde{C}_{23}}{\tilde{C}_{23}^2 - \tilde{C}_{22}\tilde{C}_{33}} \\
\tilde{Q}_{66} &= \tilde{C}_{66} + \tilde{C}_{26}\frac{\tilde{C}_{26}\tilde{C}_{33} - \tilde{C}_{36}\tilde{C}_{23}}{\tilde{C}_{23}^2 - \tilde{C}_{22}\tilde{C}_{33}} + \tilde{C}_{36}\frac{\tilde{C}_{22}\tilde{C}_{36} - \tilde{C}_{26}\tilde{C}_{23}}{\tilde{C}_{23}^2 - \tilde{C}_{22}\tilde{C}_{33}}
\end{aligned} \tag{6.44}$$

The new constitutive relations in the case of TB read:

$$\begin{aligned}
\sigma_{xx} &= \tilde{Q}_{11}\varepsilon_{xx} + \tilde{Q}_{16}\gamma_{xy} \\
\sigma_{xy} &= \tilde{Q}_{16}\varepsilon_{xx} + \tilde{Q}_{66}\gamma_{xy} \\
\sigma_{xz} = \tilde{C}_{55}\gamma_{xz} \quad \sigma_{yz} &= \tilde{C}_{45}\gamma_{xz}
\end{aligned} \tag{6.45}$$

whereas for EB, they reduce to the following equation:

$$\sigma_{xx} = \tilde{Q}_{11}\varepsilon_{xx} \tag{6.46}$$

6.3.2 Hierarchical beam theories

Hierarchical displacement-based theories can be formulated on the basis of the following generic kinematic field:

$$\mathbf{u}\,(x,y,z) = F_\tau\,(y,z)\,\mathbf{u}_\tau\,(x) \quad \text{with} \quad \tau = 1,\, 2,\, \ldots,\, N_u \tag{6.47}$$

where N_u stands for the number of unknowns and depends on the approximation order N. This latter is a free parameter of the formulation. On the basis of Einstein's notation, subscript τ is a dummy index that indicates summation over the range $[1,N_u]$. Thanks to this notation, problem's governing differential equations and boundary conditions are derived in terms of a single 'fundamental nucleo'. The theoretical formulation is valid for a generic approximation order and approximating functions $F_\tau\,(y,z)$. The functions F_τ are assumed to be Mac Laurin's polynomials. N_u and F_τ as functions of N can be obtained via Pascal's triangle (see Table 6.1). The actual governing differential equations and boundary conditions due to a fixed approximation order are obtained straightforwardly via summation of the nucleo corresponding to each term of the expansion. According to the previous choice of polynomial function, the generic N-order displacement field is:

$$\begin{aligned}
u_x &= u_{x1} + u_{x2}y + u_{x3}z + \cdots + u_{x\frac{(N^2+N+2)}{2}}y^N + \cdots + u_{x\frac{(N+1)(N+2)}{2}}z^N \\
u_y &= u_{y1} + u_{y2}y + u_{y3}z + \cdots + u_{y\frac{(N^2+N+2)}{2}}y^N + \cdots + u_{y\frac{(N+1)(N+2)}{2}}z^N \\
u_z &= u_{z1} + u_{z2}y + u_{z3}z + \cdots + u_{z\frac{(N^2+N+2)}{2}}y^N + \cdots + u_{z\frac{(N+1)(N+2)}{2}}z^N
\end{aligned} \tag{6.48}$$

As far as the first-order approximation order is concerned, the kinematic field is:

$$\begin{aligned}
u_x &= u_{x1} + u_{x2}y + u_{x3}z \\
u_y &= u_{y1} + u_{y2}y + u_{y3}z \\
u_z &= u_{z1} + u_{z2}y + u_{z3}z
\end{aligned} \tag{6.49}$$

N	N_u	F_τ
0	1	$F_1 = 1$
1	3	$F_2 = y \quad F_3 = z$
2	6	$F_4 = y^2 \quad F_5 = yz \quad F_6 = z^2$
3	10	$F_7 = y^3 \quad F_8 = y^2 z \quad F_9 = yz^2 \quad F_{10} = z^3$
...	...	...
N	$\frac{(N+1)(N+2)}{2}$	$F_{\frac{(N^2+N+2)}{2}} = y^N \quad \ldots \quad F_{\frac{(N+1)(N+2)}{2}} = z^N$

Table 6.1. Mac Laurin's polynomials via Pascal's triangle.

Classical models, such as TB:

$$\begin{aligned} u_x &= u_{x1} + u_{x2} y + u_{x3} z \\ u_y &= u_{y1} \\ u_z &= u_{z1} \end{aligned} \tag{6.50}$$

and EB:

$$\begin{aligned} u_x &= u_{x1} - u_{y1,x} y - u_{z1,x} z \\ u_y &= u_{y1} \\ u_z &= u_{z1} \end{aligned} \tag{6.51}$$

are straightforwardly derived from the first-order approximation model. Higher order models yield a more detailed description of the shear mechanics (no shear correction coefficient is required), of the in- and out-of-section deformations, of the coupling between the spatial directions due to Poisson's effect and of the torsional mechanics than classical models do. EB theory neglects them all, since it was formulated to describe the bending mechanics. TB model accounts for constant shear stress and strain components.

6.3.3 Finite element formulation

In the framework of the finite element modelling, the displacement vector is approximated as:

$$\mathbf{u}\,(x,y,z) = N_i(y,z) F_\tau(x) \mathbf{q}_{\tau i} \quad i = 1,2,\ldots,N_n \tag{6.52}$$

where $\mathbf{q}_{\tau i}$ is the nodal displacement vector:

$$\mathbf{q}_{\tau i}^T = \left\{ q_{u_{x\tau i}} \quad q_{u_{y_{\tau i}}} \quad q_{u_{z\tau i}} \right\} \tag{6.53}$$

and N_i are the shape functions as in Bathe [96]. Dummy index i ranger over the element nodes. Elements with two, three and four nodes are considered. Through the paper they are addressed as B2, B3 and B4, respectively. Elements' stiffness matrix and external loadings vector are obtained through the Principle of Virtual Displacements (PVD):

$$\delta L_{int} = \delta L_{ext} \tag{6.54}$$

δ stands for a virtual variation. L_{ext} stands for the work due to external loadings. L_{int} represents the strain energy. According to the grouping of the stress and strain components in Eqs. 6.38 and 6.39, it can be written as the sum of two contributes:

$$\delta L_{int} = \int_l \int_\Omega \left(\delta \boldsymbol{\epsilon}_n^T \boldsymbol{\sigma}_n + \delta \boldsymbol{\epsilon}_p^T \boldsymbol{\sigma}_p \right) d\Omega \; dx \tag{6.55}$$

Via substitution of Eqs. 6.40, 6.42 and 6.52, Eq. 6.55 reads:

$$\begin{aligned} \delta L_{int} = \; & \int_l \int_\Omega \delta \mathbf{q}_{\tau i}^T \Big[N_j \left(\mathbf{D}_{nx}^T N_i \right) \tilde{\mathbf{C}}_{np} F_\tau \left(\mathbf{D}_{pp} F_s \right) + F_\tau F_s \left(\mathbf{D}_{nx}^T N_i \right) \tilde{\mathbf{C}}_{nn} \left(\mathbf{D}_{nx} N_j \right) \\ & + N_j \left(\mathbf{D}_{nx}^T N_i \right) \tilde{\mathbf{C}}_{nn} F_\tau \left(\mathbf{D}_{np} F_s \right) + N_j N_i \left(\mathbf{D}_{np}^T F_\tau \right) \tilde{\mathbf{C}}_{np} \left(\mathbf{D}_{pp} F_s \right) \\ & + F_s \left(\mathbf{D}_{np}^T F_\tau \right) \tilde{\mathbf{C}}_{nn} N_i \left(\mathbf{D}_{nx} N_j \right) + N_j N_i \left(\mathbf{D}_{np}^T F_\tau \right) \tilde{\mathbf{C}}_{nn} \left(\mathbf{D}_{np} F_s \right) \\ & + N_j N_i \left(\mathbf{D}_{pp}^T F_\tau \right) \tilde{\mathbf{C}}_{pp} \left(\mathbf{D}_{pp} F_s \right) + F_s \left(\mathbf{D}_{pp}^T F_\tau \right) \tilde{\mathbf{C}}_{pn} N_i \left(\mathbf{D}_{nx} N_j \right) \\ & + N_j N_i \left(\mathbf{D}_{pp}^T F_\tau \right) \tilde{\mathbf{C}}_{pn} \left(\mathbf{D}_{np} F_s \right) \Big] \mathbf{q}_{sj} \; d\Omega \; dx \end{aligned} \tag{6.56}$$

Indexes i and j range over the number of nodes of the element, whereas τ, s are related to the expansion functions. Eq. 6.56 can be rewritten in a compact form as:

$$\delta L_{int} = \delta \mathbf{q}_{\tau i}^T \mathbf{K}^{\tau s i j} \mathbf{q}_{sj} \tag{6.57}$$

where $\mathbf{K}^{\tau s i j}$ is the fundamental nucleo of the stiffness matrix. Its components are:

$$\begin{aligned} K_{xx}^{\tau s i j} &= I_{i,xj,x} J_{\tau s}^{11} + I_{i,xj} J_{\tau s,y}^{16} + I_{ij,x} J_{\tau,ys}^{16} + I_{ij} \left(J_{\tau,ys,y}^{66} + J_{\tau,zs,z}^{66} \right) \\ K_{xy}^{\tau s i j} &= I_{i,xj,x} J_{\tau s}^{16} + I_{i,xj} J_{\tau s,y}^{12} + I_{ij,x} J_{\tau,ys}^{66} + I_{ij} \left(J_{\tau,ys,y}^{26} + J_{\tau,zs,z}^{45} \right) \\ K_{xz}^{\tau s i j} &= I_{i,xj} J_{\tau s,z}^{13} + I_{ij,x} J_{\tau,zs}^{55} + I_{ij} \left(J_{\tau,zs,y}^{36} + J_{\tau,ys,z}^{45} \right) \\ K_{xy}^{\tau s i j} &= I_{i,xj,x} J_{\tau s}^{16} + I_{i,xj} J_{\tau s,y}^{66} + I_{ij,x} J_{\tau,ys}^{12} + I_{ij} \left(J_{\tau,ys,y}^{26} + J_{\tau,zs,z}^{45} \right) \\ K_{yy}^{\tau s i j} &= I_{i,xj,x} J_{\tau s}^{66} + I_{i,xj} J_{\tau s,y}^{26} + I_{ij,x} J_{\tau,ys}^{26} + I_{ij} \left(J_{\tau,ys,y}^{22} + J_{\tau,zs,z}^{44} \right) \\ K_{yz}^{\tau s i j} &= I_{i,xj} J_{\tau s,z}^{36} + I_{ij,x} J_{\tau,zs}^{45} + I_{ij} \left(J_{\tau,zs,y}^{23} + J_{\tau,ys,z}^{44} \right) \\ K_{zx}^{\tau s i j} &= I_{i,xj} J_{\tau s,z}^{55} + I_{ij,x} J_{\tau,zs}^{13} + I_{ij} \left(J_{\tau,zs,y}^{45} + J_{\tau,ys,z}^{36} \right) \\ K_{zy}^{\tau s i j} &= I_{i,xj} J_{\tau s,z}^{45} + I_{ij,x} J_{\tau,zs}^{36} + I_{ij} \left(J_{\tau,zs,y}^{44} + J_{\tau,ys,z}^{23} \right) \\ K_{zz}^{\tau s i j} &= I_{i,xj,x} J_{\tau s}^{55} + I_{i,xj} J_{\tau s,y}^{45} + I_{ij,x} J_{\tau,ys}^{45} + I_{ij} \left(J_{\tau,ys,y}^{44} + J_{\tau,zs,z}^{33} \right) \end{aligned} \tag{6.58}$$

where:

$$I_{i_{(,x)} j_{(,x)}} = \int_l N_{i_{(,x)}} N_{j_{(,x)}} \; dx \tag{6.59}$$

and:

$$J_{\tau_{(,y)(,z)} s_{(,y)(,z)}}^{mn} = \int_\Omega \tilde{C}_{mn} F_{\tau_{(,y)(,z)}} F_{s_{(,y)(,z)}} \; d\Omega \tag{6.60}$$

Subscripts 'x', 'y' and 'z', when preceded by comma, represent derivation versus the corresponding spatial coordinate. As far as the whole structure is concerned, the constant

kinematic FEM problem in the framework of the proposed unified formulation is governed by the following equation:

$$\overline{\mathbf{K}}^{\tau sij}\overline{\mathbf{q}}_{sj} = \overline{\mathbf{P}}_{\tau i} \tag{6.61}$$

where $\overline{\mathbf{K}}^{\tau sij}$ and $\overline{\mathbf{q}}_{sj}$ are the global stiffness matrix and nodal displacement vector. $\overline{\mathbf{P}}_{\tau i}$ is a loading vector that is variationally coherent to the mechanical model through the external work.

6.4 Plate elements

Multi-layered structures are increasingly used in aerospace, automotive and ship vehicles. Nowadays, there are examples of fighter and commercial aircraft, helicopter and gliders whose structure is entirely made of composite materials. The analysis and design of composite and sandwich structures is a cumbersome subject. In order to achieve an effective design, the mechanics of multi-layered structures should be modelled as accurately as possible. In the case of bending mechanics, classical two-dimensional models are represented by Classical Lamination Theory (CLT), see Kirchhoff [97], and First-order Shear Deformation Theory (FSDT), see Reissner [98] and Mindlin [99]. Classical theories yield accurate results only in the case of thin plates and low degree of anisotropy. Many refinements of classical models have been proposed to overcome the limitations of classical theories and to include partially or completely the so called $\boldsymbol{C}_z^0$-requirements (see Carrera [100]). Both displacement and transverse stresses are $\boldsymbol{C}^0$-class functions along the thickness direction: they have, in the most general case, discontinuous first derivatives at each interface where the mechanical properties change. The fulfilment of the $\boldsymbol{C}_z^0$-requirements is a crucial point of multi-layered structures two-dimensional modelling. A complete and exhaustive discussion of several contributions appeared in literature has been covered by many state-of-the-art articles. Among these, the reviews proposed by Kapania and Raciti [87, 88], Noor and Burton [101], Reddy and Robbins [102], Carrera [103] and Hu et al. [104] should be mentioned. A UF of axiomatically refined plate models was proposed by Carrera [82]. Models formulated on the basis of the Principle of Virtual Displacements (PVD) and Reissner's Mixed Variational Theorem [105] (RMVT) were both considered. Both Equivalent Single Layer and Layer-Wise approaches were adopted. CLT and FSDT models were retrieved as particular cases. Through a concise notation for the unknowns field, problem governing equations were reduced to a 'fundamental nucleo' that does not depend upon the approximation order that is a free parameter of the formulation. A comprehensive assessment of the corresponding finite elements was addressed in Carrera [103].

6.4.1 Geometry and constitutive equations

A plate is a three-dimensional structure in which one dimension (its thickness) is negligible if compared to the in-plane dimensions. The plate has uniform thickness h and its middle plane (midway between its faces) lie in the xy plane. The z coordinate is coincident to plate's out-of-plane axis, whereas x- and y-axis coincide with two orthogonal edges of the plate. Plate's reference plane corresponds to its middle plane: it is a two-dimensional

domain defined as $\Omega = \{(x,y,z) : z = 0\}$. Plates can be monolithic or made up of several layers. The notation adopted in this work considers the case of multi-layered plate. Monolithic plates can be taken into account as single layer plates. The displacement field in a k^{th} layer is:

$$\mathbf{u}^{kT}(x,y,z) = \left\{ \begin{array}{ccc} u_x^k(x,y,z) & u_y^k(x,y,z) & u_z^k(x,y,z) \end{array} \right\} \tag{6.62}$$

in which u_x, u_y and u_z are the displacement components along x-, y- and z-axes. Superscript 'T' represents the transposition operator. Bold letters denote arrays.

Stress, $\boldsymbol{\sigma}^k$, and strain, $\boldsymbol{\varepsilon}^k$, vectors in a k^{th} layer are split into vectors $\boldsymbol{\sigma}_p^k$, $\boldsymbol{\varepsilon}_p^k$ acting on planes parallel to Ω:

$$\boldsymbol{\sigma}_p^{kT} = \left\{ \begin{array}{ccc} \sigma_{xx}^k & \sigma_{yy}^k & \sigma_{xy}^k \end{array} \right\} \quad \boldsymbol{\varepsilon}_p^{kT} = \left\{ \begin{array}{ccc} \varepsilon_{xx}^k & \varepsilon_{yy}^k & \gamma_{xy}^k \end{array} \right\} \tag{6.63}$$

and $\boldsymbol{\sigma}_n^k$, $\boldsymbol{\varepsilon}_n^k$ acting on planes perpendicular to Ω:

$$\boldsymbol{\sigma}_n^{kT} = \left\{ \begin{array}{ccc} \sigma_{xz}^k & \sigma_{yz}^k & \sigma_{zz}^k \end{array} \right\} \quad \boldsymbol{\varepsilon}_n^{kT} = \left\{ \begin{array}{ccc} \gamma_{xz}^k & \gamma_{yz}^k & \varepsilon_{zz}^k \end{array} \right\} \tag{6.64}$$

A compact vectorial notation can be adopted to express the strain vectors:

$$\begin{array}{c} \boldsymbol{\varepsilon}_p^k = \boldsymbol{D}_p \boldsymbol{u}^k \\ \boldsymbol{\varepsilon}_{nG}^k = (\boldsymbol{D}_{n\Omega} + \boldsymbol{D}_{nz}) \boldsymbol{u}^k \end{array} \tag{6.65}$$

Subscript 'G' denotes strains computed through geometrical relations. $\mathbf{D}_{n\Omega}$, $\mathbf{D}_{nz}$ and $\mathbf{D}_p$ are the following differential matrix operators:

$$\mathbf{D}_{n\Omega} = \begin{bmatrix} 0 & 0 & \dfrac{\partial}{\partial x} \\ 0 & 0 & \dfrac{\partial}{\partial y} \\ 0 & 0 & 0 \end{bmatrix} \quad \mathbf{D}_{nz} = \mathbf{I}\frac{\partial}{\partial z} \quad \mathbf{D}_p = \begin{bmatrix} \dfrac{\partial}{\partial x} & 0 & 0 \\ 0 & \dfrac{\partial}{\partial y} & 0 \\ \dfrac{\partial}{\partial y} & \dfrac{\partial}{\partial x} & 0 \end{bmatrix} \tag{6.66}$$

$\mathbf{I}$ is the unit matrix.

According to Eqs. (6.63) and (6.64), and for a reference system not coincident with the orthotropy axes, generalised Hooke's law reads:

$$\begin{array}{c} \boldsymbol{\sigma}_p^k = \boldsymbol{C}_{pp}^k \boldsymbol{\varepsilon}_p^k + \boldsymbol{C}_{pn}^k \boldsymbol{\varepsilon}_n^k \\ \boldsymbol{\sigma}_n^k = \boldsymbol{C}_{np}^k \boldsymbol{\varepsilon}_p^k + \boldsymbol{C}_{nn}^k \boldsymbol{\varepsilon}_n^k \end{array} \tag{6.67}$$

$\boldsymbol{C}_{pp}^k$, $\boldsymbol{C}_{pn}^k$, $\boldsymbol{C}_{np}^k$ and $\boldsymbol{C}_{nn}^k$ are the following material stiffness matrices:

$$\boldsymbol{C}_{pp}^k = \begin{bmatrix} C_{11}^k & C_{12}^k & C_{16}^k \\ C_{12}^k & C_{22}^k & C_{26}^k \\ C_{16}^k & C_{26}^k & C_{66}^k \end{bmatrix} \quad \boldsymbol{C}_{pn}^k = \boldsymbol{C}_{np}^{kT} = \begin{bmatrix} 0 & 0 & C_{13}^k \\ 0 & 0 & C_{23}^k \\ 0 & 0 & C_{36}^k \end{bmatrix} \quad \boldsymbol{C}_{nn}^k = \begin{bmatrix} C_{55}^k & C_{45}^k & 0 \\ C_{45}^k & C_{44}^k & 0 \\ 0 & 0 & C_{33}^k \end{bmatrix} \tag{6.68}$$

For the sake of brevity, stiffness terms C_{ij}^k as function of the engineering constants are not reported here. For more details, see Reddy [93]. In the case of a first-order expansion or

classical models, material stiffness coefficients should be reduced according to the plane stress condition as follows:

$$Q_{11}^k = C_{11}^k - \frac{C_{13}^{k^2}}{C_{33}^k} \quad Q_{22}^k = C_{22}^k - \frac{C_{23}^{k^2}}{C_{33}^k} \quad Q_{12}^k = C_{12}^k - \frac{C_{13}^k C_{23}^k}{C_{33}^k} \tag{6.69}$$

in order to avoid the thickness locking, see Carrera and Brischetto [94]. For mixed models, in which both displacements $\boldsymbol{u}$ and transverse shear/normal stresses $\boldsymbol{\sigma_n}$ are a priori variables according to RMVT, Hooke's equations should be rewritten as follows:

$$\begin{aligned} \boldsymbol{\sigma}_p^k &= \hat{\boldsymbol{C}}_{pp}^k \boldsymbol{\varepsilon}_p^k + \hat{\boldsymbol{C}}_{pn}^k \boldsymbol{\sigma}_n^k \\ \boldsymbol{\varepsilon}_{nC}^k &= \hat{\boldsymbol{C}}_{np}^k \boldsymbol{\varepsilon}_p^k + \hat{\boldsymbol{C}}_{nn}^k \boldsymbol{\sigma}_n^k \end{aligned} \tag{6.70}$$

where the new stiffness matrices are:

$$\hat{\boldsymbol{C}}_{pp}^k = \boldsymbol{C}_{pp}^k - \boldsymbol{C}_{pn}^k \boldsymbol{C}_{nn}^{k^{-1}} \boldsymbol{C}_{np}^k \quad \hat{\boldsymbol{C}}_{pn}^k = \hat{\boldsymbol{C}}_{np}^{kT} = \boldsymbol{C}_{pn}^k \boldsymbol{C}_{nn}^{k^{-1}} \quad \hat{\boldsymbol{C}}_{nn}^k = \boldsymbol{C}_{nn}^{k^{-1}} \tag{6.71}$$

and subscript 'C' denotes out-of-plane strains computed through the constitutive relations.

6.4.2 Unified formulation for plate models

Two-dimensional modelling of plate structures consists in the separation of a generic unknown $\boldsymbol{a} = \boldsymbol{a}(x,y,z)$ into a set of thickness functions F_τ depending only upon the through-the-thickness coordinate z and the correspondent variables $\boldsymbol{a}_\tau$ depending upon the in-plane coordinates (x and y). The Unified Formulation (UF) by Carrera [82] allows obtaining several two-dimensional models thanks to the following compact form:

$$\boldsymbol{a}(x,y,z) = F_\tau(z)\boldsymbol{a}_\tau(x,y) \tag{6.72}$$

where, according to Einstein's notation, τ is a dummy index standing for summation of $N+1$ terms in which N is the through-the-thickness expansion order. In this work, N is assumed to be as high as four. Thanks to the compact notation in Eq. 6.72, the governing equations can be written in terms of a fundamental nucleo that does not depend formally upon N and the unknowns description. This latter can be Equivalent Single Layer (ESL) or Layer Wise (LW). The primary unknowns can be displacements (PVD-based models) or both displacements and transverse stresses (mixed models based on RMVT).

Equivalent Single Layer Theories

Via a ESL description, problem's unknowns are assumed globally for the whole structure. The unknown field is approximated as follows:

$$\boldsymbol{a} = F_0\boldsymbol{a}_0 + F_1\boldsymbol{a}_1 + \ldots + F_N\boldsymbol{a}_N = F_\tau\boldsymbol{a}_\tau \quad \tau = 0,1,\ldots,N \tag{6.73}$$

Within UF, MacLaurin's polynomials are adopted as thickness functions F_τ:

$$F_\tau = z^\tau \tag{6.74}$$

The choice of MacLaurin's polynomials allows obtaining classical theories such as CLT and FSDT as particular cases of a linear theory by simply imposing a constant value of the transverse displacement through the thickness direction. CLT results are retrived assigning artificially high values to the shear moduli G_{13} and G_{23} in order to hinder transverse shear deformation. For more details, see Carrera and Giunta [106]. Reduced material stiffness coefficients according to a plane stress condition, as shown in Eqs. 6.69, should be adopted in the case of classical theories and ESL first order theory.

In addition to MacLaurin's polynomials, the Murakami's zig-zag function [107] can be introduced to account for the zig-zag variation of the displacements:

$$F_Z = (-1)^k \zeta_k \tag{6.75}$$

where $\zeta_k = \frac{2z_k}{h_k}$ is a non-dimensioned layer coordinate. z_k is the physical coordinate of the k^{th} layer, whose thickness is h_k. The exponent k changes the sign of the zig-zag term in each layer, reproducing the discontinuity of the first derivative of the displacement variables in the z-directions that is physically due to the intrinsic transverse anisotropy of multilayer structures.

Layer Wise Theories

According to Reddy [93], in LW theories unknowns are considered independently in a generic k^{th} layer:

$$\boldsymbol{a^k} = F_t \boldsymbol{a}_t^k + F_b \boldsymbol{a}_b^k + F_l \boldsymbol{a}_l^k = F_\tau \boldsymbol{a}_\tau^k \qquad \begin{matrix} \tau = t,b,l \\ l = 2,\ldots,N \end{matrix} \tag{6.76}$$

Subscripts t and b stands for k^{th} layer top and bottom values, l denotes higher-order terms of the through-the-thickness expansion. The thickness functions are a linear combination of Legendre's polynomials (see Carrera [103]) and they vary versus a local through-the-thickness dimensionless coordinate ζ_k:

$$\zeta_k = \frac{2z_k}{h_k} \tag{6.77}$$

being z_k a k^{th} layer local coordinate and h_k its thickness. These thickness functions have the following properties:

$$\begin{matrix} \zeta_k = 1 & : F_t = 1,\ F_b = 0,\ F_l = 0 \\ \zeta_k = -1 & : F_t = 0,\ F_b = 1,\ F_l = 0 \end{matrix} \tag{6.78}$$

In LW mixed models these properties ensure compatibility and equilibrium at layers' interfaces. $\boldsymbol{C}_z^0$-requirements are fulfilled: displacement and transverse stresses are continuous at layers' interfaces and their first derivatives may be discontinuous.

Variational Statements

The governing equations can be derived according to displacement-based or mixed variational statements. The PVD is used for the case of displacement-based models. For a laminate made of N_l layers, the PVD reads:

$$\sum_{k=1}^{N_l} \int_{\Omega_k} \int_{h_k} \left(\delta \boldsymbol{\varepsilon}_{pG}^{kT} \boldsymbol{\sigma}_{pC}^{k} + \delta \boldsymbol{\varepsilon}_{nG}^{kT} \boldsymbol{\sigma}_{nC}^{k} \right) d\Omega_k dz = \sum_{k=1}^{N_l} \delta L_{ext}^{k} \tag{6.79}$$

The integration domain Ω_k indicates the reference plane of each lamina. δ represents a virtual variation. L_{ext}^{k} is the expression of the external work that accounts for a external load acting on a generic k layer.

RMVT is adopted when both displacements and transverse shear and normal stresses are a priori variables, see Reissner [105, 108]. RMVT is obtained via the addition of a Lagrange's multiplier that allows modelling the transverse stress vector $\boldsymbol{\sigma_n}$:

$$\sum_{k=1}^{N_l} \int_{\Omega_k} \int_{h_k} \left[\delta \boldsymbol{\varepsilon}_{pG}^{kT} \boldsymbol{\sigma}_{pC}^{k} + \delta \boldsymbol{\varepsilon}_{nG}^{kT} \boldsymbol{\sigma}_{nM}^{k} + \delta \boldsymbol{\sigma}_{nM}^{kT} \left(\boldsymbol{\varepsilon}_{nG}^{k} - \boldsymbol{\varepsilon}_{nC}^{k} \right) \right] d\Omega_k dz = \sum_{k=1}^{N_l} \delta L_{ext}^{k} \tag{6.80}$$

'M' indicates that $\boldsymbol{\sigma_n}$ is a-priori assumed and, therefore, modelled.

Acronyms System

The following acronyms system is adopted for addressing the two-dimensional models that can be obtained via UF. The first letter indicates the approximation approach and it can be either 'E' for an ESL approach or 'L' for a LW one. The second letter refers to the main unknowns: 'D' stands for displacements-based models and 'M' for mixed theories. A number indicates the order of expansion. For instance, 'ED1'-'ED4' are linear to fourth-order, ESL displacement-based models, whereas 'LD1'-'LD4' and 'LM1'-'LM4' are linear to fourth-order displacement based and mixed LW models, respectively. ESL mixed models are not considered in the present work. ESL models with Murakami zig-zag function are addressed as EDNZ.

6.4.3 Finite element formulation

The generic unknown $\boldsymbol{a}_{\tau}^{k}$ is expressed in terms of the nodal unknowns $\boldsymbol{q}_{\tau i}^{kT}$ and the shape functions N_i (see Bathe [96]):

$$\boldsymbol{a}_{\tau}^{k}(x,y) = N_i(x,y) \boldsymbol{q}_{\tau i}^{k} \quad i = 1,2,\ldots,N_n \tag{6.81}$$

Via substitution of Eq. 6.81 into Eq. 6.73 (ESL models) or Eqs. 6.76 (LW models), the following expression is obtained:

$$\boldsymbol{a}^{k}(x,y,z) = F_{\tau}(z) N_i(x,y) \boldsymbol{q}_{\tau i}^{k} \tag{6.82}$$

The formulation of RMVT-based elements is addressed in details. Both displacements and transverse shear and normal stresses are modelled as primary unknowns:

$$\boldsymbol{q}^{kT}_{\tau i} = \left\{ \boldsymbol{q}^{kT}_{u\tau i}, \boldsymbol{q}^{kT}_{\sigma\tau i} \right\} = \left\{ \left\{ q^{k}_{u_x\tau i}, q^{k}_{u_y\tau i}, q^{k}_{u_z\tau i} \right\}, \left\{ q^{k}_{\sigma_{zz}\tau i}, q^{k}_{\sigma_{xz}\tau i}, q^{k}_{\sigma_{yz}\tau i} \right\} \right\} \tag{6.83}$$

where $\boldsymbol{q}^{kT}_{u\tau i}$ is the nodal displacements vector and $\boldsymbol{q}^{kT}_{\sigma\tau i}$ is the nodal transverse stresses vector. Due to the finite element (FE) discretisation, the geometrical relations in Eqs. 6.65 read:

$$\begin{aligned} \boldsymbol{\varepsilon}^{k}_{pG} &= F_\tau \boldsymbol{D}_p (N_i \boldsymbol{I}) \boldsymbol{q}^{k}_{u\tau i} \\ \boldsymbol{\varepsilon}^{k}_{nG} &= F_\tau \boldsymbol{D}_{n\Omega} (N_i \boldsymbol{I}) \boldsymbol{q}^{k}_{u\tau i} + F_{\tau,z} N_i \boldsymbol{q}^{k}_{u\tau i} \end{aligned} \tag{6.84}$$

Subscripts preceded by comma represent differentiation. Upon substitution of Eqs. 6.84, 6.82 and 6.70 into Eq. 6.80, the internal virtual work for a k^{th} layer can be rewritten in the following compact form:

$$\delta L^{k}_{i} = \delta \boldsymbol{q}^{kT}_{\tau i} \boldsymbol{K}^{k\tau sij} \boldsymbol{q}^{k}_{sj} \tag{6.85}$$

where $\boldsymbol{K}^{k\tau sij} \in \mathbb{R}^{6\times 6}$ is the fundamental nucleo of the FE stiffness matrix. According to the nodal vector unknowns separation in Eq. 6.83, Eq. 6.85 reads:

$$\delta L^{k}_{i} = \delta \boldsymbol{q}^{kT}_{u\tau i} \left(\boldsymbol{K}^{k\tau sij}_{uu} \boldsymbol{q}^{k}_{usj} + \boldsymbol{K}^{k\tau sij}_{u\sigma} \boldsymbol{q}^{k}_{\sigma sj} \right) + \delta \boldsymbol{q}^{kT}_{\sigma\tau i} \left(\boldsymbol{K}^{k\tau sij}_{\sigma u} \boldsymbol{q}^{k}_{usj} + \boldsymbol{K}^{k\tau sij}_{\sigma\sigma} \boldsymbol{q}^{k}_{\sigma sj} \right) \tag{6.86}$$

where the following arrays in $\mathbb{R}^{3\times 3}$:

$$\begin{aligned} \boldsymbol{K}^{k\tau sij}_{uu} &= \triangleleft \boldsymbol{D}^{T}_{p} \left(N_i \boldsymbol{I} \right) \boldsymbol{Z}^{k\tau s}_{pp} \boldsymbol{D}_{p} \left(N_j \boldsymbol{I} \right) \triangleright_{\Omega_k} \\ \boldsymbol{K}^{k\tau sij}_{u\sigma} &= \triangleleft \boldsymbol{D}^{T}_{p} \left(N_i \boldsymbol{I} \right) \boldsymbol{Z}^{k\tau s}_{pn} \left(N_i \boldsymbol{I} \right) N_j + \boldsymbol{D}^{T}_{n\Omega} \left(N_i \boldsymbol{I} \right) E^{\tau s} N_j + E^{\tau, z s} N_i N_j \boldsymbol{I} \triangleright_{\Omega_k} \\ \boldsymbol{K}^{k\tau sij}_{\sigma u} &= \triangleleft N_i E^{\tau s} \boldsymbol{D}_{n\Omega} \left(N_j \boldsymbol{I} \right) + E^{\tau s, z} N_i N_j \boldsymbol{I} - N_i \boldsymbol{Z}^{k\tau s}_{np} \boldsymbol{D}_{p} \left(N_j \boldsymbol{I} \right) \triangleright_{\Omega_k} \\ \boldsymbol{K}^{k\tau sij}_{\sigma\sigma} &= \triangleleft - N_i \boldsymbol{Z}^{k\tau s}_{nn} N_j \triangleright_{\Omega_k} \end{aligned} \tag{6.87}$$

represent the sub-block components of $\boldsymbol{K}^{k\tau sij}$. Symbol $\triangleleft \ldots \triangleright_{\Omega_k}$ denotes the integral on Ω_k. Subscripts τ and s count the expansion terms along the thickness direction, whereas subscripts i and j range over the element nodes number. The generic term $\boldsymbol{Z}^{k\tau_{(,z)} s_{(,z)}}_{\eta\zeta}$ is a through-the-thickness layer integral accounting for material and geometric stiffness:

$$\begin{aligned} \boldsymbol{Z}^{k\tau_{(,z)} s_{(,z)}}_{\eta\zeta} &= \hat{\boldsymbol{C}}^{k}_{\eta\zeta} E^{\tau_{(,z)} s_{(,z)}} \quad \eta,\zeta = p,n \\ E^{\tau_{(,z)} s_{(,z)}} &= \int_{h_k} F_{\tau_{(,z)}} F_{s_{(,z)}} dz \end{aligned} \tag{6.88}$$

As far as the whole structure is concerned, the FEM problem in the framework of the proposed UF is governed by the following equation:

$$\delta \overline{\boldsymbol{q}}^{k}_{\tau i} : \qquad \overline{\boldsymbol{K}}^{k\tau sij} \overline{\boldsymbol{q}}^{k}_{sj} = \overline{\boldsymbol{P}}^{k}_{\tau i} \tag{6.89}$$

where $\overline{\boldsymbol{K}}^{k\tau sij}$ and $\overline{\boldsymbol{q}}^{k}_{sj}$ are the global FE stiffness matrix and nodal unknowns vector. $\overline{\boldsymbol{P}}^{k}_{\tau i}$ is a loading vector that is variationally coherent to the mechanical model through the external work. In the case of RMVT-based elements, Eq.6.89 reads

$$\begin{aligned} \delta \overline{\boldsymbol{q}}^{kT}_{u\tau i} : \qquad & \overline{\boldsymbol{K}}^{k\tau sij}_{uu} \overline{\boldsymbol{q}}^{k}_{usj} + \overline{\boldsymbol{K}}^{k\tau sij}_{u\sigma} \overline{\boldsymbol{q}}^{k}_{\sigma sj} = \overline{\boldsymbol{P}}^{k}_{u\tau i} \\ \delta \overline{\boldsymbol{q}}^{kT}_{\sigma\tau i} : \qquad & \overline{\boldsymbol{K}}^{k\tau sij}_{\sigma u} \overline{\boldsymbol{q}}^{k}_{usj} + \overline{\boldsymbol{K}}^{k\tau sij}_{\sigma\sigma} \overline{\boldsymbol{q}}^{k}_{\sigma sj} = 0 \end{aligned} \tag{6.90}$$

where the stiffness matrix and the load vector are partitioned according to the separation of primary unknowns in displacements and stresses.

PVD-based elements can be obtained in a similar manner as the RMVT-based ones where $\boldsymbol{q}_{\tau i}^{kT} = \boldsymbol{q}_{u\tau i}^{kT}$ and $\boldsymbol{K}^{k\tau sij} \in \mathbb{R}^{3\times 3}$:

$$\begin{aligned}\boldsymbol{K}^{k\tau sij} = \triangleleft \boldsymbol{D}_p^T \left(N_i \boldsymbol{I}\right) \left[\boldsymbol{Z}_{pp}^{k\tau s} \boldsymbol{D}_p \left(N_j \boldsymbol{I}\right) + \boldsymbol{Z}_{pn}^{k\tau s} \boldsymbol{D}_{n\Omega} \left(N_j \boldsymbol{I}\right) + \boldsymbol{Z}_{pn}^{k\tau s,z} N_j\right] + \\ + \boldsymbol{D}_{n\Omega}^T \left(N_i \boldsymbol{I}\right) \left[\boldsymbol{Z}_{np}^{k\tau s} \boldsymbol{D}_p \left(N_j \boldsymbol{I}\right) + \boldsymbol{Z}_{nn}^{k\tau s} \boldsymbol{D}_{n\Omega} \left(N_j \boldsymbol{I}\right) + \boldsymbol{Z}_{nn}^{k\tau s,z} N_j\right] + \\ + N_i \left[\boldsymbol{Z}_{np}^{k\tau,z s} \boldsymbol{D}_p \left(N_j \boldsymbol{I}\right) + \boldsymbol{Z}_{nn}^{k\tau,z s} \boldsymbol{D}_{n\Omega} \left(N_j \boldsymbol{I}\right) + \boldsymbol{Z}_{nn}^{k\tau,z s,z} N_j\right] \triangleright_{\Omega_k}\end{aligned} \tag{6.91}$$

$\boldsymbol{Z}_{\eta\zeta}^{k\tau_{(,z)} s_{(,z)}}$ is computed using the generalised Hooke's law as in Eqs. 6.67, that is $\boldsymbol{C}_{\eta\zeta}^k$ instead of $\hat{\boldsymbol{C}}_{\eta\zeta}^k$. The FEM problem of the whole structure reads:

$$\delta \overline{\boldsymbol{q}}_{u\tau i}^k : \quad \overline{\boldsymbol{K}}^{k\tau sij} \overline{\boldsymbol{q}}_{usj}^k = \overline{\boldsymbol{P}}_{u\tau i}^k \tag{6.92}$$

Demasi and Carrera [109] presented hybrid RMVT-based elements in which the a-priori assumed stresses are eliminated at element level via a static condensation. Being the primary unknowns only displacements, the element stiffness matrix has the same dimension as the one of a corresponding PVD-based element. In the present work, the full mixed implementation is retained. Linear (with four nodes) and quadratic (with nine nodes) quadrilateral elements are considered in this work. In linear elements one Gauss point, instead of 2×2 Gauss points, is considered in the numerical integration of the shape functions N_i and their derivatives in order to contrast shear locking. There are other numerical integration schemes and techniques to contrast shear locking. Carrera et al. [110] considered some of these in the case of multilayered plates.

6.4.4 Extension to piezoelasticity

Smart structures represent the next generation design in the aerospace industry. Piezoelectric materials are extensively used in this context as sensors and actuators thanks to the so-called direct and inverse effect, respectively. Layers of piezoelectric ceramics can be integrated directly in multilayered plates or can be surface bonded. The analysis and design of such structures is a cumbersome subject. Accurate results requires refined models which are computationally expensive. In the review article by Saravons and Heyliger [111] several laminate theories, analytical solutions and numerical solutions have been taken into account for laminates with piezoelectric actuators or sensors. Benjeddou [112] presented a survey on finite elements for adaptive structural elements. Common assumptions in the formulation of piezoelectric elements, such as through-the-thickness linear variation of the electric potential, have been analysed and their limitations pointed out. Several plate finite elements have been considered, both with and without electric degrees of freedom. In most cases the latter adopt an equivalent single layer model. The piezoelectric effect is included via its equivalent electric load or the converse constitutive equations. Wang and Yang [113] review considers higher order theories in a systematic way, according to the through-the-thickness interpolation of displacement components and electric potential in the plate.

Auricchio, Bisegna and Lovadina [114] developed a finite element for piezoelectric plates based on a Reissner-Mindlin-type modelling. Sheikh, Topdar and Halder [115] proposed a finite element model based on First-order Shear Deformation Theory (FSDT) description for the mechanical part with layer-wise electric potential. Sze, Yang and Fan [116] took into account piecewise constant and piecewise linear assumptions on the spatial distributions of the electric variables. Thornburgh and Chattopadhyay [117] adopted a third order theory to develop a general framework for coupled piezoelectric-mechanical plate problems. Robbins and Chopra [118] examined the effect of the mesh density, the transverse kinematic assumption, the adhesive bond layer thickness and the span-to-thickness ratio on the global response of a plate actuated via piezoelectric patches. Mechanical variable kinematic finite element are adopted, since an induced strain approach is used. A similar analysis in terms of strain energy distribution is carried out by Robbins and Chopra [119]. UF was adopted by Carrera and Nali [120] to derive finite elements with variable kinematic for multifield problems. D'Ottavio and Kroplin [121] presented an extension of Reissner Mixed Variational Theorem (RMVT) to multifield problems, in particular for multilayered structures embedding piezoelectric layers. Carrera and Nali [122] proposed a finite element formulation based on RMVT modified to account for interlaminar continuous transverse electric displacement, named RMVT-D$_z$. A reliable prediction of the transverse electric displacement is necessary for the calculation of the electric charge, which is important for the development of robust control algorithms. A particular form of RMVT (RMVT-D$_z$-$\boldsymbol{\sigma}_n$) was considered by Carrera, Buttner and Nali [123] to a priori fulfil the interlaminar continuity of transverse electromechanical variables.

Constitutive equations

Physical constitutive equations depend on the choice of the variational statement. Three variational statements are considered to obtain the governing equations. In the case of Principle of Virtual Displacement (PVD) the constitutive equations are reported in Eqs. 2.6. They can be rewritten splitting in-plane and out-of-plane components in matrix form:

$$\begin{aligned}
\boldsymbol{\sigma}_p &= \boldsymbol{C}_{pp}\boldsymbol{\varepsilon}_p + \boldsymbol{C}_{pn}\boldsymbol{\varepsilon}_n - \boldsymbol{e}_{pp}^T\boldsymbol{E}_p - \boldsymbol{e}_{np}^T E_n \\
\boldsymbol{\sigma}_n &= \boldsymbol{C}_{pn}^T\boldsymbol{\varepsilon}_p + \boldsymbol{C}_{nn}\boldsymbol{\varepsilon}_n - \boldsymbol{e}_{pn}^T\boldsymbol{E}_p - \boldsymbol{e}_{nn}^T E_n \\
\boldsymbol{D}_p &= \boldsymbol{e}_{pp}\boldsymbol{\varepsilon}_p + \boldsymbol{e}_{pn}\boldsymbol{\varepsilon}_n + \boldsymbol{\epsilon}_{pp}\boldsymbol{E}_p + \boldsymbol{\epsilon}_{pn}E_n \\
D_n &= \boldsymbol{e}_{np}\boldsymbol{\varepsilon}_p + \boldsymbol{e}_{nn}\boldsymbol{\varepsilon}_n + \boldsymbol{\epsilon}_{pn}^T\boldsymbol{E}_p + \epsilon_{nn}E_n
\end{aligned} \tag{6.93}$$

where subscript p stands for in-plane component, n for out-of-plane component. Index k accounting for the layer is dropped for clearness. The following linear relations hold:

$$\begin{aligned}
\boldsymbol{\varepsilon}_p &= \boldsymbol{D}_p\boldsymbol{u} \\
\boldsymbol{\varepsilon}_n &= (\boldsymbol{D}_{n\Omega} + \boldsymbol{D}_{nz})\boldsymbol{u} \\
\boldsymbol{E}_p &= \boldsymbol{D}_{pE}\phi \\
\boldsymbol{E}_n &= \frac{\partial\phi}{\partial z}
\end{aligned} \tag{6.94}$$

$\boldsymbol{u}$ is the vector containing the three components of displacement and ϕ is the electric potential. $\boldsymbol{D}_{pE}$ is the following differential matrix operator:

$$\boldsymbol{D}_{pE} = \begin{bmatrix} \dfrac{\partial}{\partial x} \\ \dfrac{\partial}{\partial y} \end{bmatrix} \tag{6.95}$$

The PVD in the case of electromechanical coupling is:

$$\int_V \left\{ \delta\boldsymbol{\varepsilon}_{pG}^T \boldsymbol{\sigma}_{pH} + \delta\boldsymbol{\varepsilon}_{nG}^T \boldsymbol{\sigma}_{nH} - \delta\boldsymbol{E}_{pG}^T \boldsymbol{D}_{pH} - \delta E_{nG} D_{nH} \right\} dV = \delta L_{ext} \tag{6.96}$$

Primary set of variables contains the three components of displacement and the electric potential. Subscript G stands for a quantity obtained by geometrical relations, H by constitutive relations. δL_{ext} is the expression of the virtual external work that accounts for external loads.

In the case of RMVT-D$_z$ the transverse electric displacement $D_z = D_n$ is assumed in addition to displacements and electric potential. A modified set of constitutive equations must be adopted:

$$\begin{aligned}
\boldsymbol{\sigma}_p &= \left(\boldsymbol{C}_{pp} + \boldsymbol{e}_{np}^T \epsilon_{nn}^{-1} \boldsymbol{e}_{np}\right) \boldsymbol{\varepsilon}_p + \left(\boldsymbol{C}_{pn} + \boldsymbol{e}_{np}^T \epsilon_{nn}^{-1} \boldsymbol{e}_{nn}\right) \boldsymbol{\varepsilon}_n \\
&\quad + \left(-\boldsymbol{e}_{pp}^T + \boldsymbol{e}_{np}^T \epsilon_{nn}^{-1} \boldsymbol{\epsilon}_{pn}^T\right) \boldsymbol{E}_p + \left(-\boldsymbol{e}_{np}^T \epsilon_{nn}^{-1}\right) D_n \\
\boldsymbol{\sigma}_n &= \left(\boldsymbol{C}_{pn}^T + \boldsymbol{e}_{nn}^T \epsilon_{nn}^{-1} \boldsymbol{e}_{np}\right) \boldsymbol{\varepsilon}_p + \left(\boldsymbol{C}_{nn} + \boldsymbol{e}_{nn}^T \epsilon_{nn}^{-1} \boldsymbol{e}_{nn}\right) \boldsymbol{\varepsilon}_n \\
&\quad + \left(-\boldsymbol{e}_{pn}^T + \boldsymbol{e}_{nn}^T \epsilon_{nn}^{-1} \boldsymbol{\epsilon}_{pn}^T\right) \boldsymbol{E}_p + \left(-\boldsymbol{e}_{nn}^T \epsilon_{nn}^{-1}\right) D_n \\
\boldsymbol{D}_p &= \left(\boldsymbol{e}_{pp} + \boldsymbol{\epsilon}_{pn} \epsilon_{nn}^{-1} \boldsymbol{e}_{np}\right) \boldsymbol{\varepsilon}_p + \left(\boldsymbol{e}_{pn} + \boldsymbol{\epsilon}_{pn} \epsilon_{nn}^{-1} \boldsymbol{e}_{nn}\right) \boldsymbol{\varepsilon}_n \\
&\quad + \left(\boldsymbol{\epsilon}_{pp} - \boldsymbol{\epsilon}_{pn} \epsilon_{nn}^{-1} \boldsymbol{\epsilon}_{pn}^T\right) \boldsymbol{E}_p + \left(\boldsymbol{\epsilon}_{pn} \epsilon_{nn}^{-1}\right) D_n \\
E_n &= -\epsilon_{nn}^{-1} \boldsymbol{e}_{np} \boldsymbol{\varepsilon}_p - \epsilon_{nn}^{-1} \boldsymbol{e}_{nn} \boldsymbol{\varepsilon}_n - \epsilon_{nn}^{-1} \boldsymbol{\epsilon}_{pn}^T \boldsymbol{E}_p + \epsilon_{nn}^{-1} D_n
\end{aligned} \tag{6.97}$$

The variational principle reads:

$$\int_V \left\{ \delta\boldsymbol{\varepsilon}_{pG}^T \boldsymbol{\sigma}_{pH} + \delta\boldsymbol{\varepsilon}_{nG}^T \boldsymbol{\sigma}_{nH} - \delta\boldsymbol{E}_{pG}^T \boldsymbol{D}_{pH} - \delta E_{nG} D_{nM} - \delta D_{nM} \left(E_{nG} - E_{nH}\right) \right\} dV = \delta L_{ext} \tag{6.98}$$

Subscript M stands for a quantity modelled as primary variable.

In the case of RMVT-D$_z$-$\boldsymbol{\sigma}_n$, primary set of variables contains transverse stresses $\boldsymbol{\sigma}_n = \{\sigma_{xz}, \sigma_{yz}, \sigma_{zz}\}$ in addition to RMVT-D$_z$ primary variables. The corresponding set of modified constitutive equations is not reported here and can be found in [123]. The variational principle reads:

$$\begin{aligned}
\int_V \Big\{ &\delta\boldsymbol{\varepsilon}_{pG}^T \boldsymbol{\sigma}_{pH} + \delta\boldsymbol{\varepsilon}_{nG}^T \boldsymbol{\sigma}_{nM} - \delta\boldsymbol{E}_{pG}^T \boldsymbol{D}_{pH} - \delta E_{nG} D_{nM} \\
&- \delta D_{nM} \left(E_{nG} - E_{nH}\right) + \delta\sigma_{nM}^T \left(\varepsilon_{nG} - \varepsilon_{nH}\right) \Big\} dV = \delta L_{ext}
\end{aligned} \tag{6.99}$$

Theories

Only LW theories are considered because of the need to impose at layers' interfaces the values of the electric potential in the analyses. A similar imposition with ESL theories would have been possible, but not as direct to implement as with LW theories. In the hierarchical piezoelectric plate thoeries, primary unknowns vector $\boldsymbol{a}_s^k$ is expressed as:

$$\boldsymbol{a}_s^k\,(x,y) = N_j(x,y)\boldsymbol{q}_{sj}^k \quad j = 1,2,\ldots,N_n \tag{6.100}$$

Superscript k stands for the k-th layer, N_j are the shape functions and N_n is the number of nodes for the considered element. $\boldsymbol{q}_{sj}^k$ is the vector of nodal values of primary unknowns. In case of RMVT-D$_z$-$\boldsymbol{\sigma}_n$:

$$\boldsymbol{q}_{sj}^{kT} = \left\{\boldsymbol{q}_{\boldsymbol{u}sj}^{kT},q_{\phi sj}^{kT},q_{D_zsj}^{kT},\boldsymbol{q}_{\boldsymbol{\sigma_n}sj}^{kT}\right\} = \left\{\left\{q_{u_xsj}^k,q_{u_ysj}^k,q_{u_zsj}^k\right\},q_{\phi sj}^k,q_{D_zsj}^{kT},\left\{q_{\sigma_{zz}sj}^k,q_{\sigma_{xz}sj}^k,q_{\sigma_{yz}sj}^k\right\}\right\} \tag{6.101}$$

where subscripts $\boldsymbol{u}$, ϕ, D_z and $\boldsymbol{\sigma_n}$ stand for the respective primary variables. In case of RMVT-D$_z$ $\boldsymbol{q}_{sj}^{kT} = \left\{\boldsymbol{q}_{\boldsymbol{u}sj}^{kT},q_{\phi sj}^k,q_{D_zsj}^{kT}\right\}$, whereas for PVD-based elements $\boldsymbol{q}_{sj}^{kT} = \left\{\boldsymbol{q}_{\boldsymbol{u}sj}^{kT},q_{\phi sj}^k\right\}$. The virtual variation is:

$$\delta\boldsymbol{a}_\tau^k\,(x,y) = N_i(x,y)\delta\boldsymbol{q}_{\tau i}^k \quad i = 1,2,\ldots,N_n \tag{6.102}$$

Variational statement in Eq. (6.96), in Eq. (6.98) or in Eq. (6.99) leads to a set of equilibrium equations that can be put in the form:

$$\delta\boldsymbol{q}_{\tau i}^k : \boldsymbol{K}^{k\tau sij}\boldsymbol{q}_{sj}^k = \boldsymbol{P}_{\tau i}^k \tag{6.103}$$

with the related boundary conditions $\overline{\boldsymbol{B}}^k$. $\boldsymbol{P}_{\tau i}^k$ is the vector of external loads variationally coherent to the the model through the external work. Matrix $\boldsymbol{K}^{k\tau sij}$ is the fundamental nucleus of the stiffness matrix. In case of PVD it is a 4 x 4 array, in case of RMVT-D$_z$ it is a 5 x 5 array, whereas in case of RMVT-D$_z$-$\boldsymbol{\sigma}_n$ it is a 8 x 8 array. The complete derivation of the nuclei can be found in [122, 120, 123]. As far as the whole structure is concerned, the FEM problem in the framework of the proposed UF is governed by the following equations:

$$\overline{\mathbf{K}}^{k\tau sij}\overline{\mathbf{q}}_{sj}^k = \overline{\mathbf{P}}_{\tau i}^k \tag{6.104}$$

Chapter 7

Coupling of mechanical finite elements via the Arlequin method

The mechanics of a structure should be modelled as accurately as possible to achieve an effective design. The drawback of refined beam and plate theories or three-dimensional (3D) analyses is represented by the high number of degress of freedom and, therefore, of the computational cost. The structure to be analysed can be decomposed in several sub-domains that are coupled via computational techniques known as adaptation method or mixed-dimensional methods. Higher order elements or solid elements can be adopted in specific sub-domains of the structure where the stress field is quasi-3D. The remaining sub-domains can be modelled with computationally cheap lower-order beam and plate finite elements. Several numerical methods have been formulated in the last years to couple "refined" and "coarse" sub-domains. In such a manner accurate results can be obtained with a reduced computational cost. In the sequential adaptation methods, structure's sub-domains differ in mesh size (h-adaptation, Bank [124]) or degrees of freedom of the shape functions (p-adaptation, see Szabo and Babuska [125]) or both (hp-adaptation, see Bathe [96]). Mesh size and shape functions are modified according to a sequential approach based on the iteration of analysis and error estimation. In the multi-grid method (see Fish et al. [126]), coarse and fine meshes share information inside an iterative algorithm. In the extended finite element method by Möes [127], the basis of the shape functions is enriched to account for the discontinuity of the displacement field. The previous methods can be addressed as mono-model methods. In the case of multi-models methods, structure's sub-domains differ in the kinematic assumptions, that is, the very numerical models are adapted. In the s-version method (see Fish [128] and Fish and Markolefas [129]), incompatible meshes (different element size and polynomial order) with a local-global border are coupled. Park and Filippa [130] presented a continuum-based variational principle for the formulation of discrete governing equations of partitioned structural systems, including coupled substructures as well as sub-domains obtained by mesh decomposition. In the three field formulation by Brezzi and Marini [131], an additional grid at the interface is introduced. The unknowns are represented independently in each sub-domain and on the

interface, the matching been provided by suitable Lagrange multipliers. A variational approach to couple kinematically incompatible structural models was presented by Blanco et al. [132]. Ben Dhia et al. [133, 134, 135, 136] proposed the Arlequin method. The coupling among different numerical models is obtained through Lagrange multipliers. The coupling among finite elements of different type is presented in this chapter both for mechanical analyses and for piezoelectric analyses. The Arlequin method is adopted and the coupling matrices are written in the framework of the UF.

7.1 The Arlequin method

The volume of the structure (V) is divided into two sub-domains A_1 and A_2 that are partially overlapped. S represents the overlapping volume. For each sub-domain, a different model is assumed. The global mechanical problem is solved by merging together the two sub-domains via the Arlequin method. The internal and external virtual works are computed for each sub-domain. The structural integrity in the overlapping volume is ensured via a Lagrangian multiplier field $(\boldsymbol{\lambda})$ and a coupling operator (C_ξ) that links the degrees of freedom of each sub-domain within the overlapping volume. The PVD in Eq. 6.9 becomes in each sub-domain:

$$\delta L_{int}^{\xi}\left(\mathbf{u}_\xi\right) + \delta L_c^{\xi}\left(\mathbf{u}_\xi\right) = \delta L_{ext}^{\xi} \tag{7.1}$$

ξ is a dummy index that counts the sub-domains. The virtual variation of the strain energy in each sub-domain is:

$$\delta L_{int}^{\xi} = \int_{A_\xi} \alpha_\xi \left(\delta\boldsymbol{\epsilon}^T \boldsymbol{\sigma}\right) dV \quad \text{with} \quad \begin{cases} \alpha_\xi = 1 \text{ in } A_\xi \setminus S \\ \alpha_1 + \alpha_2 = 1 \text{ in } S \end{cases} \tag{7.2}$$

α_ξ are weighting functions for scaling the energy in each sub-domain in order to not consider the energy in the overlapping volume twice. According to Ben Dhia [134], they should be such that the sub-domain with a more accurate description has a higher weight in the global equilibrium. Unless differently stated, a constant value equal to 0.98 is assumed for the sub-domain in which the refined model is adopted. The virtual external work is treated in a similar manner. δL_c^{ξ} is the virtual coupling work:

$$\delta L_c^{\xi} = (-1)^{\xi} C_\xi\left(\delta\boldsymbol{\lambda},\mathbf{u}_\xi\right) \tag{7.3}$$

Two coupling operators are considered (see Ben Dhia and Rateau [135] and Guidault and Belytschko [137]):

- L^2 coupling:

$$\delta C_\xi = \int_{S_\xi} \delta\boldsymbol{\lambda}^T \mathbf{u}_\xi \; dV \tag{7.4}$$

- H^1 coupling:

$$\delta C_\xi = \int_{S_\xi} \left\{\delta\boldsymbol{\lambda}^T \mathbf{u}_\xi + \tilde{l}^2 \delta\boldsymbol{\varepsilon}^T\left(\boldsymbol{\lambda}\right)\boldsymbol{\varepsilon}\left(\mathbf{u}_\xi\right)\right\} \; dV \tag{7.5}$$

$\tilde{l}$ is a real parameter representative of a characteristic length. $\boldsymbol{\varepsilon}(\boldsymbol{\lambda})$ is defined in the same manner as the mechanical strain $\boldsymbol{\varepsilon}(\mathbf{u}_\xi)$ where the Lagrangian multiplier field is used instead of the displacement one. Ben Dhia [136] proved that L^2 coupling operator is meaningless for the continuous Arlequin problem. In the discrete problem, it can be considered as an approximation of a dual Lagrange field linked to a dual continuous Arlequin coupling.

7.2 Beam elements with different order

Arlequin method was adopted by Hu et al. [104, 138] for the linear and non-linear analysis of sandwich beams modelled via one- and two-dimensional finite elements. In this section, beam elements of different order formulated in Sec. 6.3 are coupled via the Arelquin method. The beam volume is axially divided into two sub-domains and that are partially overlapped, see Fig. 7.1. For each sub-domain, a different expansion order is assumed:

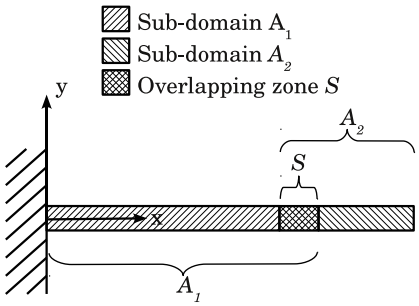

Figure 7.1. Beam structure divided into two overlapping sub-domains.

$$\mathbf{u}_\xi = N_i F_{\tau_\xi} \mathbf{q}_{\tau_\xi i} \quad \text{with} \quad \tau_\xi = 1,2,\ldots,N_u^{A_\xi}, \;\; \xi = 1,2 \tag{7.6}$$

The coupling operators are rewritten as:

- L^2 coupling:

$$\delta C_\xi = \int_{S_\xi} \delta\boldsymbol{\lambda}^T \mathbf{u}_\xi \; dV \tag{7.7}$$

- H^1 coupling:

$$\delta C_\xi = \int_{S_\xi} \left\{ \delta\boldsymbol{\lambda}^T \mathbf{u}_\xi + \tilde{l}^2 \left[\delta\boldsymbol{\varepsilon}_n^T(\boldsymbol{\lambda})\, \boldsymbol{\varepsilon}_n(\mathbf{u}_\xi) + \delta\boldsymbol{\varepsilon}_p^T(\boldsymbol{\lambda})\, \boldsymbol{\varepsilon}_p(\mathbf{u}_\xi) \right] \right\} \; dV \tag{7.8}$$

The Lagrangian multiplier is discretised according to the UF:

$$\boldsymbol{\lambda} = N_i F_{\tau_\lambda} \boldsymbol{\Lambda}_{\tau_\lambda i} \tag{7.9}$$

where $\mathbf{\Lambda}_{\tau_\lambda i}$ is the nodal unknown vector. The fundamental nucleo of the coupling matrix $\mathbf{C}_\xi^{ij\tau_\xi s_\lambda}$ is derived coherently to Eq. 6.57 via substitution of Eq. 7.9 into Eq. 7.7 or 7.8:

$$\delta C_\xi = \delta \mathbf{\Lambda}^T_{\tau_\lambda i} \mathbf{C}_\xi^{\tau_\lambda s_\xi ij} \mathbf{q}_{s_\xi j} \tag{7.10}$$

In the case of L^2 coupling, the fundamental nucleo is diagonal and its components are:

$$C_{\xi mn}^{\tau_\lambda s_\xi ij} = \delta_{nm} I_{ij} J_{\tau_\lambda s_\xi} \quad \text{with} \quad m,n = x,y,z \tag{7.11}$$

where δ_{nm} is Kronecker's delta. Terms I_{ij} have been defined in Eq. 6.59 and:

$$J_{\tau_\xi s_\lambda} = \int_\Omega F_{\tau_\xi} F_{s_\lambda} \, d\Omega \tag{7.12}$$

For the coupling operator H^1, coupling matrix fundamental nucleo can be obtained straightforwardly noticing that H^1 coupling operator is the sum of the L^2 one and a term similar to the virtual internal work in Eq. 6.55. The components of this latter term are those of the stiffness matrix that correspond to the diagonal terms of the constitutive matrices $\tilde{\mathbf{C}}_{pp}$ and $\tilde{\mathbf{C}}_{nn}$:

$$\begin{aligned}
C_{\xi xx}^{\tau_\lambda s_\xi ij} = C_{\xi yy}^{\tau_\lambda s_\xi ij} = C_{\xi zz}^{\tau_\lambda s_\xi ij} &= I_{ij} J_{\tau_\lambda s_\xi} + \tilde{l}^2 \left[I_{i,xj,x} J_{\tau_\lambda s_\xi} + I_{ij} \left(J_{\tau_{\lambda,y} s_{\xi,y}} + J_{\tau_{\lambda,z} s_{\xi,z}} \right) \right] \\
C_{\xi xy}^{\tau_\lambda s_\xi ij} &= \tilde{l}^2 I_{ij,x} J_{\tau_{\lambda,y} s_\xi} \qquad C_{\xi yx}^{\tau_\lambda s_\xi ij} = \tilde{l}^2 I_{i,xj} J_{\tau_\lambda s_{\xi,y}} \\
C_{\xi xz}^{\tau_\lambda s_\xi ij} &= \tilde{l}^2 I_{ij,x} J_{\tau_{\lambda,z} s_\xi} \qquad C_{\xi zx}^{\tau_\lambda s_\xi ij} = \tilde{l}^2 I_{i,xj} J_{\tau_\lambda s_{\xi,z}} \\
C_{\xi yz}^{\tau_\lambda s_\xi ij} &= \tilde{l}^2 I_{ij} J_{\tau_{\lambda,z} s_{\xi,y}} \qquad C_{\xi zy}^{\tau_\lambda s_\xi ij} = \tilde{l}^2 I_{ij} J_{\tau_{\lambda,y} s_{\xi,z}}
\end{aligned} \tag{7.13}$$

where:

$$J_{\tau_{\lambda(,y)(,z)} s_{\xi(,y)(,z)}} = \int_\Omega F_{\tau_{\lambda(,y)(,z)}} F_{s_{\xi(,y)(,z)}} \, d\Omega \tag{7.14}$$

According to Ben Dhia [134] and Guidault and Belytschko [137], the same approximation order should be assumed for the low-order model and the Lagrangian multiplier. This choice avoids a locking phenomenon that arises when the approximation of the more refined model is adopted for the discretisation of the Lagrangian multiplier field. Considering the whole structure and assuming that the refined model is adopted in the sub-domain A_2 (see Fig. 7.1) the governing equations of the variable kinematic problem in the framework of

the proposed unified formulation coupled via the Arlequin method are:

$$\begin{bmatrix} \overline{\mathbf{K}}^{\tau_1 s_1 ij}_{A_1\setminus S} & \mathbf{0} & \mathbf{0} & \mathbf{0} & \mathbf{0} \\ \mathbf{0} & (1-\alpha)\,\overline{\mathbf{K}}^{\tau_1 s_1 ij}_{A_1\cap S} & \mathbf{0} & \mathbf{0} & \overline{\mathbf{C}}_1^{\tau_1 s_1 ijT} \\ \mathbf{0} & \mathbf{0} & \overline{\mathbf{K}}^{\tau_2 s_2 ij}_{A_2\setminus S} & \mathbf{0} & \mathbf{0} \\ \mathbf{0} & \mathbf{0} & \mathbf{0} & \alpha\overline{\mathbf{K}}^{\tau_2 s_2 ij}_{A_2\cap S} & -\overline{\mathbf{C}}_2^{\tau_2 s_1 ijT} \\ \mathbf{0} & \overline{\mathbf{C}}_1^{\tau_1 s_1 ij} & \mathbf{0} & -\overline{\mathbf{C}}_2^{\tau_2 s_1 ij} & \mathbf{0} \end{bmatrix} \begin{Bmatrix} \overline{\mathbf{q}}^{A_1\setminus S}_{s_1 j} \\ \overline{\mathbf{q}}^{A_1\cap S}_{s_1 j} \\ \overline{\mathbf{q}}^{A_2\setminus S}_{s_2 j} \\ \overline{\mathbf{q}}^{A_2\cap S}_{s_2 j} \\ \overline{\mathbf{\Lambda}}_{s_1 j} \end{Bmatrix} = \tag{7.15}$$

$$= \begin{Bmatrix} \overline{\mathbf{P}}^{A_1\setminus S}_{\tau_1 i} \\ (1-\alpha)\,\overline{\mathbf{P}}^{A_1\cap S}_{\tau_1 i} \\ \overline{\mathbf{P}}^{A_2\setminus S}_{\tau_2 i} \\ \alpha\overline{\mathbf{P}}^{A_2\cap S}_{\tau_2 i} \\ 0 \end{Bmatrix}$$

7.2.1 Results and discussion

Analyses are carried out considering a square and a thin-walled I-shaped cross-section. In the latter, the wall thickness is equal to 10% of a main cross-section dimension a equal to 0.2 m. Slender ($l/a = 100$), moderately deep ($l/a = 30$) and deep ($l/a = 10$) beams are accounted for. Beams are simply supported at both ends. They undergo a localised uniform pressure (P) equal to 1 Pa acting on 10% of the length and centred at mid-span. The loading is applied to the top of the cross-section, see Figs. 7.18. Out-of-plane displacement u_x and shear stress component σ_{xy} are evaluated at $x = 0$, whereas in-plane displacement components (u_y and u_z) and normal stresses (σ_{xx}, σ_{yy} and σ_{zz}) are computed at beam mid-span. For each cross-section, the proposed finite elements are first validated towards the corresponding closed form, Navier-type solution (see Carrera and Giunta [91]). For these latter, the localised loading is approximated via a Fourier series expansion. The number of the approximation terms is such that displacement and stress components converge up to three significant digits. Results are also validated towards three-dimensional FEM solutions obtained via the commercial code ABAQUS. For all the analyses, the quadratic C3DR20 element is used (see [63]). As far as a I-shaped cross-section is concerned, FEM models using plate elements are commonly considered as reference solutions in literature. A three-dimensional FEM model has been here considered since plate elements available on commercial FEM codes are generally based on classical Kirchhoff's or Reissner's models and they do not yield the complete three-dimensional stress field. Meshes are such that the maximum displacement components converge up to four significant digits. After validation, elements based on a first- or second-order theory (low-order model) are coupled to those based on a fourth- or a 15^{th}-order one (refined model) via the Arlequin method. Non-conforming meshes are not considered. Two configurations are considered. In the first one, addressed as "Arlequin^a", the refined sub-domain is near the loading application area. For the second configuration (Arlequin^b), the refined sub-domain is near the constraint,

see Figs. 7.2. These configurations have been addressed since load application regions and

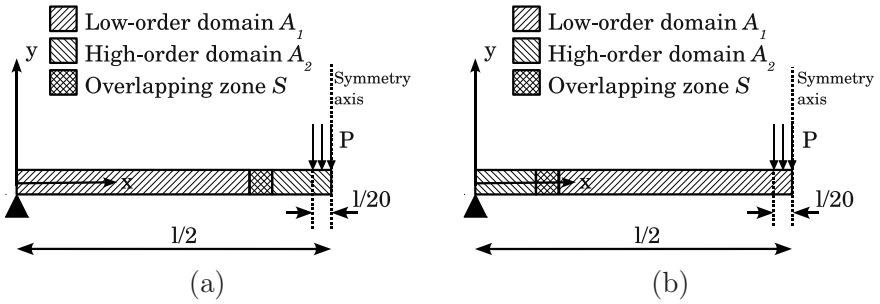

Figure 7.2. Simply supported beams under a localised uniform pressure P. Arlequin model with refined elements near (a) the loading application zone or (b) the constraint.

constrained regions are likely to present a three-dimensional stress field. In the general case in which the location of a three-dimensional stress field cannot be determined a priori, refined sub-domains should be chosen on the basis of experience and preliminary analyses via low-order models. Analyses have been carried out considering both L^2 and H^1 coupling. For this latter, different values of $\tilde{l}$ in Eq. 7.5 have been accounted for. In general, no relevant differences have been found. Unless differently stated, L^2 coupling is, therefore, used. Due to the symmetry of the problem, only half of the structure is investigated and only a superimposition volume is needed, see Figs. 7.18.

Square Cross-Section Beam

Cross-section geometry and loading are shown in Fig. 7.3. The figure presents also the

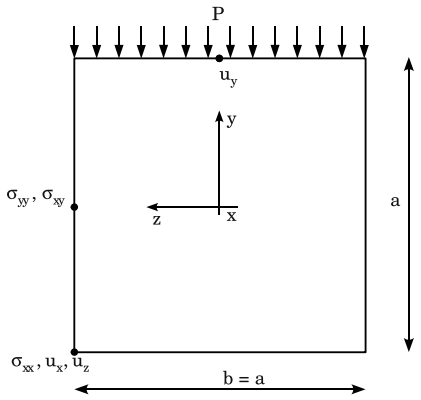

Figure 7.3. Square cross-section geometry, loading and verification points.

points on the cross-section where displacements and stresses are evaluated. Beams are made of an isotropic material whose properties are: Young's modulus (E) equal to 75 GPa

and Poisson's ratio (ν) equal to 0.3. Displacements and stresses are put in a dimensionless form as follows:

$$(\overline{u}_x,\overline{u}_y,\overline{u}_z) = \frac{4Ea}{l^2P}\,(u_x,u_y,u_z) \tag{7.16}$$

$$(\overline{\sigma}_{xx},\overline{\sigma}_{yy},\overline{\sigma}_{xy}) = \frac{1}{P}\,(\sigma_{xx},\sigma_{yy},\sigma_{xy}) \tag{7.17}$$

Table 7.1 presents the displacement components for a slender beam. Results are computed

	$\overline{u}_x$			$10^{-2}\times\overline{u}_y$			$10^{2}\times\overline{u}_z$		
FEM 3D		3.737			2.488			2.125	
UF	B2	B3/4	AS*	B2	B3/4	AS	B2	B3/4	AS
N=3	3.735	3.737	3.737	2.485	2.488	2.488	2.137	2.137	2.137
N=2	3.735	3.737	3.737	2.485	2.488	2.488	2.137	2.137	2.137
N=1	3.736	3.737	3.737	2.485	2.488	2.488	0.000	0.000	0.000
TB	3.735	3.737	3.737	2.485	2.488	2.488	0.000	0.000	0.000
EB	3.735	3.737	3.737	2.484	2.487	2.487	0.000	0.000	0.000

(∗): Analytical UF solution.

Table 7.1. Dimensionless displacements for square cross-section beam, $l/a = 100$.

considering 20 elements of the same length. Bending mechanics is predominant. Classical models, therefore, yield accurate results for $\overline{u}_x$ and $\overline{u}_y$. In order to predict correctly $\overline{u}_z$, a second-order theory is required. Finite element results converge to the analytical solution. Displacement components for the case of a deep beam are presented in Table 7.2. EB

	$10^{1}\times\overline{u}_x$			$\overline{u}_y$			$10^{2}\times\overline{u}_z$		
FEM 3D		3.742			2.544			2.125	
UF	B2	B3/4	AS*	B2	B3/4	AS	B2	B3/4	AS
N=3	3.740	3.741	3.741	2.541	2.544	2.544	2.111	2.113	2.113
N=2	3.734	3.736	3.736	2.531	2.533	2.533	2.099	2.100	2.106
N=1	3.747	3.749	3.749	2.549	2.522	2.522	−0.055	−0.053	−0.053
TB	3.735	3.737	3.737	2.546	2.549	2.549	0.000	0.000	0.000
EB	3.736	3.737	3.737	2.484	2.487	2.487	0.000	0.000	0.000

(∗): Analytical UF solution.

Table 7.2. Dimensionless displacements for square cross-section beam, $l/a = 10$.

model underestimates $\overline{u}_y$ by about 1.2% since it does not account for shear effects. An accurate prediction of $\overline{u}_z$ calls for a second-order theory. Dimensionless stresses for slender and deep beams are reported in Table 7.3 and 7.4, respectively. Stress component $\overline{\sigma}_{xx}$ converges to the analytical solution regardless the number of nodes per element. In the

	$-10^{-3} \times \overline{\sigma}_{xx}$			$\overline{\sigma}_{xy}$			$10^{1} \times \overline{\sigma}_{yy}$		
FEM 3D	1.425			8.583			5.000		
				Analytical UF					
N=4	1.425			8.461			5.000		
N=3	1.425			8.461			4.997		
N=1	1.425			5.000			5.242		
TB	1.425			5.000			–		
EB	1.425			–			–		
				FEM UF					
	B2	B3	B4	B2	B3	B4	B2	B3	B4
N=4	1.412	1.429	1.425	−27.59	20.48	8.461	0.806	4.141	5.578
N=3	1.412	1.429	1.425	−27.59	20.48	8.461	0.722	4.088	5.552
N=1	1.415	1.428	1.425	−31.05	17.01	5.000	2.367	4.349	5.074
TB	1.415	1.428	1.425	−31.05	17.01	5.000	–	–	–
EB	1.415	1.428	1.425	–	–	–	–	–	–

Table 7.3. Dimensionless stresses in the case of beam with square cross-section, $l/a = 100$.

	$-10^{-1} \times \overline{\sigma}_{xx}$			$10^{1} \times \overline{\sigma}_{xy}$			$10^{1} \times \overline{\sigma}_{yy}$		
FEM 3D	1.428			8.595			5.278		
				Analytical UF					
N=4	1.425			8.462			5.208		
N=3	1.432			8.462			5.245		
N=1	1.446			5.000			4.871		
TB	1.425			5.000			–		
EB	1.425			–			–		
				FEM UF					
	B2	B3	B4	B2	B3	B4	B2	B3	B4
N=4	1.410	1.427	1.425	8.100	8.581	8.461	6.015	5.192	5.214
N=3	1.423	1.436	1.432	8.100	8.581	8.461	5.998	5.235	5.250
N=1	1.437	1.450	1.446	4.639	5.120	5.000	5.020	4.865	4.870
TB	1.415	1.428	1.425	4.639	5.120	5.000	–	–	–
EB	1.415	1.428	1.425	–	–	–	–	–	–

Table 7.4. Dimensionless stresses in the case of beam with square cross-section, $l/a = 10$.

case of $\overline{\sigma}_{xy}$ and $\overline{\sigma}_{yy}$, B2 and B3 elements call for a finer mesh. Convergence analysis is presented in Figs. 7.4 and 7.5 for slender and deep beams, respectively. A third-order model is considered. Ten elements are sufficient in the case of B4 elements. Convergence for slender beams is slower than for deep ones. Classical theories correctly predicts only

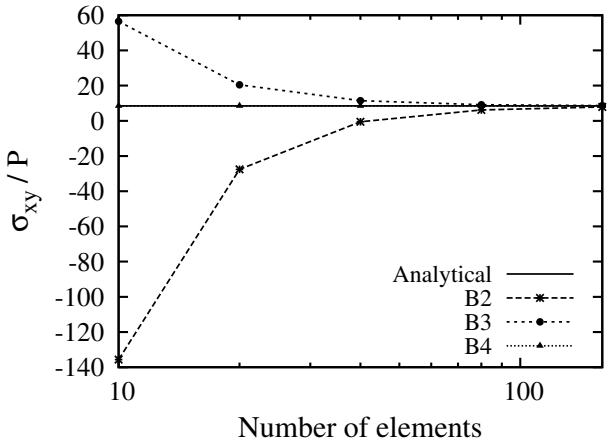

Figure 7.4. Dimensionless stress $\overline{\sigma}_{xy}$ at $x = 0$ versus the number of elements for square cross-section beam, $l/a = 100$, third-order model.

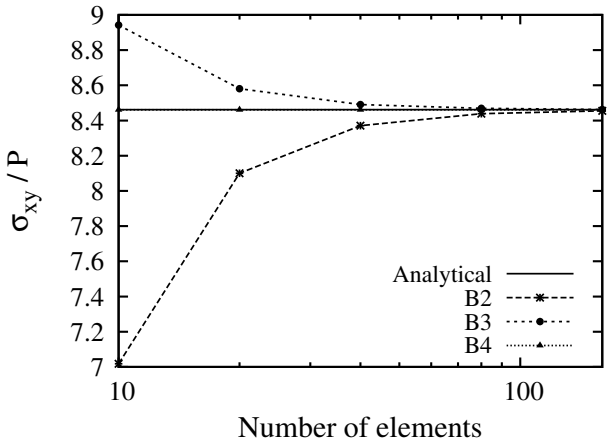

Figure 7.5. Dimensionless stress $\overline{\sigma}_{xy}$ at $x = 0$ versus the number of elements for square cross-section beam, $l/a = 10$, third-order model.

$\overline{\sigma}_{xx}$. An accurate evaluation of $\overline{\sigma}_{xy}$ and $\overline{\sigma}_{yy}$ calls for at least a third-order theory. As far as a variable kinematic solution is concerned, the coarse sub-domain A_1 is meshed via 16 first-order, B4 elements whereas five fourth-order, B4 elements are considered for sub-domain A_2. A superimposed element, whose length is l_{el}, is considered in the overlapping volume. Displacements and stresses for a deep beam are reported in Table 7.5. The total degrees of freedom (DOF) of each solution are also reported there. Results are aligned with those obtained through mono-theories models having the same expansion order, proving the effectiveness of the Arlequin method in coupling domains having finite elements based on theories with different expansion order. The case in which more than one superimposed element is present have been also investigated, but no significant difference has been found.

	$10^1 \times \overline{u}_x$	$\overline{u}_y$	$10^2 \times \overline{u}_z$	$-10^{-1} \times \overline{\sigma}_{xx}$	$10^1 \times \overline{\sigma}_{xy}$	$10^1 \times \overline{\sigma}_{yy}$	DOF*
N=4	3.741	2.544	2.118	1.425	8.461	5.214	2745
N=1	3.749	2.522	−0.053	1.446	5.000	4.870	549
Arlequin[a]	3.729	2.537	2.116	1.424	5.000	5.217	1197
Arlequin[b]	3.716	2.547	−0.056	1.444	8.352	4.807	1197

[a] Refined elements near the loading application zone.
[b] Refined elements near the simply support.
* DOF: degrees of freedom.

Table 7.5. Mono-theories and variable kinematic models, square cross-section beam, $l/a = 10$.

In order to reduce the number of degrees of freedom, the best choice consists in only a superimposed element. A comparison between the considered variable kinematic models and the fourth-order mono-model shows that the total number of degrees of freedom is reduced by more than a half. Figs. 7.6 to 7.8 show the variation along the beam axis of u_y, u_z and σ_{yy}, respectively. Arlequin[a] solution is compared to a model with 20 fourth-order

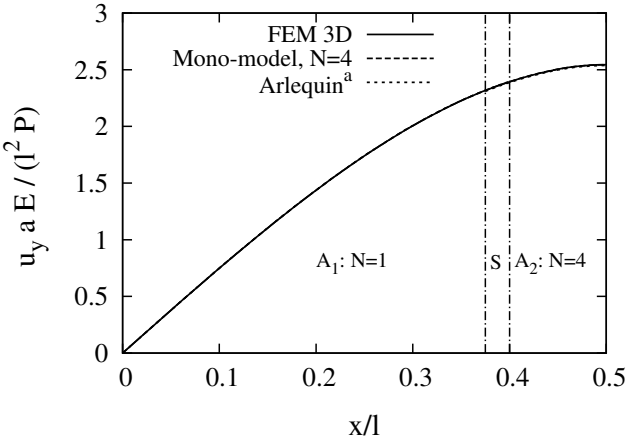

Figure 7.6. Dimensionless displacement $\overline{u}_y$ along the beam axis for square cross-section, $l/a = 10$.

elements (named as "Reference"). In the overlapping volume S, two solutions exist. Their values do not necessarily match. Global bending response u_y is accurately described by both first- and fourth-order models. In the case of u_z, first-order theory does not account for the warping of the section, whereas fourth-order elements match the reference solution. In the case of σ_{yy}, both L^2 and H^1 coupling operators have been accounted for. In the case of H^1 coupling, the parameter $\tilde{l}$ is equal to l_{el}. Results differ slightly in the superimposed volume only. They do not change increasing $\tilde{l}$. H^1 solution converges to the L^2 one decreasing $\tilde{l}$. As far as the sensitivity of the Arlequin method upon the weighting functions α_ξ in Eq. 7.2 is concerned, Fig. 7.9 presents the influence of α_2 on σ_{yy}. α_2 influences the solution in the coupling domain. Increasing α_2, σ_{yy} becomes smoother and smoother since

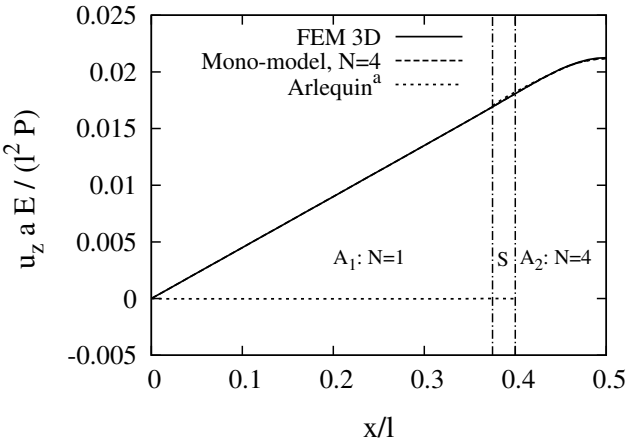

Figure 7.7. Dimensionless displacement $\overline{u}_z$ along the beam axis for square cross-section, $l/a = 10$.

the refined model assumes more and more relevance. Outside the coupling domain, α_2 does not affect the solution. A qualitatively comparison of the stress component $\overline{\sigma}_{xy}$ via three-dimensional FEM solution, fourth-order model and Arlequin^b solution is presented in Fig. 7.10 in the form of colour maps above the cross-section. Results are in good agreement.

I-Shaped Cross-Section Beam

Fig. 7.11 presents the geometry of the considered I-shaped cross-section, loading and verification points. Beam is made of an isotropic material whose Young's modulus is equal to 75 GPa and whose Poisson's ratio is equal to 0.3. A moderately deep beam $l/a = 30$ is considered. Displacements are put in a dimensionless form according to Eqs. 7.16. Stress components σ_{xx}, σ_{yy}, σ_{zz} and σ_{xy} are normalised towards the loading amplitude P. An expansion order as high as 15 is accounted for. Table 7.6 shows the displacement components. Results are computed considering 20 elements. They converge to the analytical solution. Displacement $\overline{u}_x$ is accurately modelled by classical theories. $\overline{u}_y$ predicted via a fourth-order model differs from the reference solution by about 0.3%. Component $\overline{u}_z$ is due to the localised loading and an accurate prediction calls for high-order theories. Fourth-order model underestimates it by about 20%, whereas the difference is about 4% in the case of a 15^{th}-order theory. Dimensionless stresses are reported in Tables 7.7 and 7.8.

Classical models yield the same value for $\overline{\sigma}^I_{xx}$ and $\overline{\sigma}^{II}_{xx}$, being the error about 1.4 and 6%, respectively. $\overline{\sigma}^I_{xx}$ is accurately predicted for N as low as three. $\overline{\sigma}^{II}_{xx}$ evaluated via a 15^{th}-order model differs from the reference solution by about 2%. Stress components $\overline{\sigma}_{xy}$, $\overline{\sigma}_{zz}$ and $\overline{\sigma}_{yy}$ call for higher-order models, being the error in the case of a 15^{th}-order theory about 2.2, 6.2 and 10%, respectively. A more accurate description of normal stress components can be obtained via a localised modelling approach, that is, displacements are approximated in each cross-section subdomain by polynomial functions, such as Lagrange's

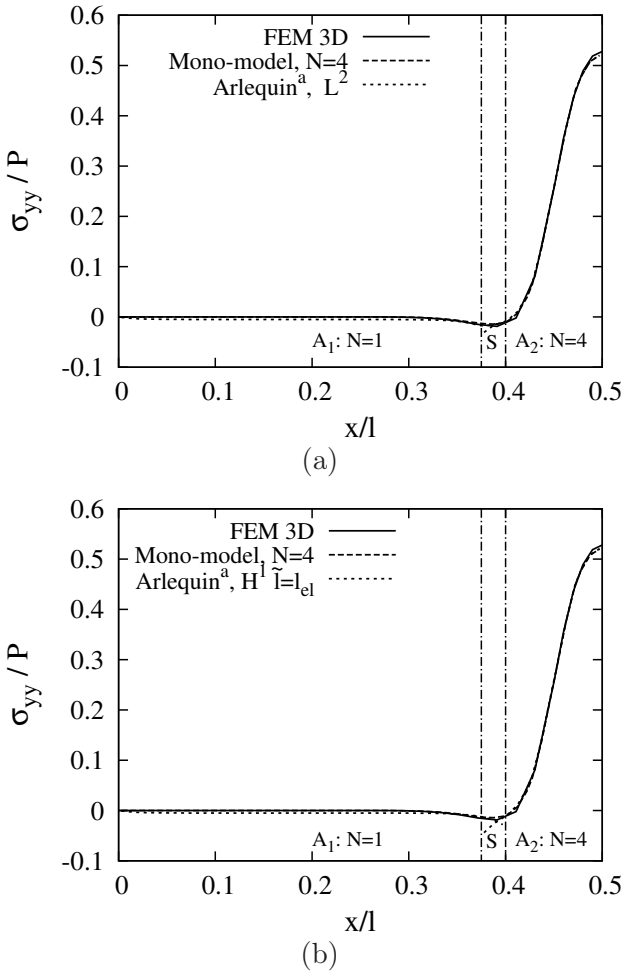

Figure 7.8. Dimensionless stress $\overline{\sigma}_{yy}$ along the beam axis for square cross-section, $l/a = 10$, via (a) L^2 coupling and (b) H^1 coupling with $\tilde{l} = l_{el}$.

or Legendre's, that ensure the congruency of the displacement fields within subdomains' shared borders. This will be matter of future investigations. Results computed via the Arlequin method are reported in Table 7.9. Unless differently stated, the coarse sub-domain A_1 is meshed via 16 second-order, B4 elements whereas five 15^{th}-order, B4 elements are considered for sub-domain A_2. The Arlequin method proves to be effective in merging sub-domains having different finite elements. The total number of degrees of freedom in the analysis is reduced to less than a third. The variation of $\overline{u}_z$ along the beam axis is presented in Fig. 7.12. The coupling operators are compared in Fig. 7.13. Results differ significantly in the superimposed volume and in its neighbourhood increasing $\tilde{l}$, Solutions become coincident moving away from the the coupling domain. Fig 7.14 shows the deformed section at mid-span. The deformed section computed via mono-model 15^{th}-order theory and the variable kinematic model differ mainly by a rigid translation. Arlequin

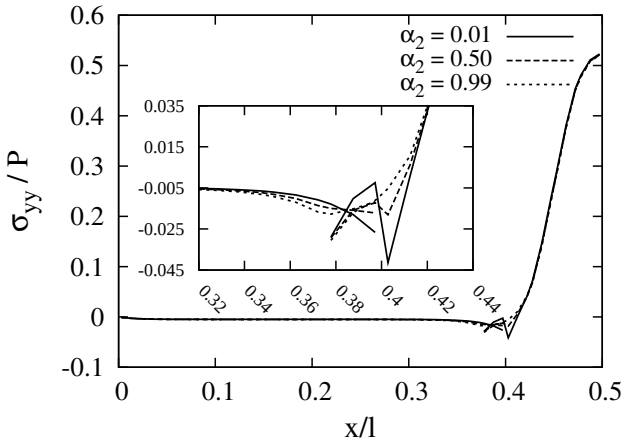

Figure 7.9. Dimensionless stress $\overline{\sigma}_{yy}$ along the beam axis varying α_2, square cross-section, $l/a = 10$.

	$-\overline{u}_x$			$10^{-1} \times \overline{u}_y$			$-10^2 \times \overline{u}_z$			
FEM 3D		2.082			4.233			5.216		
UF	B2	B3/B4	AS*	B2	B3/B4	AS	B2	B3	B4	AS
N=15	2.072	2.073	2.078	4.226	4.231	4.231	5.062	4.987	4.992	4.993
N=11	2.072	2.073	2.078	4.224	4.228	4.228	4.916	4.855	4.859	4.860
N=7	2.072	2.073	2.078	4.219	4.223	4.224	4.532	4.505	4.509	4.509
N=4	2.072	2.073	2.078	4.206	4.211	4.211	4.175	4.177	4.176	4.176
N=3	2.072	2.073	2.078	4.206	4.211	4.211	4.047	4.050	4.050	4.050
N=2	2.072	2.073	2.078	4.169	4.174	4.174	4.002	4.004	4.003	4.003
N=1	2.072	2.072	2.078	4.169	4.174	4.174	0.026	0.024	0.024	0.024
TB	2.073	2.074	2.079	4.169	4.174	4.174	0.000	0.000	0.000	0.000
EB	2.073	2.074	2.079	4.147	4.152	4.152	0.000	0.000	0.000	0.000

(∗): Analytical UF solution.

Table 7.6. Dimensionless displacements for I-shaped cross-section beam, $l/a = 30$.

method captures local phenomena such as the absolute value of $\overline{u}_z$ and the variation of $\overline{u}_y$ along z axis, responsible for the shape of the deformed section. If a quantity in the high-order part of the model strongly depends upon its value in the low-order part where it is not correctly modelled, the inaccuracy propagates from the low- to the high-order part. This is the case of the absolute value of $\overline{u}_y$ that is responsible for the position of the deformed section. A qualitatively comparison of the stress component $\overline{\sigma}_{yy}$ among three-dimensional reference solution, fourth-order model with 20 B4 elements and Arlequin-based solution linking first- and fourth-order models is presented in Fig. 7.10. Beam finite element models are not able to predict stress concentration. Results are in good agreement except near internal corners. Fig. 7.16 shows the variation of $\overline{\sigma}_{xy}$ along the beam axis. The oscillations in the coupling zone yield small oscillations in its neighbourhood. They depend upon the

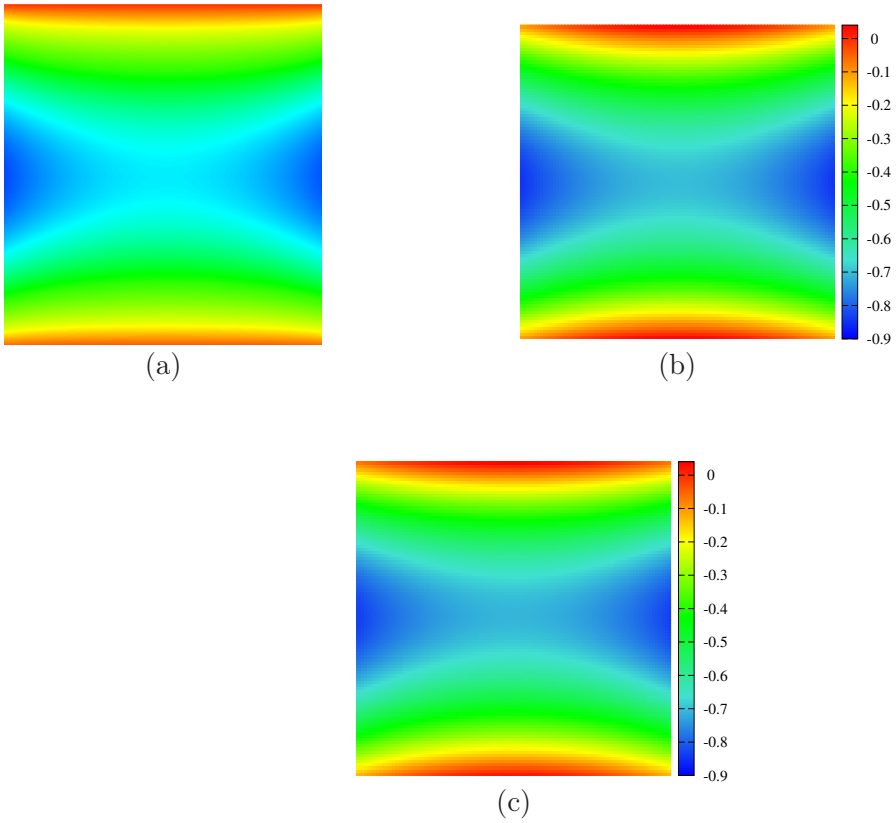

Figure 7.10. Dimensionless stress $\overline{\sigma}_{xy}$ above the cross-section at $x = 0$ via (a) FEM 3D solution, (b) fourth-order model and (c) Arlequin-based solution, $l/a = 10$.

coupling operator as shown in Fig. 7.17. H^1 coupling operator yields a smoother solution. Nevertheless, high values of $\tilde{l}$ cause a loss of accuracy.

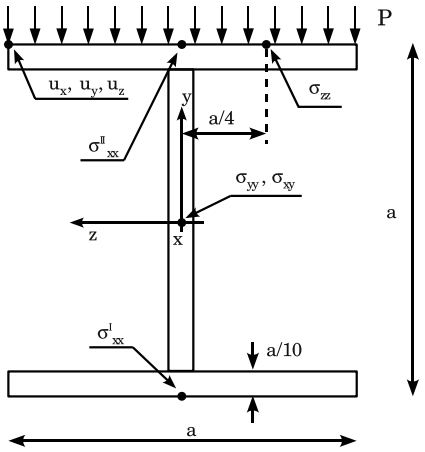

Figure 7.11. I-shaped cross-section geometry, loading and verification points.

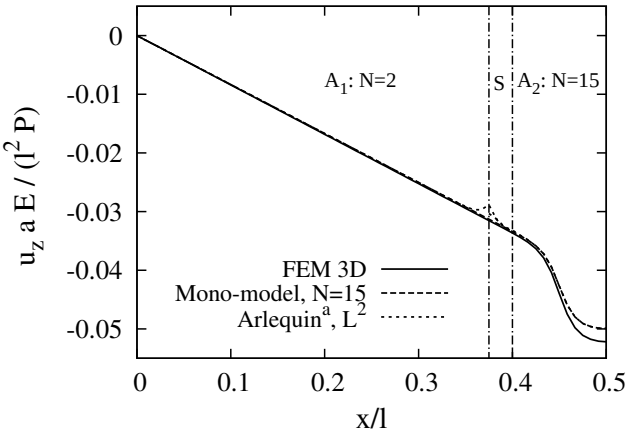

Figure 7.12. Dimensionless displacement $\overline{u}_z$ along the axis of the beam, I-shaped cross–section beam, $l/a = 30$, via L^2 coupling.

	$-10^{-2} \times \overline{\sigma}^{I}_{xx}$			$10^{-2} \times \overline{\sigma}^{II}_{xx}$			$10^{-1} \times \overline{\sigma}_{xy}$		
FEM 3D	2.412			2.244			1.769		
				Analytical UF					
N=15	2.411			2.298			1.727		
N=11	2.412			2.322			1.817		
N=7	2.415			2.351			1.651		
N=4	2.397			2.368			1.974		
N=3	2.419			2.389			1.974		
N=2	2.378			2.378			0.555		
N=1	2.386			2.370			0.535		
TB	2.378			2.378			0.535		
EB	2.378			2.378			–		
				FEM UF					
	B2	B3	B4	B2	B3	B4	B2	B3	B4
N=15	2.390	2.419	2.411	2.274	2.301	2.294	1.546	1.787	1.727
N=11	2.391	2.420	2.412	2.298	2.325	2.318	1.636	1.877	1.817
N=7	2.394	2.422	2.414	2.331	2.355	2.349	1.470	1.711	1.651
N=4	2.375	2.405	2.397	2.348	2.373	2.367	1.793	2.034	1.974
N=3	2.396	2.427	2.419	2.367	2.394	2.389	1.793	2.034	1.974
N=2	2.357	2.384	2.378	2.354	2.385	2.378	0.374	0.615	0.555
N=1	2.371	2.391	2.386	2.354	2.375	2.370	0.355	0.595	0.535
TB	2.362	2.383	2.378	2.362	2.383	2.378	0.355	0.595	0.535
EB	2.362	2.383	2.378	2.362	2.383	2.378	–	–	–

Table 7.7. Dimensionless stresses $\overline{\sigma}_{xx}$ and $\overline{\sigma}_{xy}$ in the case of beam with I-shaped cross-section, $l/a = 30$.

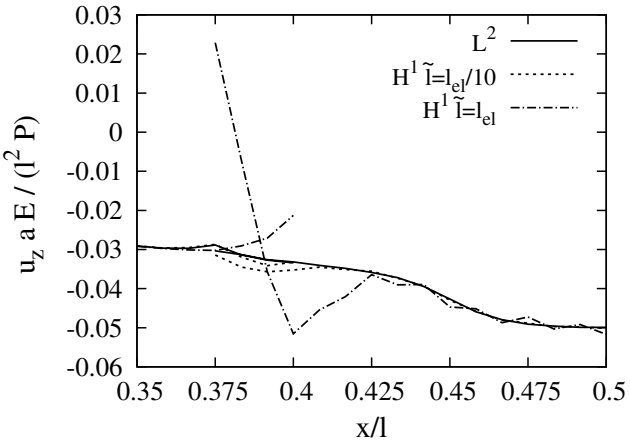

Figure 7.13. Coupling operators comparison for dimensionless displacement $\overline{u}_z$ along the axis of the beam, I-shaped cross-section beam, $l/a = 30$.

	$10^{-1} \times \overline{\sigma}_{zz}$			$\overline{\sigma}_{yy}$		
FEM 3D	1.868			5.090		
	Analytical UF					
N=15	1.950			4.565		
N=11	2.076			4.073		
N=7	1.100			4.156		
N=4	0.474			5.771		
N=3	0.099			5.738		
N=2	0.002			1.788		
N=1	0.044			1.865		
	FEM UF					
	B2	B3	B4	B2	B3	B4
N=15	2.227	1.938	1.985	4.801	4.569	4.557
N=11	2.384	2.061	2.110	4.146	4.067	4.062
N=7	1.257	1.096	1.128	4.471	4.128	4.150
N=4	0.564	0.467	0.485	5.111	5.953	5.806
N=3	0.203	0.084	0.103	5.704	5.785	5.762
N=2	0.115	−0.022	0.003	1.565	1.779	1.785
N=1	0.046	0.044	0.044	1.802	1.858	1.865

Table 7.8. Dimensionless stresses $\overline{\sigma}_{yy}$ and $\overline{\sigma}_{zz}$ in the case of beam with I-shaped cross-section, $l/a = 30$.

	$-\overline{u}_x$	$10^{-1} \times \overline{u}_y$	$-10^2 \times \overline{u}_z$	$10^{-2} \times \overline{\sigma}_{xx}^{11}$	$10^{-1} \times \overline{\sigma}_{xy}$	$\overline{\sigma}_{yy}$	$10^{-1} \times \overline{\sigma}_{zz}$	DOF*
N=15	2.073	4.231	4.992	2.294	1.727	4.557	1.985	24888
N=2	2.073	4.174	4.003	2.378	0.555	1.785	0.003	1098
Arlequin[a]	2.079	4.192	4.990	2.297	0.555	4.563	1.949	7482
Arlequin[b]	2.079	4.188	4.004	2.378	1.725	1.725	0.003	7482

[a] Refined elements near the loading application zone.

[b] Refined elements near the simply support.

* DOF: degrees of freedom.

Table 7.9. Results with the Arlequin method compared to mono-theories models. I-shaped cross-section beam, $l/a = 30$.

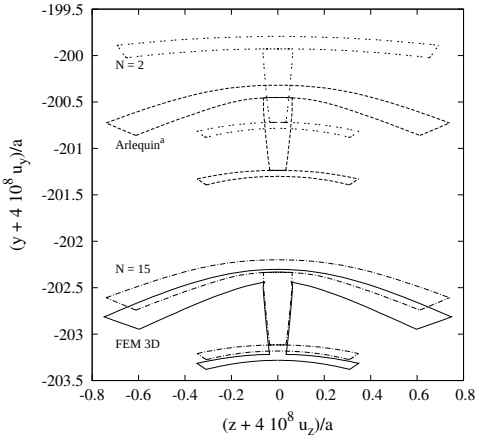

Figure 7.14. Deformed cross-section at mid-span in the case of I-shaped cross-section beam, $l/a = 30$.

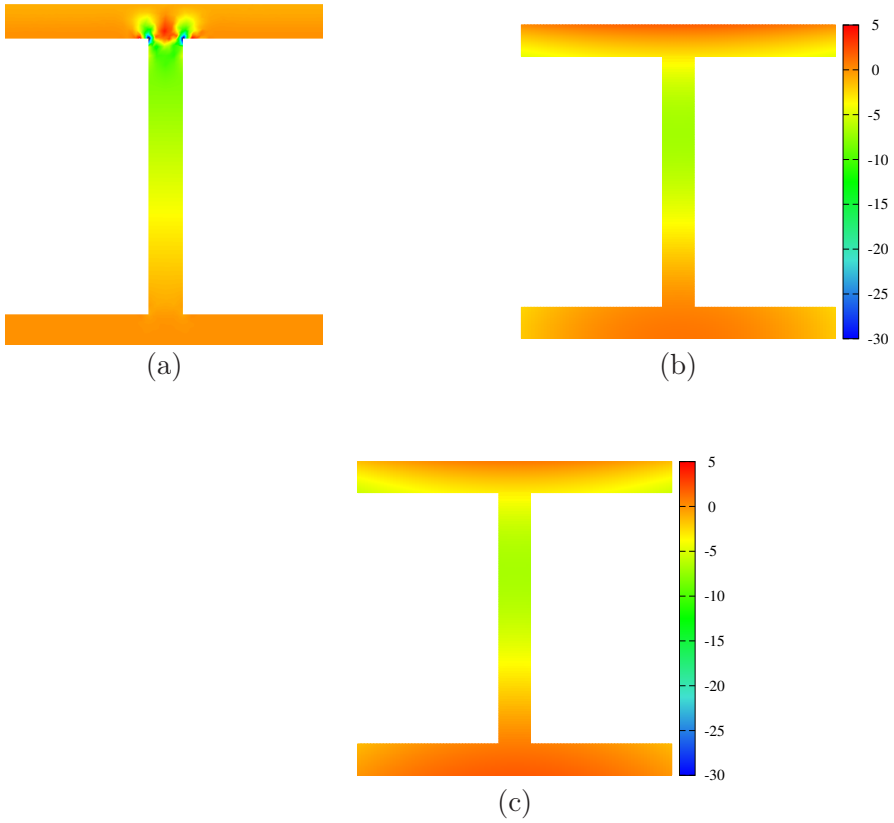

Figure 7.15. Dimensionless stress $\overline{\sigma}_{yy}$ above the mid-span cross section via (a) FEM 3D solution, (b) fourth-order model and (c) Arlequin-based solution linking first- and fourth-order models, $l/a = 30$.

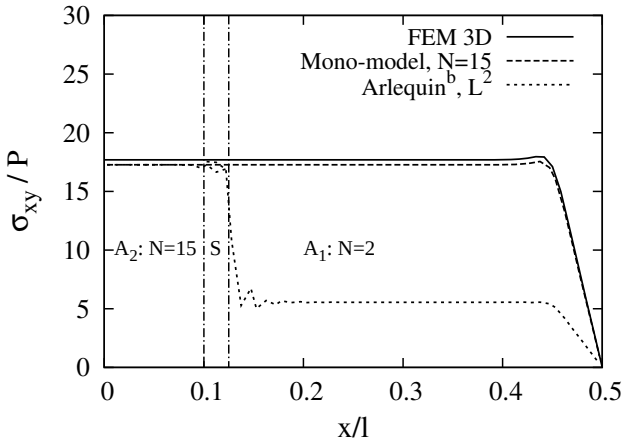

Figure 7.16. Dimensionless stress $\overline{\sigma}_{xy}$ along the axis of the beam, I-shaped cross-section beam, $l/a = 30$, via L^2 coupling.

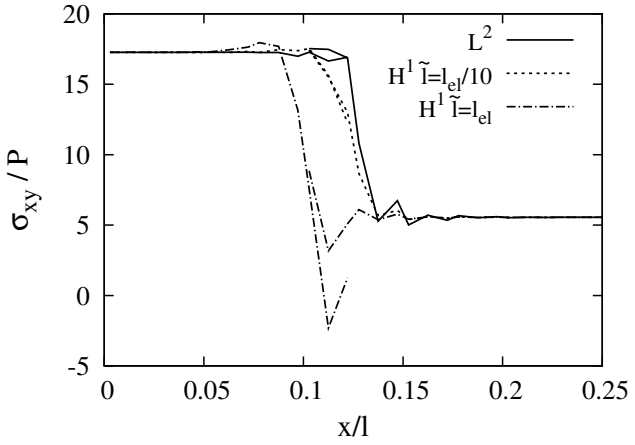

Figure 7.17. Coupling operators comparison for dimensionless stress $\overline{\sigma}_{xy}$ along the axis of the beam, I-shaped cross-section beam, $l/a = 30$.

7.3 Plate elements with different kinematic and variational principle

Reddy and Robbins [102] and Reddy [93] presented a multi-model method based on a variable kinematic theory and on mesh superposition in the sense of Fish [126] and Fish and Markolefas [129]. Coupling is obtained by linking the FSDT variables, which are present in all the considered models, without using Lagrangian multipliers. In contrast with the Arlequin method, total superposition is required in the case of non-conforming meshes. In this section, the plate elements based on different kinematics and variational principles presented in Sec. 6.4 are coupled via the Arelquin method. Plate's volume is divided into two sub-domains that are partially overlapped as shown in Fig. 7.18. For each

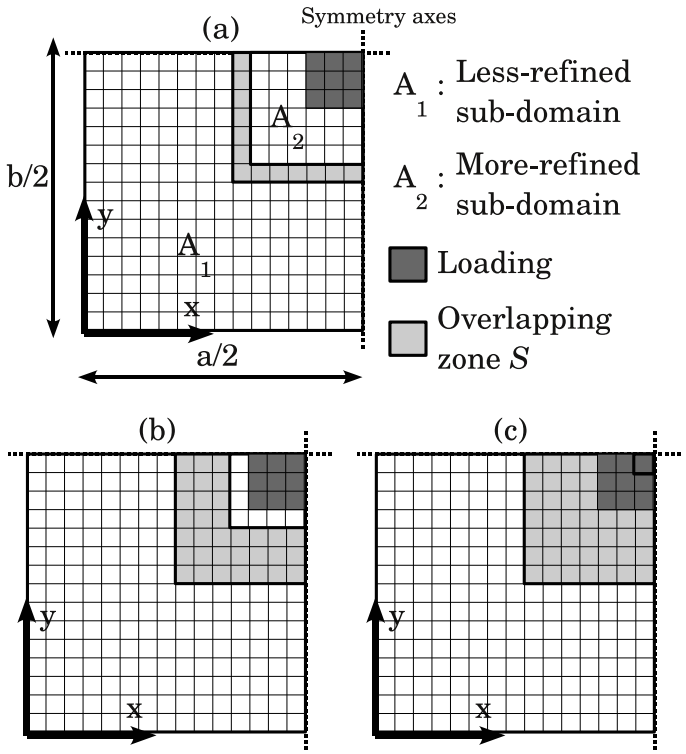

Figure 7.18. Plate mesh, loading and sub-domains considering several superimposition zones: (a) minimum S^a, (b) reduced S^b and (c) extended S^c.

sub-domain, a different model is assumed:

$$\boldsymbol{a}_\xi^k = N_i F_{\tau_\xi} \boldsymbol{q}_{\tau_\xi i}^k \quad \text{with} \quad \tau_\xi = 1,2,\ldots,N_u^{A_\xi}, \;\; \xi = 1,2 \tag{7.18}$$

The two coupling operators are rewritten as:

- L^2 coupling:

$$\delta C_\xi^k = \int_{S_\xi^k} \delta \boldsymbol{\lambda}^{kT} \boldsymbol{u}_\xi^k \, dV_k \tag{7.19}$$

- H^1 coupling:

$$\delta C_\xi^k = \int_{S_\xi^k} \left\{ \delta \boldsymbol{\lambda}^{kT} \boldsymbol{u}_\xi^k + \tilde{l}^2 \left[\boldsymbol{\varepsilon}_{pG}^{kT} \left(\delta \boldsymbol{\lambda}^k \right) \boldsymbol{\varepsilon}_{pG}^k \left(\boldsymbol{u}_\xi^k \right) + \boldsymbol{\varepsilon}_{nG}^{kT} \left(\delta \boldsymbol{\lambda}^k \right) \boldsymbol{\varepsilon}_{nG}^k \left(\boldsymbol{u}_\xi^k \right) \right] \right\} \, dV_k \tag{7.20}$$

The Lagrangian multiplier field is discretised according to the UF:

$$\boldsymbol{\lambda}^k = N_i F_{\tau_\lambda} \boldsymbol{\Lambda}_{\tau_\lambda i}^k \tag{7.21}$$

where $\boldsymbol{\Lambda}_{\tau_\lambda i}^k$ is the nodal unknown vector. The virtual work for a k^{th} layer is derived coherently to Eq. 6.85 via substitution of Eq. 7.21 into Eq. 7.19 or 7.20:

$$\delta C_\xi^k = \delta \boldsymbol{\Lambda}_{\tau_\lambda i}^{kT} \mathbf{C}_\xi^{k\tau_\lambda s_\xi ij} \boldsymbol{q}_{us_\xi j}^k \tag{7.22}$$

$\mathbf{C}_\xi^{k\tau_\lambda s_\xi ij}$ is the fundamental nucleo of the coupling matrix. In the case of L^2 coupling, this is diagonal and its components are:

$$C_{\xi mn}^{k\tau_\lambda s_\xi ij} = \delta_{mn} E_{\tau_\lambda s_\xi}^k \lhd N_i N_j \rhd_\Omega \quad \text{with} \quad m,n = 1,2,3 \tag{7.23}$$

where δ_{mn} is Kronecker's delta. Terms $E_{\tau_\lambda s_\xi}^k$ are defined as:

$$E_{\tau_\lambda s_\xi}^k = \int_{h_k} F_{\tau_\lambda} F_{s_\xi} \, dz \tag{7.24}$$

For the coupling operator H^1, coupling matrix fundamental nucleo is:

$$\begin{aligned}
C_{11}^{k\tau_\lambda s_\xi ij} &= C_{22}^{k\tau_\lambda s_\xi ij} = C_{33}^{k\tau_\lambda s_\xi ij} = E_{\tau_\lambda s_\xi}^k \lhd N_i N_j \rhd_\Omega + \\
&+ \tilde{l}^2 \left[E_{\tau_\lambda s_\xi}^k \left(\lhd N_{i,x} N_{j,x} \rhd_\Omega + \lhd N_{i,y} N_{j,y} \rhd_\Omega \right) + E_{\tau_{\lambda,z} s_{\xi,z}}^k \lhd N_i N_j \rhd_\Omega \right] \\
C_{12}^{k\tau_\lambda s_\xi ij} &= \tilde{l}^2 E_{\tau_\lambda s_\xi}^k \lhd N_{i,y} N_{j,x} \rhd_\Omega \quad C_{13}^{k\tau_\lambda s_\xi ij} = \tilde{l}^2 E_{\tau_{\lambda,z} s_\xi}^k \lhd N_i N_{j,x} \rhd_\Omega \\
C_{21}^{k\tau_\lambda s_\xi ij} &= \tilde{l}^2 E_{\tau_\lambda s_\xi}^k \lhd N_{i,x} N_{j,y} \rhd_\Omega \quad C_{23}^{k\tau_\lambda s_\xi ij} = \tilde{l}^2 E_{\tau_{\lambda,z} s_\xi}^k \lhd N_i N_{j,y} \rhd_\Omega \\
C_{31}^{k\tau_\lambda s_\xi ij} &= \tilde{l}^2 E_{\tau_\lambda s_{\xi,z}}^k \lhd N_{i,x} N_j \rhd_\Omega \quad C_{32}^{k\tau_\lambda s_\xi ij} = \tilde{l}^2 E_{\tau_\lambda s_{\xi,z}}^k \lhd N_{i,y} N_j \rhd_\Omega
\end{aligned} \tag{7.25}$$

where:

$$E_{\tau_{\lambda(,y)(,z)} s_{\xi(,y)(,z)}}^k = \int_{h_k} F_{\tau_{\lambda(,y)(,z)}} F_{s_{\xi(,y)(,z)}} \, dz \tag{7.26}$$

Coupling matrices are not affected by shear locking: full integration is adopted for the Lagrange multiplier shape functions N_i and their derivatives. The same approximation order

should be assumed for the low-order model and the Lagrangian multiplier. Considering the whole structure and assuming that the refined model is adopted in the sub-domain A_2, the governing equations of the variable kinematic problem are:

$$\begin{bmatrix} \overline{\boldsymbol{K}}^{\tau_1 s_1 ij}_{A_1\setminus S} & \mathbf{0} & \mathbf{0} & \mathbf{0} & \mathbf{0} \\ \mathbf{0} & (1-\alpha)\,\overline{\boldsymbol{K}}^{\tau_1 s_1 ij}_{A_1\cap S} & \mathbf{0} & \mathbf{0} & \overline{\mathbf{C}}_1^{\tau_1 s_1 ijT} \\ \mathbf{0} & \mathbf{0} & \overline{\boldsymbol{K}}^{\tau_2 s_2 ij}_{A_2\setminus S} & \mathbf{0} & \mathbf{0} \\ \mathbf{0} & \mathbf{0} & \mathbf{0} & \alpha\overline{\boldsymbol{K}}^{\tau_2 s_2 ij}_{A_2\cap S} & -\overline{\mathbf{C}}_2^{\tau_2 s_1 ijT} \\ \mathbf{0} & \overline{\mathbf{C}}_1^{\tau_1 s_1 ij} & \mathbf{0} & -\overline{\mathbf{C}}_2^{\tau_2 s_1 ij} & \mathbf{0} \end{bmatrix} \begin{Bmatrix} \overline{\boldsymbol{q}}^{A_1\setminus S}_{s_1 j} \\ \overline{\boldsymbol{q}}^{A_1\cap S}_{s_1 j} \\ \overline{\boldsymbol{q}}^{A_2\setminus S}_{s_2 j} \\ \overline{\boldsymbol{q}}^{A_2\cap S}_{s_2 j} \\ \overline{\boldsymbol{\Lambda}}_{s_\lambda j} \end{Bmatrix} = \begin{Bmatrix} \overline{\boldsymbol{P}}^{A_1\setminus S}_{\tau_1 i} \\ (1-\alpha)\,\overline{\boldsymbol{P}}^{A_1\cap S}_{\tau_1 i} \\ \overline{\boldsymbol{P}}^{A_2\setminus S}_{\tau_2 i} \\ \alpha\overline{\boldsymbol{P}}^{A_2\cap S}_{\tau_2 i} \\ 0 \end{Bmatrix} \tag{7.27}$$

where overlined terms refer to the whole structure. Assuming that a refined RMVT-based model is adopted in the sub-domain A_2, whereas sub-domain A_1 is modelled via PVD-based elements, Eq. 7.27 is rewritten as:

$$\begin{bmatrix} \overline{\boldsymbol{K}}^{\tau_1 s_1 ij}_{A_1\setminus S} & \mathbf{0} & \mathbf{0} & \mathbf{0} & \mathbf{0} & \mathbf{0} & \mathbf{0} \\ \mathbf{0} & (1-\alpha)\,\overline{\boldsymbol{K}}^{\tau_1 s_1 ij}_{A_1\cap S} & \mathbf{0} & \mathbf{0} & \mathbf{0} & \mathbf{0} & \overline{\mathbf{C}}_1^{\tau_1 s_1 ijT} \\ \mathbf{0} & \mathbf{0} & \overline{\boldsymbol{K}}^{\tau_2 s_2 ij}_{uuA_2\setminus S} & \overline{\boldsymbol{K}}^{\tau_2 s_2 ij}_{u\sigma A_2\setminus S} & \mathbf{0} & \mathbf{0} & \mathbf{0} \\ \mathbf{0} & \mathbf{0} & \overline{\boldsymbol{K}}^{\tau_2 s_2 ij}_{\sigma uA_2\setminus S} & \overline{\boldsymbol{K}}^{\tau_2 s_2 ij}_{\sigma\sigma A_2\setminus S} & \mathbf{0} & \mathbf{0} & \mathbf{0} \\ \mathbf{0} & \mathbf{0} & \mathbf{0} & \mathbf{0} & \alpha\overline{\boldsymbol{K}}^{\tau_2 s_2 ij}_{uuA_2\cap S} & \alpha\overline{\boldsymbol{K}}^{\tau_2 s_2 ij}_{u\sigma A_2\cap S} & -\overline{\mathbf{C}}_2^{\tau_2 s_1 ijT} \\ \mathbf{0} & \mathbf{0} & \mathbf{0} & \mathbf{0} & \alpha\overline{\boldsymbol{K}}^{\tau_2 s_2 ij}_{\sigma uA_2\cap S} & \alpha\overline{\boldsymbol{K}}^{\tau_2 s_2 ij}_{\sigma\sigma A_2\cap S} & \mathbf{0} \\ \mathbf{0} & \overline{\mathbf{C}}_1^{\tau_1 s_1 ij} & \mathbf{0} & \mathbf{0} & -\overline{\mathbf{C}}_2^{\tau_2 s_1 ij} & \mathbf{0} & \mathbf{0} \end{bmatrix}$$

$$\begin{Bmatrix} \overline{\boldsymbol{q}}^{A_1\setminus S}_{s_1 j} \\ \overline{\boldsymbol{q}}^{A_1\cap S}_{s_1 j} \\ \overline{\boldsymbol{q}}^{A_2\setminus S}_{us_2 j} \\ \overline{\boldsymbol{q}}^{A_2\setminus S}_{\sigma s_2 j} \\ \overline{\boldsymbol{q}}^{A_2\cap S}_{us_2 j} \\ \overline{\boldsymbol{q}}^{A_2\cap S}_{\sigma s_2 j} \\ \overline{\boldsymbol{\Lambda}}_{s_\lambda j} \end{Bmatrix} = \begin{Bmatrix} \overline{\boldsymbol{P}}^{A_1\setminus S}_{\tau_1 i} \\ (1-\alpha)\,\overline{\boldsymbol{P}}^{A_1\cap S}_{\tau_1 i} \\ \overline{\boldsymbol{P}}^{A_2\setminus S}_{u\tau_2 i} \\ 0 \\ \alpha\overline{\boldsymbol{P}}^{A_2\cap S}_{u\tau_2 i} \\ 0 \\ 0 \end{Bmatrix} \tag{7.28}$$

7.3.1 Results and discussion

Square plates having sides length a equal to 0.1 m are considered. The side-to-thickness ratio a/h is equal to ten. Relatively thick plates are, therefore, investigated. A localised transverse pressure (P) equal to 1 MPa is applied on a square region of side length equal to $a/5$ centred at point ($a/2$,$a/2$,$h/2$) as shown in Fig. 7.18. This configuration has been considered since the region close to the loading application is likely to present a three-dimensional stress field and a refined model is there required. In the general case in which the location of a three-dimensional stress field cannot be determined a priori, refined sub-domains should be chosen on the basis of experience and preliminary analyses via low-order models. A symmetric [0/90/0] and an anti-symmetric $[90/0]_2$ stacking sequences are considered. The stacking sequence starts from the plate top. Ply angles are measured versus the x-axis. The layers are all made of the same orthotropic material, whose mechanical properties are: $E_L = 1.325 \cdot 10^5$ MPa, $E_T = 1.08 \cdot 10^4$ MPa, $G_{LT} = 5.7 \cdot 10^3$ MPa, $G_{TT} = 3.4 \cdot 10^3$ MPa, $\nu_{LT} = 0.24$ and $\nu_{TT} = 0.49$. Four-node quadrilateral elements are employed. Due to the problem symmetry, only a quarter of the plate is modelled. Results are presented in terms of the transverse displacement u_z, in-plane normal stresses σ_{xx}, σ_{yy} and the out-of-plane shear stress σ_{xz} Unless differently stated, u_z, σ_{xx} and σ_{yy} are evaluated at ($a/2$,$a/2$,$-h/2$) and σ_{xz} is computed at ($5a/12$,$a/2$,0).

Mono-model solutions are first presented. The accuracy of the proposed theories is discussed showing the fulfilment of the C_z^0 requirements and the through-the-thickness equilibrium. The convergence of the solution versus the number of elements in the mesh is also investigated through comparison with the corresponding closed-form analytical solution and a three-dimensional (3D) exact solution based upon Pagano's solution [139]. The variable kinematic models are then addressed. Their accuracy is assessed towards the corresponding mono-model results and 3D exact solutions. Non-conforming meshes are not considered. The effect of the coupling operator, the extension of the superposition zone and the weight parameters is investigated.

Preliminary Mono-model Results

Pagano's 3D solution is here extended in order to assess the accuracy of the UF models. The localised loading is approximated by a Fourier expansion being n_F the number of harmonic terms along x and y directions. The convergence of the transverse displacement u_z, in-plane normal stresses σ_{xx}, σ_{yy} and the out-of-plane shear stress σ_{xz} versus n_F is presented in Fig. 7.19. The symmetric [0/90/0] plate is considered. Results are normalised with respect to the values for $n_F = 101$. This latter value of n_F has been chosen in order to ensure a convergence of the shear stress with four significant digits. The convergence of the transverse displacement u_z and the in-plane normal stresses σ_{xx} versus the number of elements is presented in Figs. 7.20 and 7.21, respectively. FE results are compared to the analytical ones obtained by a Navier-type solution with $n_F = 101$ in the Fourier expansion of the loading. The mesh convergence rate is similar for all the considered theories. The transverse displacement u_z and the normal stresses σ_{xx} with a mesh of 15×15 elements differ from those with a mesh of 20×20 elements by less than 0.5%. A regular mesh of

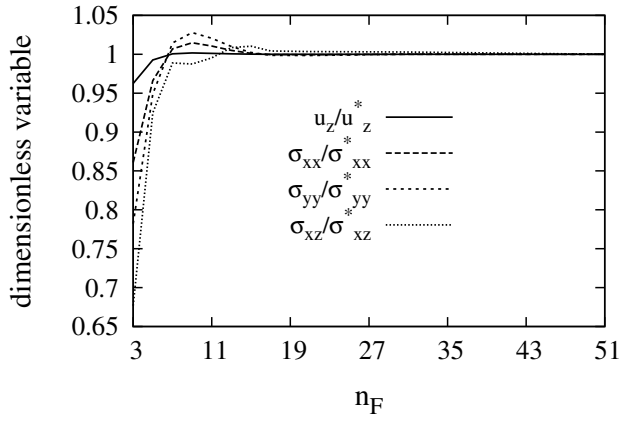

Figure 7.19. Convergence of Pagano's solution for a [0/90/0] plate. Starred results have been obtained with $n_F = 101$.

15×15 elements is, therefore, adopted in the following analyses. Elements' sides length l_{el} is equal to $a/30$. Transverse displacement and stresses for the symmetric [0/90/0] plate are reported in Table 7.10. Results are computed via 3D exact theory and both UF analytical

	$-10^5 \times u_z$ [m]		σ_{xx} [MPa]		σ_{yy} [MPa]		$-10 \times \sigma_{xz}$ [MPa]		DOF
3D	1.674		11.94		2.019		6.524		
	FE	AS[a]	FE	AS	FE	AS	FE	AS	
LM4	1.681	1.675	11.89	11.94	1.993	2.020	6.523	6.540	19968
LD4	1.672	1.675	11.83	11.94	1.983	2.020	6.464	6.523	9984
LD1	1.634	1.637	11.22	11.35	2.102	2.142	6.422	6.519	3072
ED4	1.657	1.660	11.85	11.95	1.985	2.005	5.830	5.865	3840
ED1	1.587	1.609	10.38	10.44	1.604	1.852	3.872	3.813	1536
FSDT	1.605	1.609	10.33	10.44	1.826	1.852	3.872	3.813	1280
CLT	1.255	1.260	10.88	11.00	1.617	1.642	–	–	768

[a] UF analytical solution.

Table 7.10. Transverse displacement and stresses for the [0/90/0] plate.

(AS) and FE mono-model solutions. Higher-order LW analytical results match the 3D reference solution. ESL, displacement based models do not predict σ_{xz} accurately. As far as the FE solution is concerned, LM4 model yields results that differ from the reference solution by about 1%, at worst. In the case of transverse displacement predicted by ED1 theory, the error is about 6%. For the assumed mesh, the difference in the transverse displacement between the FE solution and the corresponding analytical one is about 1.4%,

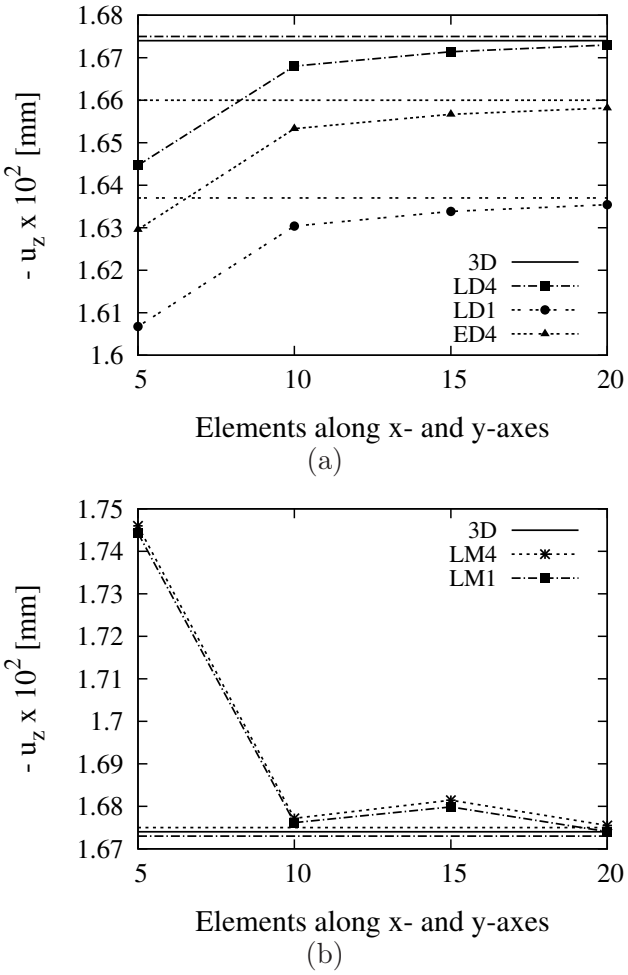

Figure 7.20. Convergence of the transverse displacement u_z versus the number of elements in the case of (a) PVD- and (b) RMVT-based theories. [0/90/0] stacking sequence. Horizontal lines without dots report the corresponding analytical solutions.

at worst. The last column in the Table represents the number of DOF of the FE solution.

The case of an anti-symmetric $[90/0]_2$ plate is presented in Table 7.11. As far as accuracy and convergence of the solutions are concerned, the same conclusions as for Table 7.10 are valid. The out-of-plane shear stress σ_{xz} is computed at both the bottom of the second layer and the top of the third one, in order to show that layer-wise mixed models satisfy the through-the-thickness equilibrium. The through-the-thickness variation of u_x and σ_{xz} is presented in Figs. 7.22. The displacement component u_x is computed at $x/a = 5/12$, $y/b = 1/2$. $\boldsymbol{C}_z^0$-requirements for displacements are satisfied by LW theories. The transverse shear stress continuity at layers' interface is fulfilled by the RMVT-based theories.

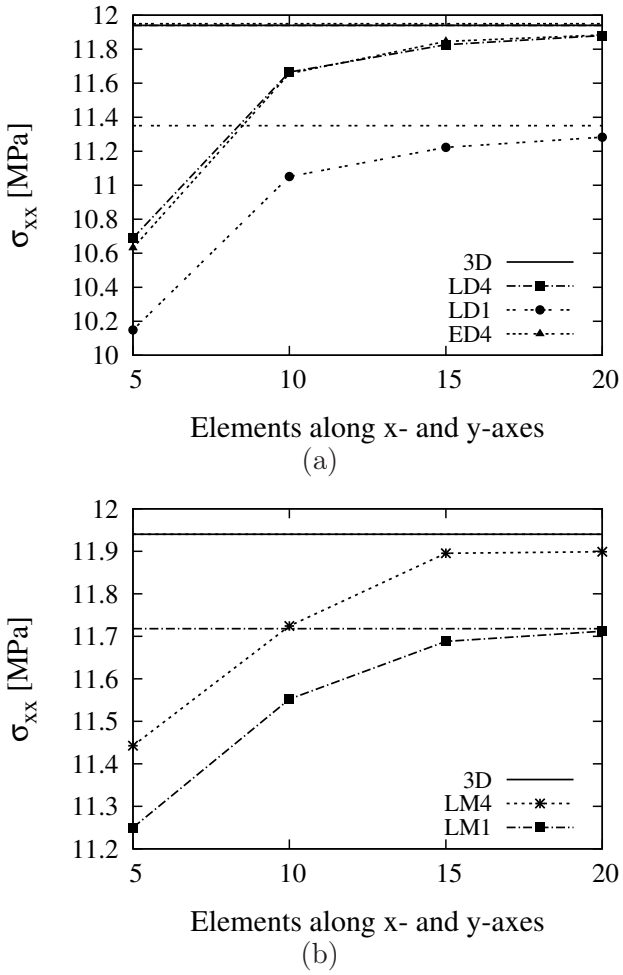

Figure 7.21. Convergence of the normal stress σ_{xx} versus the number of elements in the case of (a) PVD- and (b) RMVT-based theories. [0/90/0] stacking sequence. Horizontal lines without dots report the corresponding analytical solutions.

Variable Kinematic Results

Finite elements that differ by the variables description (ESL or LW) and the through-the-thickness expansion order are coupled. The coupling between PVD- and RMVT-based elements is also addressed. Fig. 7.18 presents the plate division into sub-domains and the mesh. Refined models are assumed for sub-domain A_2 that has been discretised via 49 elements. As shown in Fig. 7.18, three different overlapping zone S are considered. They differ by the extensions along x and y axes. A sensitivity analysis is carried out in terms of: 1. length parameter $\tilde{l}$, 2. extension of the superposition zone and 3. weighting function α_ξ.

	$-10^5 \times u_z$ [m]		σ_{xx} [MPa]		σ_{yy} [MPa]		$-10 \times \sigma^a_{xz}$ [MPa]		$-10 \times \sigma^b_{xz}$ [MPa]		DOF
3D	1.719		11.28		1.823		6.104		6.104		
	FE	AS[c]	FE	AS	FE	AS	FE	AS	FE	AS	
LM4	1.725	1.719	11.23	11.28	1.807	1.824	6.141	6.121	6.141	6.121	26112
LD4	1.717	1.719	11.17	11.28	1.802	1.824	6.118	6.145	6.069	6.104	13056
LD1	1.692	1.694	10.78	10.91	1.909	1.931	5.263	5.297	6.308	6.376	3840
ED4	1.698	1.700	11.19	11.28	1.778	1.789	8.214	8.267	4.899	4.931	3840
ED2	1.600	1.644	9.429	9.741	1.476	1.544	5.484	5.465	3.271	3.260	2304
ED1	1.596	1.634	9.937	10.16	1.202	1.446	5.806	5.562	3.463	3.318	1536
FSDT	1.614	1.634	9.938	10.16	1.420	1.446	5.671	5.562	3.382	3.318	1280
CLT	1.323	1.344	9.812	10.03	1.406	1.431	–	–	–	–	768

[a] Value at the bottom of the second layer.
[b] Value at the top of the third layer.
[c] UF analytical solution.

Table 7.11. Transverse displacement and stresses for the $[90/0]_2$ plate.

Length parameter Three values of $\tilde{l}$ are considered: zero, l_e and l_c. The latter is the length of the superposition zone along the x- or y-axis. It should be noticed that L^2 coupling operator can be considered as a particular case of H^1 one with $\tilde{l}$ equal to zero. The superposition zone as in Fig. 7.18(c) and addressed as S^c is used. Such a large superposition zone, which includes most of the refined sub-domain, is not well suited for practical application of the Arlequin method. It is here considered in order to highlight the spatial variation of quantities inside the overlapping volume. The coupling of two identical kinematic models ED1 is considered in the first place. According to Ben Dhia and Rateau [135], weighting functions equal to 0.5 are assumed. Fig. 7.23 presents the Lagrangian multiplier λ_z along x axis at $y/b = 1/2$ and $z = 0$ for a [0/90/0] plate. Results are normalised versus their absolute maximum values $|\lambda_z|_{MAX}$. Two meshes are considered: the mesh shown in Fig. 7.18(c) and a refined mesh with halved elements side length. As noticed in Ben Dhia and Rateau [135] and confirmed in Guidault and Belytschko [137], the coupling operator L^2 yields a multiplier field that tends to be singular on the interfaces of the superposition zone: the multiplier field is almost null everywhere except near the boundaries of the overlapping volume where it oscillates. If the elements size is reduced, the oscillation regions become smaller. As explained by Ben Dhia [136], the multiplier field seems to converge up to a homogenisation factor to a surface-Lagrange multiplier. The transverse displacement, the normal in-plane stresses and the shear stresses match the case of mono-model solution regardless the choice of the length parameter. For sake of brevity, they are not explicitly reported. In the second case, a LD2 model (sub-domain A_1) is coupled with a LD4 model (sub-domain A_2). According to Ben Dhia and Rateau [135] and unless differently stated, α_2 equal to 0.98 is used. Fig. 7.24 presents the Lagrangian multiplier λ_z along x axis at $y/b = 1/2$ at mid-plane. For L^2, λ_z tends to be singular at the interface with the unrefined model. The distribution of σ_{xx} along x axis for $y/a = 1/2$ at plate bottom is shown in Figs. 7.25. The case $\tilde{l} = l_{el}$ yields the least perturbed solution,

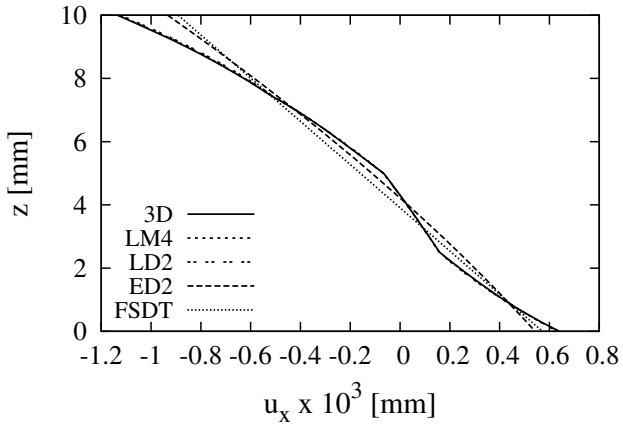

(a)

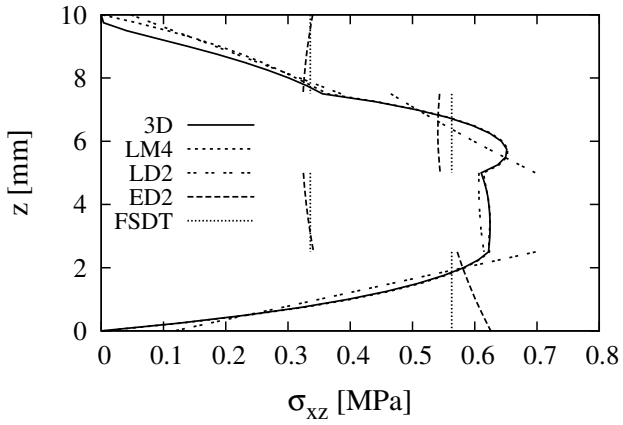

(b)

Figure 7.22. Through-the-thickness variation of (a) u_x and (b) σ_{xz} computed at $x/a = 5/12$, $y/a = 1/2$, $[90/0]_2$ plate.

whereas for $\tilde{l} = l_c$ the oscillation in the coupling zone yields an underestimated value of σ_{xx} in the refined zone. Figs. 7.26 present the variation of σ_{xz} along x axis. The shear stress is computed at $y/b = 1/2$ and $z = 0$. The variation of the length parameter affects the solution mainly in the coupling zone. It has been observed that the transverse displacement via LD2-LD4 coupled solution matches the corresponding mono-model one. It is not reported here for the sake of brevity.

An ED1-ED4 coupled solution is also considered in order to investigated the coupling between lower and higher ESL theories. The transverse displacement along x axis for $y/a = 1/2$ at mid-plane is presented in Fig. 7.27. Results for $\tilde{l} = l_{el}$ and $\tilde{l} = 0$ are very similar and only the latter is, therefore, presented in the figure. The variable kinematic results are not very accurate because of the ED1 model in the coupled solution. The distribution of σ_{xx} is shown in Figs. 7.28. L^2 coupling operator yields better results that

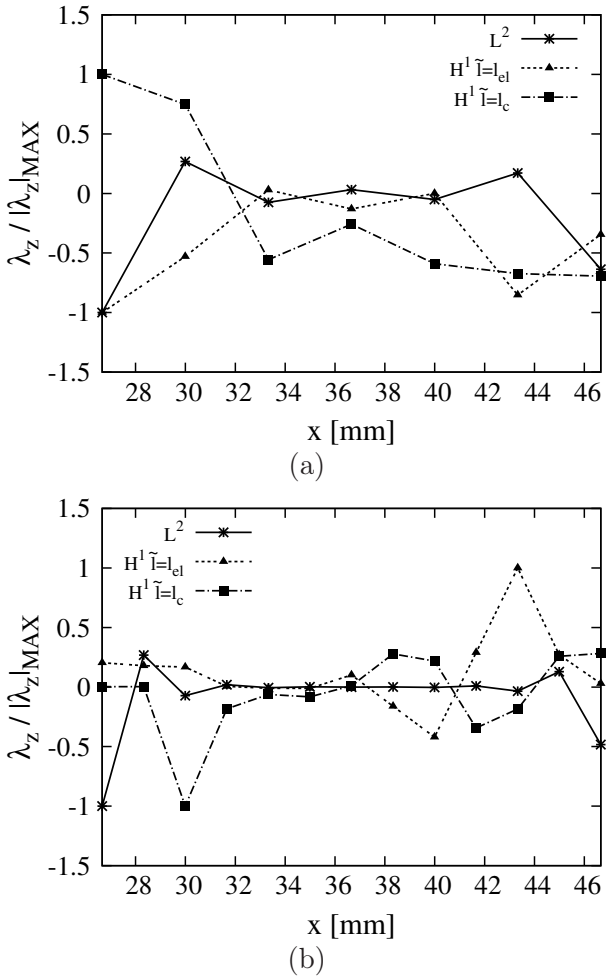

Figure 7.23. Variation of the Lagrangian multiplier λ_z along x axis at $y/b = 1/2$ and $z = 0$ for a [0/90/0] plate in the case of the coupling of two ED1 models with (a) mesh represented in Fig. 7.18 and (b) refined mesh with halved elements' side length.

the H^1 does. Similar considerations hold for the variation of σ_{xz}. For both normal and shear stresses, results obtained with $\tilde{l} = l_{el}$ are better than those obtained with $\tilde{l} = l_c$. The presented results confirm what reported by Ben Dhia and Rateau [135] and Guidault and Belytschko [137]: L^2 coupling operator presents a multiplier field that tends to be singular near the interfaces of the superposition zone. This is not the case of H^1, which yields a smoother multiplier field. When coupling identical kinematic models or models with similarly accurate kinematics, results obtained via H^1 are similar to those by L^2. Nevertheless, in the considered cases, H^1 may yield inaccurate results if the unrefined theories are not appropriate to model the mechanics of the structure (especially when the transverse shear is important). This behaviour is emphasised by high values of $\tilde{l}$. The

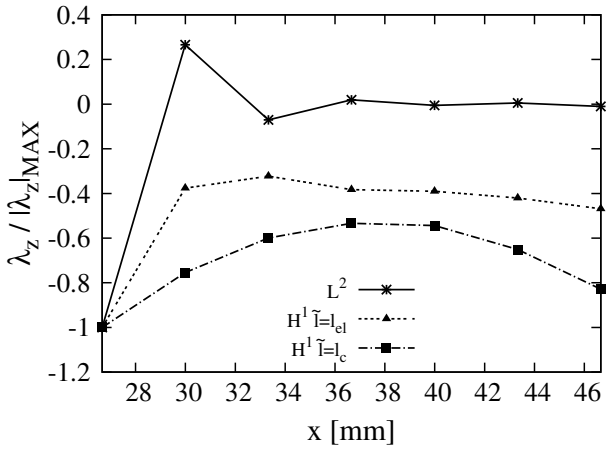

Figure 7.24. Variation of the Lagrangian multiplier λ_z along x axis at $y/b = 1/2$ and $z = 0$ for a [0/90/0] plate in the case of LD2-LD4 coupled solution.

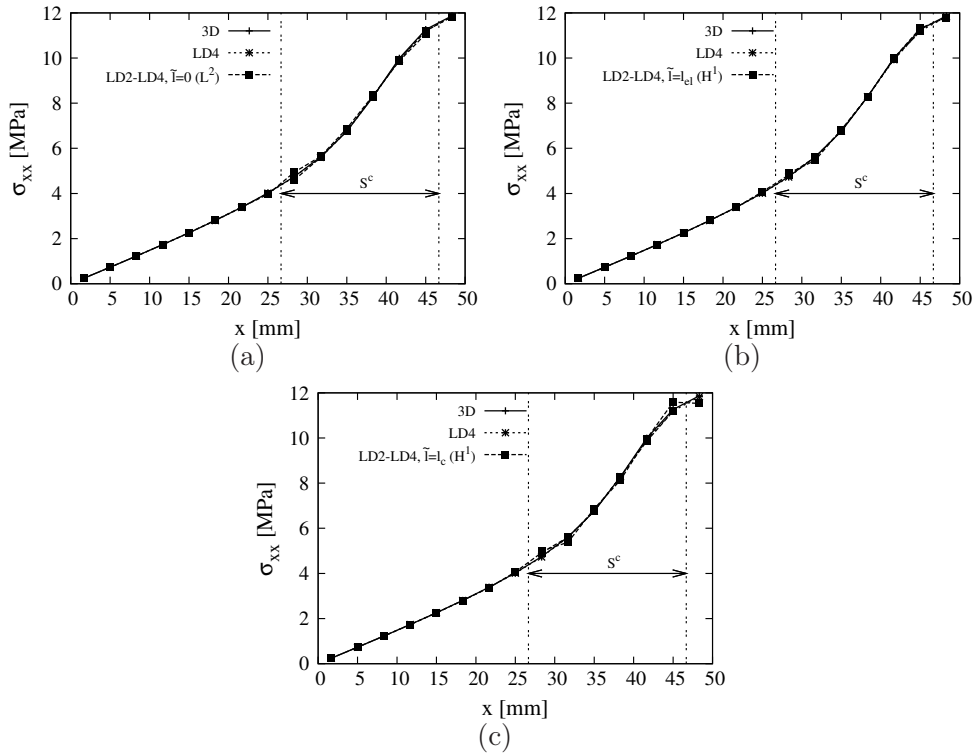

Figure 7.25. σ_{xx} along x axis for $y/b = 1/2$ at plate bottom for a [0/90/0] plate. LD2-LD4 coupled solution with (a) $\tilde{l} = 0$, (b) $\tilde{l} = l_{el}$, (c) $\tilde{l} = l_c$.

relation enforced by H^1 (see Guidault and Belytschko [137]) in the superposition zone is:

$$(\boldsymbol{u}_1 - \boldsymbol{u}_2) - \tilde{l}^2 \left[\Delta(\boldsymbol{u}_1) - \Delta(\boldsymbol{u}_2)\right] = 0 \tag{7.29}$$

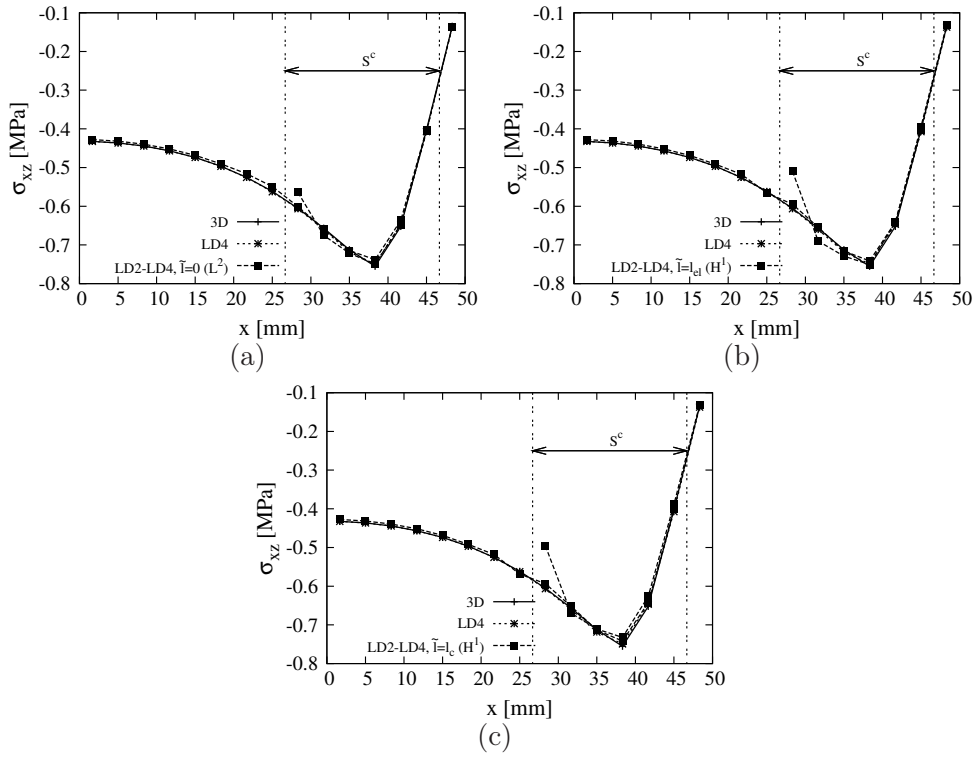

Figure 7.26. σ_{xz} along x axis for $y/b = 1/2$ at mid-plane for a [0/90/0] plate. LD2-LD4 coupled solution with (a) $\tilde{l} = 0$, (b) $\tilde{l} = l_{el}$, (c) $\tilde{l} = l_c$.

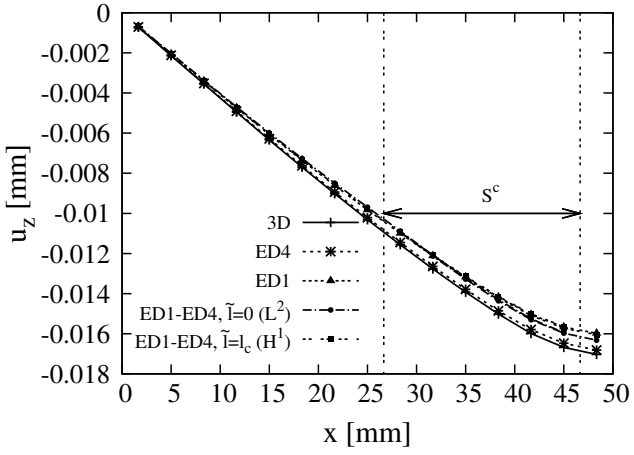

Figure 7.27. u_z along x axis for $y/b = 1/2$ at mid-plane for a [0/90/0] plate. ED1-ED4 coupled solution.

where Δ is the Laplacian. The higher the parameter $\tilde{l}$, the higher the contribution of the

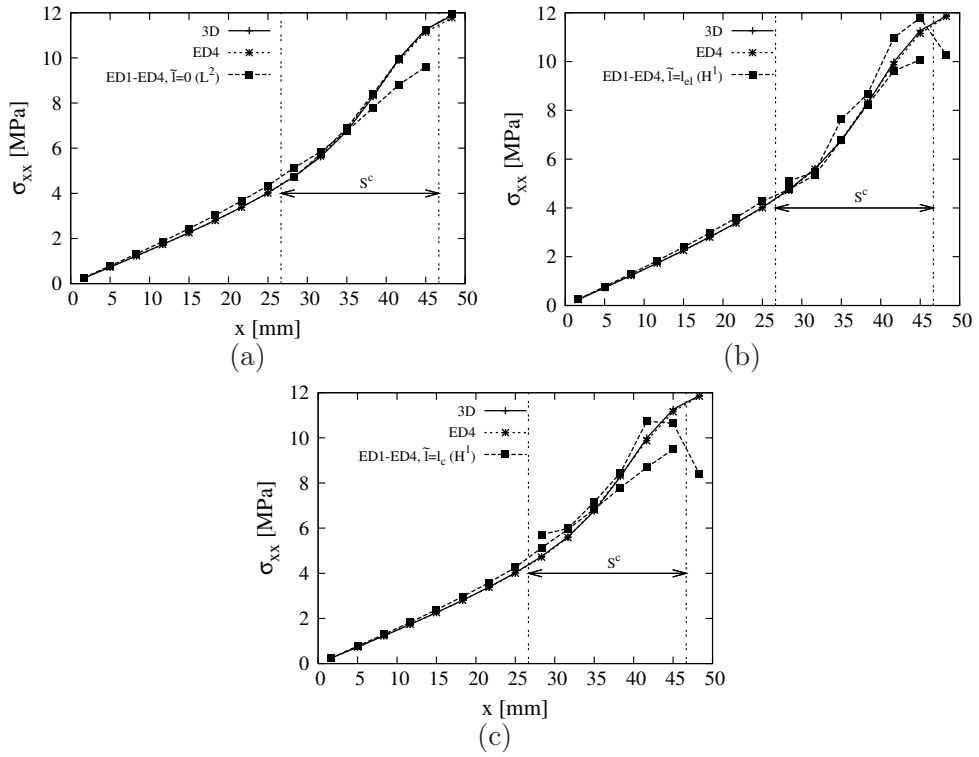

Figure 7.28. σ_{xx} along x axis for $y/b = 1/2$ at plate bottom for a [0/90/0] plate. ED1-ED4 coupled solution with (a) $\tilde{l} = 0$, (b) $\tilde{l} = l_{el}$, (c) $\tilde{l} = l_c$.

derivatives of the displacements in Eq. 7.29. As shown in Table 7.10, the ED1 model, especially for the prediction of the transverse shear stresses, is not accurate. The contribution due to the derivatives of strain components may introduce a disturbance in the superposition zone. L^2 couples only the displacements that are, in general, more accurate than the transverse strains in lower-order plate models.

Extension of the superposition zone The influence of the extension of the superposition zone on the coupling is investigated. Several superposition zones, as shown in Fig. 7.18, are considered. Both L^2 and H^1 coupling operators are considered. For the latter case, a length parameter $\tilde{l}$ equal to l_{el} is considered. In order to avoid the perturbation in the coupling due to the plate theories, two refined models are coupled (ED3 model in sub-domain A_1 and LD4 model in A_2). Figs. 7.29 present σ_{xx} and σ_{xz} in the case of L^2. The extension of the superposition zone does not affect the results in a significant manner. This conclusion is supported by the fact, as shown in Fig. 7.24, that the Lagrangian multipliers contribution is concentrated at the interface with the low-order model. The case of H^1 coupling is shown in Figs. 7.30. For the considered cases, the effect of the size of the superposition zone is very small, being the curves in the figures barely distinguishable: the superposition zone does not affect significantly the accuracy of the solution. On the

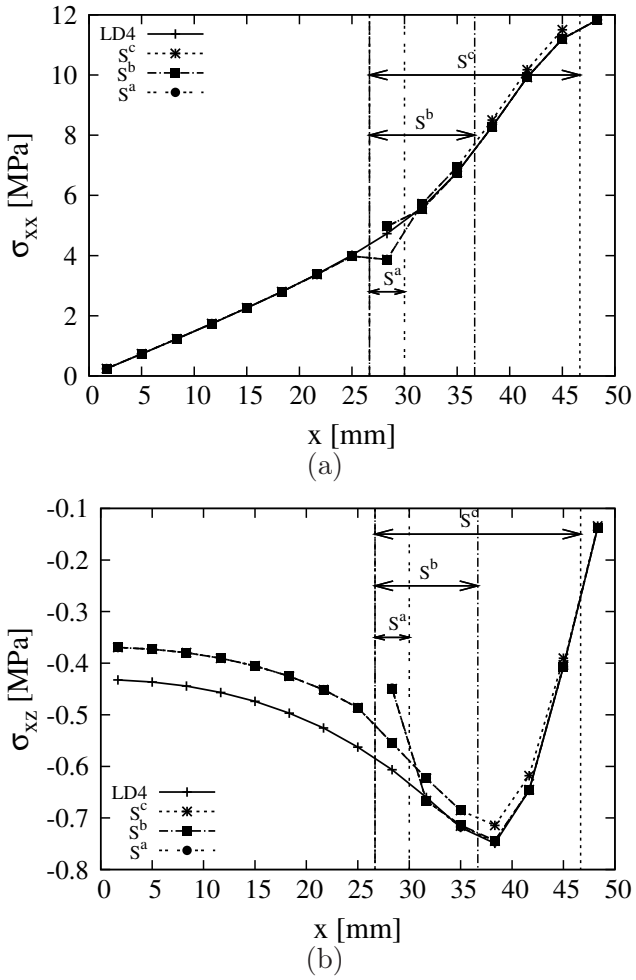

Figure 7.29. ED3-LD4 coupled solution with $\tilde{l} = 0$ for a [0/90/0] plate for different superposition volumes. (a) σ_{xx} at plate bottom and (b) σ_{xz} at mid-plane along x axis for $y/b = 1/2$.

other side, the bigger the extension of the superposition zone, the higher the number of DOF and, therefore, small superposition volumes should be used.

Weight parameters Three different values of α_2, the weight parameter of the refined model, are used: 0.02, 0.5 and 0.98. Superposition zone S^a is considered. A length parameter $\tilde{l}$ equal to zero and l_{el} is considered. A ED3 model is coupled to a LD4 model. The variation of σ_{xx} and σ_{xz} along x axis at $y/a = 1/2$ is presented in Figs. 7.31 and Figs. 7.32, respectively. For the considered cases, H^1 coupling operator is more sensitive than the L^2 one to the weight parameters. The results confirm, as reported in Ben Dhia and Rateau [135], that the sub-domain with the most refined description should have a higher weight in the global equilibrium.

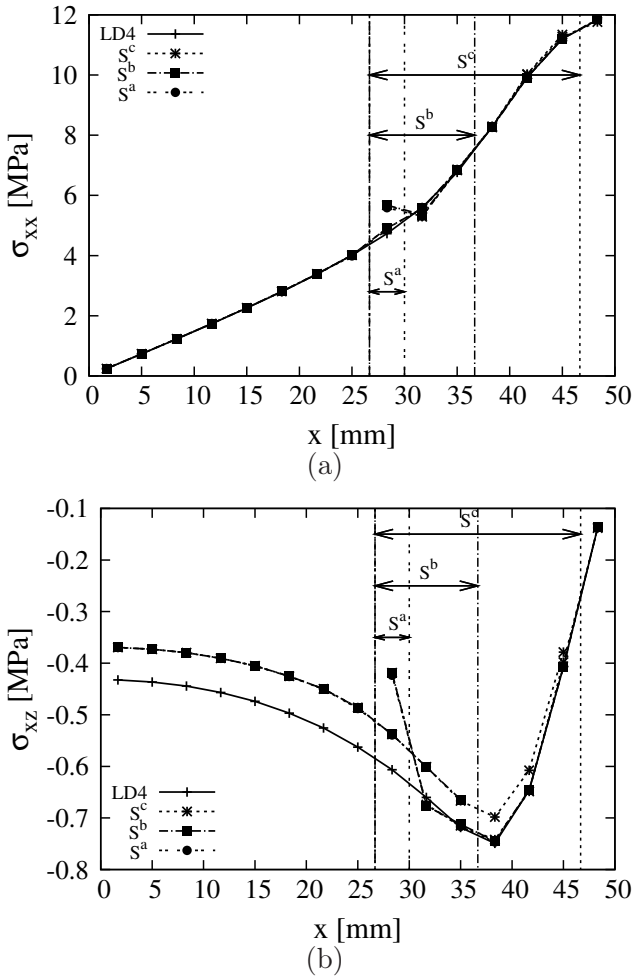

Figure 7.30. ED3-LD4 coupled solution with $\tilde{l} = l_{el}$ for a [0/90/0] plate for different superposition volumes. (a) σ_{xx} at plate bottom and (b) σ_{xz} at mid-plane along x axis for $y/b = 1/2$.

Different kinematics and variational principles UF models that differ in the type of the main unknowns, expansion order and approximation level (ESL or LW) are coupled. The coupling parameters are fixed coherently to what previously obtained: 1. the smallest superposition zone S^a is used, 2. higher weight in the global equilibrium is given to the most refined model ($\alpha_2 = 0.98$) and 3. both L^2 and H^1 (with $\tilde{l} = l_{el}$) operators are adopted. Table 7.12 presents the transverse displacement and the normal and shear stress components for a symmetric [0/90/0] plate. The number of DOF of variable kinematic FE solutions is also addressed. Multi-model solutions match the corresponding mono-model results, proving the effectiveness of the Arlequin method in merging domains discretised via finite elements derived from different theories. Results are similar for the two coupling operators. Accurate results are obtained coupling PVD- and RMVT-based models, i.e.

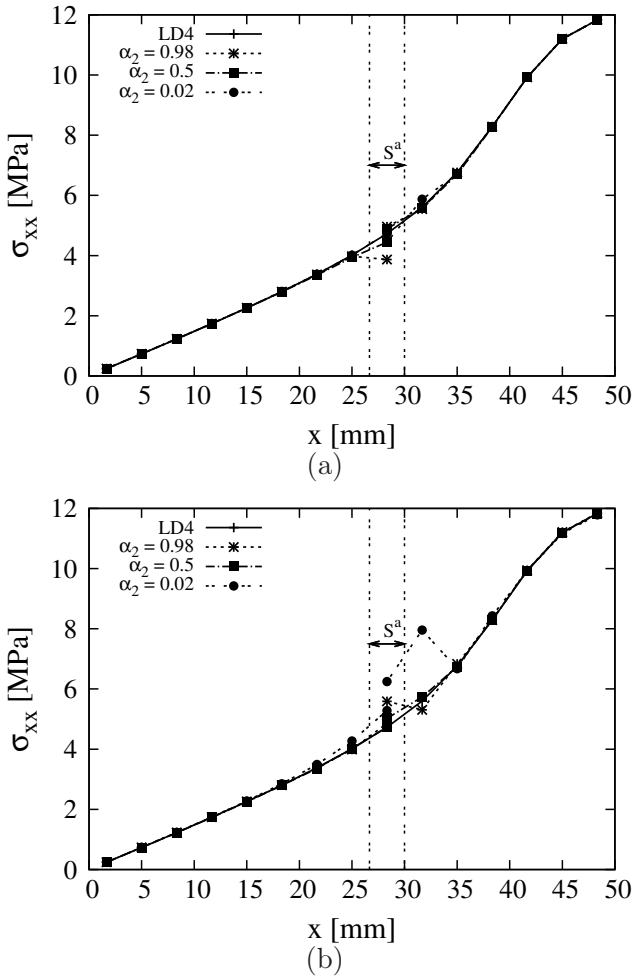

Figure 7.31. σ_{xx} along x axis for $y/b = 1/2$ at plate bottom for a [0/90/0] plate. ED3-LD4 coupled solution for different α_ξ with (a) $\tilde{l} = 0$ and (b) $\tilde{l} = l_{el}$.

LD1-LM4. The number of degrees of freedom is significantly reduced. When ED1 or FSDT is adopted as unrefined theory, results may exhibit inconsistent behaviour with respect to the corresponding mono-model results and, being the two models similar, do not differ up to four significant digits. For instance, in the case of ED1-ED4 coupled solution σ_{xx} is higher than the corresponding mono-model results, see Table 7.10. It should be noticed that, anyway, the difference from ED4 model is less than 1%. This may be due to the first-order model inability to capture the mechanics of the structure. Results in the case of an anti-symmetric $[90/0]_2$ plate are presented in Table 7.13. For the transverse displacement, a coupling between FSDT or ED1 model and a higher-order one yields overestimated results by about 3% with respect to the correspondent mono-model solution. At least a second-order model should be assumed for the unrefined sub-domain. The difference in the transverse displacement from the mono-model solution when H^1 coupling operator is

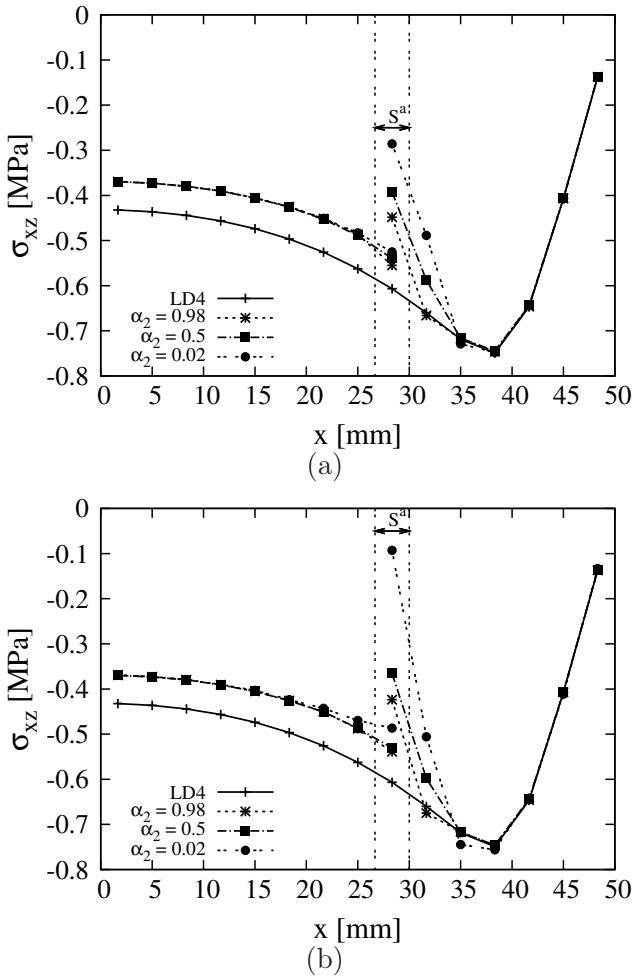

Figure 7.32. σ_{xz} along x axis for $y/b = 1/2$ at mid-plane for a [0/90/0] plate. ED3-LD4 coupled solution for different α_ξ with (a) $\tilde{l} = 0$ and (b) $\tilde{l} = l_{el}$.

used may be due to the shift introduced by this operator in bending problems as reported in Guidault and Belytschko [137]. The choice of the unrefined model in the considered cases is of primary importance: if the unrefined model does not model correctly the global response of the plate, results in the refined sub-domain are less accurate.

	$-10^5 \times u_z$ [m]	σ_{xx} [MPa]	σ_{yy} [MPa]	$-10 \times \sigma_{xz}$ [MPa]	DOF
		L^2 coupling operator			
LD1-LM4	$1.658, -1.36^a$	$11.82, -0.58$	$1.975, -0.90$	$6.478, -0.69$	7968
ED4-LD4	$1.665, -0.41$	$11.83, +0.00$	$1.976, -0.35$	$6.465, +0.01$	6216
LD1-LD4	$1.660, -0.71$	$11.84, +0.08$	$1.977, -0.30$	$6.497, +0.51$	5472
ED1-LD4	$1.617, -3.28$	$11.91, +0.67$	$1.953, -1.51$	$6.481, +0.26$	3984
FSDT-LD4	$1.617, -3.28$	$11.91, +0.67$	$1.953, -1.51$	$6.481, +0.26$	3736
ED3-ED4	$1.657, +0.00$	$11.84, -0.08$	$1.985, +0.00$	$5.831, +0.01$	3936
ED1-ED4	$1.609, -2.89$	$11.92, +0.59$	$1.962, -1.15$	$5.848, +0.30$	2448
FSDT-ED4	$1.609, -2.89$	$11.92, +0.59$	$1.962, -1.15$	$5.848, +0.30$	2200
		H^1 coupling operator			
LD1-LM4	$1.661, -1.19$	$11.81, -0.67$	$1.974, -0.95$	$6.490, -0.50$	7968
ED4-LD4	$1.666, -0.35$	$11.85, +0.16$	$1.978, -0.25$	$6.467, +0.04$	6216
LD1-LD4	$1.663, -0.58$	$11.85, +0.16$	$1.974, -0.45$	$6.485, +0.32$	5472
ED1-LD4	$1.620, -3.11$	$11.92, +0.76$	$1.953, -1.51$	$6.458, -0.09$	3984
FSDT-LD4	$1.620, -3.11$	$11.92, +0.76$	$1.953, -1.51$	$6.458, -0.09$	3736
ED3-ED4	$1.657, +0.00$	$11.84, -0.08$	$1.985, +0.00$	$5.832, +0.03$	3936
ED1-ED4	$1.611, -2.77$	$11.92, +0.59$	$1.963, -1.10$	$5.838, +0.13$	2448
FSDT-ED4	$1.611, -2.77$	$11.92, +0.59$	$1.963, -1.10$	$5.838, +0.13$	2200

[a] Percentage difference with respect to the corresponding mono-model FE results.

Table 7.12. Transverse displacement and stresses for the [0/90/0] plate, variable kinematic.

	$-10^5 \times u_z$ [m]	σ_{xx} [MPa]	σ_{yy} [MPa]	$-10 \times \sigma^a_{xz}$ [MPa]	$-10 \times \sigma^b_{xz}$ [MPa]	DOF
			L^2 coupling operator			
LD1-LM4	$1.714, -0.63^c$	$11.13, -0.89$	$1.794, -0.71$	$6.051, -1.46$	$6.051, -1.46$	10248
LD1-LD4	$1.717, +0.00$	$11.15, -0.17$	$1.796, -0.33$	$6.090, -0.45$	$6.099, +0.49$	6984
ED2-LD4	$1.688, -1.68$	$11.17, +0.00$	$1.796, -0.33$	$6.123, +0.08$	$6.139, +1.15$	5496
ED1-LD4	$1.769, +3.02$	$10.91, -2.32$	$1.768, -1.88$	$6.265, +2.40$	$6.187, +1.94$	4752
FSDT-LD4	$1.763, +2.67$	$10.93, -2.14$	$1.772, -1.60$	$6.265, +2.40$	$6.169, +1.64$	4504
ED2-ED4	$1.668, -1.76$	$11.20, +0.08$	$1.778, +0.00$	$8.259, +0.54$	$4.926, +0.55$	3192
ED1-ED4	$1.746, +2.82$	$10.95, -2.14$	$1.750, -1.57$	$8.262, +0.58$	$4.928, +0.59$	2448
FSDT-ED4	$1.739, +2.41$	$10.97, -1.96$	$1.753, -1.40$	$8.262, +0.58$	$4.928, +0.59$	2200
			H^1 coupling operator			
LD1-LM4	$1.761, +2.08$	$10.97, -2.31$	$1.775, -1.77$	$6.131, -0.16$	$6.131, -0.16$	10248
LD1-LD4	$1.746, +1.68$	$11.09, -0.71$	$1.780, -1.22$	$6.128, +0.16$	$6.047, -0.36$	6984
ED2-LD4	$1.707, -0.58$	$11.17, +0.00$	$1.796, -0.33$	$6.123, +0.08$	$6.139, +1.15$	5496
ED1-LD4	$1.783, +3.84$	$10.81, -3.22$	$1.763, -2.16$	$6.189, +1.16$	$6.179, +1.81$	4752
FSDT-LD4	$1.769, +3.02$	$10.85, -2.86$	$1.772, -1.66$	$6.135, +0.27$	$6.190, +1.99$	4504
ED2-ED4	$1.685, -0.76$	$11.16, -0.26$	$1.773, -0.28$	$8.237, +0.28$	$4.913, +0.28$	3192
ED1-ED4	$1.761, +3.71$	$10.90, -2.59$	$1.745, -1.85$	$8.220, +0.07$	$4.903, +0.08$	2448
FSDT-ED4	$1.747, +2.88$	$10.97, -1.96$	$1.753, -1.40$	$8.249, +0.42$	$4.920, +0.42$	2200

[a] Value at the bottom of the second layer.
[b] Value at the top of the third layer.
[c] Percentage difference with respect to the corresponding mono-model FE results.

Table 7.13. Transverse displacement and stresses for the $[90/0]_2$ plate, variable kinematic.

7.4 Solid and higher-order plate elements

Surana [140] presented an isoparametric transition finite element to link solid elements and shell elements. This work was later extended in [141] to a non-linear transition finite element based on a total lagrangian approach. The formulation employs non-linear functions of nodal rotations in the description of the element displacement field and it is capable of handling large rotations. Garusi and Tralli [142] presented a transition element based upon the hybrid stress method for modelling solid-to-beam and plate-to-beam connections. Spurious kinematic modes that arise from hypostatic formulation are eliminated via a penalty method. McCune et al. [143] proposed a displacement coupling between regions of different dimension for both 2D-1D and 3D-2D models. The components of force and moment are transmitted across adjacent models and the variation of stress is continuous at the interfaces. In a follow up study by Shim et al. [144], the coupling of shells to solids is based on a refined theory of shells. The in-plane stress and the out-of plane shear stress are assumed to vary linearly and parabolically respectively through the shell thickness. Multipoint constraint equations provide the relationship among nodal degrees of freedom of elements of differnet types. Osawa et al. [145] presented a technique for shell-solid coupling based on a fictitious shell plane perpendicular to the original shell plane. The method was developed in the context of fatigue assessment of ship structures.

Mixed-dimensional analysis with higher-order elements is a topic not yet addressed in literature. Solid and higher-order ESL plate elements are here coupled via the Arlequin method. The volume of the structure is divided into two sub-domains. Q represents the overlapping volume. In the following, A_S is the sub-domain with solid elements, whereas A_P is the one with plate elements. The kinematic field is chosen accordingly:

$$\boldsymbol{u} = \boldsymbol{u}_S\,(x,y,z) = N_i(x,y,z)\boldsymbol{q}_i \quad \text{with} \quad i = 1,2,\ldots,N_n \quad \forall\,(x,y,z) \in A_S \tag{7.30}$$

$$\boldsymbol{u} = \boldsymbol{u}_P\,(x,y,z) = M_i(x,y)F_\tau(z)\boldsymbol{q}_{\tau i} \quad \text{with} \quad \tau = 1,2,\ldots,N_u,\ i = 1,2,\ldots,M_n \quad \forall\,(x,y,z) \in A_P \tag{7.31}$$

The virtual coupling work in the two sub-domains is:

$$\begin{aligned} \delta L_{cS} &= -\delta C_S\,(\delta\boldsymbol{\lambda},\boldsymbol{u}_S) \\ \delta L_{cP} &= \delta C_P\,(\delta\boldsymbol{\lambda},\boldsymbol{u}_P) \end{aligned} \tag{7.32}$$

The H^1 coupling operator is adopted. the Lagrangian multiplier field is discretised as the displacements field in the plate elements:

$$\boldsymbol{\lambda} = N_i F_{\tau_\lambda} \boldsymbol{\Lambda}_{\tau_\lambda i} \quad \text{with} \quad \tau_\lambda = 1,2,\ldots,N_u, \quad i = 1,2,\ldots,N_{nP} \tag{7.33}$$

where $\boldsymbol{\Lambda}_{\tau_\lambda i}$ is the nodal unknown vector. The virtual work of a k^{th} layer in sub-domain A_P is derived via substitution of Eqs. 7.33 and 7.31 into Eq. 7.5:

$$\delta C_P = \delta\boldsymbol{\Lambda}^T_{\tau_\lambda i}\mathbf{C}_P^{\tau_\lambda sij}\boldsymbol{q}_{sj} \tag{7.34}$$

$\mathbf{C}_P^{\tau_\lambda sij} \in \mathbb{R}^{3\times 3}$ is the fundamental nucleo of the coupling matrix for the sub-domain A_P:

$$\begin{aligned}
C_{P_{11}}^{\tau_\lambda sij} = C_{P_{22}}^{\tau_\lambda sij} = C_{P_{33}}^{\tau_\lambda sij} = E_{\tau_\lambda s} \lhd N_i N_j \rhd_\Omega + \\
+\tilde{l}^2 \left[E_{\tau_\lambda s} \left(\lhd N_{i,x} N_{j,x} \rhd_\Omega + \lhd N_{i,y} N_{j,y} \rhd_\Omega \right) + E_{\tau_{\lambda,z} s,z} \lhd N_i N_j \rhd_\Omega \right] \\
C_{P_{12}}^{\tau_\lambda sij} = \tilde{l}^2 E_{\tau_\lambda s} \lhd N_{i,y} N_{j,x} \rhd_\Omega \,, \quad C_{P_{13}}^{\tau_\lambda sij} = \tilde{l}^2 E_{\tau_{\lambda,z} s} \lhd N_i N_{j,x} \rhd_\Omega \\
C_{P_{21}}^{\tau_\lambda sij} = \tilde{l}^2 E_{\tau_\lambda s} \lhd N_{i,x} N_{j,y} \rhd_\Omega \,, \quad C_{P_{23}}^{\tau_\lambda sij} = \tilde{l}^2 E_{\tau_{\lambda,z} s} \lhd N_i N_{j,y} \rhd_\Omega \\
C_{P_{31}}^{\tau_\lambda sij} = \tilde{l}^2 E_{\tau_\lambda s,z} \lhd N_{i,x} N_j \rhd_\Omega \,, \quad C_{P_{32}}^{\tau_\lambda sij} = \tilde{l}^2 E_{\tau_\lambda s,z} \lhd N_{i,y} N_j \rhd_\Omega
\end{aligned} \tag{7.35}$$

where:

$$E_{\tau_{\lambda(,y)(,z)} s_{(,y)(,z)}} = \int_h F_{\tau_{\lambda(,y)(,z)}} F_{s_{(,y)(,z)}} \, dz \tag{7.36}$$

The virtual work in sub-domain A_S is derived via substitution of Eqs. 7.33 and 7.30 into Eq. 7.5:

$$\delta C_S = \delta \mathbf{\Lambda}_{\tau_\lambda i}^T \mathbf{C}_S^{\tau_\lambda ij} \boldsymbol{q}_j \tag{7.37}$$

$\mathbf{C}_S^{\tau_\lambda ij} \in \mathbb{R}^{3\times 3}$ is the fundamental nucleo of the coupling matrix for the sub-domain A_S:

$$\begin{aligned}
C_{S_{11}}^{\tau_\lambda ij} = C_{S_{22}}^{\tau_\lambda ij} = C_{S_{33}}^{\tau_\lambda ij} = \lhd F_{\tau_\lambda} M_i N_j \rhd_V \\
+\tilde{l}^2 \left[\lhd F_{\tau_\lambda} M_{i,x} N_{j,x} \rhd_V + \lhd F_{\tau_\lambda} M_{i,y} N_{j,y} \rhd_V + \lhd F_{\tau_{\lambda,z}} M_i N_{j,z} \rhd_V \right] \\
C_{S_{12}}^{\tau_\lambda ij} = \tilde{l}^2 \lhd F_{\tau_\lambda} M_{i,y} N_{j,x} \rhd_V \,, \quad C_{S_{13}}^{\tau_\lambda ij} = \tilde{l}^2 \lhd F_{\tau_{\lambda,z}} M_i N_{j,x} \rhd_V \\
C_{S_{21}}^{\tau_\lambda ij} = \tilde{l}^2 \lhd F_{\tau_\lambda} M_{i,x} N_{j,y} \rhd_V \,, \quad C_{S_{23}}^{\tau_\lambda ij} = \tilde{l}^2 \lhd F_{\tau_{\lambda,z}} M_i N_{j,y} \rhd_V \\
C_{S_{31}}^{\tau_\lambda ij} = \tilde{l}^2 \lhd F_{\tau_\lambda} M_{i,x} N_{j,z} \rhd_V \,, \quad C_{S_{32}}^{\tau_\lambda ij} = \tilde{l}^2 \lhd F_{\tau_\lambda} M_{i,y} N_{j,z} \rhd_V
\end{aligned} \tag{7.38}$$

Considering the whole structure the governing equations of the problem are:

$$\begin{bmatrix}
\overline{\boldsymbol{K}}_{A_S\setminus Q}^{ij} & \mathbf{0} & \mathbf{0} & \mathbf{0} & \mathbf{0} \\
\mathbf{0} & \alpha \overline{\boldsymbol{K}}_{A_S\cap Q}^{ij} & \mathbf{0} & \mathbf{0} & \overline{\mathbf{C}}_S^{\tau ijT} \\
\mathbf{0} & \mathbf{0} & \overline{\boldsymbol{K}}_{A_P\setminus Q}^{\tau sij} & \mathbf{0} & \mathbf{0} \\
\mathbf{0} & \mathbf{0} & \mathbf{0} & (1-\alpha)\, \overline{\boldsymbol{K}}_{A_P\cap Q}^{\tau sij} & -\overline{\mathbf{C}}_P^{\tau sijT} \\
\mathbf{0} & \overline{\mathbf{C}}_S^{\tau ij} & \mathbf{0} & -\overline{\mathbf{C}}_P^{\tau sij} & \mathbf{0}
\end{bmatrix}
\begin{Bmatrix}
\overline{\boldsymbol{q}}_j^{A_S\setminus Q} \\
\overline{\boldsymbol{q}}_j^{A_S\cap Q} \\
\overline{\boldsymbol{q}}_{sj}^{A_P\setminus Q} \\
\overline{\boldsymbol{q}}_{sj}^{A_P\cap Q} \\
\overline{\mathbf{\Lambda}}_{s_\lambda j}
\end{Bmatrix} =
\begin{Bmatrix}
\overline{\boldsymbol{P}}_i^{A_S\setminus Q} \\
\alpha \overline{\boldsymbol{P}}_i^{A_S\cap Q} \\
\overline{\boldsymbol{P}}_{\tau i}^{A_P\setminus Q} \\
(1-\alpha)\, \overline{\boldsymbol{P}}_{\tau i}^{A_P\cap Q} \\
0
\end{Bmatrix} \tag{7.39}$$

7.4.1 Results and discussion

The case of a shell fixed to a wall is presented. In the mixed-dimensional solution, the wall is modelled via solid elements and the shelf via higher-order plate elements. Results are compared to a mono-model solution with solid elements and to ABAQUS solution with C3D20 elements, see [63]. The superposition region is as small as possible, according to Guidault and Belytschko [137].

A wall (dimensions $0.06 \times 0.1 \times 0.26$ m) with a fixed shelf ($a = 0.2$ m and $b = 0.1$ m) is considered. The shelf has a sandwich structure whose total thickness is 0.02 m. Each face accounts for 10% of the total thickness. A localised transverse pressure (P) equal to 1000 Pa is applied on the shelf in the rectangular region with sides $\frac{a}{10} \times b$ near its free edge, see Fig. 7.33. The wall is fixed at its base. The wall and the two faces of the shelf share the

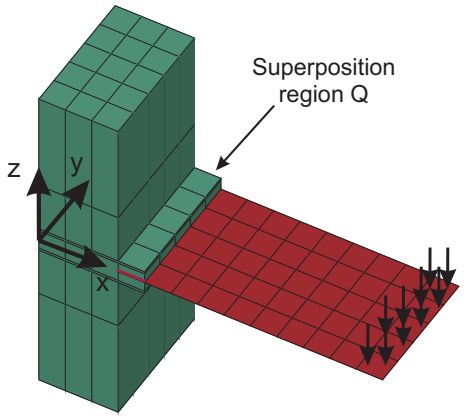

Figure 7.33. Shelf fixed to a wall. The wall is modelled with solid elements, whereas the shelf adopts plate elements.

same isotropic material whose properties are: $E^F = 73000$ MPa, $\nu^F = 0.34$. Two different Young's moduli are considered for the core: $E^C = \frac{E^F}{12}$ and $E^C = \frac{E^F}{120}$. Poisson's ratio of the core is $\nu^C = \nu^F$. The solutions obtained with solid elements adopt a regular mesh of $3 \times 5 \times 7$ elements for the wall and $10 \times 5 \times 3$ elements for the shelf. In the case of the coupled solution, the first sub-domain is modelled with $3 \times 5 \times 7$ plus $1 \times 5 \times 3$ (superpositon region) solid elements, whereas the second sub-domain is modelled with 10×5 plate elements, as shown in Fig. 7.33. In the superposition region, $1 \times 5 \times 3$ solid elements are coupled to 1×5 plate elements.

Results are presented in Tab. 7.14. Transverse displacement u_z is computed at the top of the shelf in the middle of its free edge. Displacement u_x is computed at the top of the wall ($x = 0.06$ m, $y = 0.05$). In-plane normal stresses σ_{xx} is computed at the top of the shelf at its centre and out-of-plane shear stress σ_{xz} is evaluated at the top of the core at the shelf centre. In the mixed-dimensional solution, the mechanics of the wall and the shelf are correctly modelled and coupled. In the shelf region, zig-zag function in the plate elements is not necessary to obtain accurate results for the transverse displacement in the case of $E^C = \frac{E^F}{12}$. On the contrary, third-order plate model without zig-zag function does

	$-10^6 \times u_z$ [m]	$10^8 \times u_x$ [m]	$10^{-4} \times \sigma_{xx}$ [Pa]	$-10^{-3} \times \sigma_{xz}$ [Pa]
		$\frac{E^F}{E^C} = 12$		
ABAQUS C3D20	1.474	8.215	3.426	1.100
S27	1.485	8.242	3.430	1.108
S27-ED3	1.458	8.242	3.430	0.409
S27-ED2Z	1.483	8.242	3.427	1.108
		$\frac{E^F}{E^C} = 120$		
ABAQUS C3D20	2.129	8.227	3.519	1.193
S27	2.146	8.253	3.520	1.193
S27-ED3	1.521	8.242	3.509	0.078
S27-ED2Z	2.078	8.242	3.543	1.190

Table 7.14. Shelf fixed to a wall.

not predict accurately the transverse displacement in the case of $E^C = \frac{E^F}{120}$. Shear stress is correctly evaluated only with the zig-zag function for both the ratios $\frac{E^F}{E^C}$.

Fig. 7.34 presents the through-the-thickness variation of the in-plane displacement u_x at the centre of the shelf. It is is accurately predicted by the model which includes the

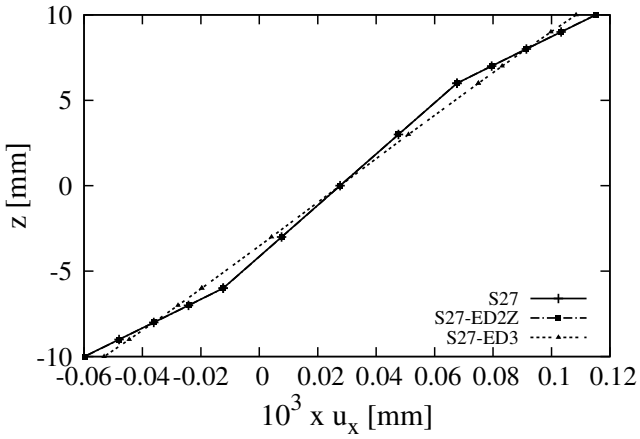

Figure 7.34. u_x through-the-thickness at the centre of the shelf, $E^C = \frac{E^F}{120}$.

zig-zag function. The higher-order model without the zig-zag function provides accurate results but approximate its through-the-thickness variation as almost linear instead of zig-zag. The variation of σ_{xz} along the x axis for $y/b = 1/2$ at the top of the core of the shelf is presented in Fig. 7.35. The coupled solution with plate elements which includes the zig-zag function match the three-dimensional solution for both $E^C = \frac{E^F}{12}$ and $E^C = \frac{E^F}{120}$.

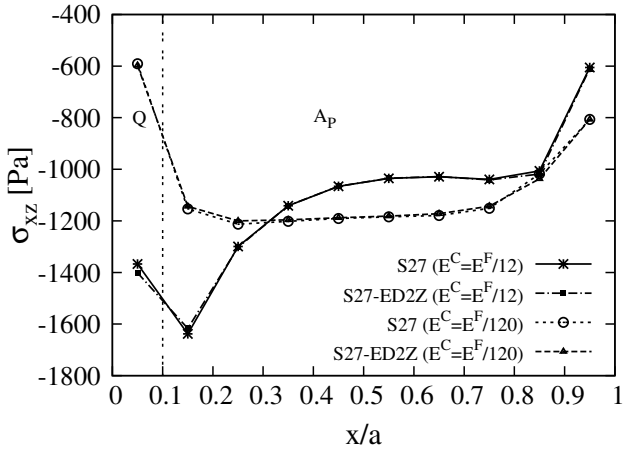

Figure 7.35. σ_{xz} along x axis for $y/b = 1/2$ at the top of the core of the shelf.

Chapter 8

Extension of the Arlequin method to piezoelectric analyses

Domain decomposition methods for multi-field problems, such as piezoelectric analyses, are not as well developed as for mechanical problems. In this section, the Arlequin method is extended to take into account electric quantities, such as the electric potential and the electric field, in the coupling operators. The global electro-mechanical problem is solved merging together the sub-domains. Similarly to Eq. 7.1, the generic variational principle becomes:

$$\delta L_{int}^{\xi}\left(\mathbf{a}_{\xi}\right)+\delta L_{c}^{\xi}\left(\mathbf{a}_{\xi}\right)=\delta L_{ext}^{\xi} \tag{8.1}$$

In the case of PVD-based models, the virtual variation of the strain energy is:

$$\begin{gathered}\delta L_{int}^{\xi}=\int_{A_{\xi}} \alpha_{\xi}\left(\delta \boldsymbol{\varepsilon}_{pG}^{T} \boldsymbol{\sigma}_{pH}+\delta \boldsymbol{\varepsilon}_{nG}^{T} \boldsymbol{\sigma}_{nH}-\delta \boldsymbol{E}_{pG}^{T} \boldsymbol{D}_{pH}-\delta E_{nG} D_{nH}\right) dV \\ \text{with } \left\{\begin{array}{l}\alpha_{\xi}=1 \text{ in } A_{\xi} \setminus S \\ \alpha_{1}+\alpha_{2}=1 \text{ in } S\end{array}\right.\end{gathered} \tag{8.2}$$

α_{ξ} are weighting functions to scale energy in each sub-domain. In the case of RMVT-D$_z$ or RMVT-D$_z$-$\boldsymbol{\sigma}_n$ models, Eq. (8.2) changes according to Eq. (6.98) and Eq. (6.99), respectively. Two coupling operators are proposed as extension of classical mechanical ones presented in Eqs. 7.4 and 7.5:

- L^2 electro-mechanical coupling:

$$\delta C_{\xi}=\int_{S_{\xi}} \delta \boldsymbol{\lambda}^{T} \mathbf{a}_{\xi} \, dV=\int_{S_{\xi}} \delta \boldsymbol{\lambda}_{\boldsymbol{u}}^{T} \mathbf{u}_{\xi}+\delta \lambda_{\phi}^{T} \phi_{\xi} \, dV \tag{8.3}$$

- H^1 electro-mechanical coupling:

$$\begin{aligned}\delta C_\xi = &\int_{S_\xi} \left\{ \delta \boldsymbol{\lambda}_{\boldsymbol{u}}^T \mathbf{u}_\xi + \delta \lambda_\phi^T \phi_\xi \right\} \, dV + \\ &\int_{S_\xi} \left\{ \tilde{l}^2 \boldsymbol{\varepsilon}^T \left(\delta \boldsymbol{\lambda}_{\boldsymbol{u}} \right) \boldsymbol{\varepsilon} \left(\mathbf{u}_\xi \right) \right\} \, dV + \\ &\int_{S_\xi} \left\{ \tilde{l}^2 \boldsymbol{E} \left(\delta \lambda_\phi \right) \boldsymbol{E} \left(\phi_\xi \right) \right\} \, dV\end{aligned} \tag{8.4}$$

Here $\boldsymbol{\lambda}$ is divided into components related to displacements (subscript $\boldsymbol{u}$) and the component related to the electric potential (subscript ϕ). $\boldsymbol{\varepsilon}\left(\boldsymbol{\lambda}_{\boldsymbol{u}}\right)$ is defined in the same manner as the mechanical strain $\boldsymbol{\varepsilon}\left(\mathbf{u}_\xi\right)$ where the Lagrangian multiplier field is used instead of the displacement one. The same applies to $\boldsymbol{E}\left(\lambda_\phi\right)$. Applying the Green formula to Eq. (8.1) it is possible to derive the local Euler equations enforced by the coupling operator in the superposition zone. In the case of L^2 they are:

$$\begin{aligned}\left(\boldsymbol{u}_1 - \boldsymbol{u}_2\right) &= 0 \\ \left(\phi_1 - \phi_2\right) &= 0\end{aligned} \tag{8.5}$$

whereas for H^1 they are:

$$\begin{aligned}\left(\boldsymbol{u}_1 - \boldsymbol{u}_2\right) - \tilde{l}^2 \left[\Delta\left(\boldsymbol{u}_1\right) - \Delta\left(\boldsymbol{u}_2\right)\right] &= 0 \\ \left(\phi_1 - \phi_2\right) - \tilde{l}^2 \left[\Delta\left(\phi_1\right) - \Delta\left(\phi_2\right)\right] &= 0\end{aligned} \tag{8.6}$$

where Δ is the Laplacian. Eqs. (8.5) enforce a point-by-point coincidence of the displacement fields and electric potential field in the two sub-domains, whereas Eqs. (8.6) consider also the spatial derivatives of the fields. A weighted sum between the fields and their derivatives is enforced to be equal in the two sub-domains. The parameter $\tilde{l}$ multiplies the contribution of the derivatives of displacement and electric potential, determining their weight in the equations.

8.1 Piezoelectric plate elements

In this section, the mechanical and piezoelectric plate elements based on different kinematics and variational principles presented in Sec. 6.4 are coupled via the Arelquin method. Plate's volume is divided into two sub-domains A_1 and A_2 that are partially overlapped. S represents the overlapping volume. For each sub-domain, a different model is assumed:

$$\mathbf{a}_\xi^k = N_i F_{\tau_\xi} \mathbf{q}_{\tau_\xi i}^k \quad \text{with} \quad \tau_\xi = 1,2,\ldots,N_u^{A_\xi}, \;\; \xi = 1,2 \tag{8.7}$$

The Lagrangian multiplier field is discretised according to UF:

$$\boldsymbol{\lambda}^k = N_i F_{\tau_\lambda} \boldsymbol{\Lambda}_{\tau_\lambda i}^k \tag{8.8}$$

$\boldsymbol{\Lambda}$ is the vector of Lagrangian multipliers nodal unknowns.The virtual work for a k-layer is derived via substitution of Eq. (8.8) into Eq. (8.3) or (8.4):

$$\delta C_\xi^k = \delta \boldsymbol{\Lambda}_{\tau_\lambda i}^{kT} \mathbf{C}_\xi^{k\tau_\lambda s_\xi ij} \mathbf{q}_{s_\xi j}^k \tag{8.9}$$

$\mathbf{C}_{\xi}^{k\tau_\lambda s_\xi ij}$ is the fundamental nucleo of the coupling matrix. In the case of L^2 coupling, the fundamental nucleo is diagonal and its components are:

$$C_{\xi mn}^{k\tau_\lambda s_\xi ij} = \delta_{mn} E_{\tau_\lambda s_\xi} \triangleleft N_i N_j \triangleright_\Omega \quad \text{with} \quad m,n = 1,2,3,4 \tag{8.10}$$

where δ_{mn} is Dirac's delta. Terms $E_{\tau_\lambda s_\xi}$ are defined as:

$$E_{\tau_\lambda s_\xi} = \int_{h_k} F_{\tau_\lambda} F_{s_\xi} \, dz \tag{8.11}$$

In the case of H^1 coupling the components of the fundamental nucleo are:

$$\begin{aligned}
&C_{11}^{k\tau_\lambda s_\xi ij} = C_{22}^{k\tau_\lambda s_\xi ij} = C_{33}^{k\tau_\lambda s_\xi ij} = C_{44}^{k\tau_\lambda s_\xi ij} = E_{\tau_\lambda s_\xi} \triangleleft N_i N_j \triangleright_\Omega + \\
&+\tilde{l}^2 \left[E_{\tau_\lambda s_\xi} \left(\triangleleft N_{i,x} N_{j,x} \triangleright_\Omega + \triangleleft N_{i,y} N_{j,y} \triangleright_\Omega \right) + E_{\tau_{\lambda,z} s_{\xi,z}} \triangleleft N_i N_j \triangleright_\Omega \right] \\
&C_{12}^{k\tau_\lambda s_\xi ij} = \tilde{l}^2 E_{\tau_\lambda s_\xi} \triangleleft N_{i,y} N_{j,x} \triangleright_\Omega \quad C_{13}^{k\tau_\lambda s_\xi ij} = \tilde{l}^2 E_{\tau_{\lambda,z} s_\xi} \triangleleft N_i N_{j,x} \triangleright_\Omega \\
&C_{21}^{k\tau_\lambda s_\xi ij} = \tilde{l}^2 E_{\tau_\lambda s_\xi} \triangleleft N_{i,x} N_{j,y} \triangleright_\Omega \quad C_{23}^{k\tau_\lambda s_\xi ij} = \tilde{l}^2 E_{\tau_{\lambda,z} s_\xi} \triangleleft N_i N_{j,y} \triangleright_\Omega \\
&C_{31}^{k\tau_\lambda s_\xi ij} = \tilde{l}^2 E_{\tau_\lambda s_{\xi,z}} \triangleleft N_{i,x} N_j \triangleright_\Omega \quad C_{32}^{k\tau_\lambda s_\xi ij} = \tilde{l}^2 E_{\tau_\lambda s_{\xi,z}} \triangleleft N_{i,y} N_j \triangleright_\Omega \\
&C_{41}^{k\tau_\lambda s_\xi ij} = C_{42}^{k\tau_\lambda s_\xi ij} = C_{43}^{k\tau_\lambda s_\xi ij} = C_{14}^{k\tau_\lambda s_\xi ij} = C_{24}^{k\tau_\lambda s_\xi ij} = C_{34}^{k\tau_\lambda s_\xi ij} = 0
\end{aligned} \tag{8.12}$$

Considering the whole structure and assuming that the refined model is adopted in the sub-domain A_2, the governing equations of the variable kinematic problem are:

$$\begin{bmatrix}
\overline{\mathbf{K}}_{A_1 \backslash S}^{\tau_1 s_1 ij} & \mathbf{0} & \mathbf{0} & \mathbf{0} & \mathbf{0} \\
\mathbf{0} & (1-\alpha)\,\overline{\mathbf{K}}_{A_1 \cap S}^{\tau_1 s_1 ij} & \mathbf{0} & \mathbf{0} & \overline{\mathbf{C}}_1^{\tau_1 s_1 ijT} \\
\mathbf{0} & \mathbf{0} & \overline{\mathbf{K}}_{A_2 \backslash S}^{\tau_2 s_2 ij} & \mathbf{0} & \mathbf{0} \\
\mathbf{0} & \mathbf{0} & \mathbf{0} & \alpha \overline{\mathbf{K}}_{A_2 \cap S}^{\tau_2 s_2 ij} & -\overline{\mathbf{C}}_2^{\tau_2 s_1 ijT} \\
\mathbf{0} & \overline{\mathbf{C}}_1^{\tau_1 s_1 ij} & \mathbf{0} & -\overline{\mathbf{C}}_2^{\tau_2 s_1 ij} & \mathbf{0}
\end{bmatrix}
\begin{Bmatrix}
\overline{\mathbf{q}}_{s_1 i}^{A_1 \backslash S} \\
\overline{\mathbf{q}}_{s_1 j}^{A_1 \cap S} \\
\overline{\mathbf{q}}_{s_2 j}^{A_2 \backslash S} \\
\overline{\mathbf{q}}_{s_2 j}^{A_2 \cap S} \\
\overline{\mathbf{\Lambda}}_{s_\lambda j}
\end{Bmatrix} =
= \begin{Bmatrix}
\overline{\mathbf{P}}_{\tau_1 i}^{A_1 \backslash S} \\
(1-\alpha)\,\overline{\mathbf{P}}_{\tau_1 i}^{A_1 \cap S} \\
\overline{\mathbf{P}}_{\tau_2 i}^{A_2 \backslash S} \\
\alpha \overline{\mathbf{P}}_{\tau_2 i}^{A_2 \cap S} \\
0
\end{Bmatrix} \tag{8.13}$$

Coupling is performed considering only the displacement fields and the electric potential distribution. The fundamental nucleo of the coupling matrix is, therefore, a 4×4 array in the case of PVD-based models as detailed in Eqs. (8.10) or (8.12). It is extended with zeros to a 4×5 array in case of RMVT-D$_z$ and to a 4×8 array in case of RMVT-D$_z$-$\boldsymbol{\sigma}_n$.

8.1.1 Results and discussion

Solutions adopting the classical mechanical coupling operators are first addressed. A narrow plate actuated via a piezoelectric finite patch is presented. The proposed electromechanical coupling operators are then addressed. The Heyliger plate, both in sensor and actuator configuration, is considered. The accuracy of the variable kinematics solutions is assessed towards the corresponding mono-model results and towards 3D FE or exact solutions. The effect of the choice of the coupling operator is investigated.

Narrow plate actuated via piezoelectric finite patch

A narrow plate in aluminium ($E = 73$ GPa, $\nu = 0.34$), clamped on one side, is considered. Plate's in-plane dimensions along the x- and y-axes are $a = 0.1$ m and $b = 0.01$ m, respectively. Its thickness is 0.002 m. A piezoelectric finite patch (see Table 8.1 for the material properties) is bonded at the top surface of the plate near its clamped side, as shown in Figure 8.1. Patch's in-plane dimensions are 0.01×0.01 m and its thickness

Properties	Fibre-reinforced composite	PZT-4
E_1 [Gpa]	132.38	81.3
E_2 [Gpa]	10.756	81.3
E_3 [Gpa]	10.756	64.5
G_{12} [Gpa]	5.654	30.6
G_{13} [Gpa]	5.654	25.6
G_{23} [Gpa]	3.606	25.6
ν_{12}	0.24	0.329
ν_{13}	0.24	0.432
ν_{23}	0.49	0.432
$e_{31} = e_{32}$ [C/m^2]	–	−5.2
e_{33} [C/m^2]	–	15.8
$e_{24} = e_{15}$ [C/m^2]	–	12.72
$\varepsilon_{11}/\varepsilon_0$	3.5	1475
$\varepsilon_{22}/\varepsilon_0$	3.0	1475
$\varepsilon_{33}/\varepsilon_0$	3.0	1300

Table 8.1. Material properties. $\varepsilon_0 = 8.85 \times 10^{-12}$ F/m is the vacuum permittivity.

is 0.001 m. An electric potential equal to 1 V is prescribed at the top surface of the piezoelectric patch. Null electric potential is assigned at its bottom surface.

Mono-model solutions are obtained with a regular mesh of 60×1 LW piezoelectric elements, assuming two computational layers for the plate. In the variable kinematic solutions an ESL mechanical model is adopted in the sub-domain A_2, see Figure 8.1. The refined

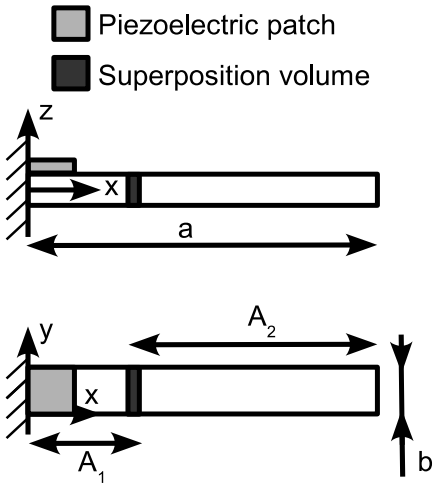

Figure 8.1. Clamped narrow plate actuated by a piezoelectric patch.

sub-domain A_1 consists of 12×1 LW piezoelectric elements. Only one element is superposed. Coupling is achieved via the classical coupling operators since in the superposition volume the electric field is not present. Reference results are obtained via the commercial FE software ABAQUS. Piezoelectric 3D FE C3D20RE, see ABAQUS (2005), have been adopted and convergence of transverse displacements within 1% has been obtained with a progressive refinement of the mesh.

Results are presented in Tab. 8.2. Transverse displacement u_z is computed at the centre of the plate and at $x = a$,$y = b/2$ on the mid-plane. Higher order LW models underestimate the reference solution by about 6%. The two coupling operators yield similar results. Variable kinematic solutions match the corresponding mono-model solutions: the mechanics of the plate far from the actuator is correctly modelled by an ESL mechanical theory, whereas the actuation of the patch requires a LW piezoelectric theory to be accurately described. The variation of u_z along the x-axis for $y = a/2$ at the top of the plate is presented in Fig. 8.2. The coupling operator H^1 is adopted. The bending induced by the piezoelectric patch can be noticed in the sub-domain A_1.

Heyliger Plate

A simply supported cross-ply [0/90] laminate composed of elastic fibre-reinforced material with piezoelectric layer bonded at the top and at the bottom surfaces is considered. Materials properties are presented in Table 8.1. The plate is square with side length a equal to 4 m. Total thickness is 1 m: each piezoelectric layer accounts for 10% and each elastic layer accounts for 40% of total thickness. Two set of boundary conditions and loadings are considered: the sensor case and the actuator case, see Fig. 8.3. Results are compared with the exact three-dimensional solutions provided by Heyliger [146]. Only a quarter of the

	$10^8 \times u_z^*$ [m]	$10^8 \times u_z^-$ [m]
3D	2.471	5.169
Mono-model solutions		
LD3	2.309	4.871
LD2	2.307	4.866
LD1	2.208	4.657
Variable kinematic solutions L^2		
LD3-ED1	2.309	4.870
LD2-ED1	2.307	4.866
LD1-ED1	2.207	4.657
Variable kinematic solutions H^1		
LD3-ED1	2.309	4.869
LD2-ED1	2.307	4.865
LD1-ED1	2.207	4.657

* Value at $x = a/2$,$y = b/2$ on mid-plane.
$^-$ Value at $x = a$,$y = b/2$ on mid-plane.

Table 8.2. Transverse displacements for the actuated narrow plate.

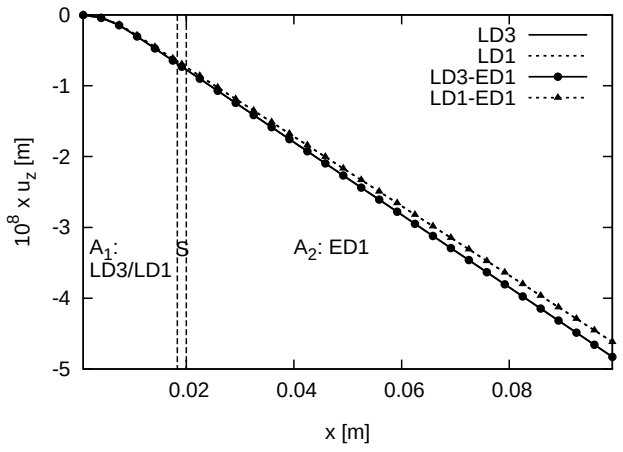

Figure 8.2. Transverse displacement along the x axis for $y = a/2$ at mid-plane of the actuated narrow plate.

plate is taken into account in the models. Mesh convergence for the transverse displacement u_z at $x = y = a/2$ at plate midplane is shown in Figs. 8.4 both for the sensor and the actuator case. In the following, mono-model results are evaluated with a mesh of 10 x 10 quadrilateral elements. Arlequin results adopt a square refined region of 5 x 5 elements at the centre of the plate, as shown in Fig. 8.5.

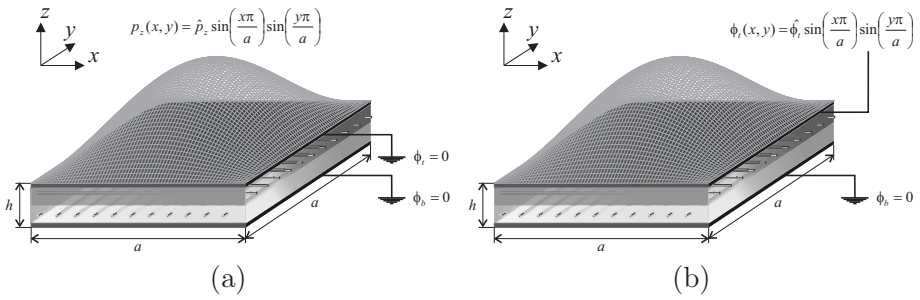

Figure 8.3. Heyliger plate in (a) sensor configuration and in (b) actuator configuration.

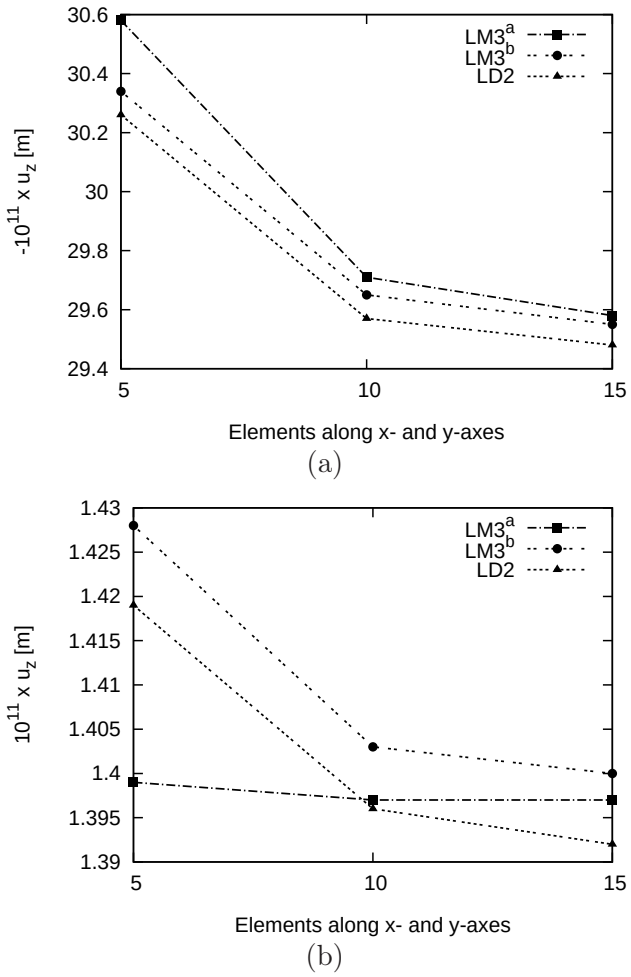

Figure 8.4. Convergence of the transverse displacement u_z versus the number of elements for the Heyliger plate (a) in the sensor case and (b) in the actuator case.

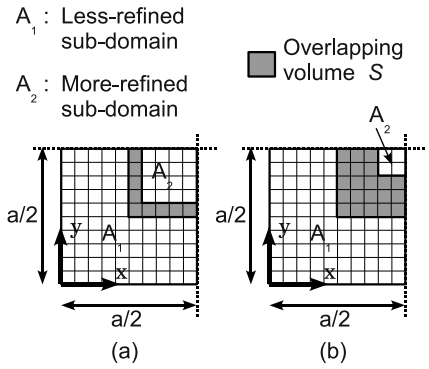

Figure 8.5. Coupling between the two sub-domains with (a) minimum superposition volume and (b) extended superposition volume.

Comparison Between The Electro-Mechanical Coupling Operators In the sensor case, a double sinusoidal pressure is applied on the top surface of the plate, see Fig. 8.3(a). Its amplitude is 1 Pa. Top and bottom surfaces are fixed at zero potential. Two superposition zone, denominated minimum and extended, are considered, as shown in Fig. 8.5. In the superposition volume two solutions that do not necessarily match exist. The electro-mechanical coupling operators in Eqs. (8.3) and (8.4) are adopted. $\tilde{l} = l_{el}$ is considered in the case of minimum superposition and $\tilde{l} = 3l_{el}$ in the case of extended superposition. Coupling between LD2- and LD4-based finite elements is adopted and results are compared with LD4 mono-model solutions. Results for primary variables are very similar for both the coupling operator and for both the superposition volume. They match the mono-model solutions. Transverse displacement u_z variation along the x axis for $y = a/2$ at the top of the plate is presented in Fig. 8.6 in the case of minimum superposition volume and H^1 coupling operator. Fig. 8.7 show the variation of the electric potential ϕ at plate mid-plane with extended superposition and L^2 coupling operator. Variable kinematic results match the mono-model results: the proposed electro-mechanical operators couple effectively the two sub-domains. The influence of the choice of the coupling operator and the superposition extension is presented in Figs. 8.8 for the stress component σ_{xx}. It is computed along the x axis for $y = a/2$ at the top of the plate. It is computed along the x axis for $y = a/2$ at the top of the plate. Difference between the results is greater in the superposition zone. In the following the reduced superpostion volume is adopted in order to reduce the total number of degrees of freedom.

Comparison With Exact Results In Sensor Case Loads and boundary conditions are as, once again, as in Fig. 8.3(a). Tables 8.3, 8.4 and 8.5 present the electric potential, the transverse normal stress and the transverse electric displacement, respectively.

Results are computed at the centre of the plate across it thickness. Mono-model solutions are based on PVD (LD1), on RMVT-D$_z$ (LM3^b) and on RMVT-D$_z$-$\boldsymbol{\sigma}_n$ (LM3^a). Variable kinematic solutions couple PVD- and RMVT-D$_z$-based sub-domains (LD1-LM3^b)

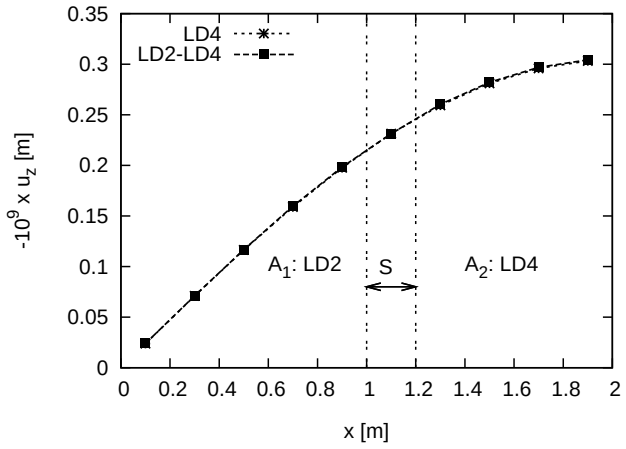

Figure 8.6. Transverse displacement along the x axis for $y = a/2$ at the top of the Heyliger plate via mono-model LD4 and variable kinematic LD2-LD4, H^1 coupling operator.

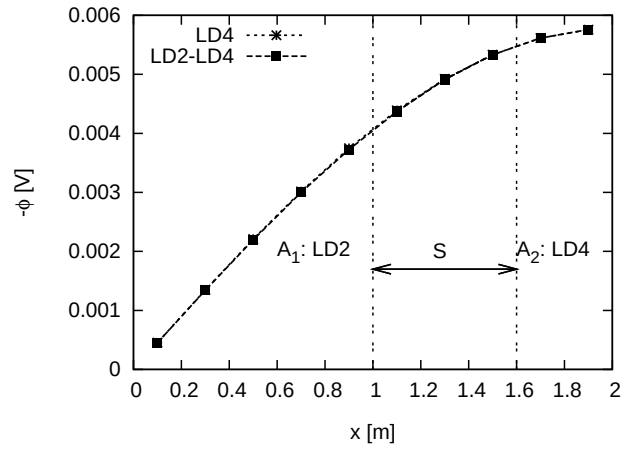

Figure 8.7. Electric potential along the x axis for $y = a/2$ at the Heyliger plate mid-plane, L^2 coupling operator.

and PVD- and RMVT-D$_z$-$\boldsymbol{\sigma}_n$-based sub-domains (LD1-LM3^a). The number of degrees of freedom is reduced by more than 35%. In Table 8.3, higher order models match the exact solution. Electric potential is accurately predicted by variable kinematic models whereas LD1 mono-model provides inaccurate results in the piezoelectric layers. Table 8.4 shows that an accurate prediction of transverse normal stress requires a RMVT-D$_z$-$\boldsymbol{\sigma}_n$ based model. LD1-LM3^a results matches the RMVT-D$_z$-$\boldsymbol{\sigma}_n$-based mono-model solution. RMVT-based models are mandatory for the computation of the transverse electric displacement, as shown in Table 8.5. Both the transverse quantities $\boldsymbol{\sigma}_{zz}$ and D$_z$ are not accurately computed in the case of variable kinematic solution LD1-LM3^b with H^1 coupling, see Table 8.4 and 8.5. The inaccuracy is due to the derivative of displacement and

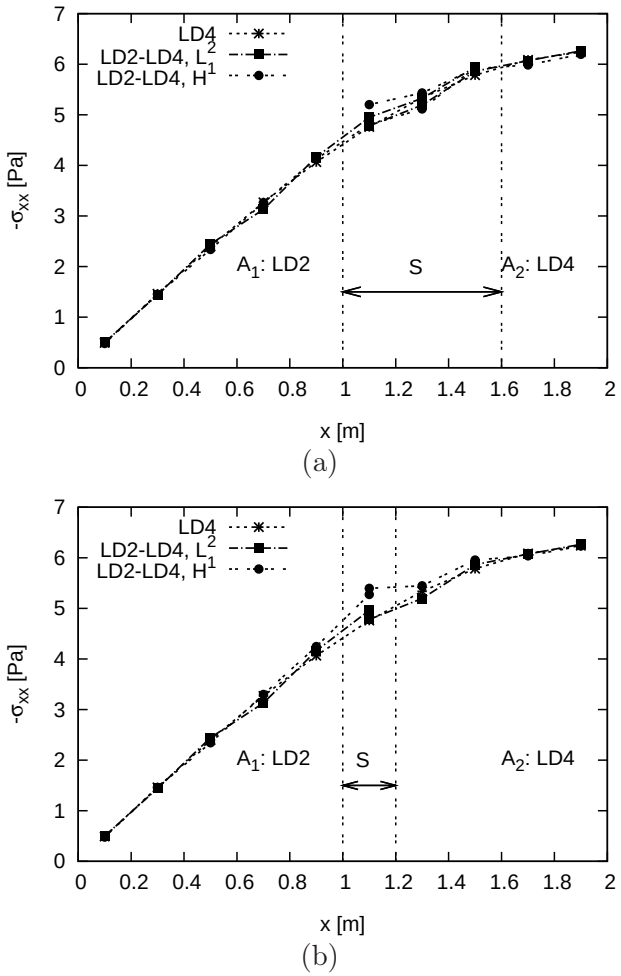

Figure 8.8. In-plane normal stress along the x axis for $y = a/2$ at the top of the Heyliger plate via mono-model LD4 and variable kinematic LD2-LD4 with (a) extended and (b) minimum superposition volume.

electric potential in the coupling operator, see Eq. (8.6). LD1 sub-model is not refined enough to compute accurately these values. If a second order model is adopted as less refined sub-model results are accurate with the H^1 coupling, as shown in Table 8.6. Midplane transverse displacement at the centre of the plate is presented in Table 8.7. LM3^a results match the reference solution. All the considered solutions are accurate. Fig. 8.9 presents the variation of D_z at the centre of the plate across its thickness. LM4^b mono-model result matches the exact reference solution, whereas LD2 mono-model superestimates it by about 20%. Arlequin results are obtained with LM4^b as refined model (sub-domain A_2) and LD2 in sub-domain A_1 using the coupling operator L^2. Arlequin results matches LM4^b mono-model results and the exact solution. With respect to LM4^b mono-model the total number of degrees of freedom is reduced by about 36%.

$-10^2 \times \phi$ [V]								
		Mono-model solutions			Variable kinematic solutions			
					L^2 coupling		H^1 coupling	
Height	3D	LM3[a]	LM3[b]	LD1	LD1-LM3[a]	LD1-LM3[b]	LD1-LM3[a]	LD1-LM3[b]
1.000	0.000	0.000	0.000	0.000	0.000	0.000	0.000	0.000
0.975	0.189	0.179	0.178	0.137	0.178	0.178	0.175	0.176
0.950	0.358	0.333	0.330	0.275	0.332	0.331	0.325	0.325
0.925	0.488	0.461	0.458	0.413	0.459	0.458	0.450	0.448
0.900	0.598	0.564	0.560	0.551	0.562	0.561	0.550	0.544
0.800	0.589	0.556	0.553	0.555	0.556	0.554	0.537	0.536
0.700	0.589	0.556	0.553	0.559	0.557	0.556	0.534	0.533
0.600	0.596	0.564	0.560	0.563	0.566	0.564	0.540	0.539
0.500	0.611	0.579	0.576	0.567	0.581	0.580	0.554	0.555
0.400	0.634	0.601	0.598	0.602	0.604	0.603	0.578	0.577
0.300	0.665	0.632	0.629	0.638	0.634	0.633	0.610	0.610
0.200	0.706	0.671	0.668	0.674	0.673	0.671	0.653	0.652
0.100	0.756	0.720	0.717	0.709	0.720	0.720	0.707	0.701
0.750	0.602	0.575	0.572	0.532	0.576	0.575	0.565	0.563
0.500	0.425	0.407	0.405	0.354	0.407	0.407	0.400	0.400
0.250	0.224	0.215	0.214	0.177	0.215	0.215	0.212	0.212
0.000	0.000	0.000	0.000	0.000	0.000	0.000	0.000	0.000
DOF*		12584	7865	2420	6244	4840	6244	4840

[a] RMVT-D$_z$-$\boldsymbol{\sigma}_n$.
[b] RMVT-D$_z$.
* Number of degrees of freedom of the model.

Table 8.3. Heyliger plate, sensor case. Electrical potential at the centre of the plate across its thickness.

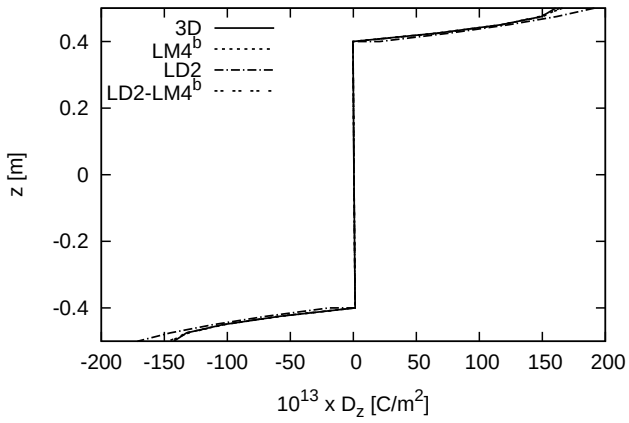

Figure 8.9. Transverse electric displacement at the centre of the Heyliger plate with H^1 coupling operator.

$-10^1 \times \sigma_{zz}$ [Pa]								
		Mono-model solutions			Variable kinematic solutions			
					L^2 coupling		H^1 coupling	
Height	3D	LM3[a]	LM3[b]	LD1	LD1-LM3[a]	LD1-LM3[b]	LD1-LM3[a]	LD1-LM3[b]
1.000	10.00	10.07	9.859	22.95	10.06	9.685	10.10	10.45
0.975	9.965	10.05	9.836	16.31	10.06	9.851	10.13	9.956
0.950	9.868	9.955	9.776	9.684	9.974	9.820	9.994	10.25
0.925	9.715	9.806	9.662	3.050	9.830	9.666	9.761	10.05
0.900	9.515	9.624	9.479	−3.583	9.671	9.465	9.525	8.045
0.900	9.515	9.624	9.749	9.225	9.671	9.761	9.525	9.809
0.800	8.519	8.627	8.555	8.257	8.608	8.487	8.279	8.412
0.700	7.374	7.463	7.456	7.290	7.388	7.384	7.061	7.244
0.600	6.168	6.226	6.285	6.322	6.140	6.231	5.948	6.128
0.500	4.983	5.012	4.871	5.355	4.990	4.806	5.021	4.888
0.500	4.983	5.012	5.156	4.568	4.990	5.184	5.021	5.159
0.400	3.804	3.827	3.772	3.653	3.899	3.807	4.126	3.921
0.300	2.613	2.601	2.612	2.737	2.664	2.670	3.014	2.803
0.200	1.482	1.447	1.523	1.822	1.456	1.583	1.808	1.645
0.100	0.486	0.473	0.351	0.906	0.446	0.353	0.632	0.286
0.100	0.486	0.473	0.623	12.74	0.446	0.630	0.632	2.110
0.750	0.284	0.270	0.438	6.580	0.231	0.446	0.314	0.027
0.500	0.131	0.126	0.322	0.411	0.106	0.281	0.091	−0.166
0.250	0.034	0.035	0.260	−5.757	0.035	0.240	−0.039	0.147
0.000	0.000	−0.007	0.235	−11.92	−0.014	0.429	−0.080	−0.415

[a] RMVT-D$_z$-$\boldsymbol{\sigma}_n$.
[b] RMVT-D$_z$.

Table 8.4. Heyliger plate, sensor case. Transverse normal stress at the centre of the plate across its thickness.

Comparison With Exact Results In Actuator Case In the actuator case, a double sinusoidal electric potential is applied on the top surface of the plate, see Fig. 8.3(b). Its amplitude is 1 V and the bottom surface is fixed at zero potential. Midplane transverse displacement at the centre of the plate is presented in Table 8.7. LD1 superestimate the reference solution by about 6%. Variable kinematic results follow closely the corresponding mono-model solutions in the case of L^2 coupling. Values with H^1 are higher than with the correspondent monomodels: as already observed in Guidault and Belytschko (2007), the relation in Eq. (8.6) enforced by H^1 may induce a displacement shift between the sub-domains which can be problematic when bending mechanics is predominant. This is especially true if the less refined sub-model does not accurately model the mechanics of the structure, as it is the case of LD1. When LD2 sub-model is adopted, results with the two coupling operators are similar. Table 8.8 presents σ_{xx} computed at the centre of the plate across it thickness. LD1 results are inaccurate, in particular in the top piezoelectric layer. Higher order mono-models follow closely the reference solution and variable kinematic solutions match the corresponding mono-models results.

$-10^{13} \times D_z$ [C/m^2]								
		Mono-model solutions			Variable kinematic solutions			
					L^2 coupling		H^1 coupling	
Height	3D	LM3^a	LM3^b	LD1	LD1-LM3^a	LD1-LM3^b	LD1-LM3^a	LD1-LM3^b
1.000	160.5	155.6	155.7	−837.1	152.0	147.7	156.7	−25.18
0.975	149.3	143.9	144.8	−372.9	143.5	137.9	160.3	333.7
0.950	117.2	113.0	113.6	91.13	117.3	133.0	131.6	166.8
0.925	66.56	64.34	64.53	555.2	70.36	98.40	76.24	−89.94
0.900	−0.338	−0.302	−0.301	1019.	−0.255	−0.277	−0.468	−0.396
0.900	−0.338	−0.302	−0.301	0.106	−0.255	−0.277	−0.468	−0.396
0.800	−0.127	−0.103	−0.101	0.106	−0.062	−0.065	−0.204	−0.161
0.700	0.081	0.095	0.096	0.106	0.128	0.131	0.036	0.049
0.600	0.291	0.295	0.295	0.106	0.317	0.319	0.268	0.262
0.500	0.505	0.498	0.498	0.106	0.506	0.508	0.502	0.501
0.500	0.505	0.498	0.498	0.944	0.506	0.508	0.502	0.501
0.400	0.725	0.708	0.708	0.944	0.704	0.701	0.742	0.749
0.300	0.956	0.928	0.927	0.944	0.914	0.912	0.992	0.979
0.200	1.199	1.160	1.159	0.944	1.139	1.146	1.269	1.223
0.100	1.458	1.408	1.406	0.944	1.385	1.409	1.588	1.509
0.100	1.458	1.408	1.406	−944.6	1.385	1.409	1.588	1.509
0.750	−58.35	−55.87	−56.06	−513.0	−62.87	−93.92	−69.13	101.9
0.500	−103.6	−99.10	−99.73	−81.47	−104.3	−122.2	−119.0	−155.8
0.250	−132.4	−126.7	−127.4	350.1	−127.0	−122.0	−144.3	−320.9
0.000	−142.4	−137.0	−137.2	781.6	−135.0	−132.1	−140.9	57.89

[a] RMVT-D$_z$-$\boldsymbol{\sigma}_n$.
[b] RMVT-D$_z$.

Table 8.5. Heyliger plate, sensor case. Transverse electric displacement at the centre of the plate across its thickness.

	$-10 \times \sigma_{zz}$ [Pa]		$-10^{13} \times D_z$ [C/m^2]	
Height	LD2	LD2-LM3[b]	LD2	LD2-LM3[b]
1.000	10.08	10.04	183.2	153.3
0.975	9.810	9.908	155.7	153.6
0.950	9.659	9.816	119.4	91.24
0.925	9.632	9.667	74.55	21.54
0.900	9.730	9.358	20.91	−0.245
0.900	9.961	9.856	−0.295	−0.245
0.800	8.521	8.599	−0.097	−0.068
0.700	7.277	7.485	0.100	0.112
0.600	6.229	6.310	0.297	0.301
0.500	5.376	4.871	0.495	0.503
0.500	4.789	5.147	0.483	0.503
0.400	3.809	3.747	0.708	0.704
0.300	2.727	2.586	0.933	0.917
0.200	1.541	1.487	1.158	1.137
0.100	0.251	0.268	1.383	1.363
0.100	0.384	0.731	−19.24	1.363
0.750	0.466	0.446	−67.51	−26.64
0.500	0.433	0.281	−107.6	−81.00
0.250	0.284	0.187	−139.7	−129.6
0.000	0.020	0.114	−163.7	−140.4

[b] RMVT-D$_z$.

Table 8.6. Heyliger plate, sensor case. Transverse normal stress and transverse electric displacement and at the centre of the plate across its thickness, H^1 coupling operator.

	$10^{11} \times u_z$ [m]	
	Sensor case	Actuator case
3D	30.02	1.471
Mono-model solutions		
LM3[a]	−29.71	1.397
LM3[b]	−29.65	1.403
LD2	−29.57	1.396
LD1	−29.44	1.519
Variable kinematic solutions L^2		
LD2-LM3[a]	−29.76	1.369
LD2-LM3[b]	−29.61	1.398
LD1-LM3[a]	−29.80	1.336
LD1-LM3[b]	−29.61	1.390
Variable kinematic solutions H^1		
LD2-LM3[a]	−29.90	1.388
LD2-LM3[b]	−29.72	1.410
LD1-LM3[a]	−30.01	1.532
LD1-LM3[b]	−29.91	1.420

[a] RMVT-D$_z$-$\boldsymbol{\sigma}_n$.
[b] RMVT-D$_z$.

Table 8.7. Midplane transverse displacement at the centre of the Heyliger plate.

$10^2 \times \sigma_{xx}$ [Pa]								
		Mono-model solutions			Variable kinematic solutions			
					L^2 coupling		H^1 coupling	
Height	3D	LM3[a]	LM3[b]	LD1	LD1-LM3[a]	LD1-LM3[b]	LD1-LM3[a]	LD1-LM3[b]
1.000	111.8	116.1	117.3	341.5	116.5	128.6	119.5	111.9
0.975	63.73	68.61	69.34	182.5	70.65	68.75	67.18	65.96
0.950	15.83	21.41	21.72	23.47	24.44	25.66	18.19	20.04
0.925	−32.00	−25.75	−25.81	−135.5	−22.06	−18.59	−29.45	−25.42
0.900	−79.86	−73.19	−73.59	−294.6	−68.93	−82.03	−77.80	−70.09
0.900	−51.68	−67.27	−67.79	−64.21	−63.11	−69.92	−73.91	−72.94
0.800	−33.13	−39.68	−39.95	−45.68	−40.60	−40.99	−38.29	−40.26
0.700	−19.84	−21.41	−21.47	−27.14	−22.75	−22.58	−21.45	−20.73
0.600	−9.773	−8.605	−8.611	−8.615	−7.992	−9.172	−12.05	−8.122
0.500	−1.390	2.620	2.399	9.917	5.220	4.769	1.305	3.817
0.500	−1.308	−1.305	−1.238	−1.175	−0.156	−1.005	−3.371	−1.234
0.400	−0.578	−0.275	−0.253	−0.114	0.916	−0.022	−2.185	−0.137
0.300	0.134	0.598	0.586	0.946	1.641	0.781	−0.924	0.796
0.200	0.846	1.439	1.427	2.007	2.253	1.572	0.343	1.712
0.100	1.572	2.370	2.416	3.068	2.984	2.517	1.550	2.751
0.100	14.52	14.30	14.34	14.34	0.15.	14.64	13.17	16.41
0.750	17.80	17.37	17.46	19.05	18.15	17.68	17.08	19.75
0.500	21.09	20.48	20.59	23.76	20.88	20.73	20.62	23.08
0.250	24.42	23.62	23.76	28.47	23.70	23.78	24.02	26.44
0.000	27.79	26.82	26.96	33.17	26.53	26.84	27.53	29.87

[a] RMVT-D$_z$-$\boldsymbol{\sigma}_n$.
[b] RMVT-D$_z$.

Table 8.8. Heyliger plate, actuator case. In-plane normal stress at the centre of the plate across its thickness.

8.2 ABAQUS implementation for piezoelectric plane stress elements

Recently, Qiao et al. [147] implemented the Arlequin method for mechanical problems in the commercial FEM software ABAQUS. Following the same approach, in this section the Arlequin method with the H^1 electro-mechanical coupling operator proposed in Eq. 8.4 is implemented in ABAQUS for piezoelectric plane stress elements. Contrary to the previously presented results, in this section the sub-domains share the same model, i.e. the same type of finite element. It is the mesh refinement that is not the same in the sub-domains.

8.2.1 Calculation of coupling matrices

Linear quadrilateral piezoelectric plane stress finite elements, known in ABAQUS [63] as CPS4E, are considered. The Lagrangian multiplier field is discretised as the less refined sub-domain to avoid a locking phenomenon. The concept of virtual element (subscript V), whose nodes coincide with the ones of the coarse element (subscript C) and is used to discretise the multiplier field, is introduced in Fig. 8.10. The virtual element is not

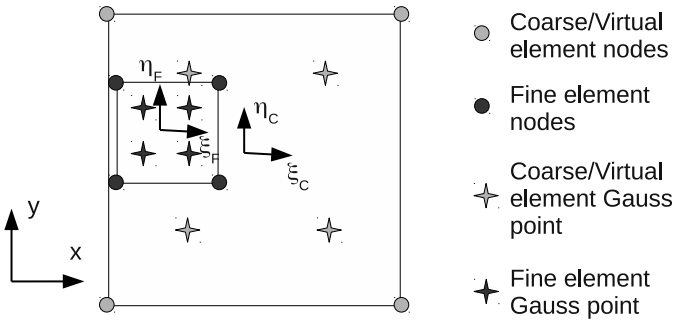

Figure 8.10. Coarse, fine and virtual element in the case of coupling between linear quadrilateral elements.

directly implemented in ABAQUS, but its nodes and its nodal quantities are employed by the Arlequin user elements defined in Sec. 8.2.2.

The displacement and electric potential fields are expressed in terms of their nodal values $\boldsymbol{q}$:

$$\left\{ \begin{array}{c} u_x \\ u_y \\ \phi \end{array} \right\} = \boldsymbol{N}\boldsymbol{q} = \left[\begin{array}{cccccccccccc} N_1 & 0 & 0 & N_2 & 0 & 0 & N_3 & 0 & 0 & N_4 & 0 & 0 \\ 0 & N_1 & 0 & 0 & N_2 & 0 & 0 & N_3 & 0 & 0 & N_4 & 0 \\ 0 & 0 & N_1 & 0 & 0 & N_2 & 0 & 0 & N_3 & 0 & 0 & N_4 \end{array} \right] \boldsymbol{q} \tag{8.14}$$

where N_i are the shape functions of the element. The strain and electric fields are given

as:

$$\left\{ \begin{array}{c} \varepsilon_{xx} \\ \varepsilon_{yy} \\ \varepsilon_{xy} \\ E_x \\ E_y \end{array} \right\} = \boldsymbol{B}\boldsymbol{q} = \left[\begin{array}{cccccccccccc} N_{1,x} & 0 & 0 & N_{2,x} & 0 & 0 & N_{3,x} & 0 & 0 & N_{4,x} & 0 & 0 \\ 0 & N_{1,y} & 0 & 0 & N_{2,y} & 0 & 0 & N_{3,y} & 0 & 0 & N_{4,y} & 0 \\ N_{1,y} & N_{1,x} & 0 & N_{2,y} & N_{2,x} & 0 & N_{3,y} & N_{3,x} & 0 & N_{4,y} & N_{4,x} & 0 \\ 0 & 0 & N_{1,x} & 0 & 0 & N_{2,x} & 0 & 0 & N_{3,x} & 0 & 0 & N_{4,x} \\ 0 & 0 & N_{1,y} & 0 & 0 & N_{2,y} & 0 & 0 & N_{3,y} & 0 & 0 & N_{4,y} \end{array} \right] \boldsymbol{q} \tag{8.15}$$

Comma denotes differentation. Similar relations hold for the Lagrangian multiplier field.

The calculation of the coupling matrix associated to the coarse element is straightforward, since the Lagrangian multiplier field and the coarse displacement field share the same discretisation. The coupling matrix related to the coarse element is:

$$\boldsymbol{C}_C = \int_{\Omega_C} \left(\boldsymbol{N}_V^T \boldsymbol{N}_C + \tilde{l}^2 \boldsymbol{B}_V^T \boldsymbol{B}_C \right) \mathrm{d}\Omega_C = \int_{\Omega_C} \left(\boldsymbol{N}_C^T \boldsymbol{N}_C + \tilde{l}^2 \boldsymbol{B}_C^T \boldsymbol{B}_C \right) \mathrm{d}\Omega_C \tag{8.16}$$

where Ω_C is the domain of the coarse element. Gaussian quadrature is used to perform numerical integration.

The major complexity is in the calculation of the coupling matrix associated to the fine element (subscript F), since Gauss points of the fine element do not coincide with those of the virtual element (see Fig. 8.10):

$$\boldsymbol{C}_F = \int_{\Omega_F} \left(\boldsymbol{N}_V^T \boldsymbol{N}_F + \tilde{l}^2 \boldsymbol{B}_V^T \boldsymbol{B}_F \right) \mathrm{d}\Omega_F \tag{8.17}$$

where Ω_F is the domain of the fine element. In this case, the generic Gauss point G used in the numerical integration is the one of the fine element. In order to evaluate $\boldsymbol{N}_V$ and $\boldsymbol{B}_V$ in G, it is necessary to compute the natural coordinates of G in the reference system of the virtual element, i.e. $\left(\xi_V^G, \eta_V^G\right)$. The first step is to compute the real coordinates of G. Since we are considering an isoparametric element:

$$\begin{array}{l} x^G = \sum_{i=1}^4 N_{Fi}\left(\xi_F^G, \eta_F^G\right) x_{Fi} \\ y^G = \sum_{i=1}^4 N_{Fi}\left(\xi_F^G, \eta_F^G\right) y_{Fi} \end{array} \tag{8.18}$$

where (x_{Fi}, y_{Fi}) are the real coordinates of the nodes of the fine element and N_{Fi} are the shape functions of the fine element. The natural coordinates of G in the fine element $\left(\xi_F^G, \eta_F^G\right)$ depend on the Gaussian integration scheme. In the case of linear quadrilateral finite elements such as CPS4E, four integration points are required. The second and final step consists in computing ξ_V^G and η_V^G on the basis of x^G and y^G solving the inverse problem:

$$\begin{array}{l} x^G = \sum_{i=1}^4 N_{Vi}\left(\xi_V^G, \eta_V^G\right) x_{Vi} \\ y^G = \sum_{i=1}^4 N_{Vi}\left(\xi_V^G, \eta_V^G\right) y_{Vi} \end{array} \tag{8.19}$$

where N_{Vi} are the shape functions of the virtual element and (x_{Vi},y_{Vi}) are the real coordinates of the nodes of the virtual element. In the case of CPS4E elements, this is a non-linear problem. It has been solved with a standard Newton-Raphson algorithm.

8.2.2 Arlequin user elements

The implementation of the Arlequin method in ABAQUS requires the use of user defined elements [147]. They are coded in a Fortran subroutine known as UEL that is linked to ABAQUS at the beginning of an analysis. According to the ABAQUS documentation [63], the stiffness matrix AMATRIX and the nodal load vector RHS have to be defined. The linear system to be solved in a static analysis for the whole structure is:

$$\begin{bmatrix} \overline{\mathbf{K}}_C^{A_1\setminus S} & \mathbf{0} & \mathbf{0} & \mathbf{0} & \mathbf{0} \\ \mathbf{0} & (1-\alpha)\,\overline{\mathbf{K}}_C^{A_1\cap S} & \mathbf{0} & \mathbf{0} & \overline{\mathbf{C}}_C^T \\ \mathbf{0} & \mathbf{0} & \overline{\mathbf{K}}_F^{A_2\setminus S} & \mathbf{0} & \mathbf{0} \\ \mathbf{0} & \mathbf{0} & \mathbf{0} & \alpha\overline{\mathbf{K}}_F^{A_2\cap S} & -\overline{\mathbf{C}}_F^T \\ \mathbf{0} & \overline{\mathbf{C}}_C & \mathbf{0} & -\overline{\mathbf{C}}_F & \mathbf{0} \end{bmatrix} \begin{Bmatrix} \overline{\mathbf{q}}_C^{A_1\setminus S} \\ \overline{\mathbf{q}}_C^{A_1\cap S} \\ \overline{\mathbf{q}}_F^{A_2\setminus S} \\ \overline{\mathbf{q}}_F^{A_2\cap S} \\ \overline{\mathbf{q}}_V^{S} \end{Bmatrix} = \begin{Bmatrix} \overline{\mathbf{P}}_C^{A_1\setminus S} \\ (1-\alpha)\,\overline{\mathbf{P}}_C^{A_1\cap S} \\ \overline{\mathbf{P}}_F^{A_2\setminus S} \\ \alpha\overline{\mathbf{P}}_F^{A_2\cap S} \\ 0 \end{Bmatrix} \tag{8.20}$$

where the coarse mesh is employed in the sub-domain A_1 and the fine mesh in A_2. V is the overlapping volume.

Two Arlequin user elements have to be defined, one related to the coarse mesh (UEL$_C$) and one to the fine mesh (UEL$_F$). In the case of CPS4E elements, both the Arlequin user elements have eight nodes:

- UEL$_C$: four nodes in common with the corresponding CPS4E coarse element plus the four nodes of the virtual element
- UEL$_F$: four nodes in common with the corresponding CPS4E fine element plus the four nodes of the virtual element

Their stiffness matrices are:

$$\begin{aligned} \text{AMATRIX}_C &= \begin{bmatrix} -\alpha\mathbf{K}_C & \mathbf{C}_C^T \\ \mathbf{C}_C & 0 \end{bmatrix} \\ \text{AMATRIX}_F &= \begin{bmatrix} -(1-\alpha)\,\mathbf{K}_F & \mathbf{C}_F^T \\ \mathbf{C}_F & 0 \end{bmatrix} \end{aligned} \tag{8.21}$$

$\mathbf{K}_C$ and $\mathbf{K}_F$ are equal to the stiffness matrices of the corresponding CPS4E coarse and fine elements, respectively. The corresponding RHS are computed in the subroutine as:

$$\begin{aligned} \mathrm{RHS}_C &= -\mathrm{AMATRIX}_C \begin{bmatrix} q_C \\ q_V \end{bmatrix} \\ \mathrm{RHS}_F &= -\mathrm{AMATRIX}_F \begin{bmatrix} q_F \\ q_V \end{bmatrix} \end{aligned} \tag{8.22}$$

since distributed loads are not accounted for in the overlapping zone S. ABAQUS in the assembly process considers the library elements CPS4E and the Arlequin user elements UEL_C and UEL_F defined in the subroutine UEL. The global linear system in Eqs. 8.20 is automatically recovered.

8.2.3 Results and discussion

A piezoelectric wafer in SONOX P502 (see Table 3.6) with interdigitated electrodes is considered, as shown in Fig. 8.11. The y-axis run through the thickness of the wafer and

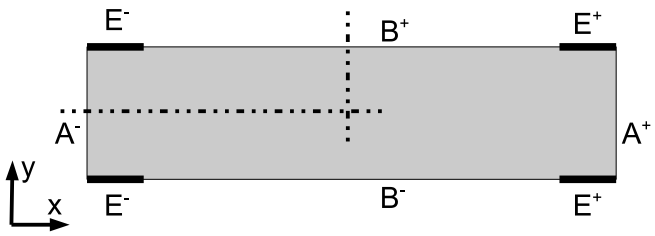

Figure 8.11. Piezoelectric wafer with interdigitated electrodes.

the material is polarised along the x-axis. Therefore indexes 1 and 3 in Table 3.6 are inverted. Thanks to the symmetries, only the top left quarter of the wafer is analysed. In the Arlequin solution the left part of the model (near the electrode E^-) is modelled with a fine mesh, whereas the right part adopts a coarse mesh. Reference solution adopt the fine mesh everywhere in the model.

Two cases are considered. In the first one, a displacement $u_x = 0.1$ m is imposed on the right edge, whereas u_x is fixed on the left edge. $u_y = 0$ on all the edges. Null electric potential is prescribed on the electrode E^-. The distribution of the magnitude of displacement is shown in Figs. 8.12 for the reference solution and for the Arlequin solution. The electric potential distribution is presented in Figs. 8.13. The electrode affects the electric potential variation in the model.

In the second case displacements are fixed on all the edges. An electric potential equal to 0.5 V is imposed on the electrode E^-. Null electric potential is prescribed on the right edge. The electric field distribution is presented in Figs. 8.14. Elements are not depicted for sake of clearness. Higher values of the electric field magnitude can be observed near the right end of the electrode. The electric field is almost constant far from the electrode in the right part of the model.

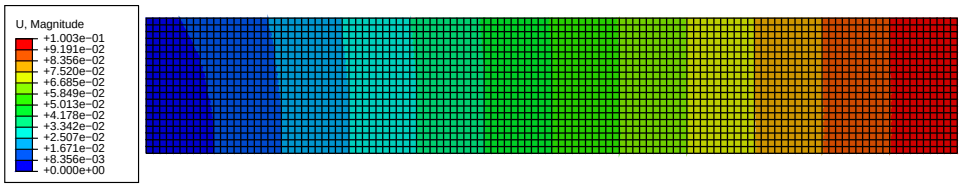

(a)

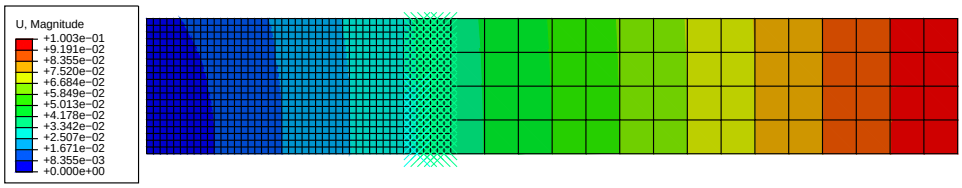

(b)

Figure 8.12. Distribution of the magnitude of displacement in the case of imposed longitudinal displacement with (a) reference and (b) Arlequin solutions.

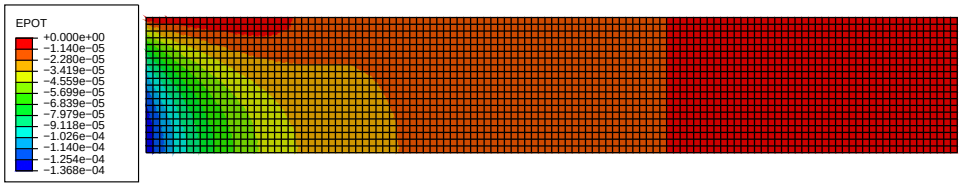

(a)

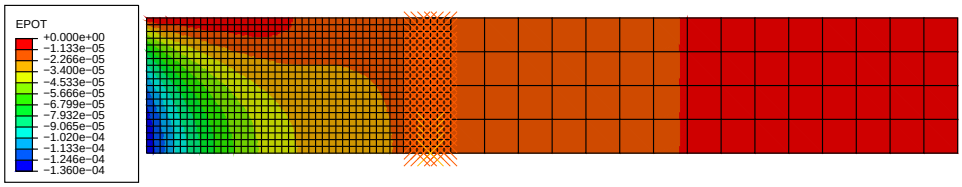

(b)

Figure 8.13. Distribution of the electric potential in the case of imposed longitudinal displacement with (a) reference and (b) Arlequin solutions.

Results obtained via the Arlequin electro-mechanical coupling match the reference solutions. Meshes of piezoelectric elements with different refinement are successfully coupled in electro-mechanical analyses.

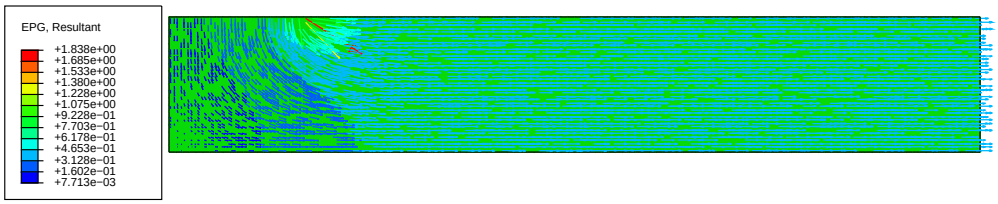

(a)

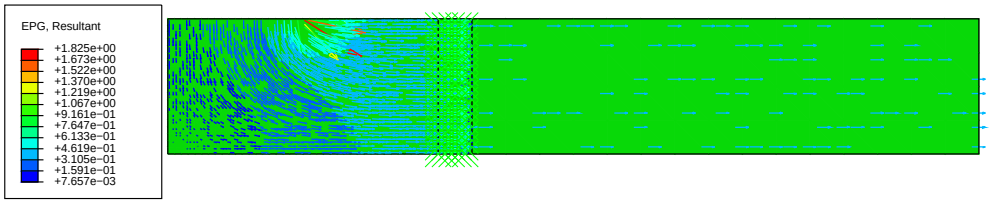

(b)

Figure 8.14. Distribution of the electric field in the case of imposed electric potential with (a) reference and (b) Arlequin solutions.

Chapter 9

Conclusions

After a brief introduction to the piezoelectric effect and a survey on piezocomposite transducers, a micromechanical model to predict the effective electro-mechanical properties of a composite has been presented. This model is based on the Eshelby tensor and its original contribution is the capability to consider non-homogeneous inclusions. The influence of the shape of the inclusion, of the polarisation direction and of the constituent materials have been analysed. The presented results show that higher effectiveness and directional dependence of the piezoelectric effect is achieved with fibre-shaped inclusions. Macro Fiber Composites (MFC) are the most promising commercial products with piezoelectric fibres and their equivalent properties have been computed via the asymptotic expansion method, since fibres with rectangular cross-section cannot be considered with the proposed Eshelby-based micromechanical model. An analytical solution, that does not take into account the electrodes, has been obtained. It corresponds exactly to the mixing rules that can be obtained adopting the uniform field method. A numerical solution based on FE analyses that considers the electrodes has been presented and validated towards results obtained via the numerical periodic homogenisation. Analytical and numerical asymptotic expansion results match the numerical periodic homogenisation ones for almost every property. The only relevant difference is observed for the transverse shear modulus in the case of high volume fraction of the piezoelectric phase. Results have been validated towards manufacturer's datasheet considering not only the active layer but also the electrodes (made of copper and epoxy) and Kapton®layers.

The directional dependence in terms of sensing/actuation of piezoelectric transducers has been investigated according to the classical plane stress assumption. The concept of maximum directional dependence has been introduced: specific quantities related to a direction perpendicular to that of maximum actuation or sensing are not actuated or sensed. Maximum directionality in terms of piezoelectric strain constants is shown to be mutually exclusive with the one in terms of piezoelectric stress constants. The mixing rules obtained with the analytical solution of the asymptotic expansion method have been used to predict the influence of the matrix on the equivalent properties of a piezocomposite similar to MFC. Results show that low Young's modulus and Poisson's ratio maximise the ratio between piezoelectric properties in longitudinal and transverse direction, i.e. the

directional dependence of the piezoelectric effect. Equivalent properties adopting some existing polymers have been presented.

The design of a multi-layered piezocomposite transducer has been considered. A configuration with a single piezoelectric layer, that can be monolithic or composite, and several mechanical layers has been taken into account. Equivalent properties have been computed via a modified version of the uniform field method, which takes into account that electrodes are at the top and bottom of the piezoelectric layer and not of the whole laminate. Results have been verified via the numerical periodic homogenisation method. Maximum directionality in terms of piezoelectric stress constants (induced stresses per unit of electric field) is shown to be not achievable with a layered configuration. This is a consequence of the multilayered structure, which is conceptually similar to a parallel configuration of the different layers in the electric circuit analogy. On the contrary, a fibre/matrix structure like that of MFC correspond to a series configuration in the electric circuit analogy and has a large influence on piezoelectric stress constants. An optimisation process is carried out to find a lamination that guarantees maximum directionality in terms of piezoelectric strain constants (induced strains per unit of electric field) for different kind of piezoelectric layers. Maximum directionality is achieved since the piezoelectric constant of the piezoelectric layer in a specific direction is contrasted by the Poisson's effect of the whole laminate. Maximum directional dependence is fulfilled only for low values of the volume fraction of the monolithic piezoelectric layer, whereas with a piezocomposite layer with conventional electrodes the volume fraction can be higher. If interdigitated electrodes are adopted, maximum directional dependence is not achievable since the whole laminate would be required to have a negative Poisson's coefficient. The behaviour of a thin patch bonded to a structure, as piezoelectric transducers are commonly employed, is investigated analytically and numerically. Unfortunately, maximum directionality in terms of equivalent piezoelectric strain constants does not guarantee maximum directionality in sensing of stress of the structure. On the contrary, maximum directionality in terms of stress constants guarantees maximum directionality in sensing of strain of the structure.

Hierarchical finite elements for structural analysis have been introduced with the corresponding theories according to a Unified Formulation (UF) proposed by Carrera. Solid, beam and plate finite elements have been addressed: for solid elements, the number of nodes is a free parameter; both the number of nodes and the order of the theory are free parameters in beam elements; plate elements can differ in variational principle, order of the theory, variable description (equivalent single layer or layerwise) and number of nodes. Higher order and multifield elements are obtained straightforwardly via the UF from a fundamental nucleus, that only depends on the choice of the variational principle. The principle of virtual displacements and mixed principles have been adopted. Piezoelectric solid and plate elements have been also considered modelling electrical quantities, such as the electric potential, as primary unknowns.

The developed hierarchical finite elements have been coupled in multi-domain structural analyses via the Arlequin method, proposed by Ben Dhia. The coupling matrices of the Arlequin method have been derived in the context of the UF. The following multi-domain analysis have been considered: beam elements of different order; plate elements based on

different variational principle, order and variable description; solid elements and higher-order equivalent single layer plate elements. The obtained results are in good agreement with three-dimensional reference results and with the corresponding mono-model solutions. The number of degrees of freedom is reduced without affecting the solution in the refined sub-domains, where a three-dimensional strain/stress state is locally present.

The Arlequin method has been extended to piezoelectric analyses with the introduction of two electro-mechanical coupling operators, that take into account electrical quantities such as the electric potential and the electric field. A piezoelectric plate and a mechanical plate with a piezoelectric patch have been considered. Variable kinematic solutions match the mono-model results. In the case of the mechanical plate it has been found that the mechanics of the plate far from the actuator is correctly modelled by an equivalent single layer mechanical theory, whereas the actuation of the patch requires a layer-wise piezoelectric theory to be accurately described. The proposed electro-mechanical coupling has been also implemented in the commercial FE software ABAQUS for piezoelectric plane stress elements. The sub-domains differ in the mesh refinement, whereas the adopted finite elements are the same. Arlequin user elements have been implemented in the ABAQUS Fortran subroutine UEL. A piezoelectric wafer with interdigitated electrodes has been considered, adopting a fine mesh near the electrodes and a coarse mesh elsewhere. Results match the reference solutions obtained with a fine mesh on the whole model.

Future resarch work may address the extension of the existing non-directional actuation and control theory for piezoelectric actuators to incorporate the response behaviour of devices with maximum directionality. Typical applications that may be considered in this context are acoustic noise control and active vibration control. Highly directional piezoelectric devices may be adopted in multi-axial sensing systems, in particular in the area of structural health monitoring since a sensor that can provide directional information for the incident energy is a more detailed “probe” for detecting changes in a structure.

Bibliography

[1] *ANSI/IEEE Std 176-1987 IEEE Standard on Piezoelectricity.* The institut of Electrical and Electronics Engineers, 1987.

[2] D.M. Barnett and J. Lothe. Dislocations and line charges in anisotropic piezoelectric insulators. *Phys. Status Solidi (b)*, 67:105–111, 1975.

[3] N. Fakri, L. Azrar, and L. El Bakkali. Electroelastic behavior modeling of piezoelectric composite materials containing spatially oriented reinforcements. *International Journal of Solids and Structures*, 40(2):361–384, 2003.

[4] B. P. Masters, J. P. Rodgers, and M. C. van Schoor. Laser machining of electroactive ceramics. Patent, 01 2002. US 6337465.

[5] Face International Corporation. Thunder application notes, 2002.

[6] K. M Mossi, G. V. Selby, and R. G. Bryant. Thin-layer composite unimorph ferroelectric driver and sensor properties. *Materials Letters*, 35:39–49, 1998.

[7] G. H. Haertling. Rainbow ceramics - a new type of ultra-high-displacement actuator. *American Ceramic Society Bulletin*, 73:93 – 96, 1994.

[8] S. A. Wise. Displacement properties of rainbow and thunder piezoelectric actuators. *Sensors and Actuators A*, 69:33–38, 1998.

[9] W.A. Smith and A. Shauov. Tailoring the properties of composite piezoelectric materials for medical ultrasonic transducers. *IEEE Ultrasonics Symposium*, 2:642–647, 1985.

[10] A.A. Shaulov, W.A. Smith, and R.Y. Ting. Modified-lead-titanate/polymer composites for hydrophone applications. *Ferroelectrics*, 93:177–182, 1989.

[11] A. Safari. Development of piezoelectric composites for transducers. *Journal de Physique III*, 4(7):1129–1149, 1994.

[12] R.B. Williams, G. Park, D.J. Inman, and W.K. Wilkie. An overview of composite actuators with piezoceramic fibers. In *Proceedings of 20th International Modal Analysis Conference*, volume 4753, pages 421–427, 2002.

[13] A. Schonecker, L. Seffner, S. Gebhardt, and W. Beckert. Piezoelectric fibers and composites for smart structures. In *Proceedings of the 8th Japanese-European Symposium on Composite Materials*, pages 247–255, Tokyo University of Science, Tokyo, Japan, 2003.

[14] N.W. Hagood and A.A. Bent. Development of piezoelectric fiber composites for structural actuation. In *Collection of Technical Papers - AIAA/ASME Structures, Structural Dynamics and Materials Conference*, pages 3625–3638, Massachusetts Inst of Technology, Cambridge, United States, 1993.

[15] N.W. Hagood, R. Kindel, K. Ghandi, and P. Gaudenzi. Improving transverse actuation of piezoceramics using interdigitated surface electrodes. In *Proceedings of SPIE*, volume 341, 1993.

[16] A.A. Bent, N.W. Hagood, and J.P. Rodgers. Anisotropic actuation with piezoelectric fiber composites. *Journal of Intelligent Material Systems and Structures*, 6(3):338, 1995.

[17] A. A. Bent and N. W. Hagood. Improved performance in piezoelectric fiber composites using interdigitated electrodes. In *Proceedings of SPIE - The International Society for Optical Engineering*, volume 2441, pages 196–212, Massachusetts Inst. of Technology,, Allston, MA, USA, 1995.

[18] A.A. Bent and N.W. Hagood. Piezoelectric fiber composites with interdigitated electrodes. *Journal of Intelligent Material Systems and Structures*, 8(11):903–919, 1997.

[19] J. P. Rodgers and N. W. Hagood. Design, manifacture, and testing of an integral twist actuated roror blade. In *Proceedings of the 8th International Conference on Adaptive Structures and Technology*, 1997.

[20] W. K. Wilkie, R. G. Bryant, J. W. High, R. L. Fox, R. F. Hellbaum, A. Jalink Jr., B. D. Little, and P. H. Mirick. Low-cost piezocomposite actuator for structural control applications. In *Proceedings of SPIE - The International Society for Optical Engineering*, volume 3991, pages 323–334, NASA Langley Research Cent, Hampton, United States, 2000.

[21] C. R. Bowen, L. J. Nelson, R. Stevens, M. G. Cain, and M. Stewart. Optimisation of interdigitated electrodes for piezoelectric actuators and active fibre composites. *Journal of Electroceramics*, 16(4):263–269, 2006.

[22] A. Deraemaeker, H. Nasser, A. Benjeddou, and A. Preumont. Mixing rules for the piezoelectric properties of macro fiber composites (mfc). *Journal of Intelligent Material Systems and Structures*, 20(12):1475–1482, 2009.

[23] B. J. Cannon and D. Brei. Feasibility study of microfabrication by coextrusion (mfcx) hollow fibers for active composites. *Journal of Intelligent Material Systems and Structures*, 11:659–670, 2000.

[24] Y. Lin and H. A. Sodano. Concept and model of a piezoelectric structural fiber for multifunctional composites. *Composites Science and Technology*, 68(7–8):1911–1918, 2008.

[25] J. Ryu, S. Priya, K. Uchino, and H.E. Kim. Magnetoelectric effect in composites of magnetostrictive and piezoelectric materials. *Journal of Electroceramics*, 8:107–119, 2002.

[26] J. H. Huang. Micromechanics determinations of thermoelectroelastic fields and effective thermoelectroelastic moduli of piezoelectric composites. *Materials Science and Engineering B*, 39(3):163–172, 1996.

[27] G.B. Olson. Designing a new material world. *Science*, 288(5468):993–998, 2000.

[28] Z.H. Tong, S.H. Lo, C.P. Jiang, and Y.K. Cheung. An exact solution for the three-phase thermo-electro-magneto-elastic cylinder model and its application to piezoelectric-magnetic fiber composites. *International Journal of Solids and Structures*, 45(20):5205–5219, October 2008.

[29] Y. Benveniste and G.J. Dvorak. Uniform fields and universal relations in piezoelectric composites. *Journal of the Mechanics and Physics of Solids*, 40(6):1295–1312, August 1992.

[30] W. Biao. Three-dimensional analysis of an ellipsoidal inclusion in a piezoelectric material. *International Journal of Solids and Structures*, 29(3):293–308, 1992.

[31] M.L. Dunn and M. Taya. Micromechanics predictions of the effective electroelastic moduli of piezoelectric composites. *International Journal of Solids Structures*, 30(2):161–175, 1993.

[32] M.L. Dunn. Micromechanics of coupled electroelastic composites: effective thermal expansion and pyroelectric coefficients. *Journal of Applied Physics*, 73(10):5131–5140, 1993.

[33] P. Tan and L. Tong. Micro-electromechanics models for piezoelectric-fiber-reinforced composite materials. *Composites Science and Technology*, 61(5):759–769, 2001.

[34] P. Tan and L. Tong. Modeling for the electro-magneto-thermo-elastic properties of piezoelectric-magnetic fiber reinforced composites. *Composites Part A: Applied Science and Manufacturing*, 33(5):631–645, 2002.

[35] H. Berger, S. Kari, U. Gabbert, R. Rodriguez-Ramos, J. Bravo-Castillero, and R. Guinovart-Diaz. A comprehensive numerical homogenisation technique for calculating effective coefficients of uniaxial piezoelectric fibre composites. *Materials Science and Engineering: A*, 412(1-2):53–60, 2005.

[36] T. Tang and W. Yu. Variational asymptotic micromechanics modeling of heterogeneous piezoelectric materials. *Mechanics of Materials*, 40(10):812–824, 2008.

[37] J.A. Oliveira, J. Pinho da Cruz, and F. Teixeira-Dias. Asymptotic homogenisation in linear elasticity. part ii: Finite element procedures and multiscale applications. *Computational Materials Science*, 45(4):1081 – 1096, 2009.

[38] H. Nasser, A. Deraemaeker, and S. Belouettar. Electric field distribution in macro fiber composite using interdigitated electrodes. *Advanced Materials Research*, 47:1173–1176, 2008.

[39] A. Deraemaeker and H. Nasser. Numerical evaluation of the equivalent properties of macro fiber composite (mfc) transducers using periodic homogenization. *International Journal of Solids and Structures*, 47:3272–3285, 2010.

[40] H. Berger, S. Kurukuri, S. Kari, U. Gabbert, R. Rodriguez-Ramos, J. Bravo-Castillero, and R. Guinovart-Diaz. Numerical and analytical approaches for calculating the effective thermo-mechanical properties of three-phase composites. *Journal of Thermal Stresses*, 30(8):801–817, 2007.

[41] J. Aboudi. Micromechanical prediction of the effective coefficients of thermo-piezoelectric multiphase composites. *Journal of intelligent material systems and structures*, 9(9):713–722, 1998.

[42] J. D. Eshelby. The determination of the elastic field of an ellipsoidal inclusion, and related problems. *Proceedings of the Royal Society of London. Series A, Mathematical and Physical Sciences*, 241(1226):376–396, 1957.

[43] J. Y. Li. Thermoelastic behavior of composites with functionally graded interphase: a multi-inclusion model. *International Journal of Solids and Structures*, 37(39):5579–5597, 2000.

[44] T. Mori and K. Tanaka. Average stress in matrix and average elastic energy of materials with misfitting inclusions. *Acta Metallurgica*, 21(5):571–574, 1973.

[45] R. Hill. A self-consistent mechanics of composite materials. *Journal of the Mechanics and Physics of Solids*, 13(4):213–222, 1965.

[46] V.M. Levin, M.I. Rakovskaja, and W.S. Kreher. The effective thermoelectroelastic properties of microinhomogeneous materials. *International journal of solids and structures*, 36(18):2683–2705, 1999.

[47] J. Bravo-Castillero, R. Guinovart-Diaz, F. J. Sabina, and R. Rodriguez-Ramos. Closed-form expressions for the effective coefficients of a fiber-reinforced composite with transversely isotropic constituents - ii. piezoelectric and square symmetry. *Mechanics of Materials*, 33(4):237–248, 2001.

[48] J. Pinho da Cruz, J.A. Oliveira, and F. Teixeira-Dias. Asymptotic homogenisation in linear elasticity. part i: Mathematical formulation and finite element modelling. *Computational Materials Science*, 45(4):1073 – 1080, 2009.

[49] J. M Guedes and N. Kikuchi. Preprocessing and postprocessing for materials based on the homogenization method with adaptive finite element methods. *Computer Methods in Applied Mechanics and Engineering*, 83:143–198, 1990.

[50] J. Bravo-Castillero and R. Rodriguez-Ramos. Homogenization of magneto-electroelastic multilaminated materials. *The Quarterly Journal of Mechanics and Applied Mathematics*, 61(3):311–332, 2008.

[51] P. Lipinski, E.H. Barhdadi, and M. Cherkaoui. Micromechanical modeling of an arbitrary ellipsoidal multi-coated inclusion. *Philosophical Magazine*, 86(10):1305–1326, 2006.

[52] Y. Koutsawa, M. Cherkaoui, and E.M. Daya. Multi-coating inhomogeneities problem for effective viscoelastic properties of particulate composite materials. *Journal of Engineering Materials and Technology*, 131(2):021012, 2008.

[53] R. Zeller and P.H. Dederichs. Elastic constants of polycrystals. *Physica Status Solidi B*, 55:831–842, 1973.

[54] J.D. Eshelby. *Elastic Inclusions and Inhomogeneities*, volume 2 of *Progress in Solid Mechanics*. Amsterdam: North-Holland, 1961.

[55] L.J. Walpole. Elastic behavior of composite materials: theoretical foundations. *Advances in Applied Mechanics*, 21:169–242, 1981.

[56] M. Cherkaoui, H. Sabar, and M. Berveiller. Micromechanical approach of the coated inclusion problem and applications to composite materials. *Journal of Engineering Materials and Technology*, 116:274–278, 1994.

[57] Yozo Mikata. Determination of piezoelectric eshelby tensor in transversely isotropic piezoelectric solids. *International Journal of Engineering Science*, 38(6):605–641, 2000.

[58] T. L. Wu and J. H. Huang. Closed-form solutions for the magnetoelectric coupling coefficients in fibrous composites with piezoelectric and piezomagnetic phases. *International Journal of Solids and Structures*, 37(21):2981–3009, 2000.

[59] A. Broohm, P. Zattarin, and P. Lipinski. Prediction of mechanical behaviour of inhomogeneous and anisotropic materials using an incremental scheme. *Archives of Mechanics*, 52(6):949–967, 2000.

[60] H.W. Chan and J. Unsworth. Simple model for piezoelectric ceramic/polymer 1-3 composites used in ultrasonic transducer applications. *IEEE Trans Ultrason Ferroelectr Freq Control*, 36(4):434–441, 1989.

[61] R.B. Williams, D.J. Inman, M.R. Schultz, M.W. Hyer, and W.K. Wilkie. Nonlinear tensile and shear behavior of macro fiber composite actuators. *Journal of Composite Materials*, 38(10):855–869, 2004.

[62] R.B. Williams, D.J. Inman, and W.K. Wilkie. Nonlinear response of the macro fiber composite actuator to monotonically increasing excitation voltage. *Journal of Intelligent Material Systems and Structures*, 17(7):601–608, 2006.

[63] *Abaqus Theory manual, version 6.5.* Hibbit and Karlson and Sorensen Inc., 2005.

[64] M. Barbezat, A.J. Brunnerand, P. Flueler, C. Huber, and X. Kornmann. Acoustic emission sensor properties of active fibre composite elements compared with commercial acoustic emission sensors. *Sensors and Actuators A*, 114:13–20, 2004.

[65] M. Barbezat, A. J. Brunner, C. Huber, and P. Flueler. Integrated active fiber composite elements: Characterization for acoustic emission and acousto-ultrasonics. *Journal of Intelligent Material Systems and Structures*, 18:515–525, 2007.

[66] H. M. Matt and F. Lanza di Scalea. Macro-fiber composite piezoelectric rosettes for acoustic source location in complex structures. *Smart Materials and Structures*, 16:1489–1499, 2007.

[67] M. Eaton, R. Pullin, K. Holford, S. Evans, C. Featherston, and A. Rose. Use of macro fibre composite transducers as acoustic emission sensors. *Remote sensing*, 1:68–79, 2009.

[68] M.I. Frecker. Recent advances in optimization of smart structures and actuators. *Journal of Intelligent Material Systems and Structures*, 14(4-5):207–216, 2003.

[69] E. C. N. Silva, J. S. Ono Fonseca, and N. Kikuchi. Optimal design of periodic piezocomposites. *Computer Methods in Applied Mechanics and Engineering*, 159:49–77, 1998.

[70] O. Sigmund, S. Torquato, and I. A. Aksay. On the design of 1-3 piezocomposites using topology optimization. *Journal of materials research*, 13(4):1038–1048, 1998.

[71] Z. Kang and L. Tong. Topology optimization-based distribution design of actuation voltage in static shape control of plates. *Computers & Structures*, 86(19-20):1885–1893, 2008.

[72] Z. Kang and X. Wang. Topology optimization of bending actuators with multilayer piezoelectric material. *Smart Materials and Structures*, 19(7):1–12, 2010.

[73] B. C. Chen, E. C. N. Silva, and N. Kikuchi. Advances in computational design and optimization with application to mems. *International Journal for Numerical Methods in Engineering*, 52:23–62, 2001.

[74] M. Kogl and E. C. N. Silva. Topology optimization of smart structures: Design of piezoelectric plate and shell actuators. *Smart Materials and Structures*, 14(2):387–399, 2005.

[75] R. C. Carbonari, E. C. N. Silva, and S. Nishiwaki. Optimum placement of piezoelectric material in piezoactuator design. *Smart Materials and Structures*, 16:207–220, 2007.

[76] H. Ghiasi, Pasinia. D., and L. Lessarda. Optimum stacking sequence design of composite materials part i: Constant stiffness design. *Composite Structures*, 90(1):1–11, 2009.

[77] H. Ghiasi, K. Fayazbakhsha, Pasinia. D., and L. Lessarda. Optimum stacking sequence design of composite materials part ii: Variable stiffness design. *Composite Structures*, 93(1):1–13, 2010.

[78] R. Spallino and G. Thierauf. Thermal buckling optimization of composite laminates by evolution strategies. *Computers & Structures*, 78(5):691–697, 2000.

[79] P. Vannucci and J. Pouget. Laminates with given piezoelectric expansion coefficients. *International Journal of Mechanics of Advanced Materials and Structures*, 13:419–427, 2006.

[80] P. Vannucci and G. Verchery. Stiffness design of laminates using the polar method. *International Journal of Solids and Structures*, 38:9281–9294, 2001.

[81] P. Vannucci. A new general approach for optimising the performances of smart laminates. *Mechanics of Advanced Materials and Structures*, in press, 2011.

[82] E. Carrera. A class of two dimensional theories for multilayered plates analysis. *Atti Accademia delle Scienze di Torino, Mem Sci. Fis.*, 19-20:49–87, 1995.

[83] S. P. Timoshenko. On the corrections for shear of the differential equation for transverse vibrations of prismatic bars. *Philosophical Magazine*, 41:744–746, 1921.

[84] S. P. Timoshenko. On the transverse vibrations of bars of uniform cross section. *Philosophical Magazine*, 43:125–131, 1922.

[85] B. Saint-Venant. Memoire sur la torsion des prismes. *Memoires des Savants Etrangers*, 14:233–560, 1855.

[86] L. Prandtl. Zur torsion von prismatischen stäben. *Zeitschrift für Physik*, 4:758–770, 1903.

[87] R. K. Kapania and S. Raciti. Recent advances in analysis of laminated beams and plates, part ii: Vibrations and wave propagation. *AIAA Journal*, 27(7):935–946, 1989.

[88] R. K. Kapania and S. Raciti. Recent advances in analysis of laminated beams and plates, part i: Shear effects and buckling. *AIAA Journal*, 27(7):923–934, 1989.

[89] D. H. Hodges. A review of composite rotor blade modeling. *AIAA Journal*, 28(3):561–565, 1990.

[90] S. N. Jung, V. V. Nagaraj, and I. Chopra. Assessment of composite rotor modeling techniques. *Journal of the American Helicopter Society*, 44(3):188–205, 1999.

[91] E. Carrera and G. Giunta. Refined beam theories based on a unified formulation. *International Journal of Applied Mechanics*, 2(1):117–143, 2010.

[92] E. Carrera, G. Giunta, P. Nali, and M. Petrolo. Refined beam elements with arbitrary cross-section geometries. *Computers and Structures*, 88(5–6):283–293, 2010.

[93] J. N. Reddy. *Mechanics of laminated composite plates and shells. Theory and Analysis*. CRC Press, 2 edition, 2004.

[94] E. Carrera and S. Brischetto. Analysis of thickness locking in classical, refined and mixed theories for layered shells. *Composite Structures*, 85(1):83–90, 2008.

[95] E. Carrera and S. Brischetto. Analysis of thickness locking in classical, refined and mixed multilayered plate theories. *Composite Structures*, 82(4):549–562, 2008.

[96] K. J. Bathe. *Finite element procedure.* Prentice Hall, 1996.

[97] G. Kirchhoff. Über das gleichgewicht und die bewegung einer elastishen sceibe. *J. Angew. Math.*, 40:51–88, 1850.

[98] E. Reissner. The effect of transverse shear deformation on the bending of elastic plates. *Journal of Applied Mechanics*, 12:69–76, 1945.

[99] E. Mindlin. Influence of the rotatory inertia and shear in flexural motions of isotropic elastic plates. *Journal of Applied Mechanics*, 18:1031–1036, 1951.

[100] E. Carrera. $\boldsymbol{C}_z^0$ requirementsï£¡models for the two dimensional analysis of multilayered structures. *Composite structures*, 37(3-4):373–383, 1997.

[101] A. K. Noor and W. S. Burton. Assessment of shear deformation theories for multilayered composite plates. *Appl. Mech. Rev.*, 41:1–18, 1989.

[102] J. N. Reddy and D.H. Robbins Jr. Theories and computational models for composite laminates. *Applied Mechancis Review*, 47(6), 6 1994.

[103] E. Carrera. Theories and finite elements for multilayered plates and shells: a unified compact formulation with numerical assessment and benchmarking. *Archives of Computational Methods in Engineering*, 10(3):215–296, 2003.

[104] H. Hu, S. Belouettar, M. Potier-Ferry, and E. M. Daya. Multi-scale modelling of sandwich structures using the arlequin method part i: Linear modelling. *Finite Elements in Analysis and Design*, 45(1):37–51, 2008.

[105] E. Reissner. On a certain mixed variational theorem and a proposed application. *International Journal of Numerical Methods in Engineering*, 20:1366–1368, 1984.

[106] E. Carrera and G. Giunta. Hierarchical evaluation of failure parameters in composite plates. *AIAA Journal*, 47(3):692–702, 2009.

[107] M. Murakami. Laminated composites plate theory with improved in-plane responses. *Journal of Applied Mechanics*, 53:661–666, 1986.

[108] E. Reissner. On a mixed variational theorem and on shear deformable plate theory. *International Journal of Numerical Methods in Engineering*, 23:193–198, 1986.

[109] L. De Masi and E. Carrera. Classical and advanced multilayered plate elements based upon pvd and rmvt. part 1. derivation of finite element matrices. *International Journal Numerical Methods in Engineering*, 55:191–231, 2002.

[110] E. Carrera, M. Cinefra, and P. Nali. Mitc technique extended to variable kinematic multilayered plate elements. *Composite Structures*, 8(92):1888 1895, 2010.

[111] Dimitris A. Saravanos and Paul R. Heyliger. Mechanics and computational models for laminated piezoelectric beams, plates, and shells. *Applied Mechanics Reviews*, 52(10):305–320, 1999.

[112] A. Benjeddou. Advances in piezoelectric finite element modelling of adaptive structural elements: a survey. *Computers and Structures*, 76(1-3):347–363, 2000.

[113] Ji Wang and Jiashi Yang. Higher-order theories of piezoelectric plates and applications. *Applied Mechanics Reviews*, 53(4):87–99, 2000.

[114] F Auricchio, P Bisegna, and C Lovadina. Finite element approximation of piezoelectric plates. *International journal for numerical methods in engineering*, 50(6):1469–1499, 2001.

[115] AH Sheikh, P Topdar, and S Halder. An appropriate fe model for through-thickness variation of displacement and potential in thin/moderately thick smart laminates.

Composite structures, 51(4):401–409, 2001.

[116] KY Sze, XM Yang, and H Fan. Electric assumptions for piezoelectric laminate analysis. *International journal of solids and structures*, 41(9-10):2363–2382, 2004.

[117] RP Thornburgh and A Chattopadhyay. Simultaneous modeling of mechanical and electrical response of smart composite structures. *AIAA journal*, 40(8), 2002.

[118] D.H. Robbins Jr. and I. Chopra. The effect of laminate kinematic assumptions on the global response of actuated plates. *Journal of Intelligent Material Systems and Structures*, 17:273–299, 2006.

[119] D.H. Robbins Jr. and I. Chopra. Quantifying the local kinematic effect in actuated plates via strain energy distribution. *Journal of Intelligent Material Systems and Structures*, 18:569–589, 2007.

[120] E. Carrera and P. Nali. Multilayered plate elements for the analysis of multifield problems. *Finite Elements in Analysis and Design*, 46(9):732–742, 2010.

[121] M D'Ottavio and B Kroplin. An extension of Reissner Mixed Variational Theorem to piezoelectric laminates. *Mechanics of advanced materials and structures*, 13(2):139–150, 2006.

[122] E. Carrera and P. Nali. Mixed piezoelectric plate elements with direct evaluation of transverse electric displacement. *International journal for numerical methods in engineering*, 80(4):403–424, 2009.

[123] E. Carrera, A. Buttner, and P. Nali. Mixed elements for the analysis of anisotropic multilayered piezoelectric plates. *Journal of Intelligent Material Systems and Structures*, 21(7):701–717, 2010.

[124] R. E. Bank. *Adaptive Computational Methods for Partial Differential Equations*. SIAM, Philadelphia, 1983.

[125] B. A. Szabo and I. Babuska. *Finite element analysis*. John Wiley & Sons, 1991.

[126] J. Fish, L. Pan, V. Belsky, and S. Gomaa. Unstructured multigrid method for shells. *International Journal for Numerical Methods in Engineering*, 39(7):1181–1197, 1996.

[127] N. Möes, J. Dolbow, and T. Belytschko. A finite element method for crack growth without remeshing. *International Journal for Numerical Methods in Engineering*, 46(1):131–150, 1999.

[128] J. Fish. The s-version of the finite element method. *Computers and Structures*, 43(3):539–547, 1992.

[129] J. Fish and S. Markolefas. Adaptive s-method for linear elastostatics. *Computational Methods in Applied Mechanics and Engineering*, 103:363–396, 1993.

[130] K. C. Park and C. A. Felippa. A variational principle for the formulation of partitioned structural systems. *International journal for numerical methods in engineering*, 47:395–418, 2000.

[131] F. Brezzi and L. D. Marini. The three-field formulation for elasticity problems. *GAMM Mitteilungen*, 28:124–153, 2005.

[132] P. J. Blanco, R. A. Feijoo, and S. A. Urquiza. A variational approach for coupling kinematically incompatible structural models. *Computer Methods in Applied Mechanics and Engineering*, 197:1577–1620, 2008.

[133] H. Ben Dhia. Multiscale mechanical problems: the arlequin method. *Comptes Rendus de l'Academie des Sciences Series IIB Mechanics Physics Astronomy*,

326(12):899–904, 1998.

[134] H. Ben Dhia. Numerical modelling of multiscale problems: the arlequin method. *CD Proceedings of ECCM'99, Munchen*, 1999.

[135] H. Ben Dhia and G. Rateau. The arlequin method as a flexible engineering tool. *International journal for numerical methods in engineering*, 62(11):1442–1462, 2005.

[136] H. Ben Dhia. Further insights by theoretical investigations of the multiscale arlequin method. *International Journal for Multiscale Computational Engineering*, 6(3):215–232, 2008.

[137] P. A. Guidault and T. Belytschko. On the l2 and the h1 couplings for an overlapping domain decomposition method using lagrange multipliers. *International Journal for Numerical Methods in Engineering*, 70(3):322 350, 2007.

[138] H. Hu, S. Belouettar, M. Potier-Ferry, E. M. Daya, and A. Makradi. Multi-scale nonlinear modelling of sandwich structures using the arlequin method. *Composite Structures*, 92(2):515–522, 2010.

[139] N. J. Pagano. Exact solutions for rectangular bidirectional composites and sandwich plates. *Journal of Composites Materials*, 4:20–34, 1970.

[140] K. S. Surana. Transition finite elements for three-dimensional stress analysis. *International Journal for Numerical Methods in Engineering*, 15(7):991–1020, 1980.

[141] K. S. Surana. Geometrically non-linear formulation for the three dimensional solid-shell transition finite elements. *Computers & Structures*, 15(5):549–566, 1982.

[142] E. Garusi and A. Tralli. A hybrid stress-assumed transition element for solid-to-beam and plate-to-beam connections. *Computers and Structures*, 80:105–115, 2002.

[143] R. W. McCune, C. G. Armstrong, and D. J. Robinson. Mixed-dimensional coupling in finite element models. *International Journal for Numerical Methods in Engineering*, 49:725–750, 2000.

[144] K. W. Shim, D. J. Monaghan, and C. G. Armstrong. Mixed dimensional coupling in finite element stress analysis. *Engineering with Computers*, 18:241–252, 2002.

[145] N. Osawa, K. Hashimoto, J. Sawamura, T. Nakai, and S. Suzuki. Study on shell solid coupling fe analysis for fatigue assessment of ship structure. *Marine Structures*, 20:143–163, 2007.

[146] Paul Heyliger. Static behavior of laminated elastic/piezoelectric plates. *AIAA journal*, 32(12):2481–2484, 1994.

[147] H. Qiao, Q.D. Yang, W.Q. Chen, and C.Z. Zhang. Implementation of the arlequin method into abaqus: Basic formulations and applications. *Advances in Engineering Software*, 42(4):197–207, 2011.

Curriculum Vitae

Name:	Fabio
Surname:	Biscani
Date of birth:	29 January 1984
Place of birth:	Trento, Italy
e-mail:	fabio.biscani@polito.it

Education

◇ **January 2009 - December 2011**: Ph.D. candidate at the Politecnico di Torino. Subject of the Ph.D. Thesis: "Modelling-based design of anisotropic piezocomposite transducers and multi-domain analysis of smart structures".
◇ **2008**: Alta Scuola Politecnica Diploma at Politecnico di Torino and Politecnico di Milano, Italy.
◇ **2008**: Double Master Degree in Aerospace Engineering at Politecnico di Torino and Politecnico di Milano, Italy, with the grade 110 out of 110 (summa cum laude).
◇ **2006**: Bachelor Degree in Aerospace Engineering at Università degli Studi di Padova, Italy, with the grade 110 out of 110 (summa cum laude).

Publications

[1] *Multi-coating inhomogeneities approach for the effective thermoelectro- elastic moduli of piezoelectric composites.* Y. Koutsawa, F. Biscani, S. Belouettar, E. Carrera, H. Nasser. Composite Structures (2010), vol. 92, p. 964-972.
[2] *Effective properties of electro-elastic composites with multi-coating inhomogeneities.* F. Biscani, Y. Koutsawa, S. Belouettar, E. Carrera. Advanced Materials Research (2010), vol. 93-94, p. 190-193.
[3] *Equivalent electro-elastic properties of Macro Fiber Composite (MFC) transducers using asymptotic expansion approach.* F. Biscani, H. Nasser, S. Belouettar, E. Carrera. Composites Part B: Engineering (2011), vol. 42, p. 444-455.
[4] *Variable kinematic beam elements coupled via Arlequin method.* F. Biscani, G. Giunta, S. Belouettar, E. Carrera, H. Hu. Composite Structures (2011), vol.93, p. 697-708.
[5] *Hierarchical Modelling of Doubly Curved Laminated Composite Shells under Distributed and Localised Loadings.* G. Giunta, F. Biscani, S. Belouettar, E. Carrera. Composites Part B: Engineering (2011), vol. 42, p. 682-681.
[6] *Analysis of thin-walled beams via a one-dimensional unified formulation through a*

navier-type solution. G. Giunta, F. Biscani, S. Belouettar, E. Carrera. International journal of applied mechanics (2011), vol. 3, p. 407-434.
[7] *Toward micromechanics of coupled fields materials containing functionally graded inhomogeneities: multi-coating approach.* F. Biscani, Y. Koutsawa, S. Belouettar, E. Carrera. Mechanics of Advanced Materials and Structures (2011), vol. 18, p. 524-530.
[8] *Multi-scale Modelling of Sandwich Structures Using Hierarchical Kinematics.* Q. Z. He, H. Hu, S. Belouettar, G. Giunta, K. Yu, Y. Liu, F. Biscani, E. Carrera, M. Potier-Ferry. Composite Structures (2011), vol. 93, p. 2375-2383.
[9] *Variable kinematic beam elements coupled via Arlequin method.* F. Biscani, P. Nali, S. Belouettar, E. Carrera, H. Hu. Journal of Intelligent Material Systems and Structures (2012), in press.